# MULTIFRAGMENT EMISSION IN CENTRAL COLLISIONS OF $^{36}Ar+^{197}Au$ AT E/A = 50, 80 AND 110 MeV

By

Larry William Phair

A DISSERTATION

Submitted to
Michigan State University
in partial fulfillment of the requirements
for the degree of

DOCTOR OF PHILOSOPHY

Department of Physics and Astronomy

1993

ABSTRACT

MULTIFRAGMENT EMISSION IN CENTRAL COLLISIONS OF $^{36}Ar+^{197}Au$ AT E/A = 50, 80 AND 110 MeV

By

Larry William Phair

Multifragment disintegrations of highly excited nuclear systems may carry information about the equation of state and the liquid-gas phase transition of low density nuclear matter. The mechanism causing multifragment decays is, however, not yet understood. To study this phenomenon we constructed a low threshold $4\pi$ charged-particle detector, the Miniball, and studied the reaction of $^{36}Ar+^{197}Au$ at E/A=50, 80 and 110 MeV.

For central collisions, the chance for equilibration of the system is highest. We therefore determined the most efficient method of selecting central collisions by comparing the ability of several global observables to select events with suppressed projectile-like fragment emission and small anisotropic azimuthal emission patterns. Similar event selection was obtained by using the following global observables: the charged particle multiplicity $N_c$, the total transverse energy $E_t$, and summed charge emitted at midrapidity $Z_y$.

An average multiplicity of 4 intermediate mass fragments (IMF) was observed for the most central collisions at E/A=110 MeV. These IMF multiplicities are consistent with predictions from a statistical model for

evaporation from an expanding compound nucleus. The statistical decay model predictions are sensitive to the low-density nuclear equation of state.

The IMF yields are also consistent with predictions from a standard percolation model for the $^{36}Ar+^{197}Au$ system. Assuming a spherical decay geometry, percolation fails, however, to predict the measured fragment multiplicities for the heavier system $^{129}Xe+^{197}Au$ at E/A=50 MeV investigated by our group. For noncompact decay configurations (bubbles and toroids) the percolation model can reproduce the large fragment multiplicities observed for this reaction.

to Kendra, Nathan and Jordan

# ACKNOWLEDGMENTS

I would first like to thank my advisor Konrad Gelbke for his time, patience, teachings and leadership. His ability to cut to the core of a problem has made my work at the laboratory fruitful and enlightening. Bill Lynch, Betty Tsang, Scott Pratt and Hartmut Schulz have given their friendship as well as invaluable instruction during the time of this analysis. Wolfgang Bauer suggested and oversaw several theoretical projects, as well as sitting on my guidance committee. Maris Abolins, Aaron Galonsky and S.D. Mahanti gave a careful reading of this work and also served on my guidance committee.

Three postdocs gave me my first exposure to experimental work here at the lab. Dave Bowman, Nelson Carlin and Romualdo de Souza taught by example the virtue of hard work and took the time to share their knowledge of experimental nuclear physics. As they left, other capable scientists took their places. Nicola Colonna, Graham Peaslee, Carsten Schwarz, Thomas Glasmacher, Bill Llope and Carlos Montoya have added their friendship and guidance to my research.

My fellow graduate students have offered much support. Mike Lisa never minded being a sounding board for my ideas (some of which were not so bright, but he was always polite telling me so). He also had many helpful suggestions for my analysis. Erik Hendrickson, Paul (Rooster) McConville, Raman Pfaff, Don Sackett, George Jeffers, Mike Wilson and others helped me survive my course work during the first two years of graduate school. I am

especially indebted to two graduate students, Cathy Mader and Paul McConnville, without whom I am pretty sure I would not have passed the comprehensive exam the first time. Observing their approach to problem solving was very instructive. The graduate students in our group: Yeongduk Kim, Hongming Xu, Fan Zhu, Tapan Nayak, Wen Guang Gong, Damian Handzy, Wen Chien Hsi, Min-Jui Huang, James Dinius and Cornelius Williams have all spent long hours building and maintaining the Miniball and/or running my thesis experiment. Easwar Ramakrishnan, Shigeru Yokoyama, Afshin Azhari, Mathias Steiner, Phil Zecher, Tong Li, Dietrich Klakow, Qiubao Pan, Brian Young, Jim Bailey, Michael Fauerbach, Stephan Hannuschke, John Kelley, Eugene Gualtieri and others have also helped to make my experience enjoyable and instructive.

All of the staff deserve my thanks, but I would like to single out Jack Ottarson and Jim Vincent. I interrupted both of them countless times with different projects, requests, problems, etc., but every time they were always willing to help (quickly). This helped to smooth out what could have been rocky times during the construction of the Miniball.

None of my education would have been possible without my parents and the selfless hours they gave in teaching me everything (from music to Scouting). They nurtured in me a desire to learn for which I am eternally indebted.

And finally I am indebted to my wife, Kendra, for her love and patience and to our two boys, Nathan and Jordan. When I came home late at night there was something about a sleepy two-year-old saying "I love you to come home, Dad" that just helped keep things in perspective.

# Table of Contents

# List of Tables

# List of Figures

# Chapter 1 Introduction

Weakly-excited nuclei decay primarily by fission and light particle evaporation. For excitation energies much higher than the binding energy, explosive disintegration into light particles ($Z \leq 2$) takes place. Between these two extremes, there is a region in which copious production of intermediate mass fragments (IMF: $3 \leq Z \leq 20$) is observed [Ogil 91, Bowm 91, Wadd 85]. The mechanism causing multifragment decays is not yet understood and is a subject of current debate.

Many mechanisms have been proposed [Bert 83, Cser 86, Lync 87, Schl 87, Gros 90, Frie 90, More 75, Frie 83a, Frie 83b, Baue 87, Peil 89, Boal 88, Boal 90, Baue 85, Baue 86, Biro 86, Cerr 88] for the production of the fragments. For example, the action of thermal pressure may force hot nuclear systems to expand to low density where the exponential growth of density fluctuations may lead to a complete disintegration of the nuclear system [Bert 83, Schl 87], in analogy to a liquid-gas phase transition in infinite nuclear matter. Unfortunately, detailed comparisons of various fragment production models to experimental data have been lacking since few experiments [Doss 87, Boug 88, Troc 89, Boug 89, Kim 89, Blum 91, Ogil 91, Bowm 91] performed to date provided sufficient phase space coverage to allow the extraction of exclusive quantities.

Exclusive experiments have become necessary as different models, based on very different approximations, often give very similar results for inclusive data. Inclusive measurements suffer from the implicit averaging over impact parameter which makes it difficult to separate and understand statistical and dynamical effects. For studies addressing the thermodynamic properties of nuclear matter, the selection of central collisions is of particular interest since reaction zones formed in central collisions promise to reach the largest degree of equilibration. To address the question of multifragment decay of highly-excited nuclear systems and to provide exclusive (i.e. impact parameter selected) measurements for constraints on various theoretical models, we have measured fragmentation in the reaction $^{36}Ar+^{197}Au$ at E/A=50, 80 and 110 MeV.

After addressing the technique of impact parameter selection we select central collisions and study the IMF yields making comparisons with two statistical models. The measured IMF multiplicities from central collisions are compared with predictions from the expanding emitting source model, a model in which an equilibrated source loses mass by evaporation as it expands. The fragment measurements are also compared to predictions from percolation theory. Simple percolation theory is of interest since it allows the study of finite system effects in a well defined model which exhibits a phase transition in the limit of infinite systems. Statistical models are of interest since microscopic transport calculations [Boal 88, Boal 90] capable of treating nonequilibrium-fragment emission predict fewer fragments than observed experimentally [Bowm 91]. Dynamics, as treated by these models, may not play the decisive role in fragment production. In this context, it is interesting to neglect dynamical effects and explore to what extent fragment formation

could be dominated by the geometric considerations contained in the percolation ansatz.

The thesis is organized as follows: the experimental details are described in Chapters 2 and 3; Chapter 4 provides a detailed study of impact parameter selection for the $^{36}Ar+^{197}Au$ reaction at intermediate energies; in Chapter 5 several reaction characteristics are evaluated as a function of bombarding energy and impact parameter; in Chapter 6 comparisons are made to predictions from the emitting expanding source model and percolation theory, and in Chapter 7 we look for intermittency signals in central collisions; a summary and conclusions are given in Chapter 8.

# Chapter 2 MSU Miniball

## 2.1 Mechanical construction

The Miniball phoswich detector array is designed to operate in a vacuum vessel. An artist's perspective of the three-dimensional geometrical assembly is shown in Figure 2.1. The array consists of 11 independent rings coaxial about the beam axis. For ease of assembly, as well as servicing, the individual rings are mounted on separate base plates which slide on two precision rails. The rings and detector mounts are made of aluminum. Good thermal conductivity between detectors and the mounting structure allows the conduction of heat generated by the photomultiplier voltage divider network into the array superstructure. This heat is removed from the Miniball by cooling the base plates to 15°C. By this means, constant operating temperature in vacuum is achieved after a brief equilibration time. The individual detector mounts are designed to allow the removal of any detector without interfering with the alignment of neighboring detectors. The entire assembly is placed on an adjustable mounting structure which allows for the alignment of the apparatus with respect to the beam axis.

Figure 2.2 shows a half-plane section of the array in the vertical plane which contains the beam axis. Individual rings are labeled by the ring

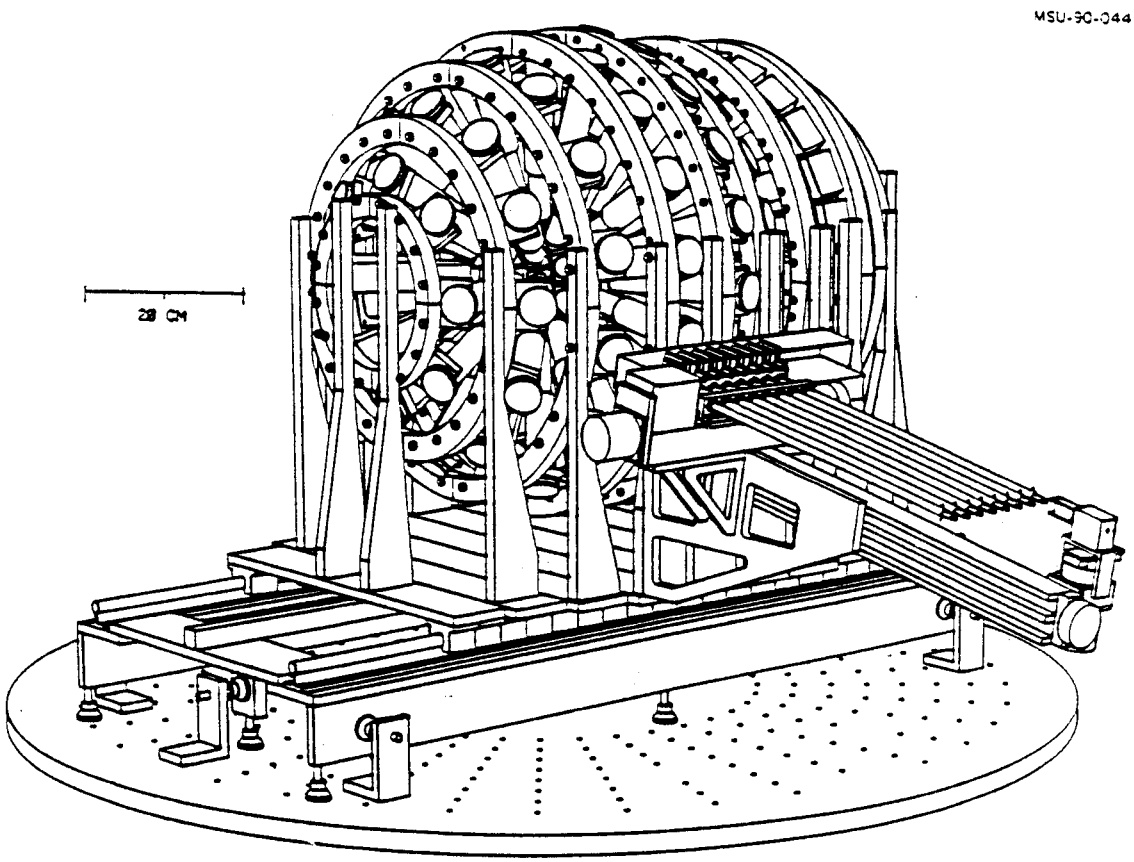


Figure 2.1 Artist's perspective of the assembly structure of the Miniball $4\pi$ fragment detection array. For clarity, electrical connections, the light pulsing system, and the cooling system have been omitted.

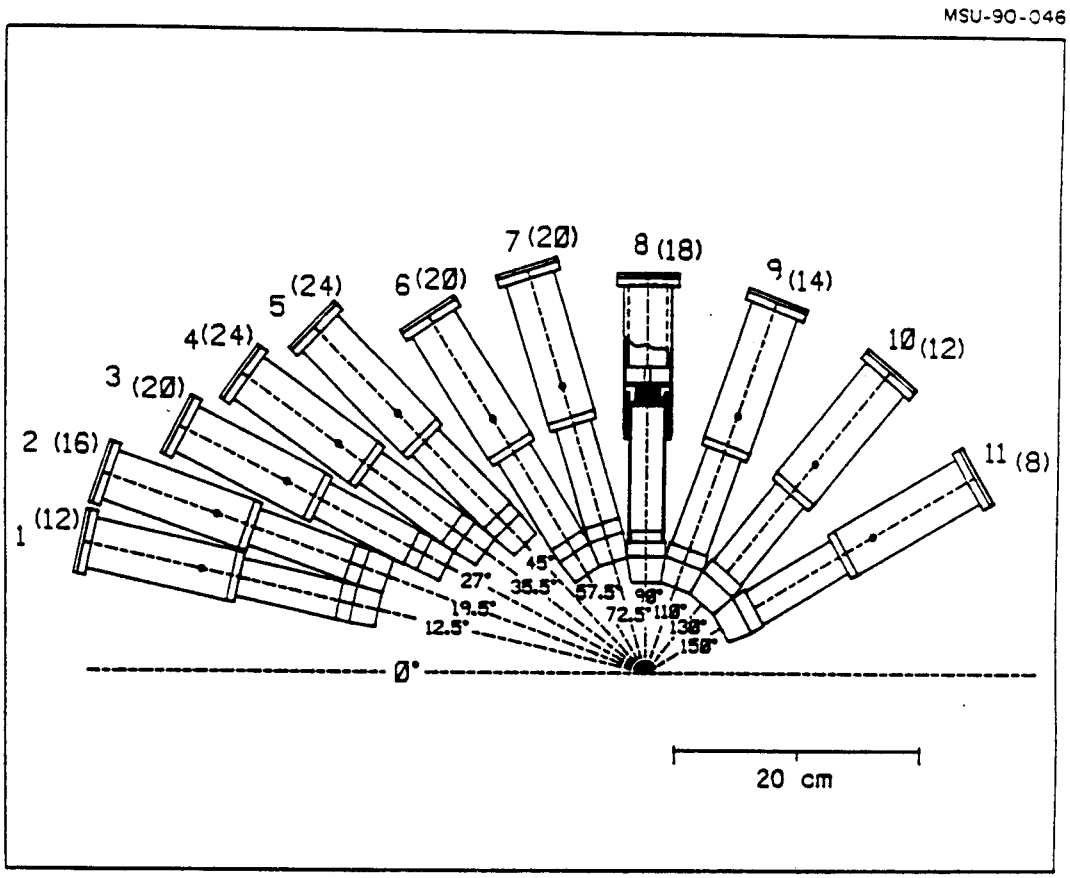


Figure 2.2 Half-plane section of the Miniball array. Individual detector rings are labeled 1 through 11. Numbers of detectors per ring are given in parentheses. The polar angles for the centers of the rings are indicated. The dashed horizontal line indicates the beam axis.

numbers 1-11 which increase from forward to backward angles. For each ring, the number of detectors is given in parentheses. For a given ring, the detectors are identical in shape and have the same polar angle coordinates with respect to the beam axis. These angles are indicated in Figure 2.2.

Since the angular distributions of the emitted particles are strongly forward peaked, the solid angle subtended by forward detectors is smaller than for backward detectors. Variations in solid angle were achieved largely by placing detectors at different distances from the target while keeping their size approximately constant. The front face geometries of the individual CsI(Tl) crystals are shown in Figure 2.3. Different detector shapes are labeled by the respective ring numbers with the number of detectors per ring given in parentheses (see Figure 2.2 for the definition of the ring numbers). The crystals are tapered such that the front and back surfaces subtend the same solid angle with respect to the target location. In order to reduce cost of fabrication, the curved surfaces were approximated by planar surfaces. The resulting loss in solid angle coverage is on the order of 2%, comparable in magnitude to the loss in solid angle coverage resulting from gaps between individual detectors (which must be provided to allow for mechanical tolerances and optical isolation between neighboring crystals). A listing of the detector solid angles is given in Table 2.1.

An isometric drawing of the target insertion mechanism is shown in Figure 2.4. The targets are mounted on frames made of flat shim stock 0.2 mm thick. Each target frame is attached to an insertion rod. The insertion rods are mounted on a tray which can be moved parallel to the beam axis. An electromagnetic clutch provides the coupling to the insertion and retraction drive once a target rod is in the appropriate position. A third drive allows rotation of an inserted target about the axis of the insertion rod. This

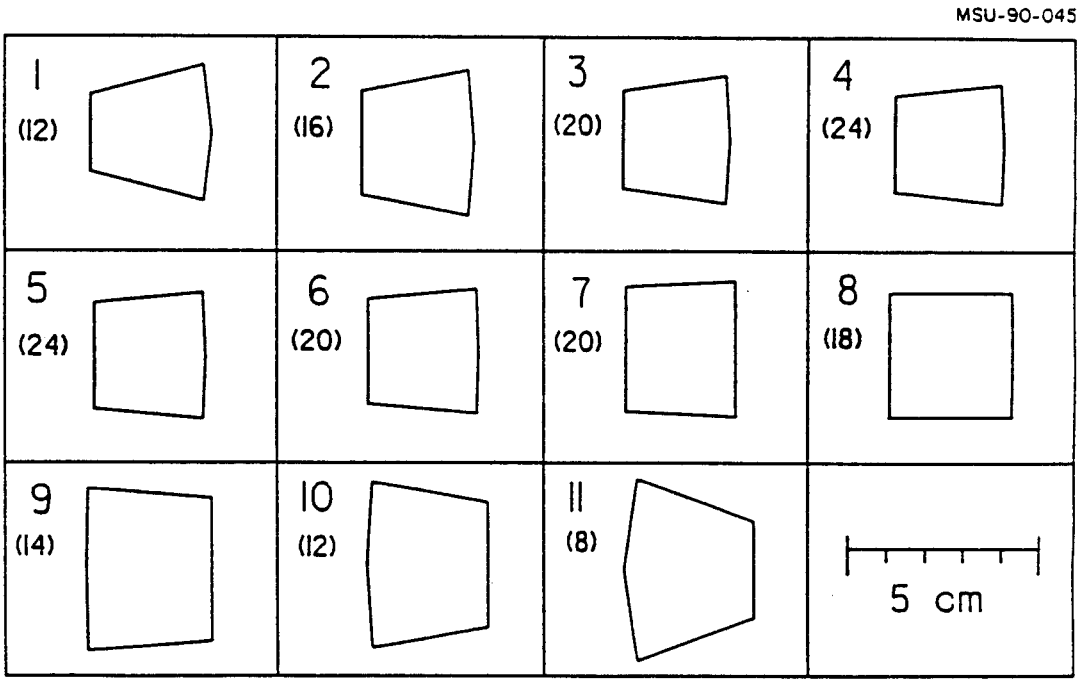


Figure 2.3 Front views of different detector shapes. The detectors are labeled by their ring number. Numbers of detectors per ring are given in parentheses.

Table 2.1 Coverage in solid angle, polar angle, azimuthal angle and distance to the target (d) for individual detectors of the Miniball.

| Ring | Detectors | $\Delta\Omega$ (msr) | $\theta$ (°) | $\Delta\theta$ (°) | $\Delta\phi$ (°) | d (mm) |
|---|---|---|---|---|---|---|
| 1 | 12 | 12.3 | 12.5 | 7 | 30.0 | 260 |
| 2 | 16 | 14.7 | 19.5 | 7 | 22.5 | 220 |
| 3 | 20 | 18.5 | 27.0 | 8 | 18.0 | 180 |
| 4 | 24 | 22.9 | 35.5 | 9 | 15.0 | 160 |
| 5 | 24 | 30.8 | 45.0 | 10 | 15.0 | 140 |
| 6 | 20 | 64.8 | 57.5 | 15 | 18.0 | 90 |
| 7 | 20 | 74.0 | 72.5 | 15 | 18.0 | 90 |
| 8 | 18 (-1) | 113.3 | 90.0 | 20 | 20.0 | 70 |
| 9 | 14 | 135.1 | 110.0 | 20 | 25.7 | 70 |
| 10 | 12 | 128.3 | 130.0 | 20 | 30.0 | 70 |
| 11 | 8 | 125.7 | 150.0 | 20 | 45.0 | 70 |

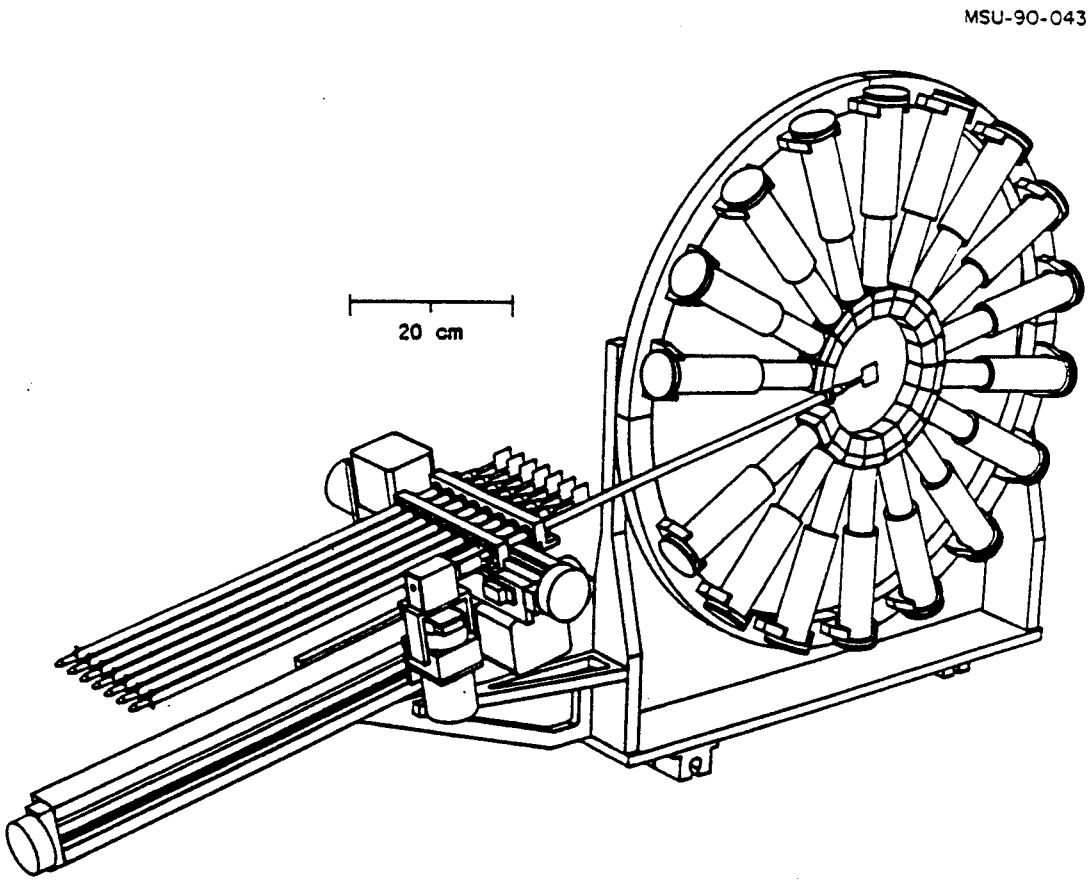


Figure 2.4 Isometric view of the target insertion mechanism.

rotation of the target is useful for the determination of the shadowing a detector experiences when it is located in the plane of the target frame. Also, sources can be mounted in the target position and rotated to point to different areas of the Miniball for debugging and calibration purposes.

In its present configuration, the detector array covers a solid angle corresponding to about 89% of $4\pi$. The loss in solid angle can be decomposed into the following contributions:

(i) beam entrance and exit holes (4% of $4\pi$);

(ii) approximation of the curved surfaces corresponding to constant polar angle by planar surfaces (2% of $4\pi$);

(iii) optical isolation of detectors and allowance for mechanical tolerances (4% of $4\pi$);

(iv) removal of one detector (ring 8 position 6) at $\theta=90°$ to provide space for target insertion mechanism (1% of $4\pi$).

## 2.2 Detector design

### Phoswich construction

All phoswich detectors of the array are composed of a thin plastic scintillator foil, spun from Bicron BC-498X scintillator solution, and a 2 cm CsI(Tl) scintillator crystal. The foils in Rings 2-11 have an average thickness of 4 mg/cm$^2$ or 40 μm while Ring 1 foils have an average thickness of 5 mg/cm$^2$ or 50 μm. A schematic of the detector design is given in Figure 2.5. In order to retain flexibility in the choice of scintillator foil thickness, the scintillator foil is placed on the front face of the CsI(Tl) crystal without bonding material. The back face of the CsI(Tl) scintillator is glued with optical cement (Bicron BC600) to a flat light guide made of UVT Plexiglas. This light guide is glued to a

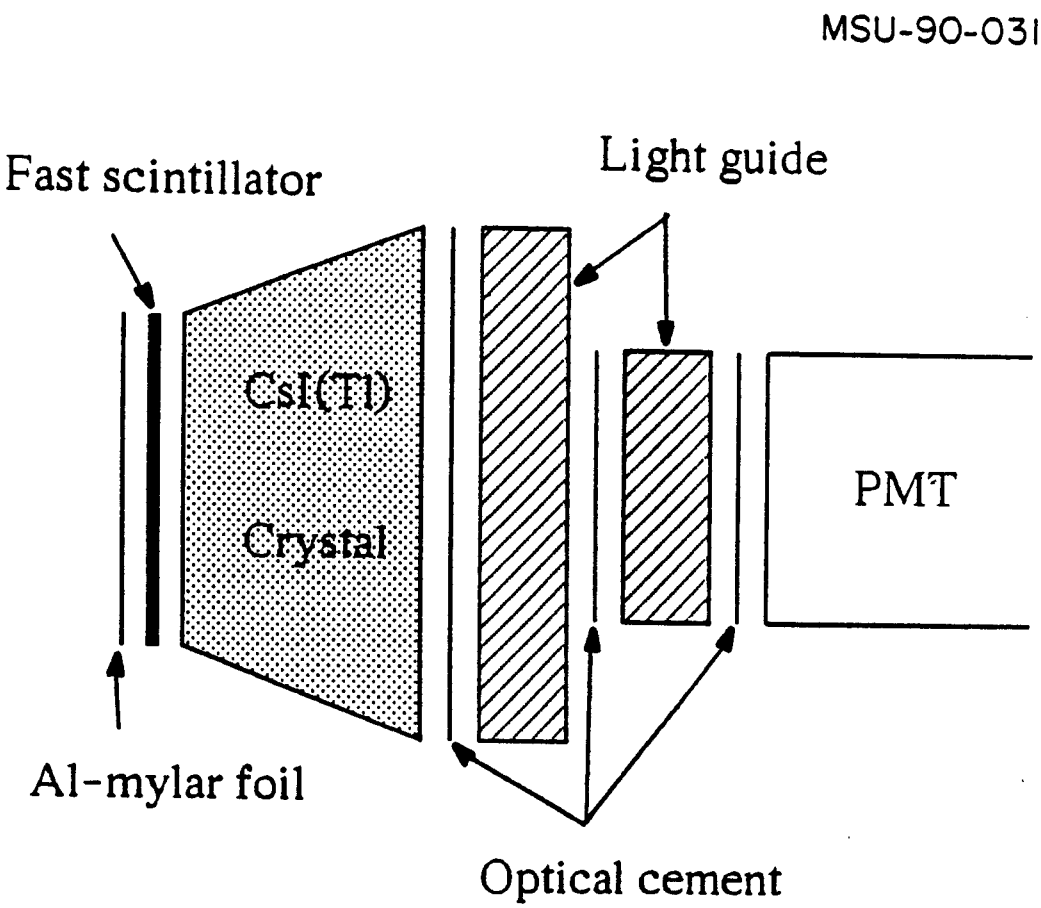


Figure 2.5 Schematic of phoswich assembly of individual detector elements. The μ-metal shield covering the photomultiplier is not included.

second cylindrical piece of UVT Plexiglas (9.5 mm thick and 25 mm in diameter) which, in turn, is glued to the front window of the photomultiplier tube (Burle Industries model C83062). The photomultiplier tube and the cylindrical light guide are surrounded by a cylindrical μ–metal shield (not shown in the figure). Front and back faces of the CsI(Tl) crystals are polished; the tapered sides are sanded and wrapped with white Teflon tape. The front face of the phoswich assembly is covered by an aluminized mylar foil (0.15 $mg/cm^2$ mylar and 0.02 $mg/cm^2$ aluminum).

The primary scintillation of the plastic scintillator used has its maximum intensity at 370 nm. In bulk material of the scintillator, the intensity maximum is shifted to 420 nm by the addition of a wavelength shifter. Our scintillator foils are, however, too thin for an effective wavelength shift and maximum emission remains in the far blue region of the spectrum. The absorption of this light in CsI(Tl) places a constraint on the maximum useful thickness of the CsI(Tl) crystals. Additional absorption in the light guides can be minimized by using UVT Plexiglas rather than standard Plexiglas light guides. Such considerations become particularly important for phoswich detectors utilizing thin scintillator foils in efforts to reduce particle detection thresholds.

Figure 2.6 shows a photograph of the basic photomultiplier assembly used for all detectors. The phoswich and matching first light guide have not yet been attached. A precision-machined aluminum ring is glued to the μ-metal shield surrounding the photomultiplier and the cylindrical light guide. This ring provides the alignment for a precision-machined aluminum can which houses the voltage divider and which defines the detector alignment when bolted to the rings of the array support structure. In order to expose the voltage divider chain, this aluminum can has been removed and placed next

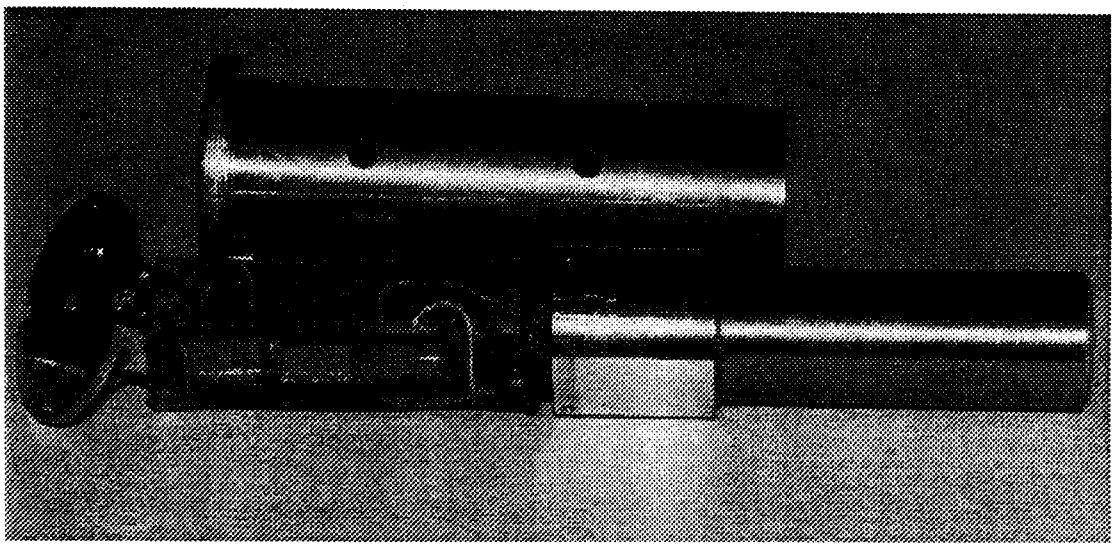

Figure 2.6 Photograph of photomultiplier assembly. The scintillator and the first matching light guide are removed. The ring glued to the μ-metal shield defines the alignment of the can housing the voltage divider. The can has been removed to expose the voltage divider.

to the photomultiplier. The active voltage divider chain is soldered to the flying leads of the phototube. To prevent destruction of the FETs by sparking during operation in poor vacuum, the entire divider chain, including the leads to the photomultiplier tube, is encapsulated in silicone rubber (Dow Chemical Sylgard 184). Vacuum accidents occurring with fully biased detectors do not lead to divider chain failures. In fact, the detectors can survive a full pumping cycle from atmospheric pressure to vacuum with bias applied to them.

The 10-stage Burle Industries model C83062E photomultiplier tube was chosen because of its good timing characteristics ($\tau_R \approx 2.3$ ns), its large nominal gain ($\approx 10^7$) and its good linearity for fast signals. Since the apparatus is designed to operate in vacuum, active divider chains were chosen to minimize the generation of heat. A schematic of the active divider chain is given in Figure 2.7. The final stages of the divider chain are of the "booster" type which provide improved linearity for high peak currents generated by large signals of the fast scintillator.

## Uniform scintillation response of CsI(Tl)

Previous experience with CsI(Tl) crystals used for the detection of energetic particles had revealed difficulties with the production of scintillators with uniform scintillation response [Gong 88, Gong 90]. Therefore, considerable attention was paid to select CsI(Tl) crystals of uniform scintillation efficiency. In previous tests of large cylindrical crystals [Gong 88, Gong 90], nonuniformities of the scintillation efficiency were detected by measuring the response to collimated $\gamma$-rays. Such measurements are relatively easy to perform since they can be done in air. However, they are less suitable for small volume crystals, since collimated $\gamma$-rays sample a relatively

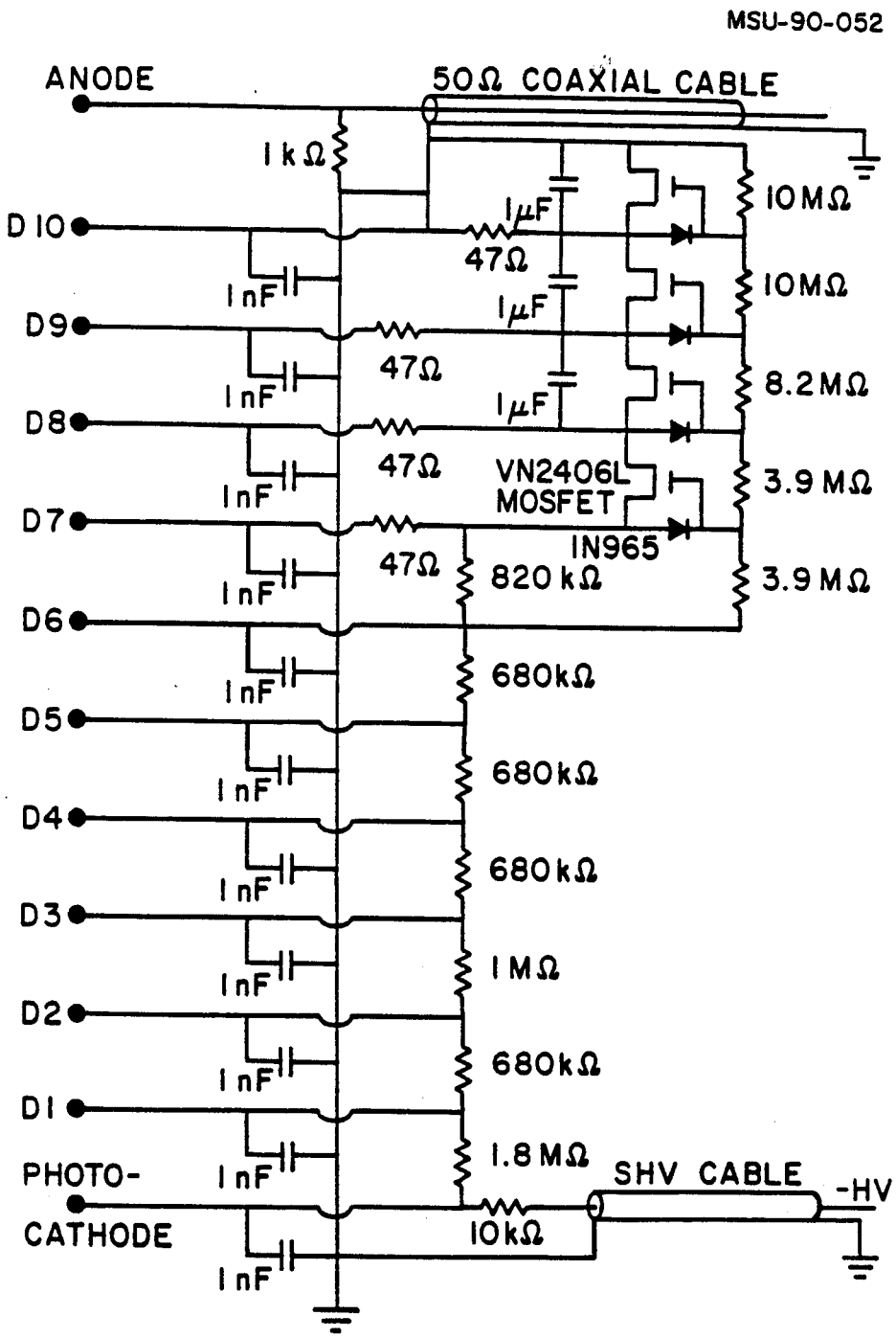


Figure 2.7 Schematic of the active voltage divider used for the Miniball detectors.

large volume of the crystal. Small scale fluctuations of the scintillation efficiency may remain undetected. In addition, measurements for small noncylindrical crystals are less precise, since the shape of the Compton background depends on the position of the collimated γ-ray source. Such dependencies lead to additional uncertainties in the extraction of the photopeak position.

It was determined, however, that nonuniformities of the scintillation efficiency can be detected very sensitively by scanning the CsI(Tl) crystals with a collimated α-source in vacuum. All crystals ordered from various manufacturers were rectangular in shape with dimensions of 2 in.×1.5 in.× 1 in. They were polished at the front and back faces (with dimensions of 2 in.×1.5 in.) and sanded at the sides. The back face was optically coupled to a clear acrylic light guide with the same dimensions as the crystal. This light guide, in turn, was optically connected to a photomultiplier tube of 1 in. diameter. The sides of the CsI(Tl) crystal and of the light guide were wrapped with white Teflon tape. By covering the front face of the CsI(Tl) scintillator with an aluminized mylar foil, a uniform light collection efficiency was achieved. (Without a reflective entrance foil, the light collection efficiency decreased by about 5% from the center of the front face to its sides.) The front face of the crystal was scanned in vacuum and the peak location of the 8.785 MeV α-line from a collimated $^{228}$Th α-source was monitored. In order to avoid edge effects, regions within about 2mm of the side boundaries of the crystal were not scanned. Most tests were performed with a simple multichannel analyzer equipped with a peak sensing ADC; in those instances the anode signal of the photomultiplier was shaped and amplified with standard electronics, using integration and differentiation times of 1 μs.

Figure 2.8 shows the results of a scan for a crystal exhibiting a large gradient of the scintillation efficiency. The horizontal axis of the plot shows the location of the collimated α-source with respect to the center, along the short symmetry axis of the front face. Different surface treatments of the front face of the scintillator did not affect the measured variation of the scintillation efficiency. In order to demonstrate that such variations were related to the bulk material of the scintillator, we exchanged the role of front and back faces of this scintillator and performed an equivalent scan of the parallel surface (i.e. the previous back face). The results of the two scans are compared by the solid and open points in Figure 2.8 (The coordinate system was kept fixed with respect to the CsI(Tl) crystal.) Nearly identical variations of the scintillation efficiency are observed across the two parallel scintillator surfaces, indicating that the measured large gradient of the scintillation efficiency persists through the bulk material of the sample.

The measurements shown in Figure 2.9 were performed by integrating the anode current of the photomultiplier with a charge integrating ADC using time gates of $\Delta t$=0.1-0.5 μs and $\Delta t$=1.1-4.1 μs, which select the fast and slow scintillation components of CsI(Tl). The fast component exhibits a larger variation of the scintillation efficiency than the slow component. Since the relative intensity of fast and slow scintillation components depends strongly on the Tl concentration [Birk 64, Mana 62], the observed variations of scintillation efficiency are most likely due to gradients in the Tl concentration.

Crystals incorporated into the Miniball were preselected by scanning the 1.5 in.× 2.0 in. rectangular surface of original crystals along two perpendicular axes and requiring a uniformity of scintillation response better than 3%. The preselected crystals were then milled into their final shapes and

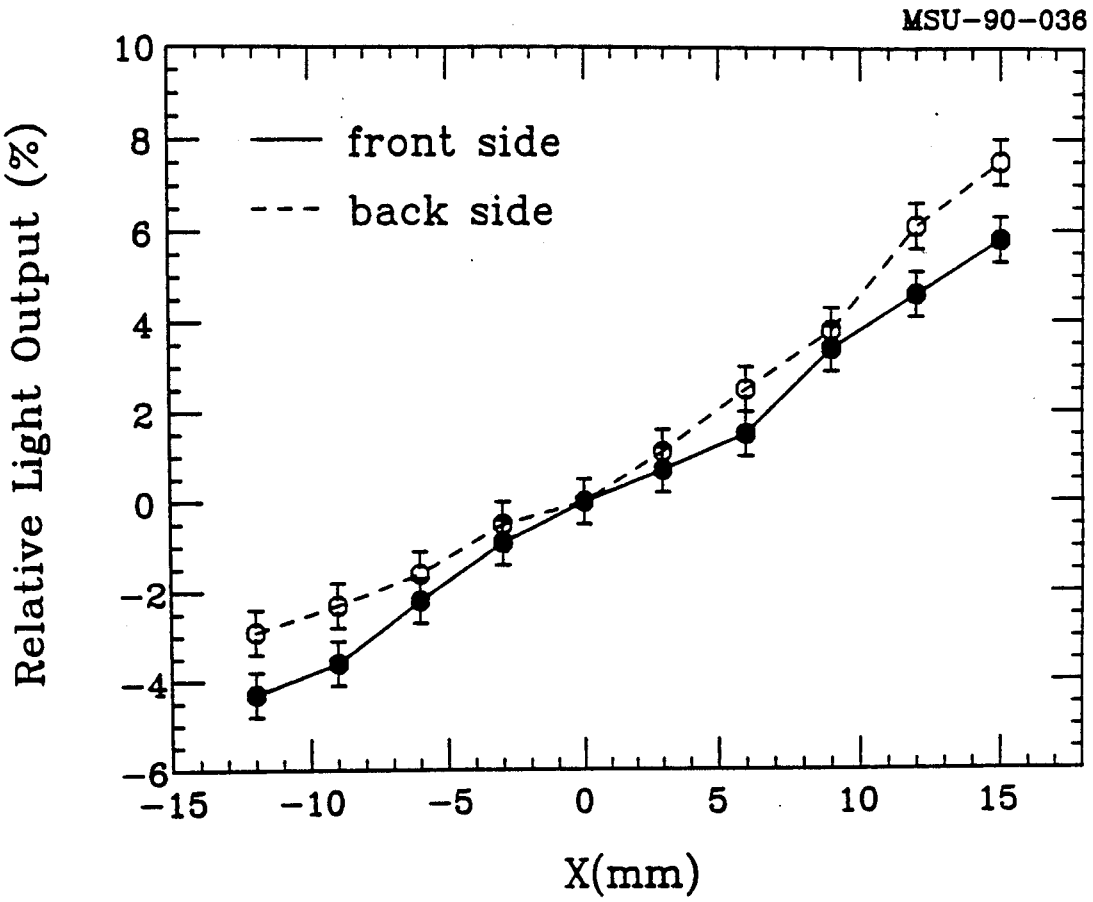


Figure 2.8 Relative variation of scintillation efficiency measured for two parallel surfaces of a CsI(Tl) crystal by using a collimated α-source. The axes of the coordinate system are parallel to the sides of the scintillator. The coordinates are fixed with respect to the scintillator.

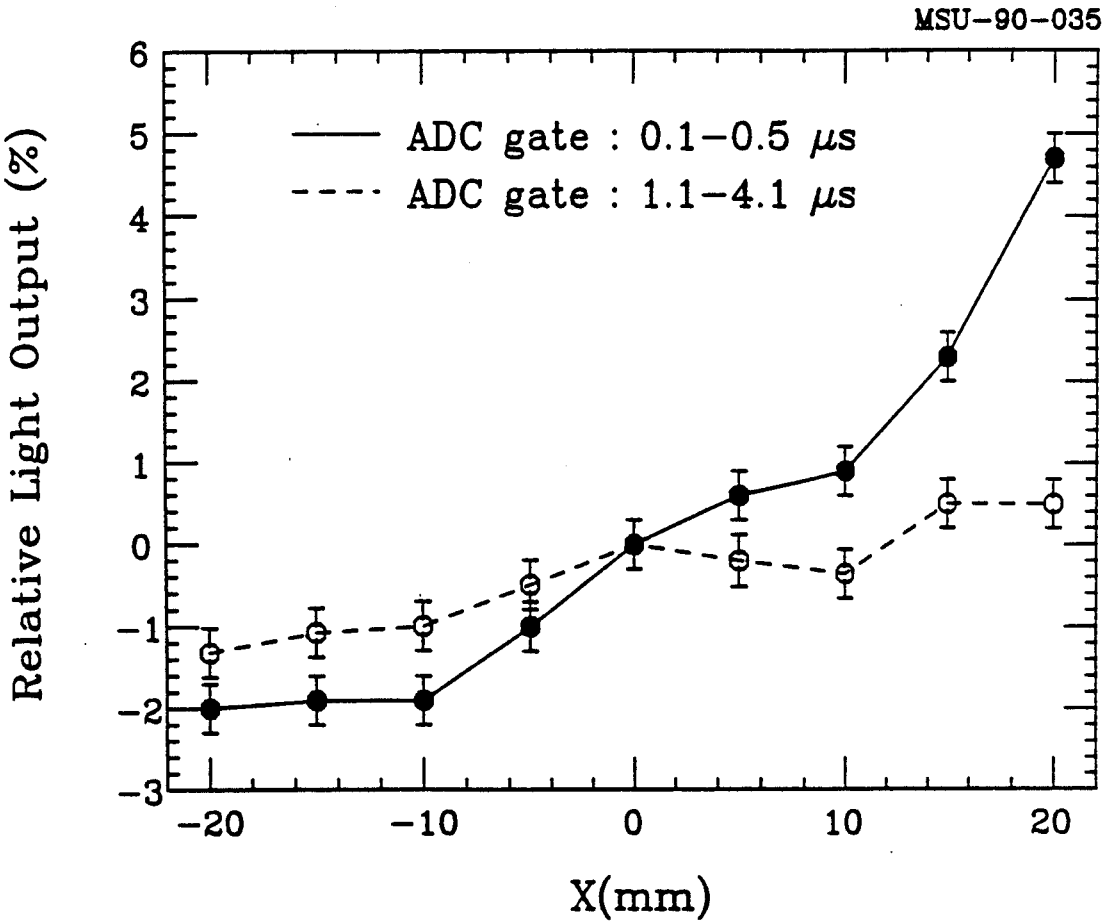


Figure 2.9 Variations of scintillation efficiency measured with a charge integrating ADC for two different time gates selecting the fast and slow components of scintillation for CsI(Tl).

scanned a second time, requiring uniformity of response within 2.5%. The preselection process avoided expensive machining of poor quality crystals; it was about 90% efficient for the selection of crystals of the desired quality.

Figure 2.10 compares variations of scintillation efficiency detected with collimated α-particles of 8.785 MeV energy (source: $^{228}$Th) and γ-rays of 662 keV energy (source: $^{137}$Cs). The left- and right-hand panels give examples for a rejected and an accepted crystal, respectively. The enhanced sensitivity of the α-particle scan is obvious. It is probably caused by the fact that α-particles sample a much smaller volume than γ-rays and that the two kinds of radiation exhibit different sensitivities to the Tl concentration [Birk 64, Mana 62].

## Scintillator foils

Scintillator foils were spun [Meye 78, Norb 87] from Betapaint, Bicron BC-498X plastic scintillator dissolved in xylene. The original solution was ordered with a 40% weight ratio of solute to solvent. It was then diluted by adding xylene until the solution had the desired viscosity of 20-30 P.

The viscosity was determined by measuring the terminal speed v of a steel ball sinking in a glass tube filled with a sample of Betapaint. Correcting Stoke's Law for the finite diameter of the glass tube gives the following expression for the viscosity [Dins 62]:

$$\eta = \frac{2gr^2(\rho_0 - \rho)}{9v}\left[1 - 2.104\left(\frac{r}{R}\right) + 2.09\left(\frac{r}{R}\right)^3 - 0.95\left(\frac{r}{R}\right)^5\right]. \qquad (2.1)$$

Here, $\eta$ denotes the viscosity, $r$ and $R$ are the diameters of the steel ball and the glass tube, $g$ is the gravitational acceleration and $\rho_0$ and $\rho$ are the densities of the steel ball and the Betapaint, respectively.

For the fabrication of scintillator foils, a glass plate of 23 cm diameter was mounted horizontally on a small platform connected to the drive of an

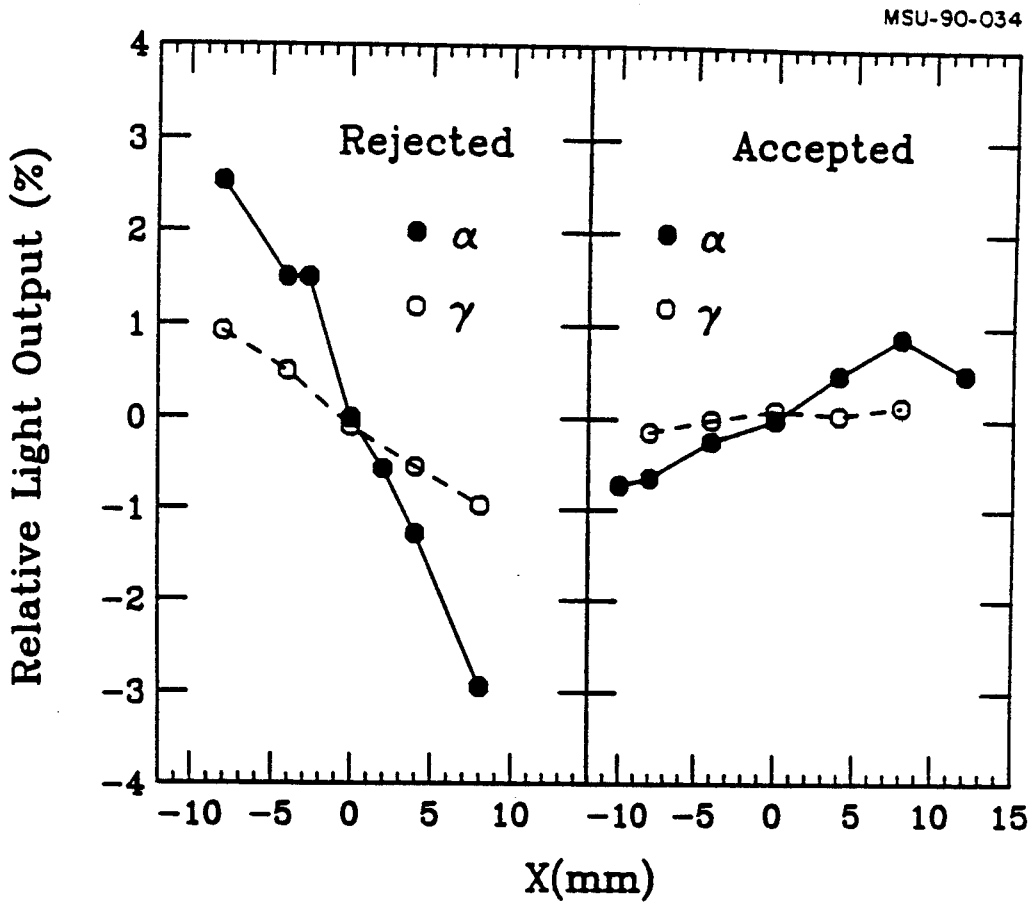


Figure 2.10 Variations of scintillation efficiency detected with collimated α-particles of 8.785 MeV energy (solid points) and collimated γ-rays of 662 keV energy (open points). The left-hand panel shows the measurement for a detector which was rejected. The right-hand panel shows the measurement for a detector which was incorporated in the Miniball.

electrical motor which allowed the plate to spin about its center at a preselected speed. To facilitate the removal of spun foils, the glass plate was covered successively with metasilicate solution and Teepol 610 and then wiped to leave only a thin film of the releasing agents on the glass substrate. An appropriate amount of Betapaint was poured on the center of a glass plate. In order to provide rapid spreading of the initial solution, the plate was spun at an enhanced speed for the first few seconds until the entire plate was covered with Betapaint. Following this rapid startup, the glass plate was spun at the preset rotational frequency for approximately 4 minutes until a solid foil had formed. After spinning, the glass plate was stored in a flow of dry nitrogen for about eight hours. The foil was then peeled from the glass plate, mounted on a frame, and placed in a dry nitrogen atmosphere for another 24 hours to allow further evaporation of residual xylene.

We obtained good and reproducible results by using dilute solutions and spinning at low rotational frequencies. A number of measurements were performed to determine the relation between rotational frequency and foil thickness. The results of these measurements are shown in Figure 2.11. For each foil, thickness and homogeneity were determined by scanning the foil in vacuum with a collimated $^{228}$Th $\alpha$-source and measuring the energy of the transmitted $\alpha$-particles in a calibrated silicon detector. The energy loss in the foil was then converted to an areal density according to reference [Litt 80]. The spun foils were uniform in thickness to within typically 1-2% over an area of $7\times7$ cm$^2$. Scintillator foils used for instrumenting the Miniball in its present configuration were selected to have a thickness of $4.0\pm0.12$ mg/cm$^2$.

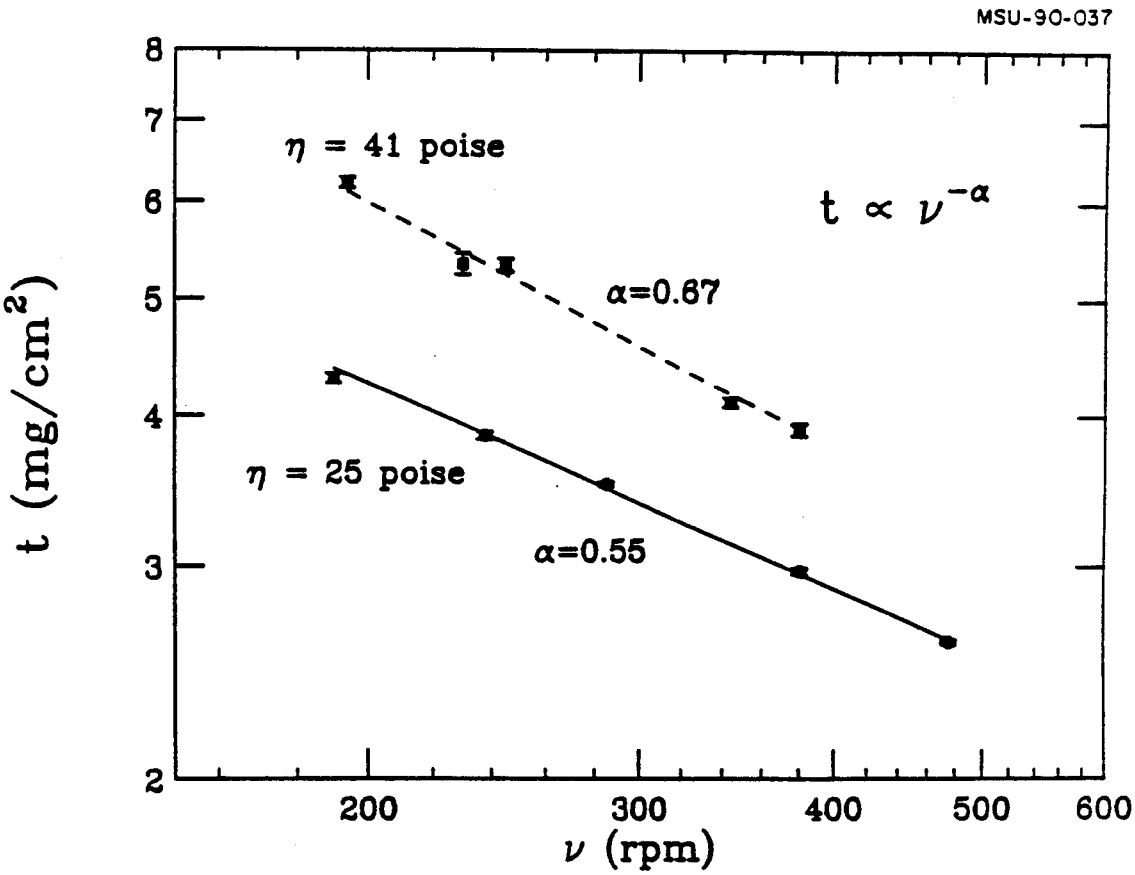


Figure 2.11 Relation between scintillator foil thickness and rotational frequency of spinning measured for solutions of Betapaint of different viscosity. The lines show fits with the power law $t \propto \nu^{-\alpha}$.

## Light pulser system

Gain drifts of the photomultiplier tubes are monitored by a simple and compact light pulser system which operates in vacuum. In order to preserve the modularity of the device and avoid unnecessary removal of optical fibers during transport, each detector ring is provided with its own light pulser system. Figure 2.12 shows schematics of the mechanical assembly of the light pulser system and of the driving circuit for the light emitting diodes (LEDs) which is triggered by an external NIM logic signal. During experiments, the light pulser is triggered at a rate of about 1 Hz. Light is generated by simultaneously pulsing an array of eight LEDs (Hewlett Packard HLMP-3950) which generate light at wavelengths around 565 nm. The emitted light is diffused by reflection from an inclined Teflon surface. Light fibers which view only the scattered light transport the light to the individual photomultiplier tubes.

Because of temperature fluctuations and aging effects, operation of light emitting diodes is not stable over long periods of time. Therefore, the intensity of each light pulse is monitored by two PIN diodes (Hamamatsu S1223) read out by standard solid state detector electronics. The ratio of the signals of the two PIN diodes can be used to monitor their stability. The ratio of PIN diode and photomultiplier signals can then be used to monitor the gain of the individual photomultiplier tubes according to the relation

$$Ch' = Ch \times \left( \frac{1 + \Delta PD}{1 + \Delta PMT} \right). \qquad (2.2)$$

Here, $Ch$ denotes the ADC conversion measured for a given event, $Ch'$ is the conversion corrected for gain shifts and $\Delta PD$ and $\Delta PMT$ are percentage changes (measured with respect to some arbitrary time t=0) of the average of the two PIN diodes and the individual photomultiplier signals for LED generated light pulser events. Better than 1% gain stabilization is achieved if

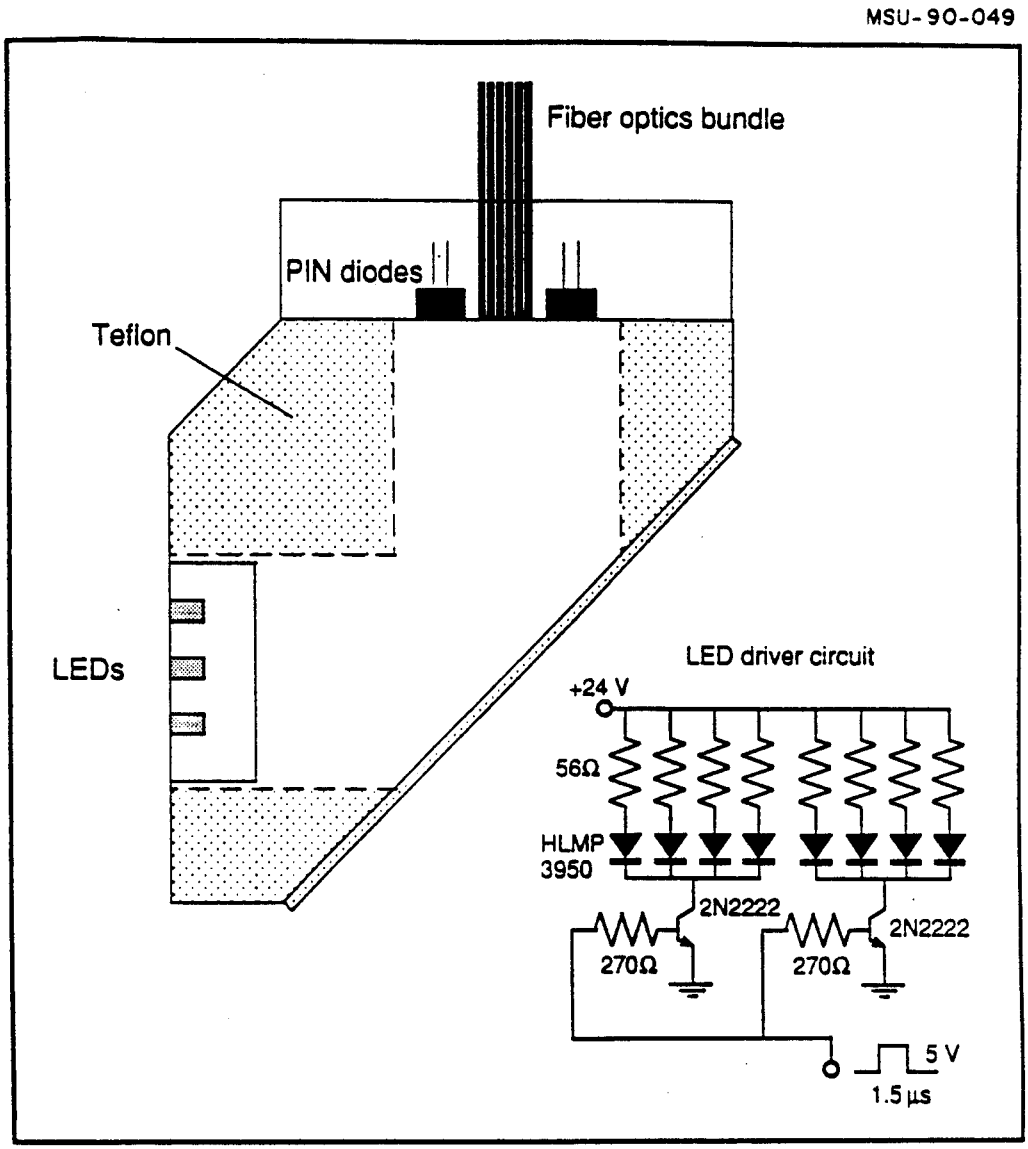


Figure 2.12 Schematics of light pulser assembly and LED trigger circuit.

the temperature of the CsI(Tl) crystals is kept constant. (Variations of the scintillation efficiency of CsI(Tl) caused by temperature fluctuations cannot be detected with the light pulser.) It was verified, however, that active cooling of the base plate ensures rapid achievement of a stable operating temperature for the Miniball.

Figure 2.13 illustrates the gain stabilization achieved with the light pulser system. The gain variations of a photomultiplier (enhanced by variations of the supply voltage) were directly measured by irradiating a CsI(Tl) crystal with α-particles emitted from a collimated 228Th source and monitoring the peak location of the 8.785 MeV α-line; they are shown by the open points in the figure. The solid points in the figure show the peak positions obtained in the off-line analysis after correcting the gain variations according to information obtained by the light pulser system. Gain stability to better than 1% was achieved.

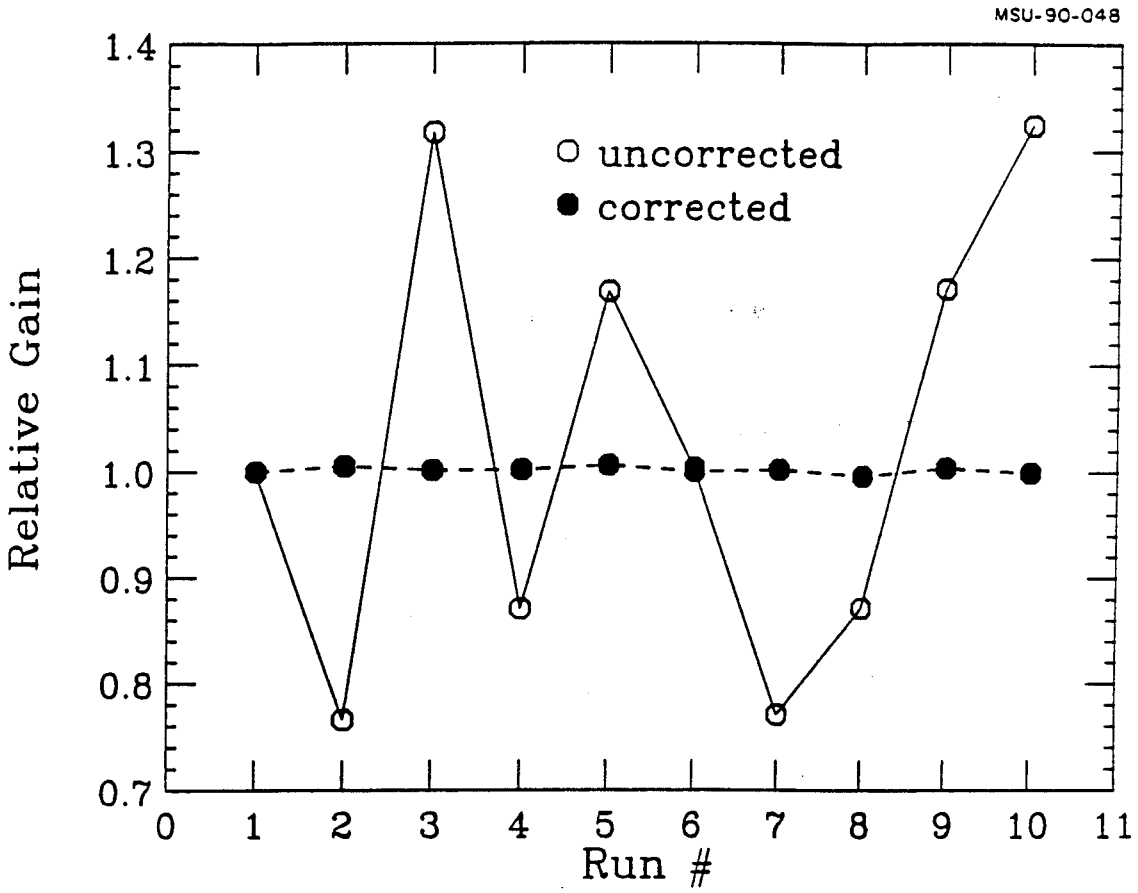


Figure 2.13 Open points – gain variations of a CsI(Tl) photomultiplier assembly determined by measuring the detector response to 8.785 MeV $\alpha$ particles. Solid points – same data corrected for gain shifts in the off-line analysis by using information from the light pulser system.

# Chapter 3 Experimental Setup and Data Reduction

Details of the $^{36}Ar+^{197}Au$ and $^{129}Xe+^{197}Au$ experiments along with techniques used to extract particle identification and energies are described in the following sections. As the thrust of this thesis work is the study of the reaction $^{36}Ar+^{197}Au$ at E/A=50, 80 and 110 MeV, the focus of this chapter will be on details of this experiment. Only sparse details will be given with respect to the $^{129}Xe+^{197}Au$ at 50 MeV/nucleon and $^{36}Ar+^{197}Au$ at 35 MeV/nucleon experiments.

## 3.1 Experimental setup

The experiments were performed with $^{36}Ar$ and $^{129}Xe$ beams extracted from the K500 and K1200 cyclotrons at the National Superconducting Cyclotron Laboratory of Michigan State University. The argon beam energies were E/A=35, 50, 80 and 110 MeV, and extracted intensities were typically $10^8$ particles per second. The xenon beam energy was E/A=50 MeV with intensities of about $10^7$ particles per second. The areal density of the gold targets was approximately 1 mg/cm$^2$.

Light particles and complex fragments were detected with the MSU Miniball phoswich detector array. For the argon beam energy of E/A=35 MeV

the array covered scattering angles of $\Theta_{lab}$=16°-160° (rings 2-11) and a solid angle corresponding to 87% of 4π. At beam energies of E/A=50, 80 and 110 MeV, the array covered scattering angles of $\Theta_{lab}$=9°-160° (rings 1-11) and a solid angle corresponding to 89% of 4π. Details about the detector geometry are given in Chapter 2.

For the $^{129}Xe+^{197}Au$ experiment the Miniball consisted of 171 detectors (rings 2-11 with 4 detectors missing from ring 2) with a solid angle coverage of approximately 87% of 4π. At very forward angles 2°-16°, fragments of charge Z=1-54 were detected with high resolution using a 16-element Si (300 μm)-Si(Li) (5 mm) - plastic (7.6 cm) array [Keho 92] with a geometrical efficiency of 64%. Where counting statistics allowed, individual atomic numbers were resolved for Z=1-54. Representative detection thresholds for fragments of Z=2, 8, 20 and 54 fragments were approximately 6, 13, 21 and 27 MeV/nucleon. Energy calibrations were obtained by directing 18 different beams ranging from Z=1 to 54 into each of the 16 detector elements [McMa 86]. The energy calibration of each of these detectors is accurate to better than 1%, and position resolutions of ±1.5 mm are obtained. The complete detector system subtended angles from 2°-160° with respect to the beam axis and had a geometric acceptance of 88% of 4π.

The detector array was actively cooled and temperature stabilized. Gain drifts of the photomultiplier tubes were monitored by a light pulser system (see Chapter 2). All events in which at least two detectors fired were recorded on magnetic tape. Random coincidences were negligible due to the low beam intensity.

Each Miniball phoswich detector consisted of a 40 μm (4 mg/cm$^2$) thick plastic scintillator foil backed by a 2 cm thick CsI(Tl) crystal. All detectors had aluminized mylar foils (0.15 mg/cm$^2$ mylar and 0.02 mg/cm$^2$ aluminum)

placed in front of the plastic scintillator foils. As a precaution against secondary electrons, the detectors of ring 11 ($\Theta_{lab}$=140°-160°) were covered by Pb-Sn foils of 5.05 mg/cm$^2$ areal density for the higher energy argon experiments (E/A=50, 80 and 110 MeV) and rings 2 and 3 were covered by aluminum foils of 0.81 mg/cm$^2$ for the lowest bombarding argon energy. In the xenon induced reaction, rings 9-11 of the Miniball were covered with the Pb-Sn foils. Particles punching through the 4 mg/cm$^2$ plastic scintillator foils were identified by atomic number up to Z=18. Hydrogen and helium were identified by isotope as well. Approximate energy thresholds are $E_{th}/A \cong 2$ MeV for Z=3, $E_{th}/A \cong 3$ MeV for Z=10 and $E_{th}/A \cong 4$ MeV for Z=18 fragments. Low energy particles stopped in the scintillator foils were recorded but could not be identified by atomic number.

## 3.2 Data acquisition electronics

Figure 3.1 shows a block diagram of the data acquisition electronics for the $^{36}Ar+^{197}Au$ experiments at E/A=50, 80 and 100 MeV where the Miniball ran as an independent detector. A fast clear circuit (not shown) was added to the acquisition electronics for the $^{129}Xe+^{197}Au$ experiment where the Miniball ran as a slave to the forward array. In events where the Miniball detected particles but nothing was detected in the forward array, the fast clear vetoed the gate to the tail FERAs, cleared the fast, slow, tail and time FERA, and cleared the bit register.

Figure 3.2 shows the gate widths for the fast, slow and tail and their relative timing along with a typical signal from a Miniball detector. During the CAMAC readout of the FERAs, integer*2 words for fast, slow, tail and time are written to tape for detectors that have signals above threshold. The dynamic range of the FERA is 2048 channels.

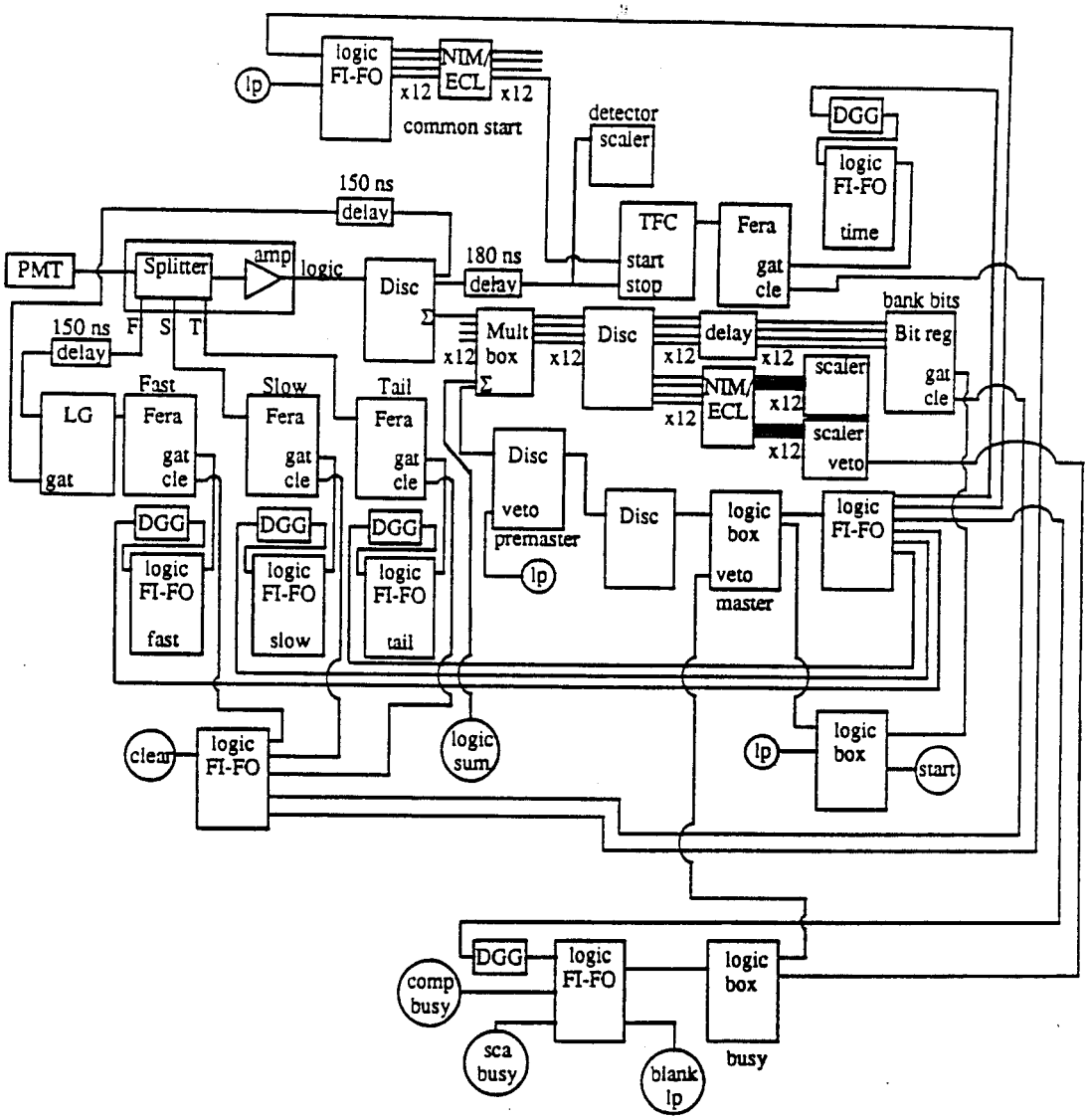


Figure 3.1 Schematic diagram of the data acquisition of the electronics of the Miniball.

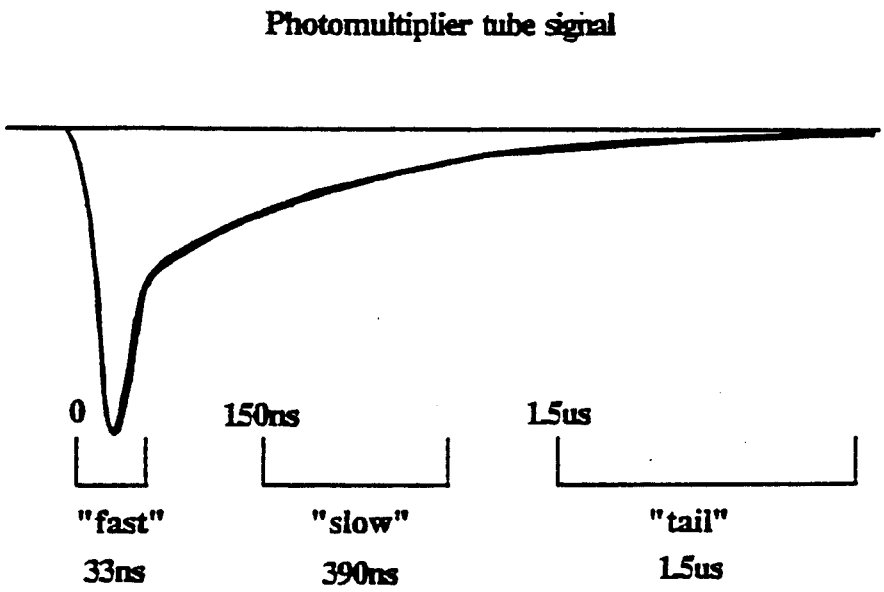


Figure 3.2 Timing and widths of the fast, slow and tail gates

## 3.3 Particle identification

Typical spectra used for on-line analysis are shown in Figures 3.3 and 3.4. These spectra were generated for detector 3-6 using one run of the $^{36}Ar+^{197}Au$ reaction at 110 MeV/nucleon (about 4 hours of beam time, $\approx 10^7$ events in the Miniball). By plotting the fast versus slow components of the signal (here slow=slow FERA word/4 and fast=fast FERA word/4), clear element identification is obtained. Using the tail (tail=tail FERA word/4) versus slow, isotope resolution for H and He is obtained. The lines in Figure 3.4 are used later to make isotope identification easier.

To facilitate the gate-setting procedure, we have constructed some simple particle identification functions. For element resolution we define

$$\text{fast}' = \frac{\text{fast} - \varepsilon(\text{slow})}{2} \tag{3.1}$$

where fast is the fast FERA word, slow is the slow FERA word and $\varepsilon$ is a detector dependent constant which ranges from 0 to 1. A spectrum of fast' versus slow (slow word/4 + 15 channels) for all runs ($^{36}Ar+^{197}Au$, E/A=50, 80 and 110 MeV) is shown in Figure 3.5. Of particular note is the separation of the double $\alpha$ line from Li. This separation allows a rather clean measurement of the number of intermediate mass fragments (particles which fall to the right of the red line with $Z \geq 3$) from the light charged particles on an event by event basis.

In order to facilitate setting the gates for isotope identification we constructed the PID function shown schematically in Figure 3.6. Using the upper and lower lines shown in Figures 3.4 and 3.6 we construct the following variables:

$$\text{tail}_r = \text{tail} + \delta \tag{3.2}$$

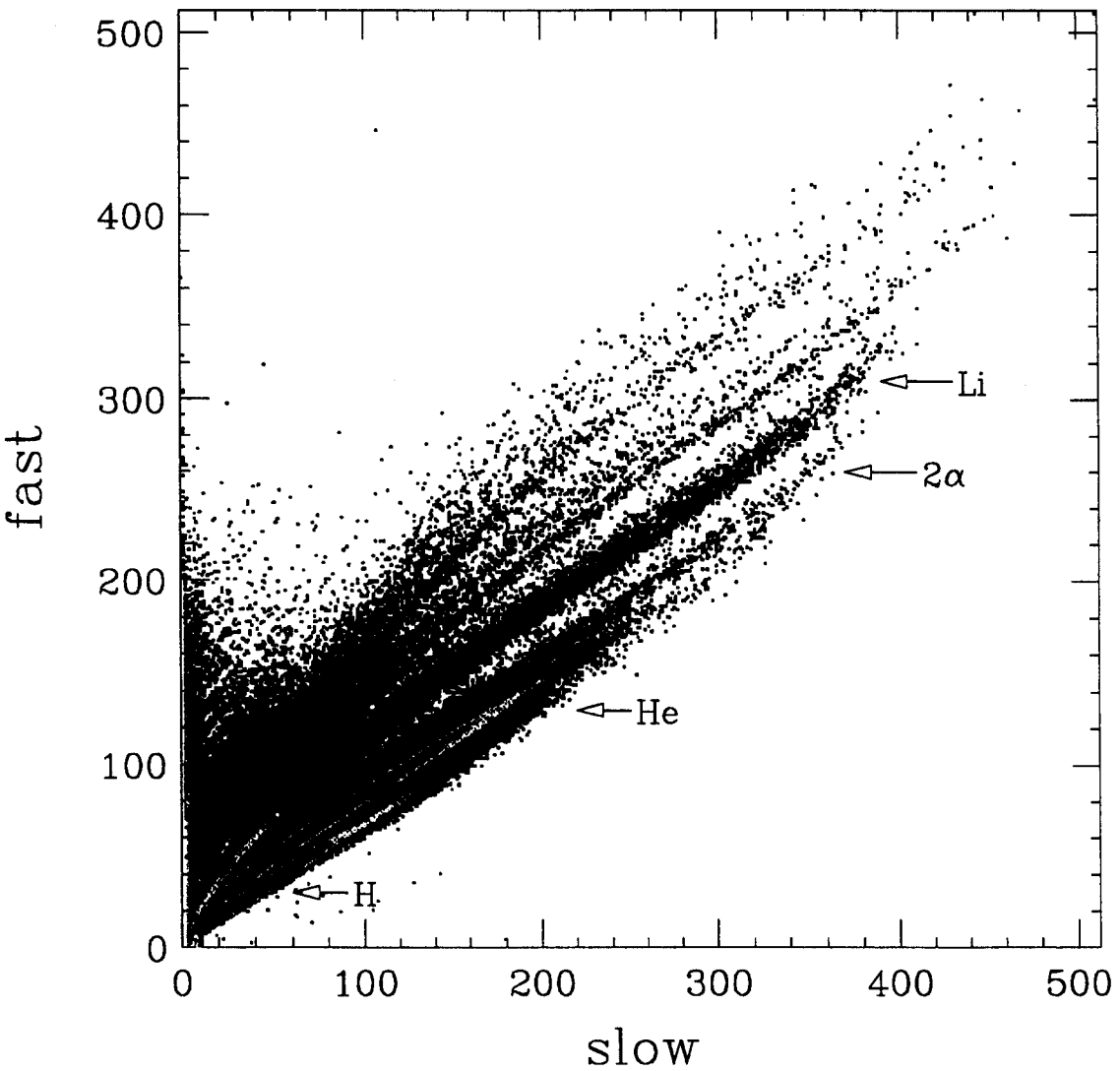


Figure 3.3 Fast versus slow spectrum for detector 3-6 (ring 3, position 6).

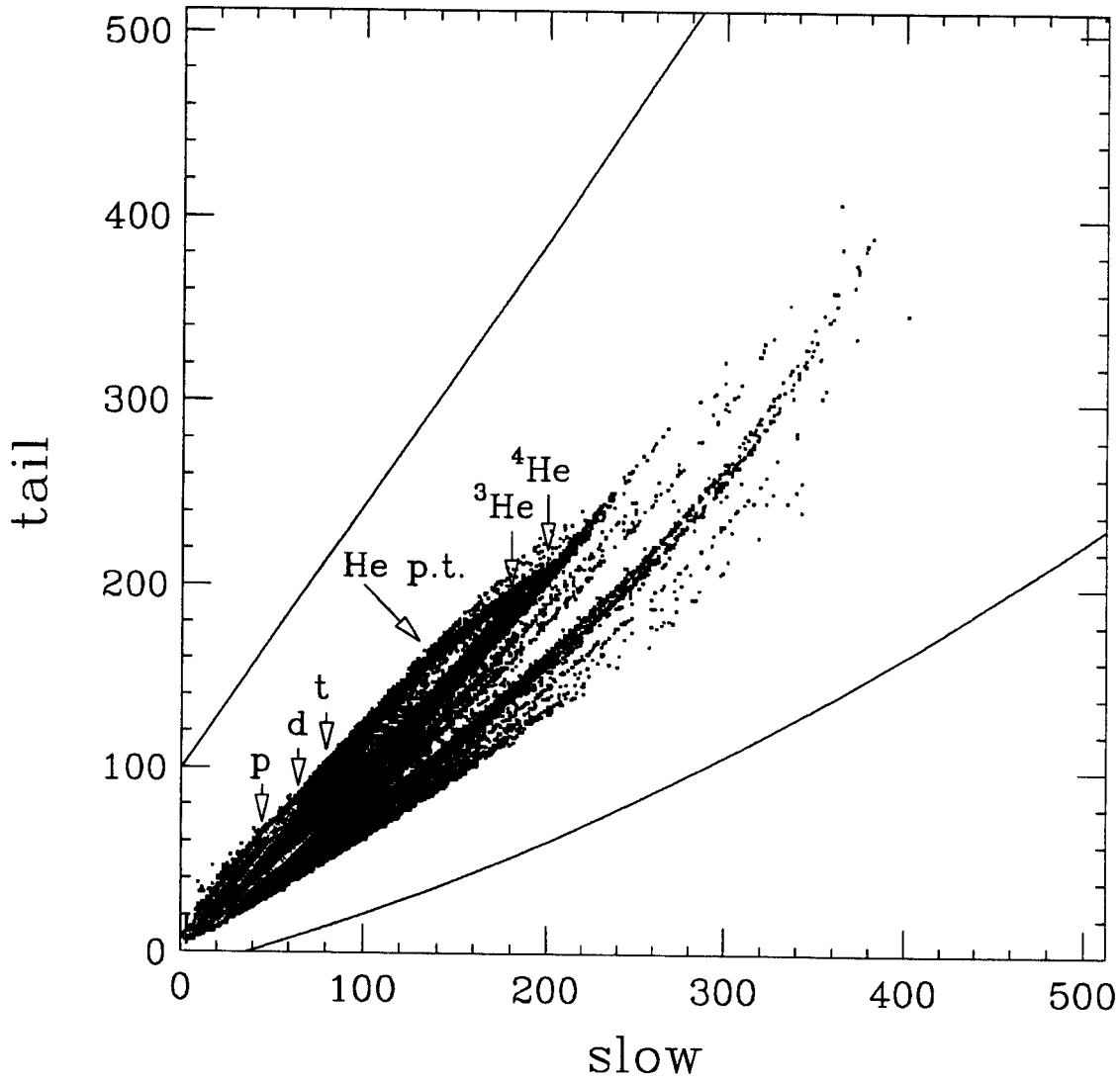


Figure 3.4 Tail versus slow spectrum for detector 3-6 (ring 3, position 6).

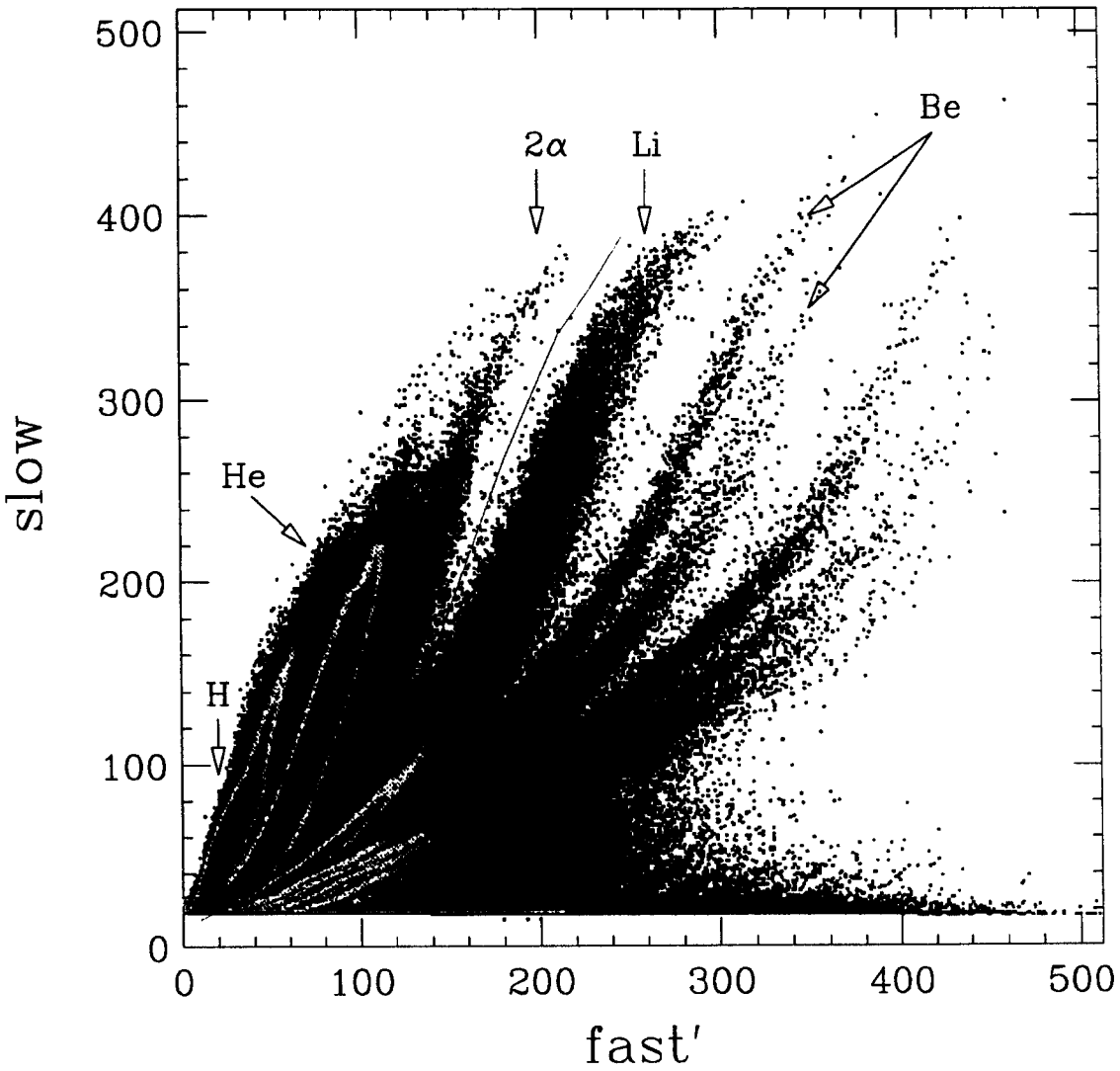


Figure 3.5 Slow versus fast' for detector 3-6. The solid line is used to separate light charged particles from intermediate mass fragments.

where $\delta$ is a random number between -0.5 and 0.5 (to remove digitization from the displayed spectra);

$$tail_1 = line_1(slow) \tag{3.3}$$

$$tail_2 = line_2(slow) \tag{3.4}$$

where $line_1$ and $line_2$ are shown by the upper and lower lines respectively in Figure 3.4 and Figure 3.6 and are parameterized as a function of slow;

$$\Delta_{max} = tail_1 - tail_2; \tag{3.5}$$

$$\Delta = tail_1 - tail_r \tag{3.6}$$

and

$$PID = 512 \times \frac{\Delta}{\Delta_{max}}. \tag{3.7}$$

Isotope resolution when using this PID function is shown in Figure 3.7 (note: slow = slow word/4 +15, the extra 15 channels just to make it easier to set the gates). In this figure are plotted only the particles that fall to the left of the rejection line in Figure 3.5 (i.e. just light charged particles). Gates were set in the valleys between different isotopes of Figure 3.7 to determine particle identification.

On the other hand, for element identification, rather than set gates in the valleys, the gates were set along the ridges in Figure 3.5. A linear interpolation between ridges was then used to determine a "real" (as opposed to "integer") Z value for the point (fast',slow) in question. The resulting identification of elements for detector 3-6 is histogrammed in Figure 3.8 for the 110 MeV per nucleon runs.

For particles which stop in the fast plastic (the horizontal line at the bottom of Figure 3.5) we cannot extract the Z value. However, it is possible to make some classification of the particles using time of flight. Figure 3.9 shows the fast signal versus time (time=$t_{detector}$-$t_{RF}$, the time difference between the

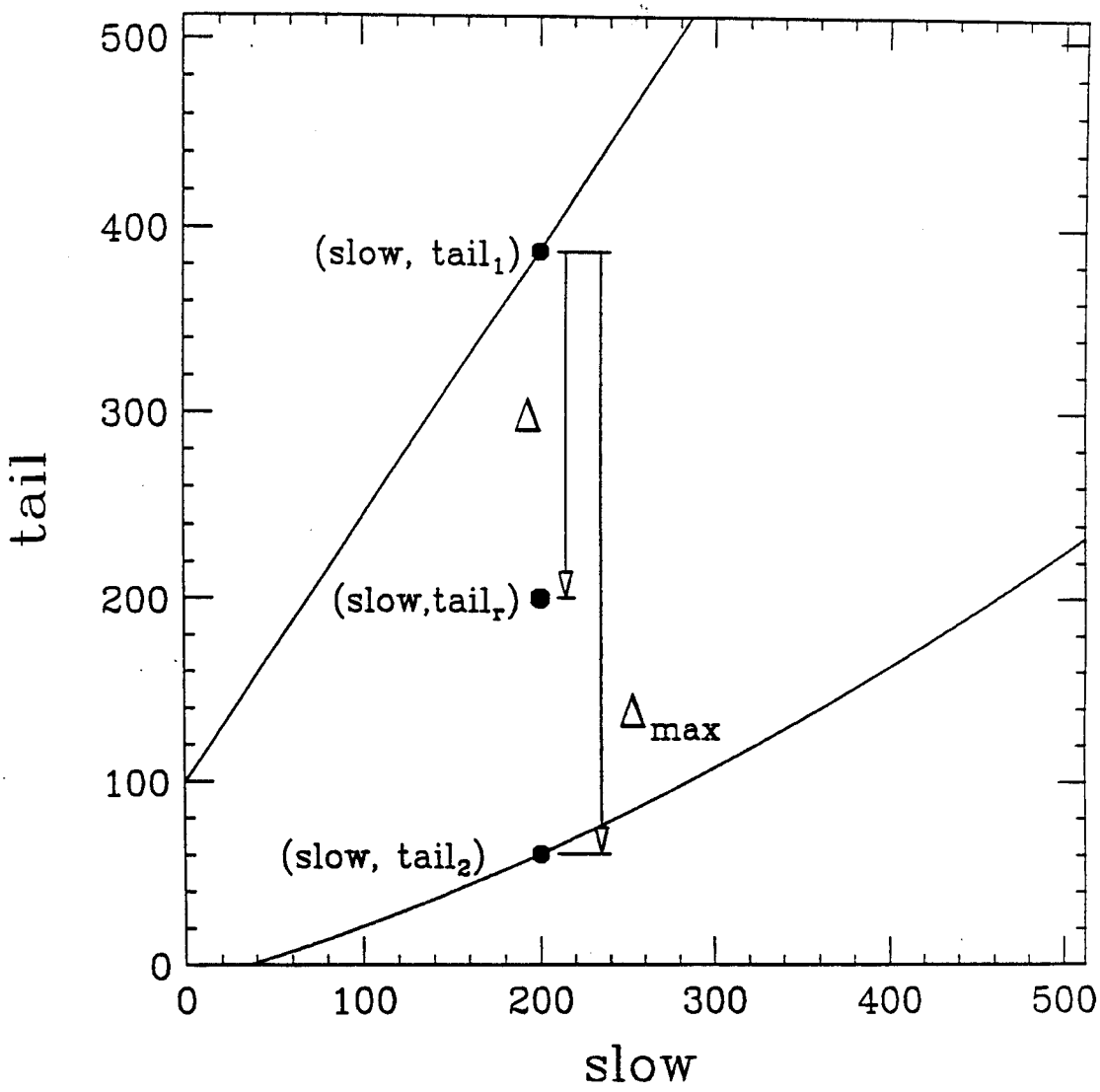


Figure 3.6 Schematic tail versus slow describing variables used in the construction of the PID function.

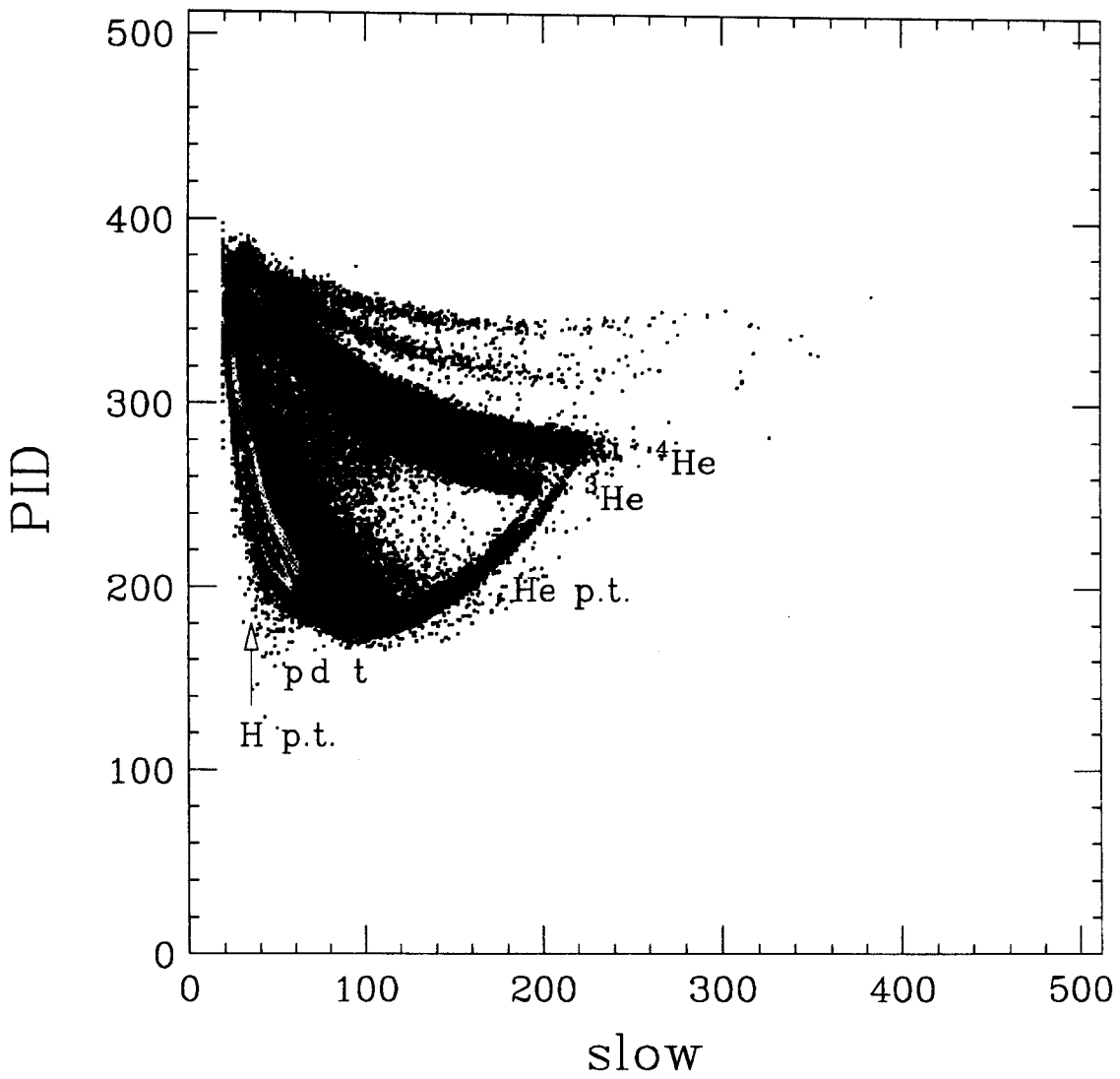


Figure 3.7 PID versus slow for detector 3-6.

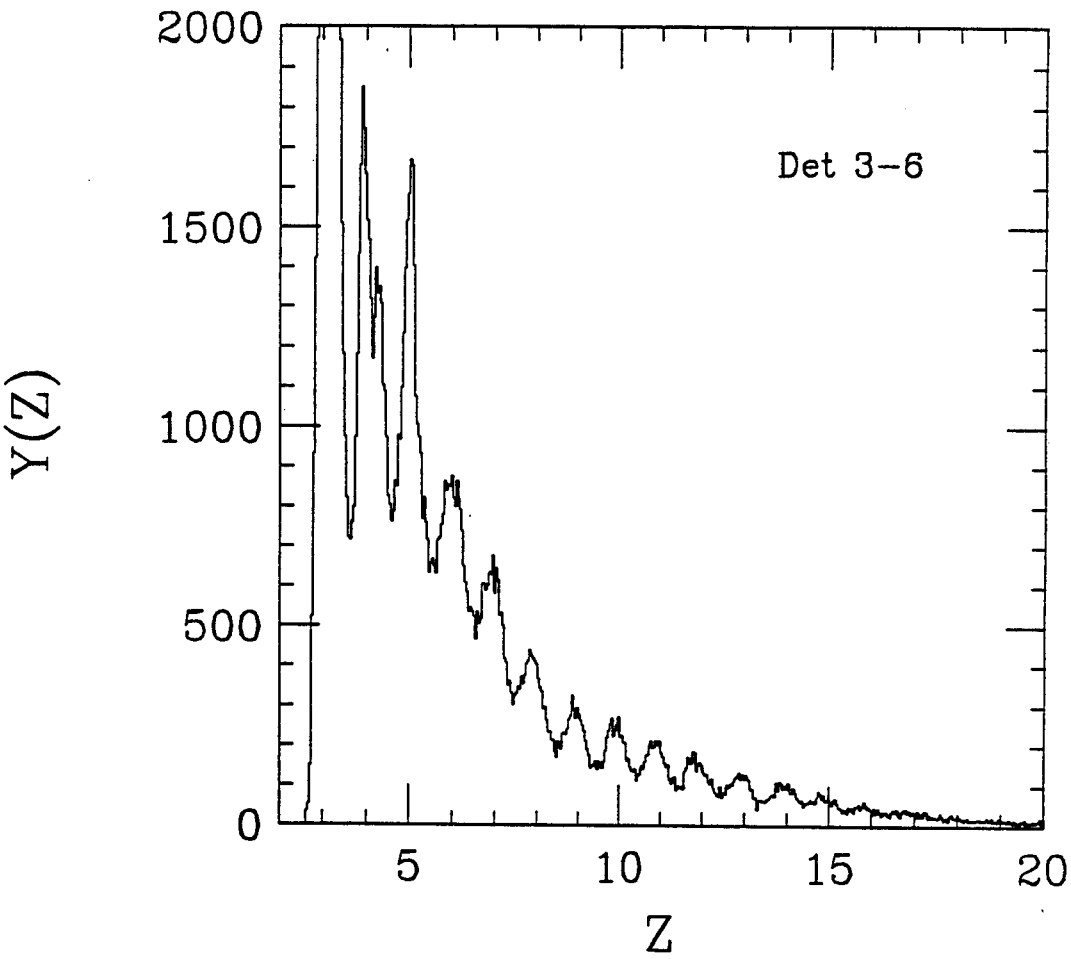


Figure 3.8 Z resolution of detector 3-6. Yield of Z (counts) as a function of Z.

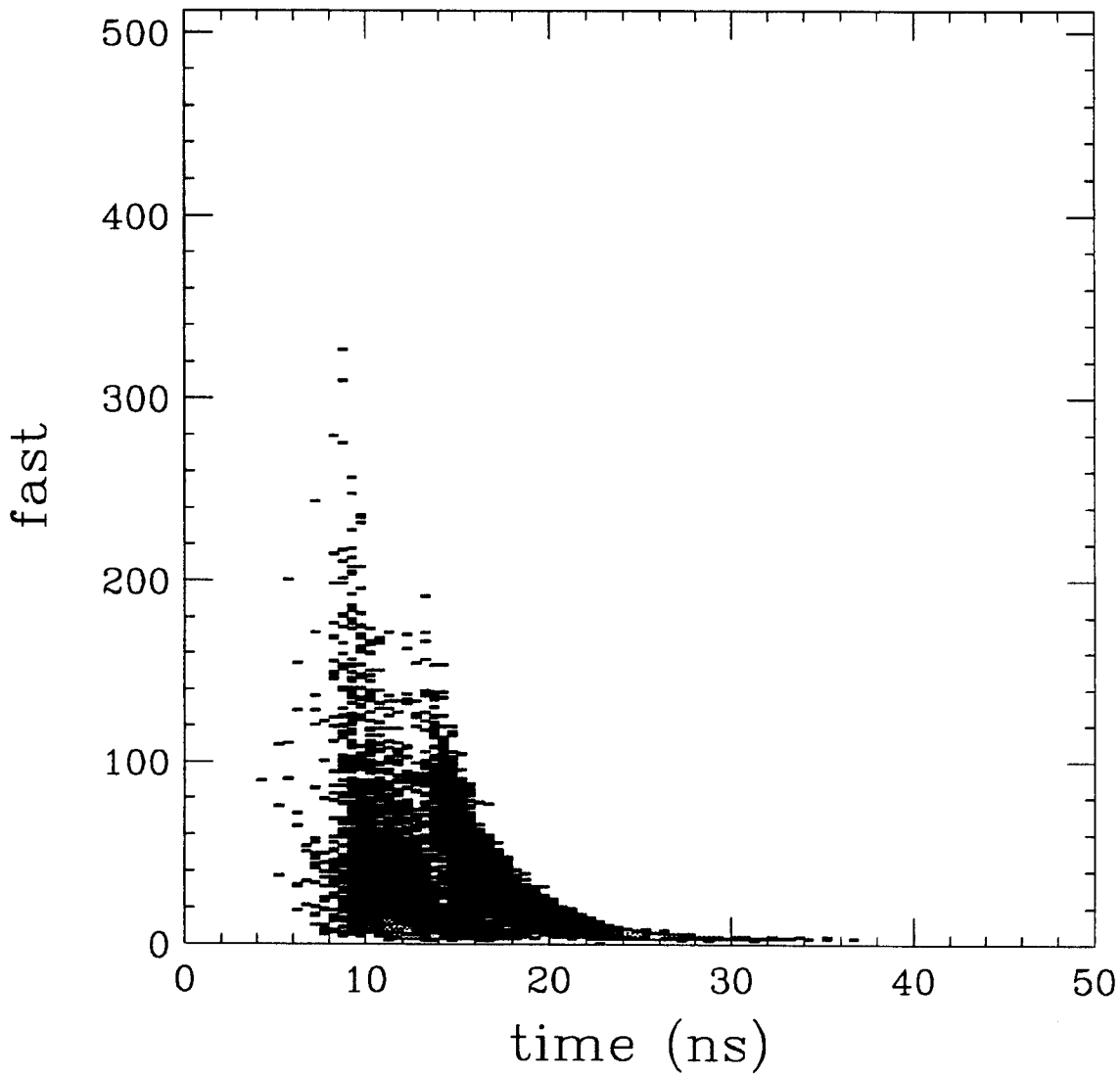


Figure 3.9 Fast versus time for particles that stop in the fast plastic of detector 3-6. Time t=0 is arbitrary.

rf time from the cyclotron and the time that a detector fires) for particles that stop in the plastic. Two branches are clearly seen – a prompt branch (on the left) and a slower branch (on the right), presumably due to fission of the heavy target. In this figure the time t=0 is arbitrary – only the relative timing between the two branches can be extracted.

## Bicron crystals

The identification techniques described above work well for more than two-thirds of the detectors in the Miniball. The remaining one-third have been classified as "Bicron-like" detectors and require special attention. Figure 3.10 shows a typical fast versus slow spectrum for detector 3-16 which has a CsI(Tl) crystal from Bicron. The characteristics of a detector which we call "Bicron-like" are two-fold: a large Z separation in fast for small slow (which quickly disappears for large slow) and poor separation of Li, He, and H particles. Improved resolution (shown in Figure 3.11) can be obtained by plotting the fast versus tail components of the PMT signal. It is now easier to separate He from Li fragments. Figure 3.12 shows fast' (replacing slow with tail in Equation 3.1) versus tail for several runs. Again a rejection line can be set to separate the Li fragments from the light charged particles. Light charged particles fall below the rejection line and are further identified by isotope using PID versus slow.

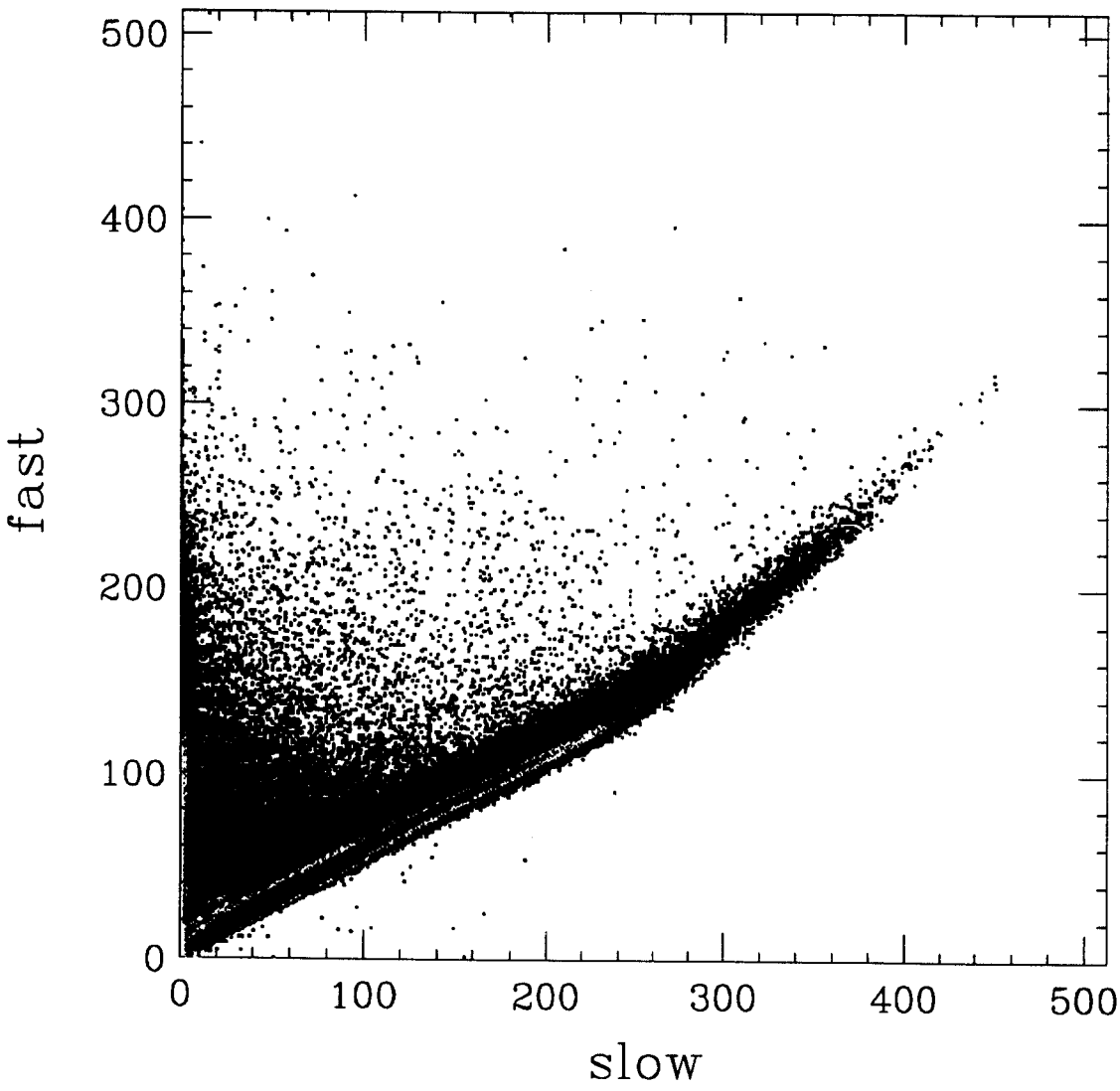


Figure 3.10 Fast versus slow for a detector with a CsI(Tl) crystal from Bicron, detector 3-16.

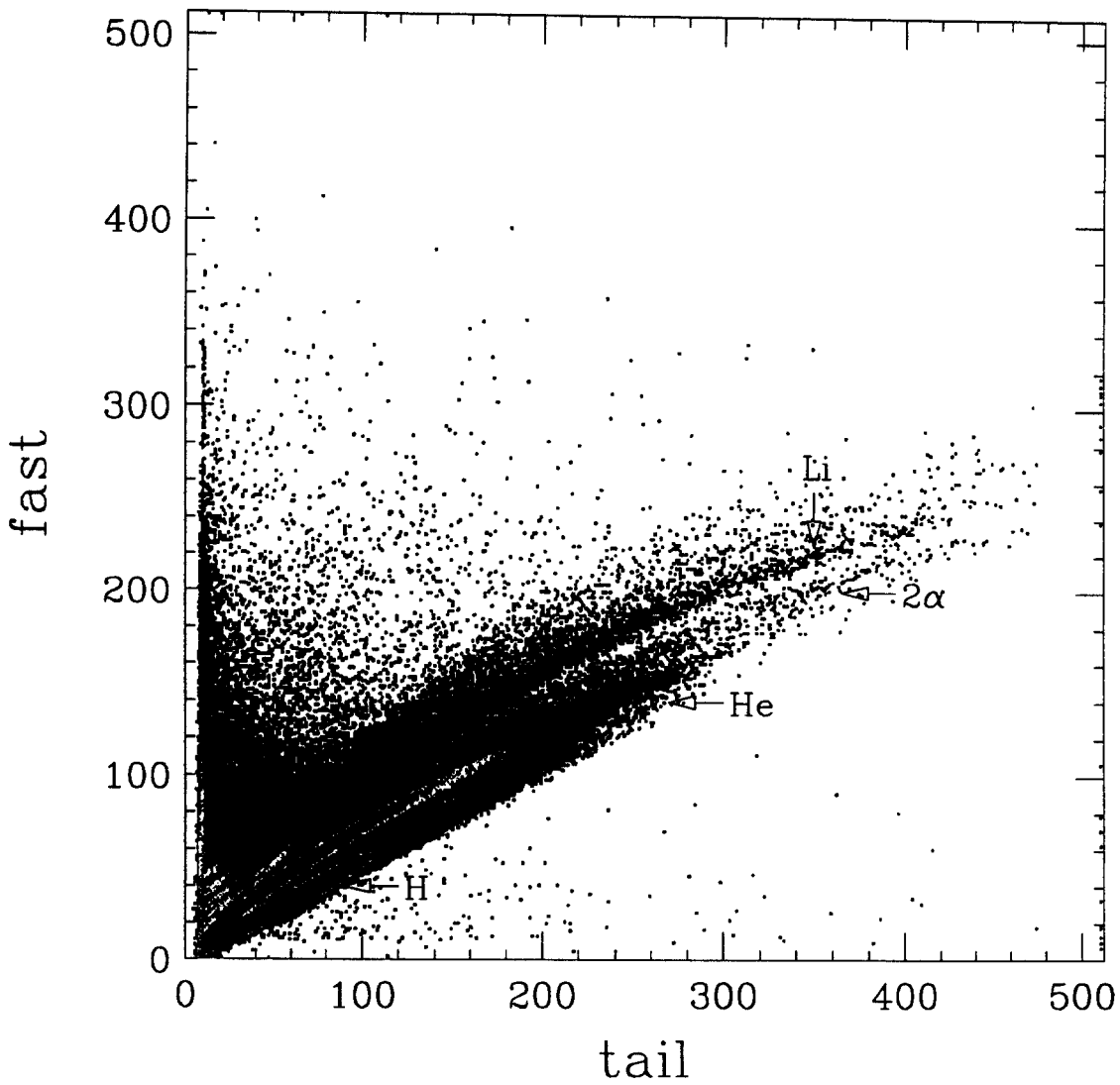


Figure 3.11 Fast versus tail for a detector with a CsI(Tl) crystal from Bicron, detector 3-16

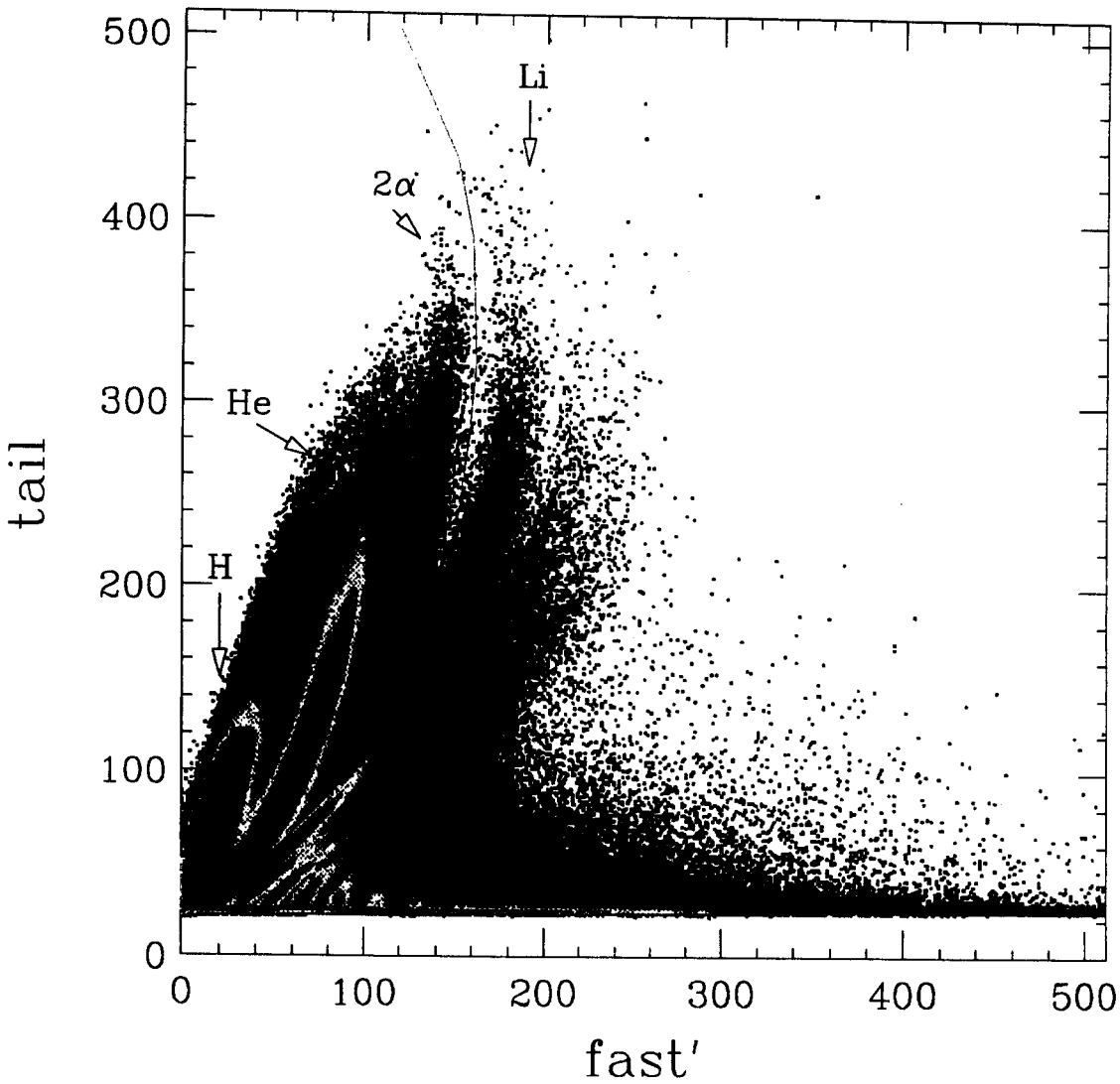


Figure 3.12 Tail versus fast' for a detector with a CsI(Tl) crystal from Bicron, detector 3-16.

## 3.4 Energy calibration

Energy calibrations of forward Miniball detectors were obtained by measuring the elastic scattering of $^{4}$He, $^{6}$Li, $^{10}$B, $^{12}$C, $^{16}$O, $^{20}$Ne and $^{35}$Cl beams from a $^{197}$Au target at incident energies of E($^{4}$He)/A=4.5, 9.4, 12.9, 16 and 20 MeV; E($^{6}$Li)/A=8.9 MeV; E($^{10}$B)/A=15 MeV; E($^{12}$C)/A=6, 8, 13 and 20 MeV; E($^{16}$O)/A=16 and 20 MeV; E($^{20}$Ne)/A=10.6, 11.3, 13.3, 15.0 and 19.8 MeV; and E($^{35}$Cl)/A=8.8, 12.3 and 15 MeV. Figure 3.13 shows the response of the light output as a function of energy deposited in the CsI crystal of detector 3-6 for the listed elements. For calibrations we assumed a functional form for the light output (slow channel) as

$$slow = \gamma E_{CsI} + \beta(e^{-\alpha E_{CsI}} - 1). \qquad (3.8)$$

$\gamma$ is the slope of the light output in the region linear with energy. The values of the parameter $\beta$ come from the extrapolation of the asymptote ($\gamma E_{CsI}$-$\beta$) to the slow axis. The values of $\alpha$ come from the data points in the low energy curved region of the response where quenching effects make the response nonlinear. For detectors in rings 1-4, these calibrations are estimated to be accurate within 5%. Calibrations of more backward detectors were obtained by using the energies of light particles punching through the CsI(Tl) crystals to normalize to extrapolations of the average response of detectors at more forward angles. The average response of rings 2-4 is shown in Figure 3.14. For elements where the light output as function of $E_{CsI}$ has not been measured, a linear interpolation between measured curves is used. Table 3.1 contains the fit parameters for the curves in Figure 3.14. The resulting uncertainties in energy calibration at more backward angles are considerably larger, typically of the order of 10% and for some detectors as large as 20%.

In the $^{36}$Ar+$^{197}$Au at E/A=110 MeV we had for the first time He and Li punching through the 2.0 cm CsI crystals in the forward detectors. The

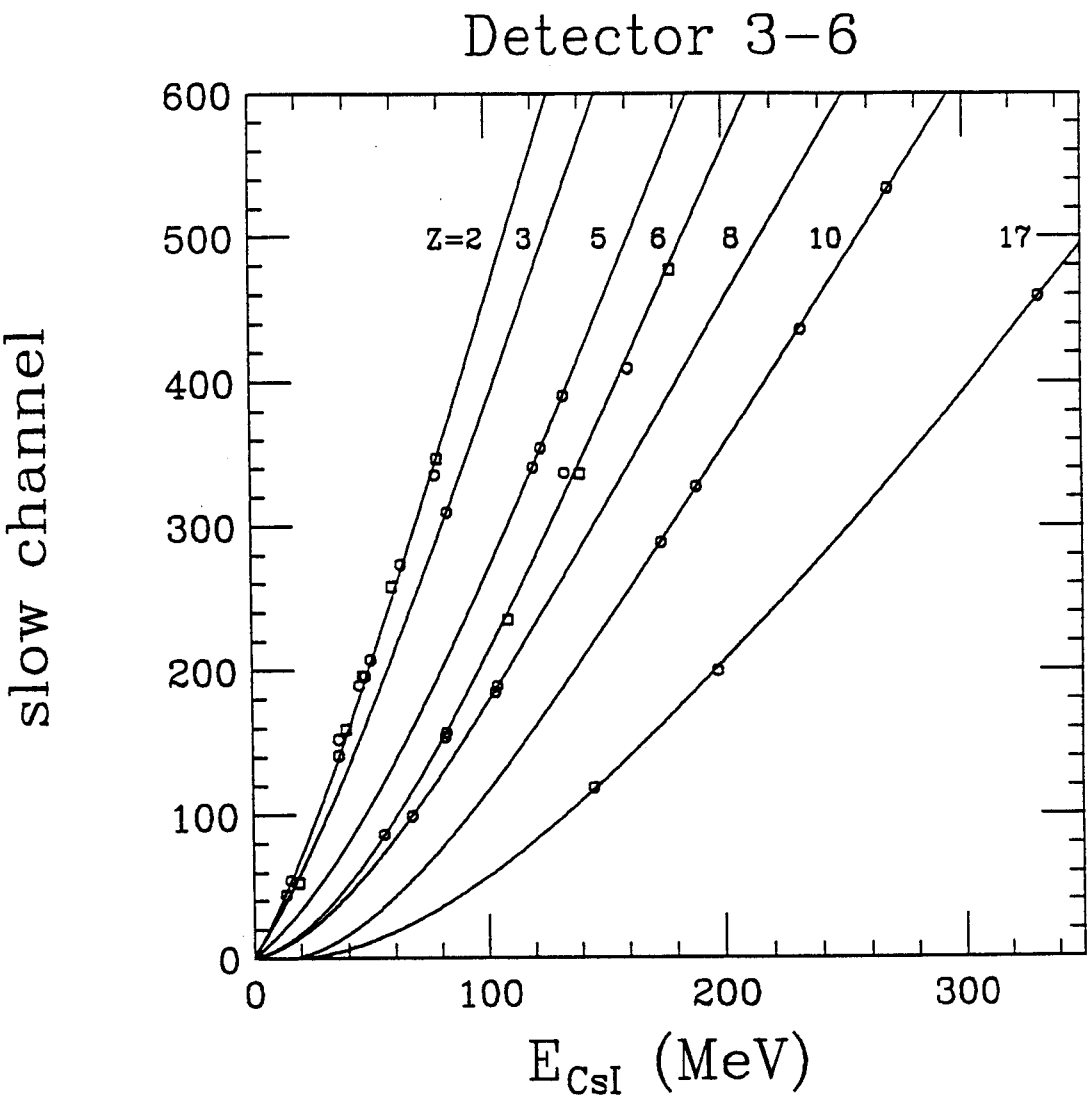


Figure 3.13 CsI calibration of detector 3-6. The light output response (slow) as a function of energy deposited in the CsI (ECsI). The circles represent all previous calibration data for this detector while the squares represent calibration taken during the present experiment. The solid lines are fits using Equation (3.8) for the elements listed.

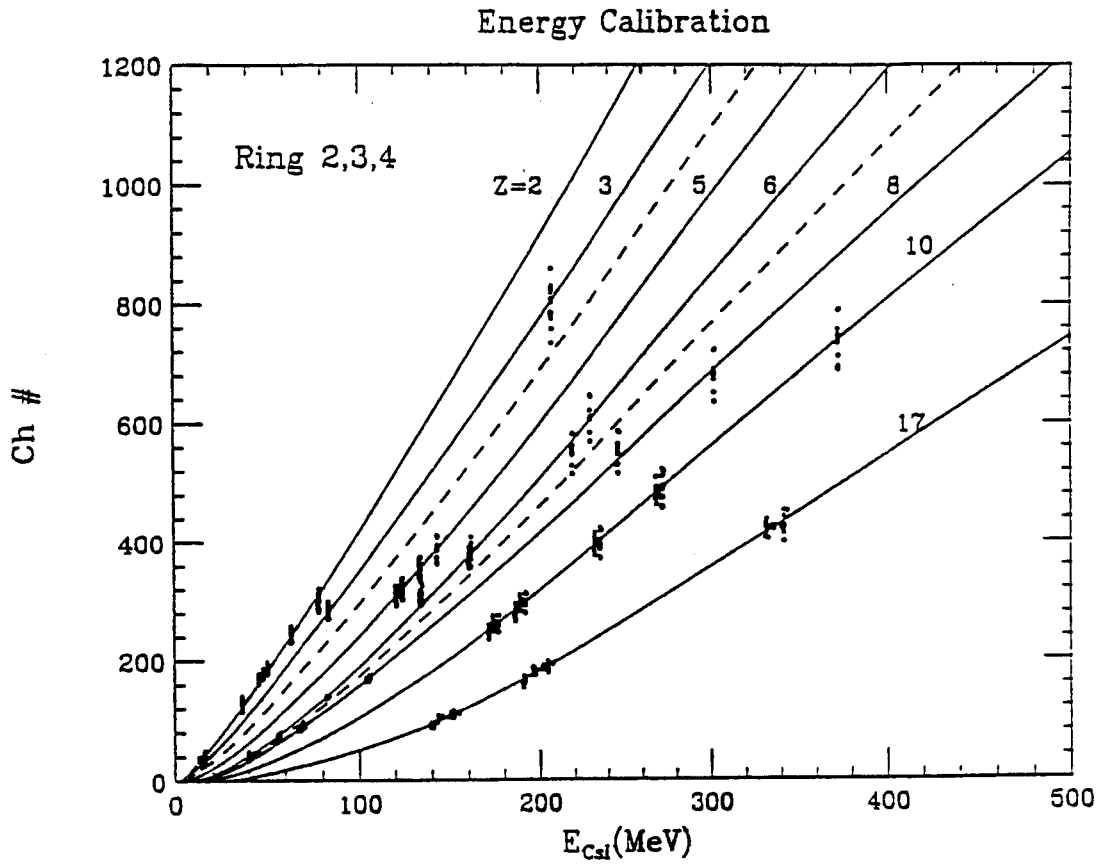


Figure 3.14 CsI calibration of Miniball rings 2-4. The average light output response (slow) as a function of energy deposited in the CsI ($E_{CsI}$). The solid lines are fits using Equation (3.8) for the elements listed. The fit parameters are given in Table 3.1.

Table 3.1 Fit parameters of Equation 3.8 for Figure 3.14

| Z | $\gamma$ | $\beta$ | $\alpha$ |
|---|---|---|---|
| 2 | 5.00842 | 84.1273 | 0.0293086 |
| 3 | 4.32194 | 86.1841 | 0.0235022 |
| 5 | 3.9500 | 199.942 | 0.0138215 |
| 6 | 3.46959 | 189.468 | 0.0164807 |
| 8 | 2.71884 | 126.610 | 0.0194922 |
| 10 | 2.4808 | 178.975 | 0.016974 |
| 17 | 2.01865 | 261.832 | 0.00867138 |

Table 3.2. Calculated energy for which the listed particle punch through 2.0 cm of CsI.

| Z | A | E (MeV) |
|---|---|---|
| 1 | 1 | 75.2 |
| 1 | 2 | 100.6 |
| 1 | 3 | 119.4 |
| 2 | 3 | 266.7 |
| 2 | 4 | 300.8 |
| 3 | 6 | 576.0 |
| 3 | 7 | 615.2 |

calculated punch through energies are listed in Table 3.2. These punch through points can be used to extend the calibration to higher energies. In doing so, it was discovered that the punch through points lie below the extrapolated He and Li curves of Figure 3.14 by typically 20%. Clearly there is a problem region (above 80 MeV for He) for which we have only the calculated punch through energy with which to calibrate. Our crude solution to this problem consisted of using the measured calibration curves out to the highest calibration point and then performing a spline fit out to the punch through point that connects the two regions (see Figure 3.15).

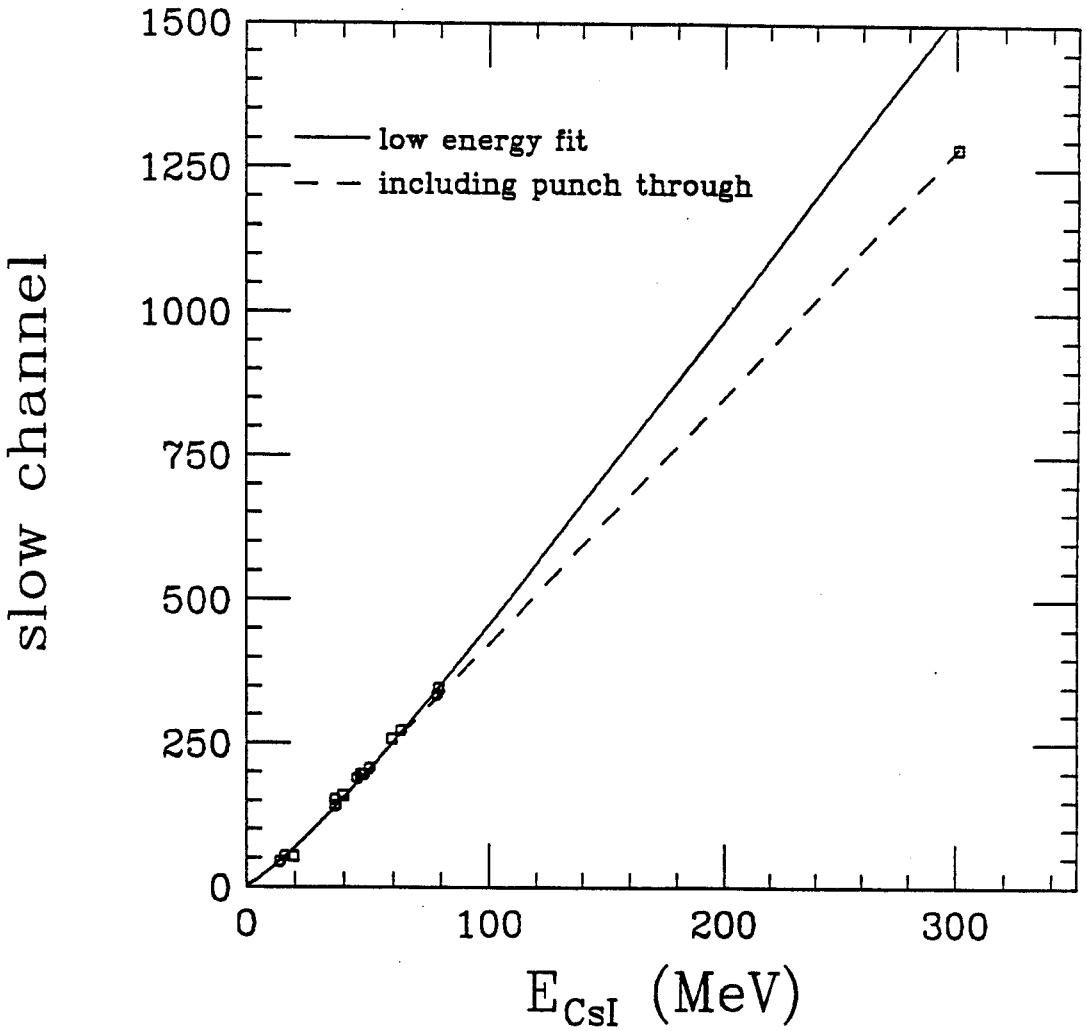


Figure 3.15 The circles represent all previous calibration He calibration data for detector 3-6 while the squares represent calibration taken during the present experiment. Solid line – from Equation 3.8 using the fit parameters for detector 3-6. Dashed line – spline fit of α punch through point to low energy calibration.

# Chapter 4 Impact Parameter Selection

## 4.1 Motivation

Still today, it is not yet clear how experimental observables from nuclear collision experiments can provide quantitative information about phase transitions in nuclear matter [Saye 76, Jaqa 83, Jaqa 84, Curt 83, Rose 84, Coll 75, Morl 79, Shur 80, McLe 81, Kuti 81, Snep 88, Schl 87, Cser 86, Lync 87] – whether it is a liquid-gas phase transition at moderate temperatures and low densities, or a transition between a nucleon gas and a quark-gluon plasma at high densities and temperatures. Intermediate energy nucleus-nucleus collisions may produce finite nuclear systems at temperatures and densities commensurate with a liquid-gas phase transition in infinite nuclear matter. However, interpretations of inclusive measurements are complicated by the implicit average over impact parameter which makes it difficult to unravel the complex interplay between statistical and dynamical effects. Comparisons between experiment and theory are expected to become more tractable and more sensitive to unknown model parameters as research becomes more focused upon exclusive experiments in which specific reaction filters are employed to select narrow ranges of impact parameter.

In most experiments, information about the impact parameter is extracted from quantities which relate to the collision geometry via simple intuitive pictures. Many impact parameter filters represent some measure of the "violence" of the reaction which, in turn, is assumed to be related to the collision geometry. Common impact parameter filters are based upon the measured multiplicity of charged particles [Tsan 89a, Stoc 86, Stöc 86, Cava 90], the transverse energy [Ritt 88], or the summed charge of particles emitted at intermediate rapidity [Ogil 89]. For collisions with incident energies of a few hundred MeV per nucleon, the summed charge, $Z_{bound}$, of particles with atomic number $Z \geq 2$ [Hube 91] has also been used. This quantity is the complement of the combined p, d, and t multiplicity. At lower energies, E/A=20-50 MeV, comparable information on impact parameter has been extracted from measurements of the velocities of fusion-like residues [Gali 85, Awes 81, Chen 87], charged-particle multiplicities [Chen 87, Tsan 89b], or neutron multiplicities [Gali 85, Morj 88]. A recent analysis of data with solid angle coverage restricted to forward angles ($\theta_{lab} \leq 30°$) suggests that improved selectivity for central collisions could be achieved by introducing a new observable, the transverse momentum directivity (defined in Section 4.6) and by simultaneous cuts on large charged-particle multiplicities and small transverse-momentum directivities [Alar 92].

A priori it is unclear to what extent the various techniques select similar or equivalent impact parameters, and whether one technique provides superior resolution to another. At low energies, cross calibrations have been performed between the linear momentum transfer techniques and the emitted charged [Tsan 89b] or neutral particle multiplicities [Gali 85]. In this chapter, we investigate $^{36}Ar+^{197}Au$ collisions at incident energies of E/A=50, 80, and 110 MeV and $^{129}Xe+^{197}Au$ collisions at E/A=50 MeV and

explore the relation between impact parameter filters based upon the charged-particle multiplicity, $N_C$, the total transverse kinetic energy of detected charged particles, $E_t$, the mid-rapidity charge, $Z_y$, and the multiplicity of hydrogen nuclei, $N_1$ (the complement of $Z_{bound}$). We also examine the usefulness of a directivity cut in selecting central collisions for these systems.

The chapter is organized as follows: in section 4.2, we define the various impact parameter filters; in section 4.3, we compare the relative scales derived from the different observables and investigate their cross-correlations; in section 4.4, the efficiency of the individual impact parameter filters is quantified in terms of their ability to suppress contributions from projectile fragments and fast particles emitted at forward angles; in section 4.5, the impact parameter filters are studied again, in terms of their ability to suppress azimuthal correlations; in section 4.6, we study the effects of impact parameter selection using directivity cuts; in section 4.7, a summary and conclusions are given.

## 4.2 Definition of filters

Throughout this work, we will use the following quantities to extract information on the magnitude of the impact parameter:

(1) The charged-particle multiplicity, $N_C$. This quantity includes all charged particles detected by the Miniball (and the forward array for the xenon induced experiment), even if they are not identified. For example, heavy fragments stopped in the scintillator foils are included in the definition of $N_C$. Multiple hits in a single detector module are counted as single hits, even if they can be clearly identified as double hits (as is generally the case for double hits by α-particles). The number $N_C$ is therefore equal to the number of detectors in which at least one charged particle is detected in a given event.

(2) The total transverse kinetic energy of identified particles, $E_t$, defined [Tsan 91] as

$$E_t = \sum_i E_i \sin^2 \theta_i = \sum_i \frac{(p_i \sin \theta_i)^2}{2m_i}. \quad (4.1)$$

Here, $E_i$, $p_i$, and $\theta_i$ denote the kinetic energy, momentum and emission angle of particle $i$ with respect to the beam axis. $E_t$ was calculated using only the Miniball detectors.

(3) The mid-rapidity charge, $Z_y$, defined [Ogil 89a] as the summed charge of all identified particles of rapidity $y$ with

$$0.25y_{c.m.} \le y \le 0.75y_{proj} + 0.25y_{c.m.} \quad (4.2a)$$

or, equivalently,

$$0.75y'_{tar} \le y' \le 0.75y'_{proj} \quad (4.2b)$$

Here, primed quantities are defined in the center-of-mass rest frame of the total system and unprimed quantities are defined in the laboratory frame of reference; $y_{c.m.}$, $y_{tar}$ and $y_{proj}$ denote the rapidities of the total center-of-mass system and of target and projectile, respectively. The rapidity, $y$, of a particle is defined [Gold 78] as

$$y = \tfrac{1}{2}\ln\left(\frac{\sqrt{m^2+p^2}+p\cos\theta}{\sqrt{m^2+p^2}-p\cos\theta}\right) = \tanh^{-1}(\beta\cos\theta), \quad (4.3)$$

where $m$, $\beta$, and $p$ denote the particle's mass, velocity and momentum, respectively.

(4) The identified hydrogen multiplicity, $N_1$. This quantity is defined as the number of detectors in which a Z=1 particle is identified. The definition includes hydrogen nuclei which punch through the CsI(Tl) crystals and double hits by p, d, or t. $N_1$ is the complement of $Z_{bound}$ [Hube 91], the summed charge of particles with atomic number of Z≥2.

Figures 4.1-4.3 show the measured correlations between the quantities $N_C$, $E_t$, $Z_y$ and $N_1$. At all incident energies, the four quantities are strongly

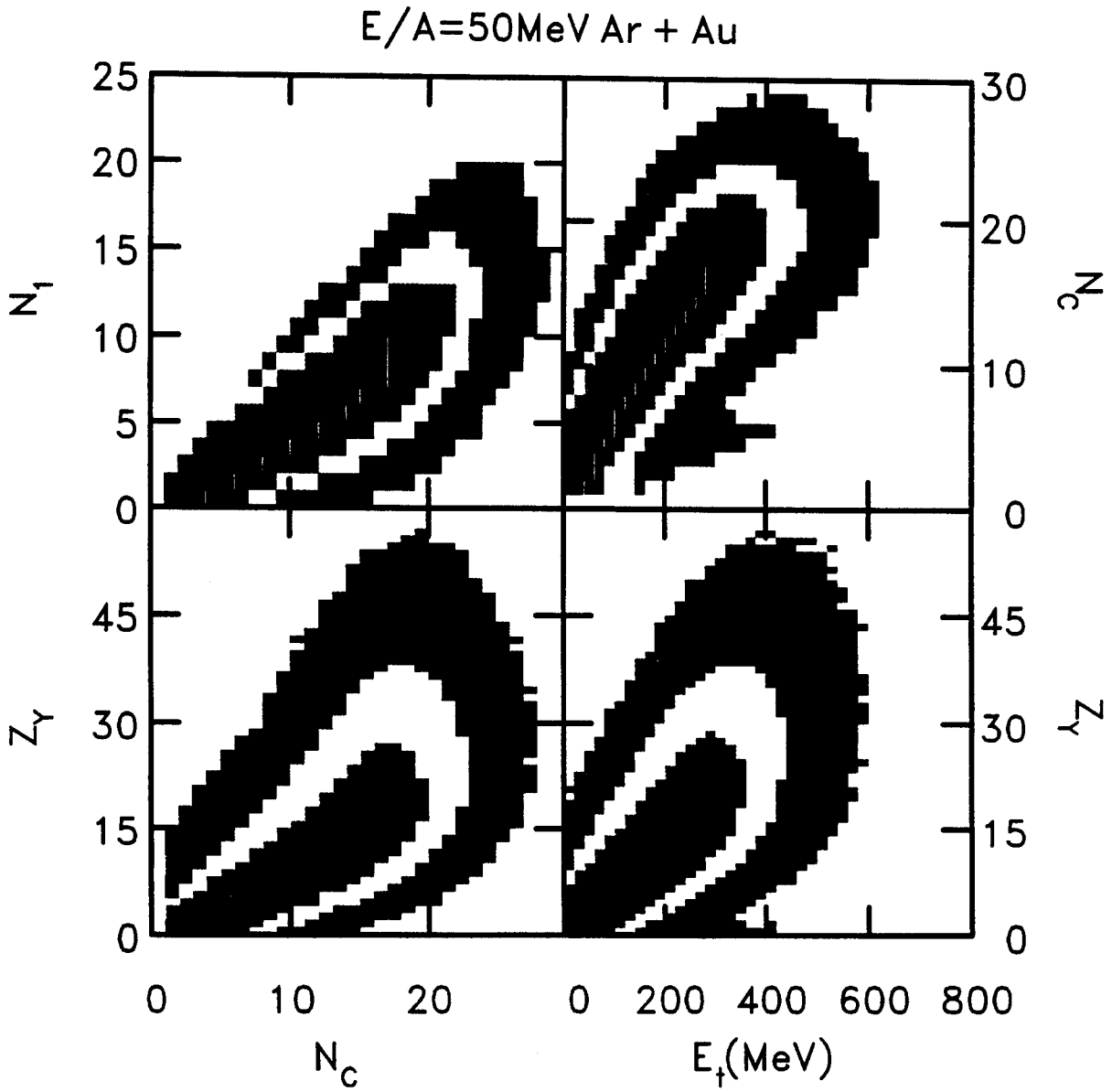


Figure 4.1 Correlations between charged-particle multiplicity $N_C$, transverse energy $E_t$. intermediate rapidity charge $Z_y$ and identified hydrogen multiplicity $N_1$ observed for $^{36}Ar+^{197}Au$ collisions at E/A=50 MeV. Adjacent contours of different color differ by factors of 5.

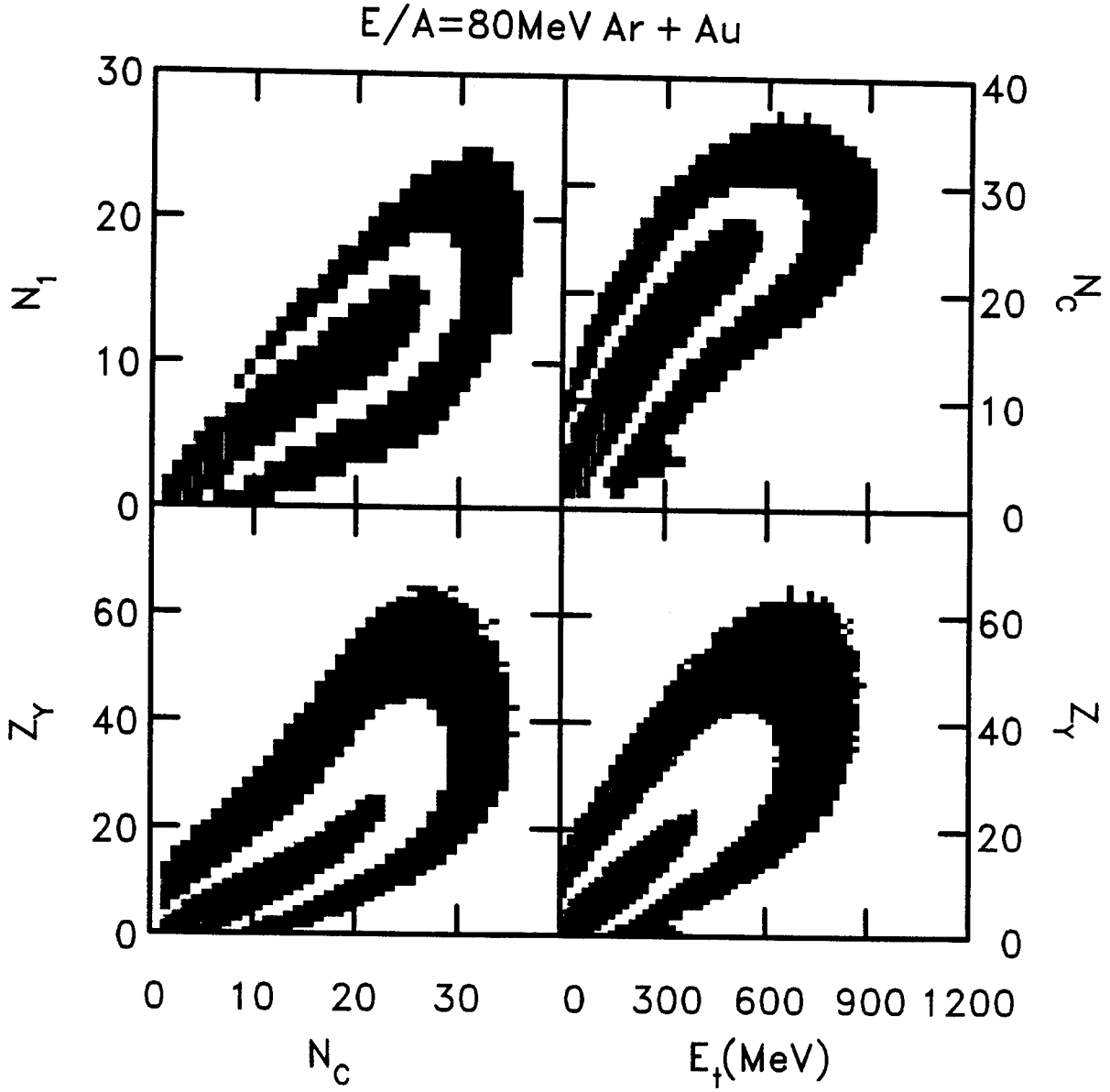


Figure 4.2 Correlations between charged-particle multiplicity $N_c$, transverse energy $E_t$, intermediate rapidity charge $Z_y$, and identified hydrogen multiplicity $N_1$ observed for $^{36}Ar+^{197}Au$ collisions at E/A=80 MeV. Adjacent contours of different color differ by factors of 5.

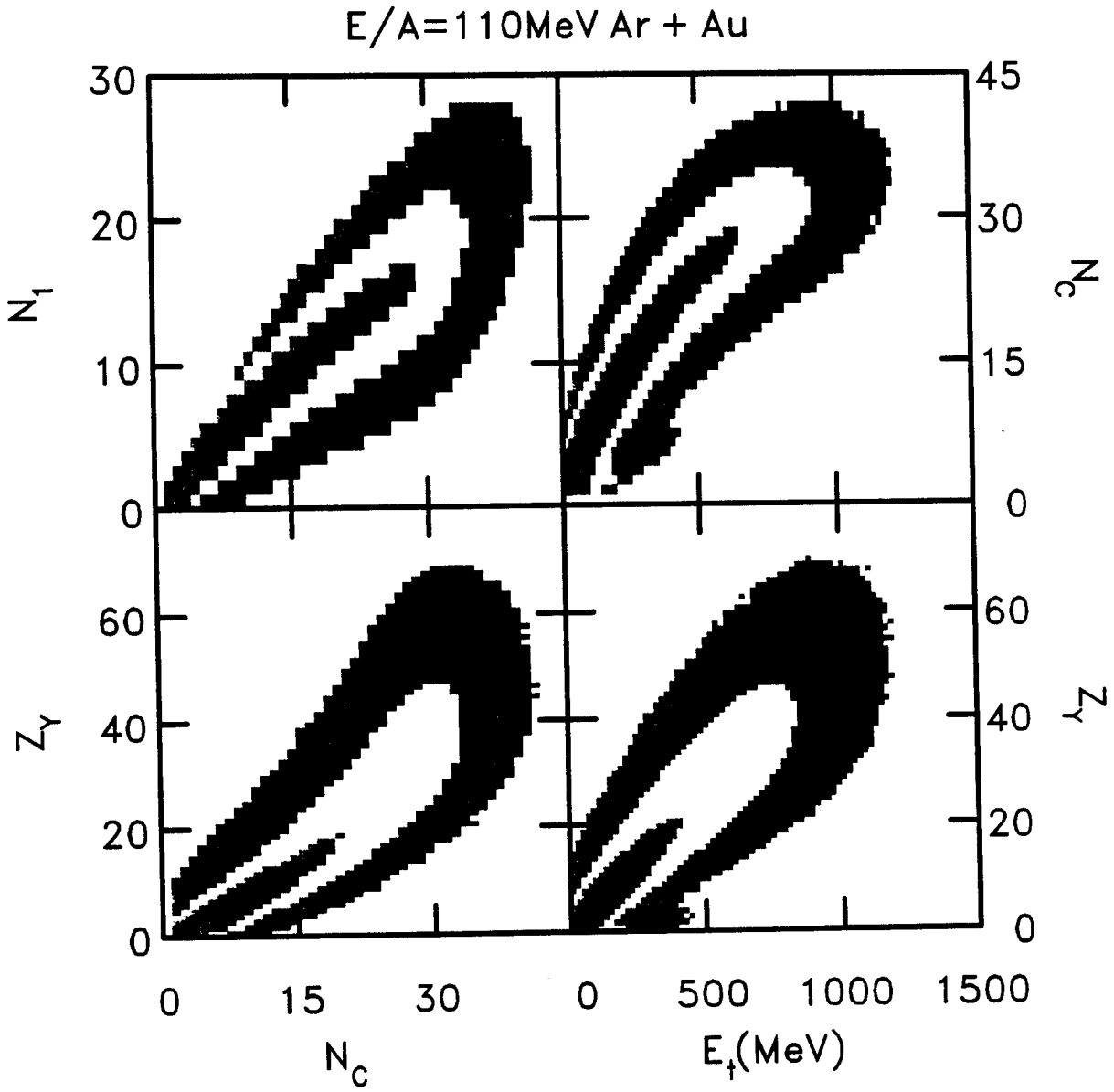


Figure 4.3 Correlations between charged-particle multiplicity $N_c$, transverse energy $E_t$, intermediate rapidity charge $Z_y$, and identified hydrogen multiplicity $N_1$ observed for $^{36}Ar+^{197}Au$ collisions at E/A=110 MeV. Adjacent contours of different color differ by factors of 5.

correlated. In general, an increase in the value of one observable is accompanied by increases in the values of the other three observables. From this observation one may already conclude that all four quantities ($N_C$, $E_t$, $Z_y$ and $N_1$) are suitable for impact parameter selection – or none of them are. However, the correlation between $E_t$ and $N_C$ gives evidence for a slight saturation of $N_C$ at high $E_t$, indicating that the transverse energy might provide a better central collision trigger than the charged-particle multiplicity.

In order to construct an approximate scale for the impact parameter, we adopt the geometrical prescription proposed by Cavata [Cava 90]. For each of the quantities $N_C$, $E_t$, $Z_y$ and $N_1$, we assume a monotonic relationship to the impact parameter and define the reduced impact parameter scale via

$$\frac{b(X)}{b_{max}} = \hat{b}(X) = \left\{ \int_X^{\infty} \frac{dP(X')}{dX'} dX' \right\}^{1/2} \tag{4.4}$$

where $X = N_C$, $E_t$, $Z_y$ and $N_1$. $dP(X)/dX$ is the normalized probability distribution for the measured quantity $X$, and $b_{max}$ is the maximum impact parameter for which particles were detected in the Miniball ($N_C \geq 2$). In the following, we will use the reduced impact parameter scale $\hat{b}$ which ranges from $\hat{b}=1$ for glancing collisions to $\hat{b}=0$ for head-on collisions.

The quantitative relation between the reduced impact parameters $\hat{b}(X)$ and the measured observables $X$ ($X = N_C$, $E_t$, $Z_y$ and $N_1$) is shown in Figure 4.4. Individual panels present the relationships between the reduced impact parameters $\hat{b}(X)$ and the observables $X = N_C$, $E_t$, $Z_y$ and $N_1$ shown on the abscissae, and the different curves show the relationships extracted for the three different incident energies.

While geometric prescriptions implicit in equation (4.4) may provide reasonable scales for the average relationship between charged-particle multiplicity and impact parameter, it is not clear, a priori, whether the scales

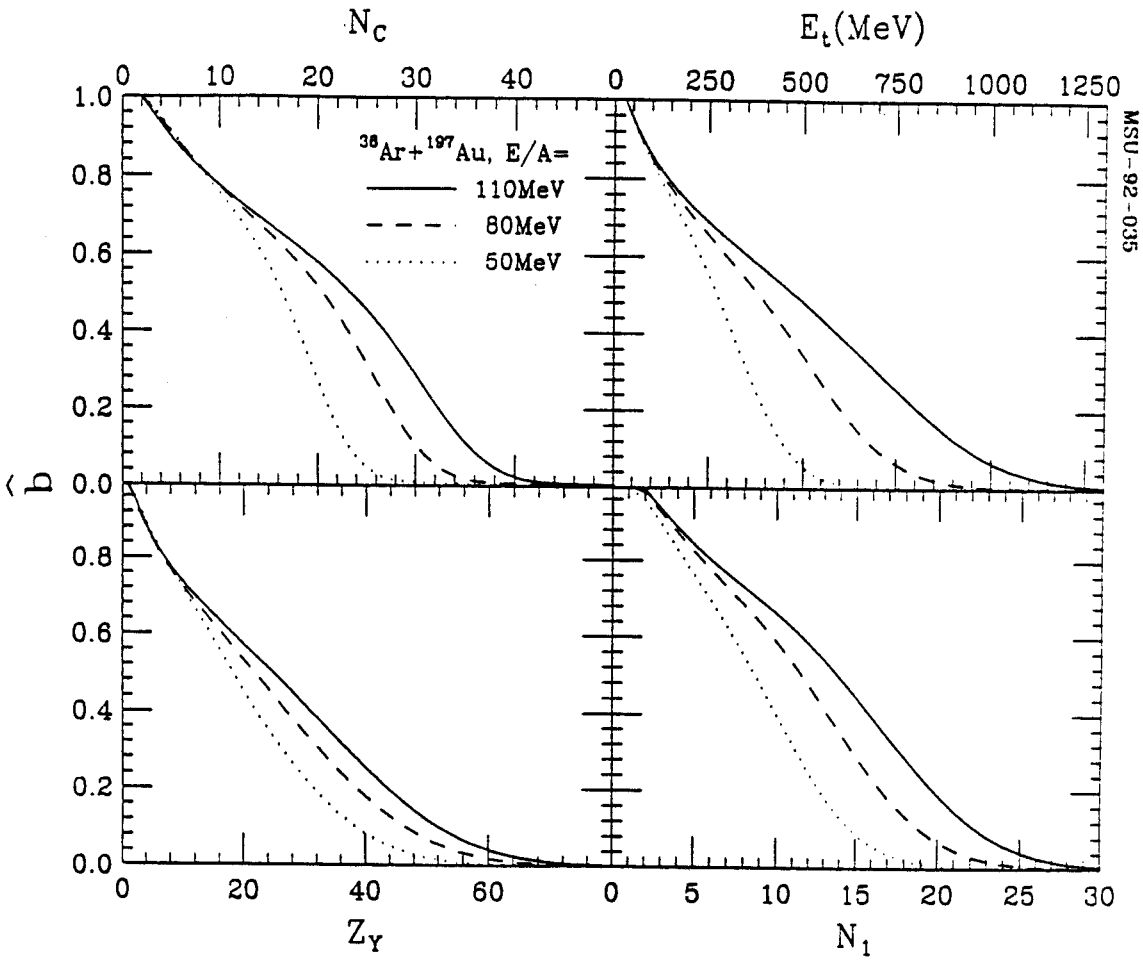


Figure 4.4 Reduced impact parameter scales $\hat{b}(X)$ extracted from the measured quantities $X = N_C$, $E_t$, $Z_y$ and $N_1$. Each panel shows the relation extracted for the indicated observable; different curves represent the relations extracted at the three incident energies.

extracted from the various quantities are commensurate. Furthermore, for collisions at fixed impact parameter, these quantities exhibit fluctuations of unknown magnitude. Therefore, reaction filters constructed from the various observables could have different resolutions. This question will be addressed in the next sections.

## 4.3 Comparison of relative scales

In order to investigate the relationship between impact parameter scales extracted via equation (4.4) from the various measured observables, we have set narrow gates on impact parameters $\hat{b}(X)$, defined by means of an observable $X$, and determined the conditional distributions of impact parameters $\hat{b}(Y)$, constructed from different observables $Y$ ($Y \neq X$ and $X,Y = N_C, E_t, Z_y, N_1$).

Conditional impact parameter distributions are presented in Figures 4.5-4.8. Individual panels of these figures show conditional impact parameter distributions $\frac{dP\left(\hat{b}(Y)\right)}{d\hat{b}}$ determined from the indicated observables $Y$. Left and right hand panels show distributions extracted for the cuts $\hat{b}(X)$=0.05-0.1 and $\hat{b}(X)$=0.35-0.45, respectively. Dashed and dotted curves show results obtained by cuts placed on one observable, and solid curves show results obtained by simultaneous cuts placed on two observables. The observables $X$ used for these cuts are indicated in the individual left-hand panels; the conventions for left and right panels are identical. For better comparison, all conditional impact parameter distributions are normalized to unit area.

For the present reaction, impact parameter filters based upon $N_1$ (the complement of $Z_{bound}$) are considerably less selective than reaction filters based upon $N_C$, $E_t$ and $Z_{bound}$. This effect is clear from Figure 4.5, which compares

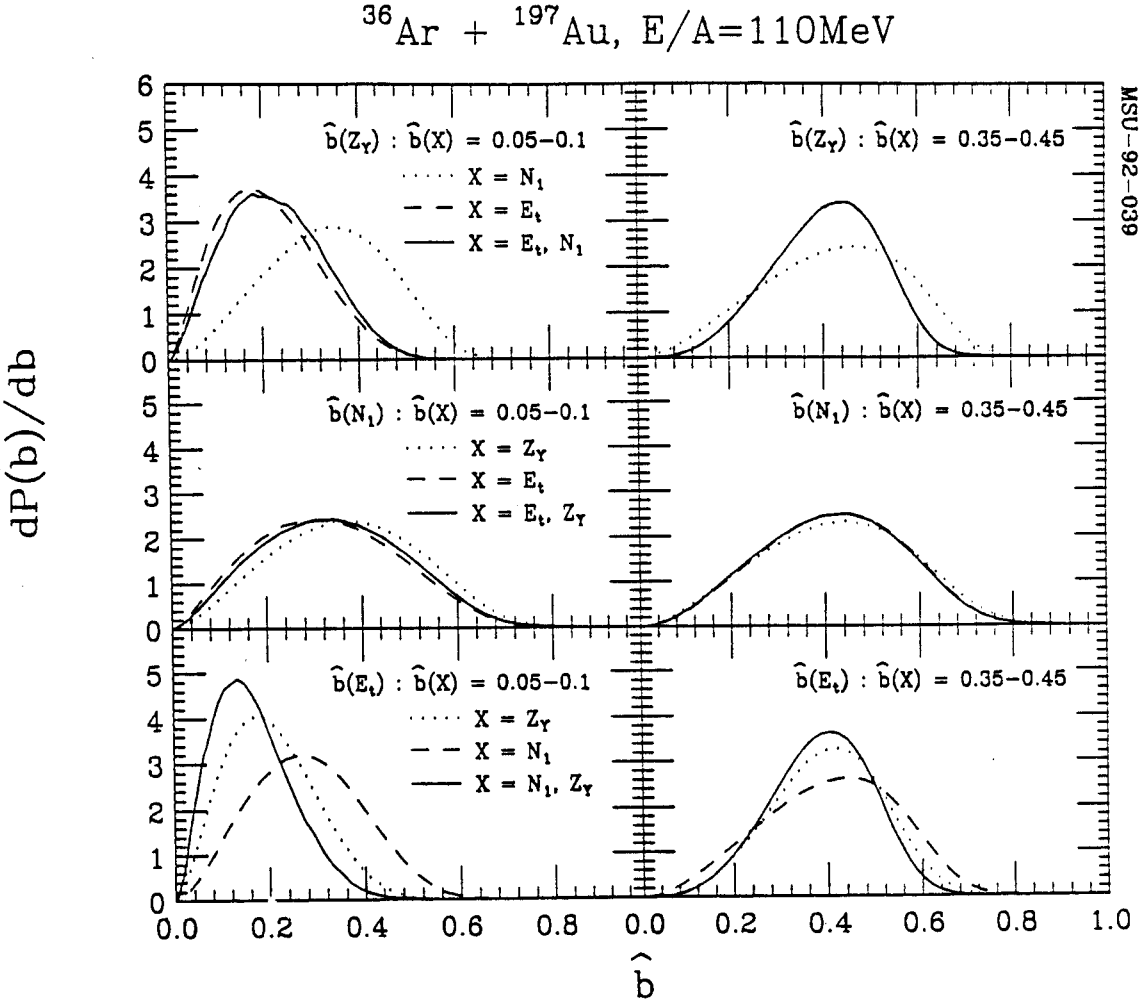


Figure 4.5 Conditional impact parameter distributions extracted for $Y = Z_y$ (top panels), $Y = N_1$ (center panels), and $Y = E_t$ (bottom panels) for the $^{36}$Ar+$^{197}$Au reaction at E/A=110 MeV. Left and right hand panels show distributions selected by impact parameter cuts $\hat{b}(X)$=0.05-0.1 and $\hat{b}(X)$=0.35-0.45 on the indicated observables ($X = N_1$, $E_t$, and $Z_y$). All impact parameter scales were constructed according to Equation (4.4).

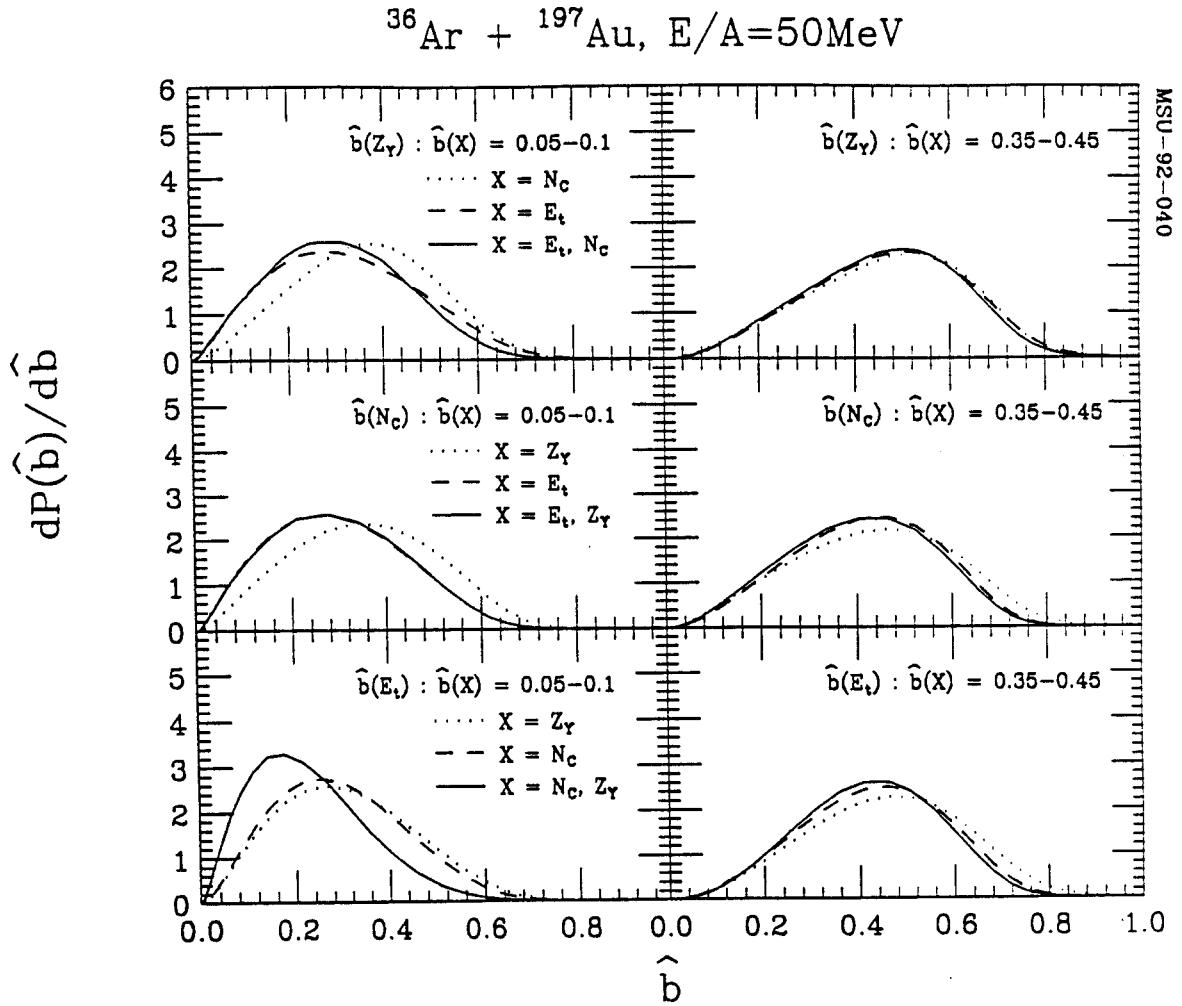


Figure 4.6 Conditional impact parameter distributions extracted for $Y = Z_y$ (top panels), $Y = N_C$ (center panels), and $Y = E_t$ (bottom panels) for the $^{36}$Ar+$^{197}$Au reaction at E/A=50 MeV. Left- and right-hand panels show distributions selected by impact parameter cuts $\hat{b}(X)$=0.05-0.1 and $\hat{b}(X)$=0.35-0.45 on the indicated observables ($X = N_C$, $E_t$ and $Z_y$). All impact parameter scales were constructed according to equation (4.4).

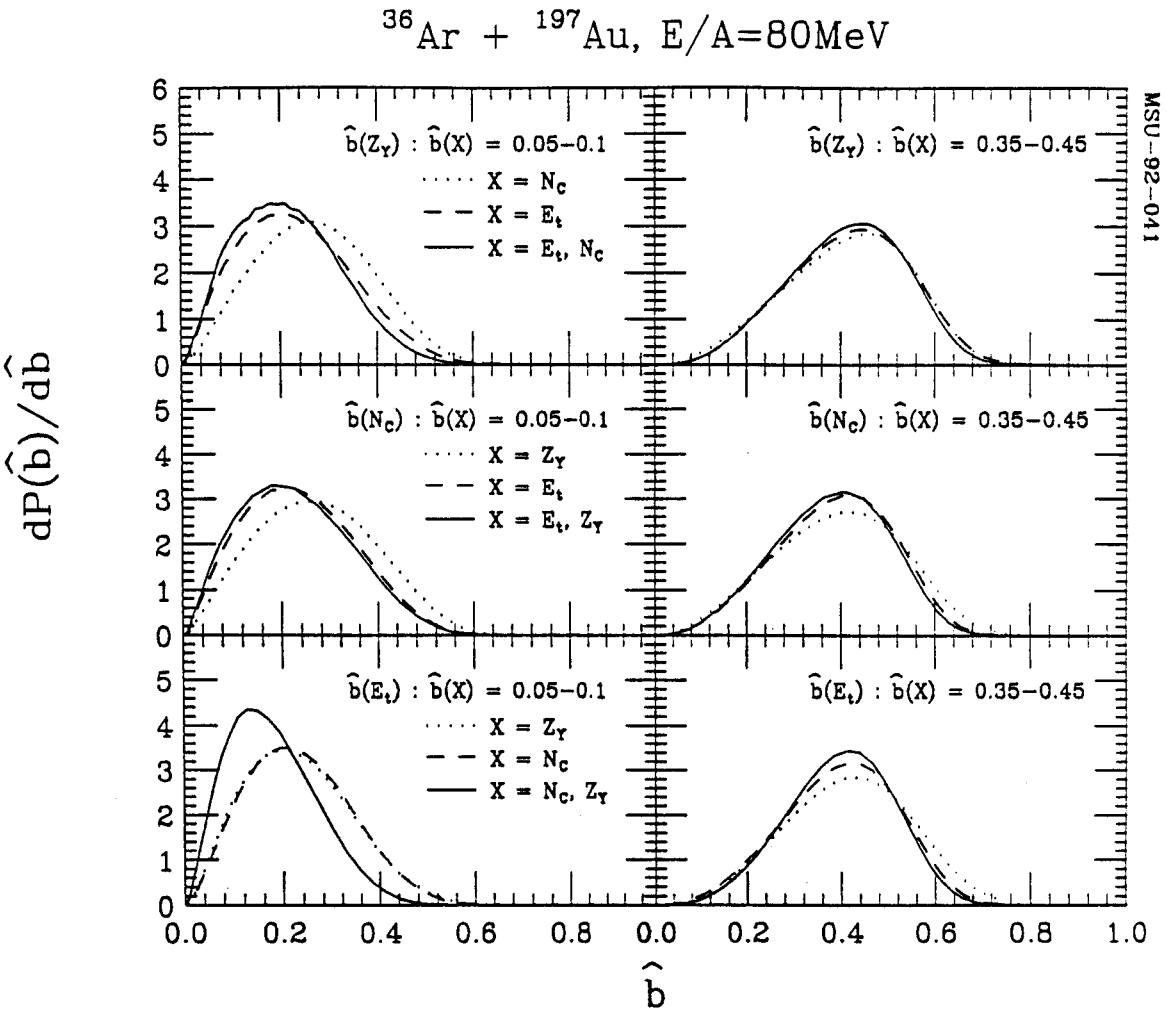


Figure 4.7 Conditional impact parameter distributions extracted for $Y = Z_y$ (top panels), $Y = N_C$ (center panels), and $Y = E_t$ (bottom panels) for the $^{36}$Ar+$^{197}$Au reaction at E/A=80 MeV. Left- and right-hand panels show distributions selected by impact parameter cuts $\hat{b}(X)$=0.05-0.1 and $\hat{b}(X)$=0.35-0.45 on the indicated observables ($X = N_C$, $E_t$, and $Z_y$). All impact parameter scales were constructed according to equation (4.4).

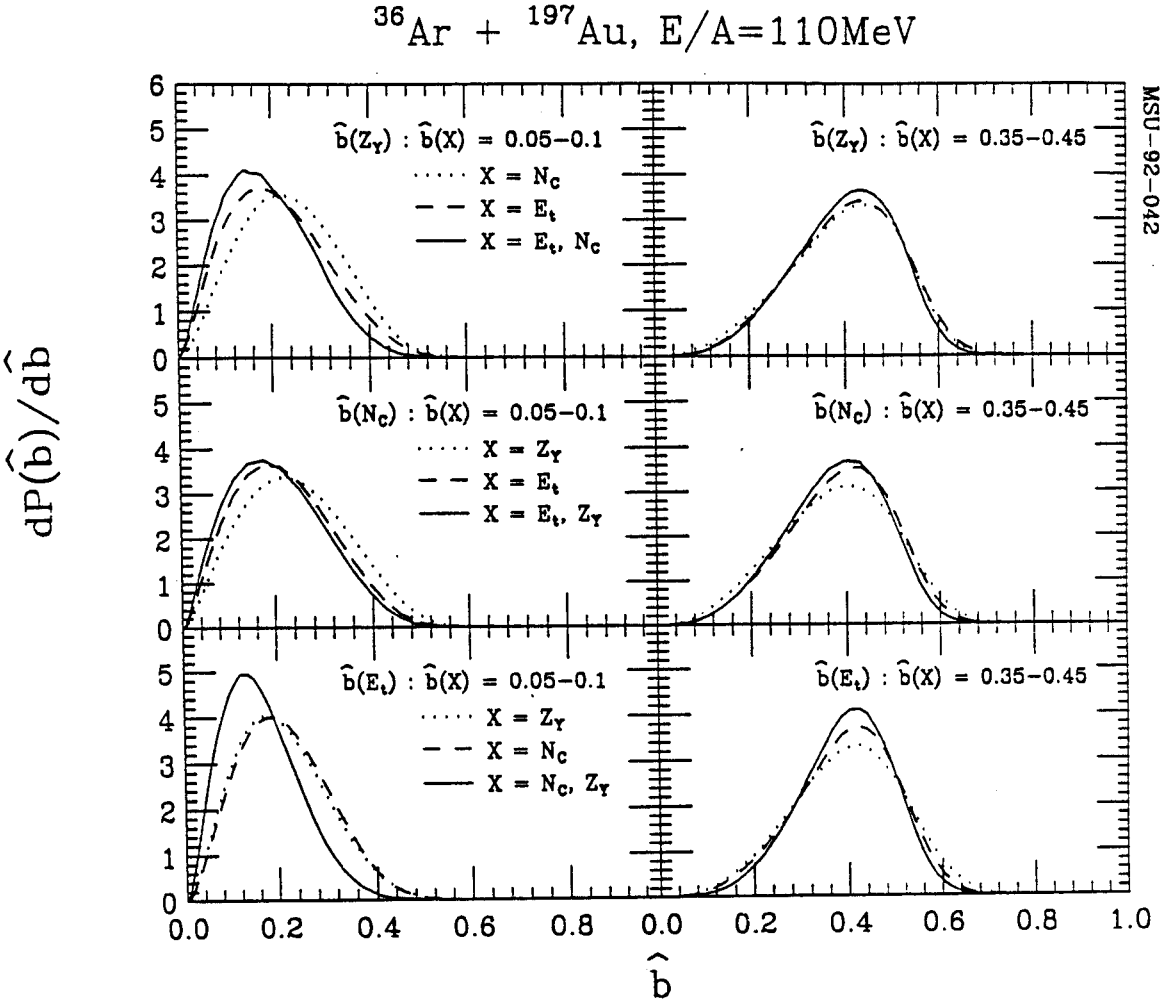


Figure 4.8 Conditional impact parameter distributions extracted for $Y = Z_y$ (top panels), $Y = N_C$ (center panels), and $Y = E_t$ (bottom panels) for the $^{36}$Ar+$^{197}$Au reaction at E/A=110 MeV. Left- and right-hand panels show distributions selected by impact parameter cuts $\hat{b}(X)$=0.05-0.1 and $\hat{b}(X)$=0.35-0.45 on the indicated observables ($X = N_C$, $E_t$ and $Z_y$). All impact parameter scales were constructed according to equation (4.4).

conditional distributions based upon $N_1$, $E_t$ and $Z_y$ for collisions at E/A=110 MeV. The reduced resolution of impact parameter filters based upon $N_1$ is most likely of statistical origin. For collisions at fixed impact parameter, the relative magnitude of statistical fluctuations is enhanced for the observable $N_1$ because it contains, by definition, only a subset of the emitted particles.

Figures 4.6, 4.7 and 4.8 present conditional impact parameter distributions at different energies. In general, the conditional impact parameter distributions become narrower with increasing particle energy. Qualitatively, this can be understood in terms of statistical fluctuations: at fixed impact parameter, statistical fluctuations lead to distributions in $X=N_C$, $E_t$, and $Z_y$ of finite widths $\Delta X$. For collisions at fixed impact parameter, the mean values of all quantities ($X=N_C$, $E_t$ and $Z_y$) increase with increasing projectile energy and the relative fluctuations, $\Delta X / X$, decrease. Hence, impact parameter determinations should become more accurate at higher energies.

At a given incident energy, rather similar conditional impact parameter distributions are extracted from the observables $N_C$, $E_t$ and $Z_y$, with little sensitivity to the applied cut on other observables. While some differences exist, they are generally small.

Cuts on small impact parameters, $\hat{b}(X)$=0.05-0.1, generally produce conditional distributions that peak at larger impact parameters, $\hat{b}(Y)$=0.2. Conditional impact parameter distributions extracted for simultaneous cuts on small impact parameters, $\hat{b}(X_1)=\hat{b}(X_2)$=0.05-0.1, are slightly narrower and they peak at lower impact parameters, $\hat{b}(Y)$=0.12-0.16, than those obtained from cuts on a single observable. Hence, somewhat improved selection of central collisions can be obtained from multi-dimensional cuts.

One-dimensional cuts on $\hat{b}(E_t)$=0.05-0.1 produce narrower distributions in $\hat{b}(N_C)$ and $\hat{b}(Z_y)$ than the alternative one-dimensional cuts on $\hat{b}(Z_y)$ and

$\hat{b}(N_C)$, respectively. Furthermore, two-dimensional cuts on small impact parameters produce narrower distributions for $\hat{b}(E_t)$ than for $\hat{b}(N_C)$ and $\hat{b}(Z_y)$. These observations suggest that filters based on $E_t$ may be more effective in selecting central collisions than filters based on the other observables investigated in this work.

For cuts on intermediate impact parameters, $\hat{b}(X)$=0.35-0.45, the conditional distributions are peaked at values close to $\hat{b}(Y)$=0.4, i.e. close to the cut on $\hat{b}(X)$. This correspondence between the impact parameter scales derived from different observables improves at higher beam energies, indicating that all impact parameter filters have improved resolution at higher energies. Again, small improvements in resolution are obtained by the application of two-dimensional cuts. However, these improvements are less pronounced than those seen for very small impact parameters.

The similarities of the various conditional impact parameter distributions shown in Figures 4.6-8 indicate that the three observables ($N_C$, $E_t$ and $Z_y$) have similar selectivity on impact parameter. Figure 4.9 summarizes and corroborates these findings in a compact form. The individual panels of the figure show the centroids (points) and widths at half maximum (vertical bars) of conditional impact parameter distributions selected by narrow cuts on impact parameters, centered at $\hat{b}(X)$=0.1...0.9 and extracted from other observables $X$. Left, center and right columns show data at E/A=50, 80, and 110 MeV, respectively.

Overall, the relation between the individual impact parameter scales is fairly linear with significant deviations occurring only for small and large impact parameters. Such deviations must be expected at the edges of the impact parameter scales whenever the two-dimensional correlations shown in Figures 4.1-3 have finite widths and some curvature.

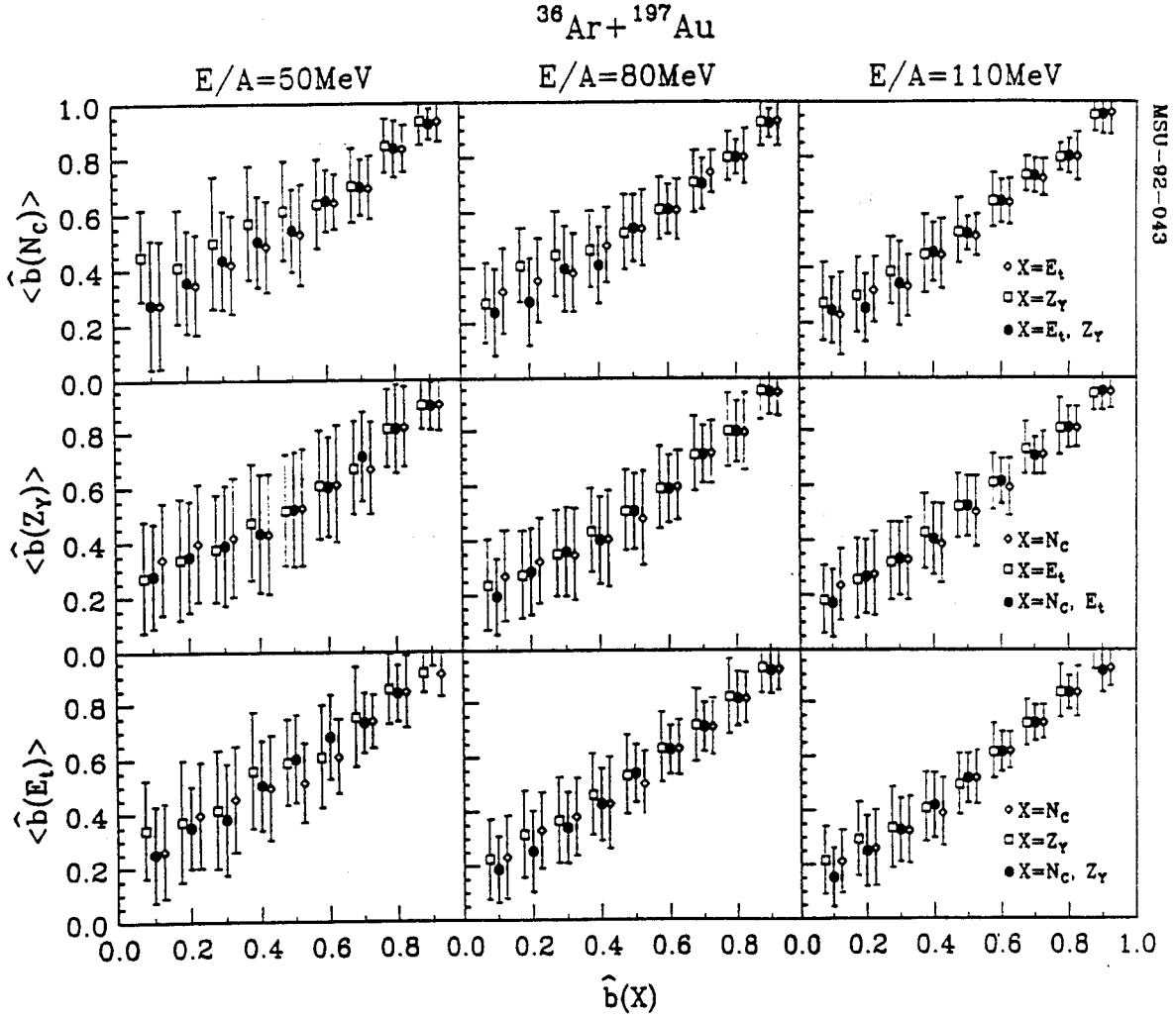


Figure 4.9 Centroids and widths at half maximum of conditional impact parameter distributions selected by cuts on impact parameters constructed from other observables $X$ indicated in the individual panels. For ease of presentation, the open points have been displaced from the centers of the gates on $\hat{b}(X)$. Top, center and bottom panels show the values for impact parameter scales constructed from $N_C$, $E_t$ and $Z_y$, respectively. Left, center and right hand columns show data for the $^{36}$Ar+$^{197}$Au reaction at E/A=50, 80, and 110 MeV.

Furthermore, the widths of the various conditional distributions are rather similar. Some modest improvement in impact parameter selection can be obtained by using multi-dimensional cuts (solid circular points). These improvements are difficult to quantify since none of the conditional distributions can be narrower than their natural widths at a given sharp impact parameter. Since the widths from one- and two-dimensional cuts are rather similar, one may surmise that the widths extracted from the two-dimensional cuts are close to the intrinsic resolution of the respective impact parameter filters.

Improved impact parameter selection could be expected from observables (or combinations of observables) which are less subject to statistical fluctuations. For example, one may argue that central collisions could be reconstructed by an accurate determination of the energy deposited into internal degrees of freedom. For fixed excitation energy, the number of emitted charged particles will exhibit considerable fluctuations due to statistical partitions of the de-excitation energy among neutrons, protons and complex particles, all of which are emitted over a broad energy spectrum. Improved reconstructions of the initial excitation energy could be expected from simultaneous measurements of neutral and charged-particle multiplicities, but some fluctuations would remain due to the finite energy distributions of the emitted particles (and varying separation energies). One should expect statistical fluctuations to be smaller for the total transverse energy of the emitted charged particles since this quantity suffers only from the random partition of the excitation energy into charged and neutral particles and into longitudinal and transverse velocities. Close inspection of Figures 4.5-8 reveals that the double-gated $\hat{b}(E_t)$ distributions are slightly narrower than the other impact parameter distributions, possibly indicating

that the transverse energy exhibits a particularly good selectivity for central collisions.

At higher energies and for noncentral collisions, geometric considerations may lead to the expectation that the intermediate rapidity charge might become competitive or even more appropriate since it could provide a better measure of the participant zone. Unfortunately, microscopic reaction models do not yet describe realistic descriptions of complex particle emission processes, and fluctuations in $Z_y$ due to fragment formation at the interfaces of the participant and spectator zones are difficult to assess. Since a substantial portion of the emitted nuclear matter emerges in the form of bound clusters, it is not clear which observables (or combinations of observables) provide optimal impact parameter selectivity. In the next section, we explore this question further by investigating an alternative measure for the selectivity of various impact parameter filters which is based upon their ability to suppress the emission of fast fragments at forward angles.

## 4.4 Suppression of projectile-like fragments

In this section, we explore the efficiency of various impact parameter filters in terms of their ability to suppress projectile-like fragments emitted with near-beam velocity at forward angles.

For illustration, Figures 4.10-12 show the energy spectra of beryllium (left-hand panels) and carbon (right-hand panels) nuclei detected in Rings 1-10 in the Miniball for incident energies of E/A=50, 80, and 110 MeV, respectively. Top and bottom panels show the energy spectra gated by cuts on the charged-particle multiplicity corresponding to $\hat{b}(N_c)>0.6$ and $\hat{b}(N_c)<0.3$, respectively. At all incident energies, the energy spectra gated by large impact

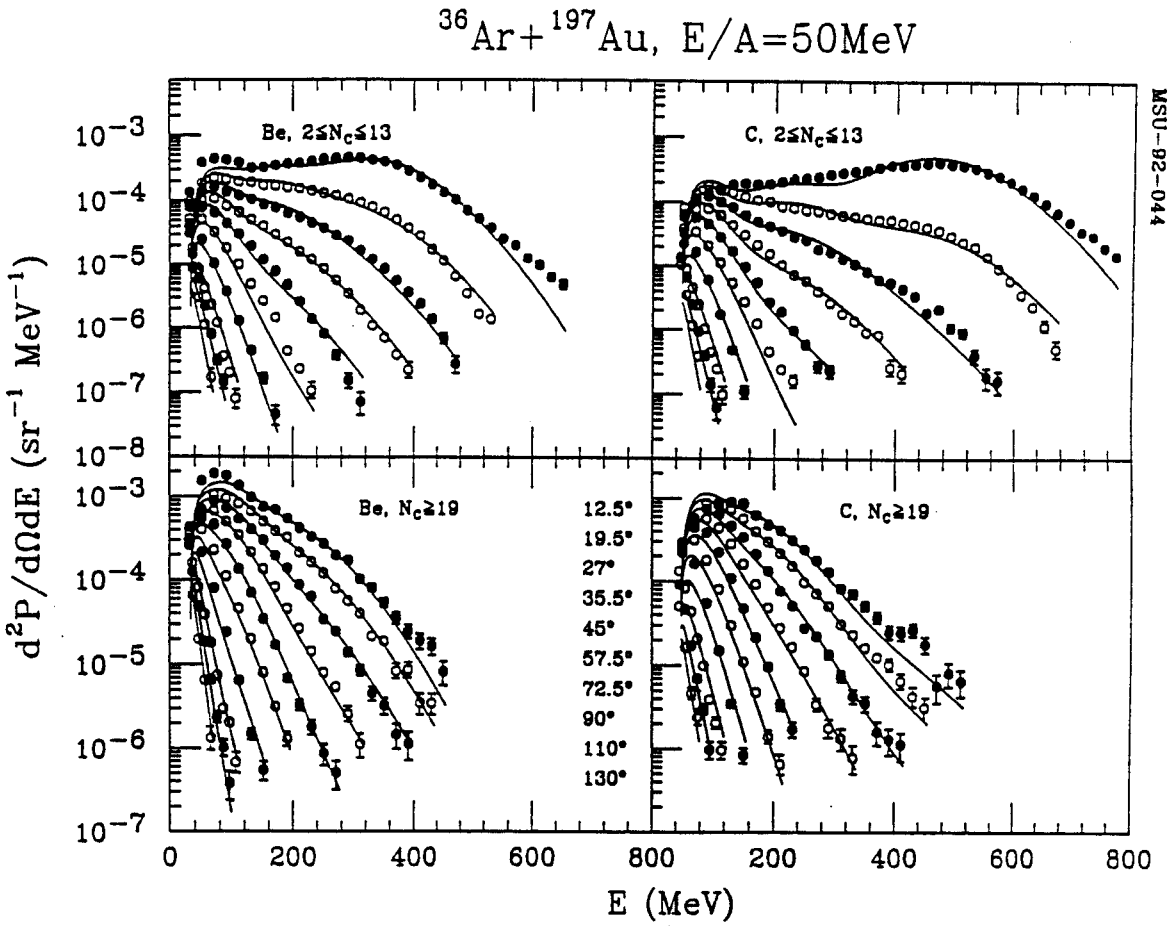


Figure 4.10 Energy spectra of beryllium (left-hand panels) and carbon (right-hand panels) nuclei emitted in peripheral ($\hat{b}$>0.6, top panels) and central ($\hat{b}$<0.3, bottom panels) $^{36}$Ar+$^{197}$Au collisions at E/A=50 MeV. The exact cuts on the measured charged-particle multiplicity are given in the figure. The solid curves are fits with equation (4.5). The parameters are listed in Table 4.1.

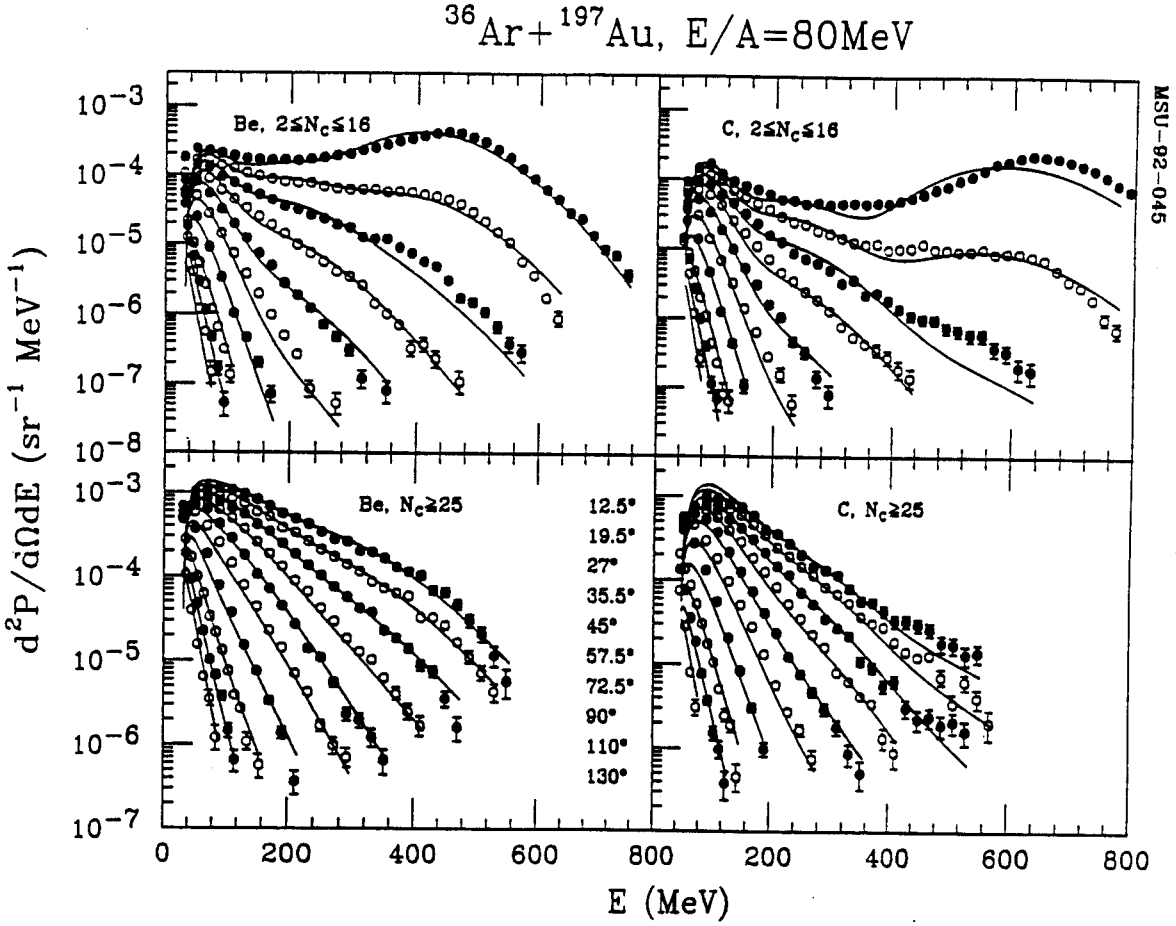


Figure 4.11 As Figure 4.10, for E/A=80 MeV.

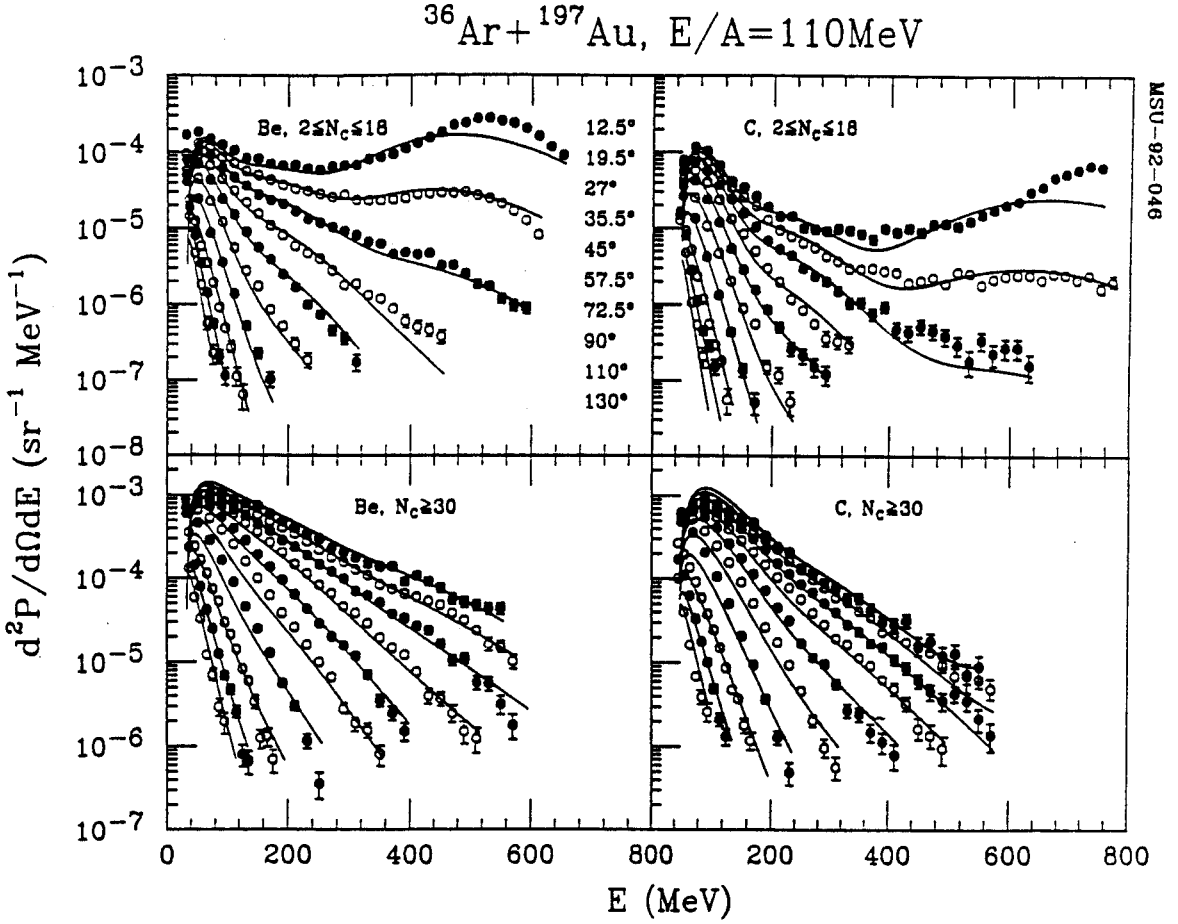


Figure 4.12 As Figure 4.10, for E/A=110 MeV.

parameters exhibit pronounced maxima at forward angles which correspond to fragment velocities close to the beam velocity. Such projectile-like contributions are strongly suppressed in the energy spectra selected by high-multiplicity cuts corresponding to $\hat{b}(N_C)<0.3$, as qualitatively expected from simple geometrical considerations within the framework of a participant-spectator approximation. These qualitative findings are consistent with observations at lower energy, E/A=35 MeV [Kim 92]. They indicate that impact parameter filters based on charged-particle multiplicity are rather effective in selecting collisions with large geometric overlap between target and projectile, even in situations where simple participant-spectator models are not expected to be accurate in detail.

In order to provide a more quantitative basis for discussing the effects of impact parameter filtering on the measured energy spectra, we fit the energy spectra with a simple three-source parameterization corresponding to the superposition of three Maxwellian distributions centered at velocities $v_i$ and characterized by temperature parameters $T_i$:

$$\frac{d^2P}{dEd\Omega} = \sum_{i=1}^{3} \sigma_i(E,\theta) = \sum_{i=1}^{3} N_i \sqrt{E - V_C} \exp\left[\frac{-\left(E - V_C + E_i - 2\sqrt{E_i(E-V_C)}\cos\theta\right)}{T_i}\right], \quad (4.5)$$

where

$$E_i = \tfrac{1}{2} m v_i^2 \quad (4.6)$$

is the energy of a particle at rest in source *i*. The parameter $V_C$ is introduced to roughly account for Coulomb repulsion from a heavy charge assumed, for simplicity, at rest in the laboratory system [Awes 81, Chit 86]. Fits obtained with this parameterization are shown as solid curves in Figures 4.10-12. The corresponding parameters are listed in Table 4.1.

A word of caution is necessary. Since our energy calibrations at backward angles have considerable uncertainties, the source parameters listed

Table 4.1 Moving source parameters used to fit the energy spectra in Figures 4.10-12[1]

| E/A | Z | $N_C$ | $N_1$ | $\beta_1$ | $T_1$ | $N_2$ | $\beta_2$ | $T_2$ | $N_3$ | $\beta_3$ | $T_3$ |
|---|---|---|---|---|---|---|---|---|---|---|---|
| 50 | 4 | 2-13 | 106 | 0.273 | 9.2 | 40.2 | 0.180 | 17.0 | 55.2 | 0.079 | 12.6 |
| 50 | 6 | 2-13 | 179 | 0.275 | 9.7 | 24.1 | 0.177 | 17.4 | 39.6 | 0.071 | 14.1 |
| 50 | 4 | ≥19 | 51 | 0.196 | 14.5 | 231 | 0.098 | 14.3 | 171 | 0.036 | 8.6 |
| 50 | 6 | ≥19 | 2.07 | 0.221 | 16.3 | 69.3 | 0.141 | 14.9 | 211 | 0067 | 14.6 |
| 80 | 4 | 2-16 | 107 | 0.303 | 11.1 | 16.3 | 0.190 | 20.2 | 44.1 | 0.073 | 12.9 |
| 80 | 6 | 2-16 | 54.7 | 0.313 | 12.5 | 5.46 | 0.169 | 20.0 | 34.6 | 0.66 | 12.4 |
| 80 | 4 | ≥25 | 28.1 | 0.218 | 21.8 | 152 | 0.106 | 21.9 | 212 | 0.046 | 12.0 |
| 80 | 6 | ≥25 | 1.08 | 0.257 | 24.5 | 31.5 | 0.142 | 24.7 | 238 | 0.071 | 16.9 |
| 110 | 4 | 2-18 | 26.1 | 0.326 | 17.5 | 6.88 | 0.165 | 24.3 | 34.6 | 0.060 | 12.6 |
| 110 | 6 | 2-18 | 4.37 | 0.333 | 19.4 | 1.67 | 0.155 | 22.3 | 25.4 | 0.057 | 12.4 |
| 110 | 4 | ≥30 | 9.48 | 0.248 | 31.9 | 91.8 | 0.123 | 29.9 | 251 | 0.055 | 15.8 |
| 110 | 6 | ≥30 | 12.1 | 0.406 | 24.3 | 17.4 | 0.142 | 34.8 | 218 | 0.068 | 19.4 |

in Table 4.1 may have large systematic uncertainties. In particular, the parameters of the slow target-like sources ($i$=3) must be viewed with caution, and the temperature parameters $T_3$ should not be misconstrued as accurate temperature measurements for target-like residues.

Nevertheless, the fits allow estimates of the relative contributions from fast projectile-like sources and intermediate-velocity "nonequilibrium" sources. At all energies, peripheral collisions ($\hat{b}$>0.6) are characterized by strong contributions from projectile-like sources. Such contributions are strongly suppressed for more "central" collisions ($\hat{b}$<0.3). However, central collisions have significant contributions from intermediate-velocity "nonequilibrium" sources representing emission during the early, nonequilibrated stages of the reaction. Our present findings are consistent with previous observations at a lower energy [Kim 92]. Clearly, accurate descriptions of energy spectra and angular distributions will require

[1]For beryllium and carbon nuclei, the Coulomb parameters were $V_C$=32.9 and 47.2 MeV, respectively. The normalization constants $N_i$ are given in units of $10^{-6}/(sr \cdot MeV^{3/2})$; units for E/A and $T_i$ are in MeV. At the energies E/A=50, 80, 110 MeV, the velocities of the projectile are: βc.m.=0.051, 0.065 and 0.07, respectively.

theoretical treatments which allow the incorporation of emission from the earlier non-equilibrated phases of the reaction, as well as from the later more equilibrated stages.

In order to provide a more quantitative measure of the selectivity of the impact parameter filter based upon the charged-particle multiplicity, we have fitted the multiplicity selected energy spectra of representative complex particles (He, Li, Be, C) with equations (4.5-6) and determined the relative contribution, $\sigma_{proj} / \sigma_{tot}$, of the projectile-like source to the total particle yield. This contribution was evaluated by integrating the respective sources over all angles and energies:

$$\sigma_{proj} = \iint \sigma_1(E,\theta) dE d\Omega , \tag{4.7}$$

$$\sigma_{tot} = \sum_{i=1}^{3} \iint \sigma_i(E,\theta) dE d\Omega , \tag{4.8}$$

We did not analyze the energy spectra of hydrogen nuclei, because of the restricted dynamic range of the Miniball (75 MeV protons punch the CsI crystals). Moreover, light particles (especially nucleons) are less suitable for such an analysis, because of their comparatively large mean free path and because "thermal" smearing of the energy spectra is more serious for light particles than for intermediate mass fragments. As a consequence, collective source velocity components are more difficult to unravel from the energy spectra of light particles.

Figure 4.13 shows ratios $\sigma_{proj} / \sigma_{tot}$ extracted from the energy spectra of He, Li, Be and C nuclei selected by different cuts on charged-particle multiplicity for the $^{36}Ar+^{197}Au$ reactions at E/A=110 MeV. For illustration, a scale of the reduced impact parameter $\hat{b}(N_C)$ and a pictorial illustration of the geometric overlap between projectile and target nuclei are included in the figure. While such a simplistic graphic visualization must not be taken too

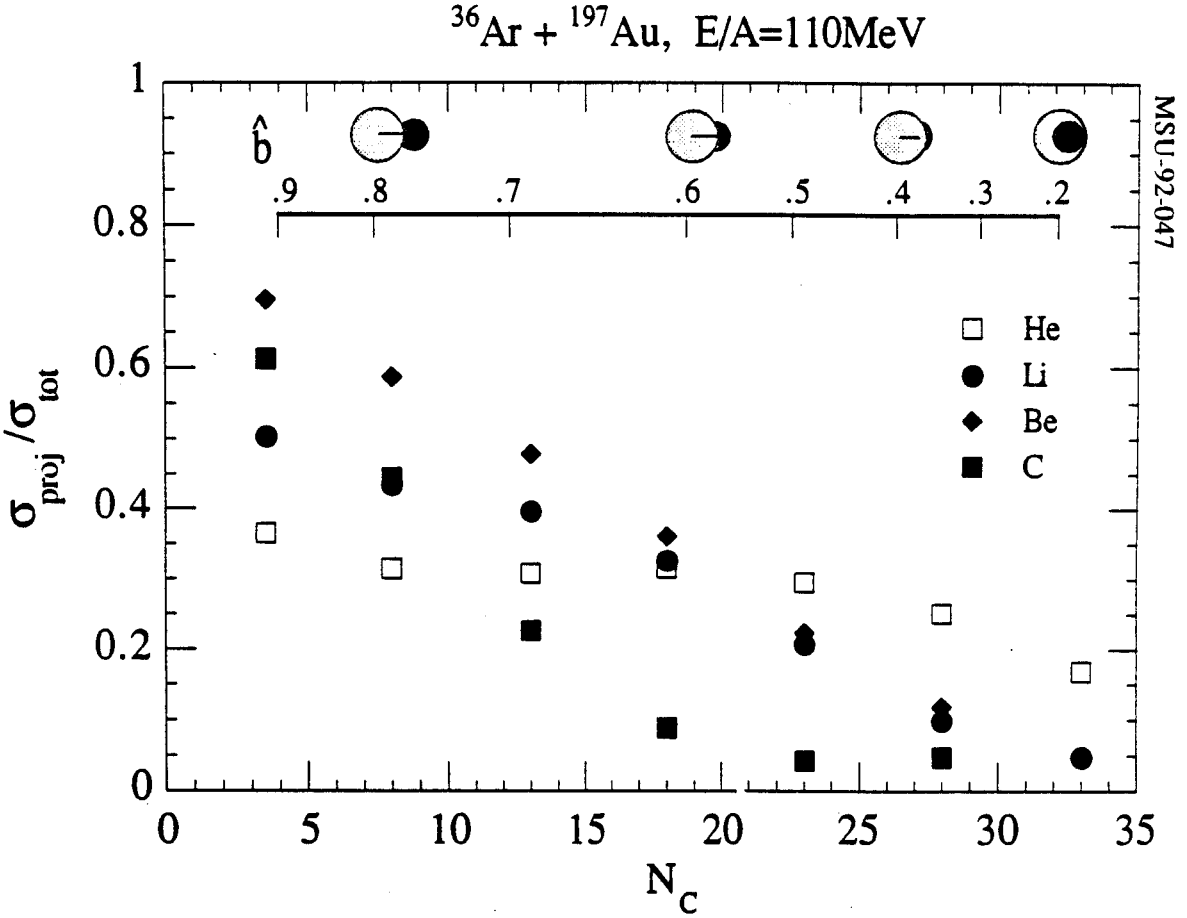


Figure 4.13 Relative contribution of projectile-like source extracted from the energy spectra of He, Li, Be and C nuclei selected by different cuts on charged-particle multiplicity for $^{36}$Ar+$^{197}$Au collisions at E/A=110 MeV. A scale of the reduced impact parameter $\hat{b}(N_c)$ and a pictorial illustration of the geometric overlap between projectile and target nuclei are included.

seriously, it nevertheless illustrates that complete overlap between projectile and target nuclei is only achieved for relatively small impact parameters, representing less than 10% of the total reaction cross section. Even in such a naive geometric picture, some emission from projectile-like sources must be expected down to impact parameters of $\hat{b}$=0.4. These simple expectations are fulfilled rather nicely for the emission of intermediate mass fragments for which projectile-like contributions are strongly suppressed at large multiplicities (small impact parameters). The suppression of projectile-like contributions is more effective for heavier (e.g. carbon nuclei) than for lighter particles (e.g. α-particles). In fact, the emission of fast α-particles does not follow the simple trends expected from simple geometric arguments. Possibly α-particle emission already sets in at the early contact phase of the reaction and can, therefore, not be described by a simple participant-spectator picture.

In order to compare of the effects of different impact parameter filters on the shapes of the energy spectra at forward angles, we have analyzed the energy spectra of particles detected in rings 1 and 2 ($\theta$=9°-23°) and determined the "fast-particle fraction" $\sigma\left(v > \frac{1}{2}v_p\right) / \sigma_{tot}$, defined as the fraction of particles detected in rings 1 and 2 with velocities larger than half the projectile velocity. This simple quantity provides qualitatively similar insight as the quantity $\sigma_{proj} / \sigma_{tot}$ obtained from the moving source decomposition, without necessitating cumbersome multi-parameter fits with equation (4.5). The fast-particle fraction is well defined and it can be established with good statistical accuracy even for narrow cuts on impact parameter. Furthermore, this quantity is insensitive to source-parameter ambiguities associated with fits to energy spectra which have poor statistical accuracy due to narrow cuts on impact parameter.

Fast-particle fractions extracted for various cuts on impact parameter are shown Figures 4.14-16. Different figures show results for the three incident energies. Individual panels show the fast-particle fractions for He, Li, Be and C nuclei, and different symbols depict results obtained by different impact parameter filters.

At all energies, the fast-particle fractions are monotonic functions of the reduced impact parameter. The suppression of fast particles for cuts on small impact parameters is particularly effective for beryllium and carbon nuclei. The suppression of fast particles is less effective for α-particles. These qualitative observations are consistent with the results obtained with the moving source decomposition shown in Figure 4.14. For impact parameters $\hat{b}$<0.6, all three impact parameter filters produce rather consistent fast-particle fractions. For intermediate and small impact parameters ($\hat{b}$<0.6), filters constructed from $N_C$, $E_t$ and $Z_y$ appear to provide comparable resolution. Slightly better suppressions of the fast-particle fractions can be obtained by employing triple cuts on values of the impact parameters reconstructed from $N_C$, $E_t$ and $Z_y$ (see star-shaped points). Consistent with our previous findings, these improvements are relatively inconspicuous.

For larger impact parameters, however, the differences between the various techniques become more significant, particularly at the higher energies. Such differences may be caused by statistical fluctuations of the quantities $N_C$, $E_t$ and $Z_y$. The relative magnitude of these fluctuations should be largest for peripheral collisions which are characterized by small mean values $<N_C>$, $<E_t>$, and $<Z_y>$. As a consequence, selections of large impact parameters may be associated with larger uncertainties than selections of smaller impact parameters.

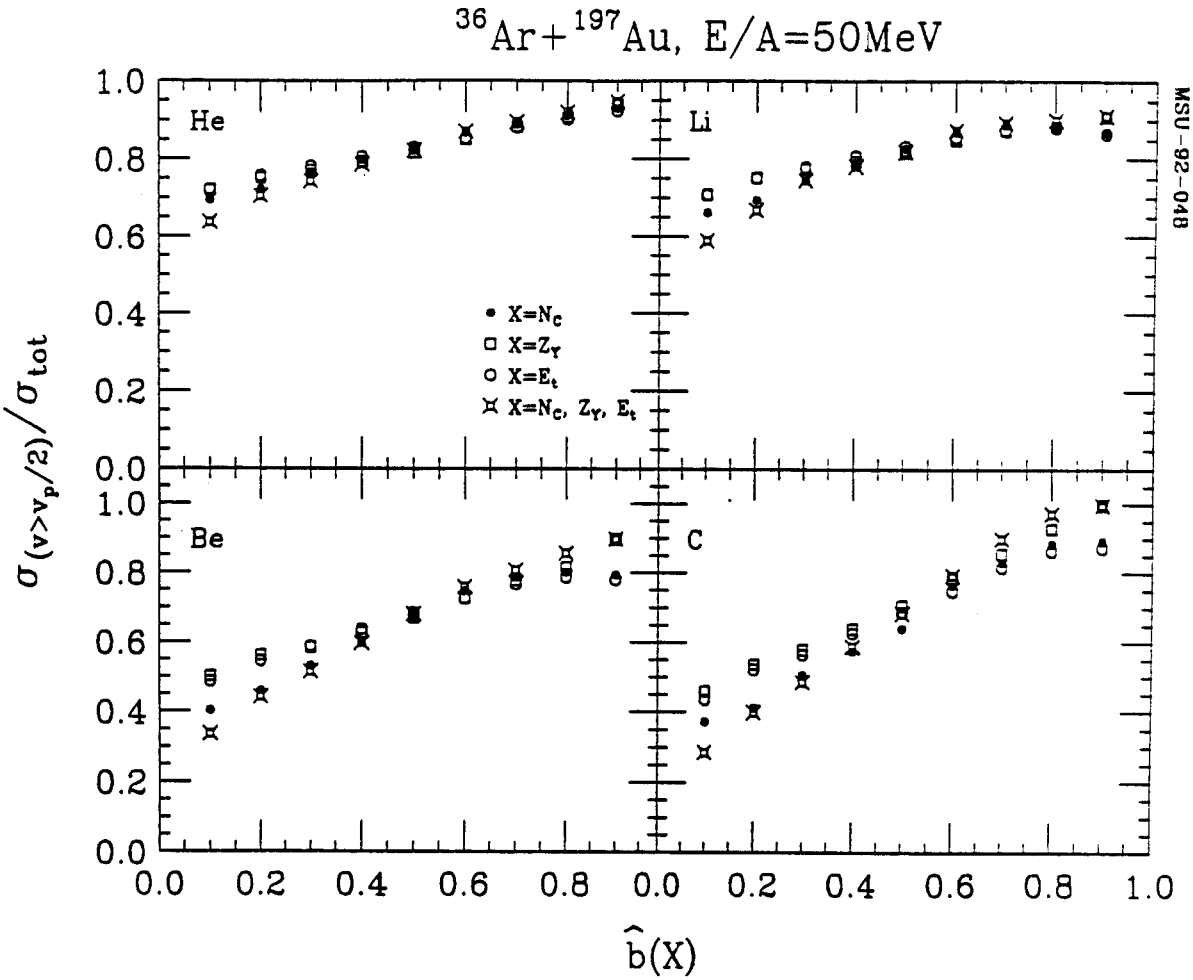


Figure 4.14 Fast-particle fractions (fractions of particles detected at $\theta$=9°-23° with velocities greater than half the beam velocity) for $^{36}Ar+^{197}Au$ collisions at E/A=50 MeV. Solid points, open squares and open circles depict values determined for narrow cuts on the reduced impact parameters determined from $N_C$, $E_t$ and $Z_y$. Star-shaped points represent simultaneous cuts on $\hat{b}(N_C)$, $\hat{b}(E_t)$ and $\hat{b}(Z_y)$.

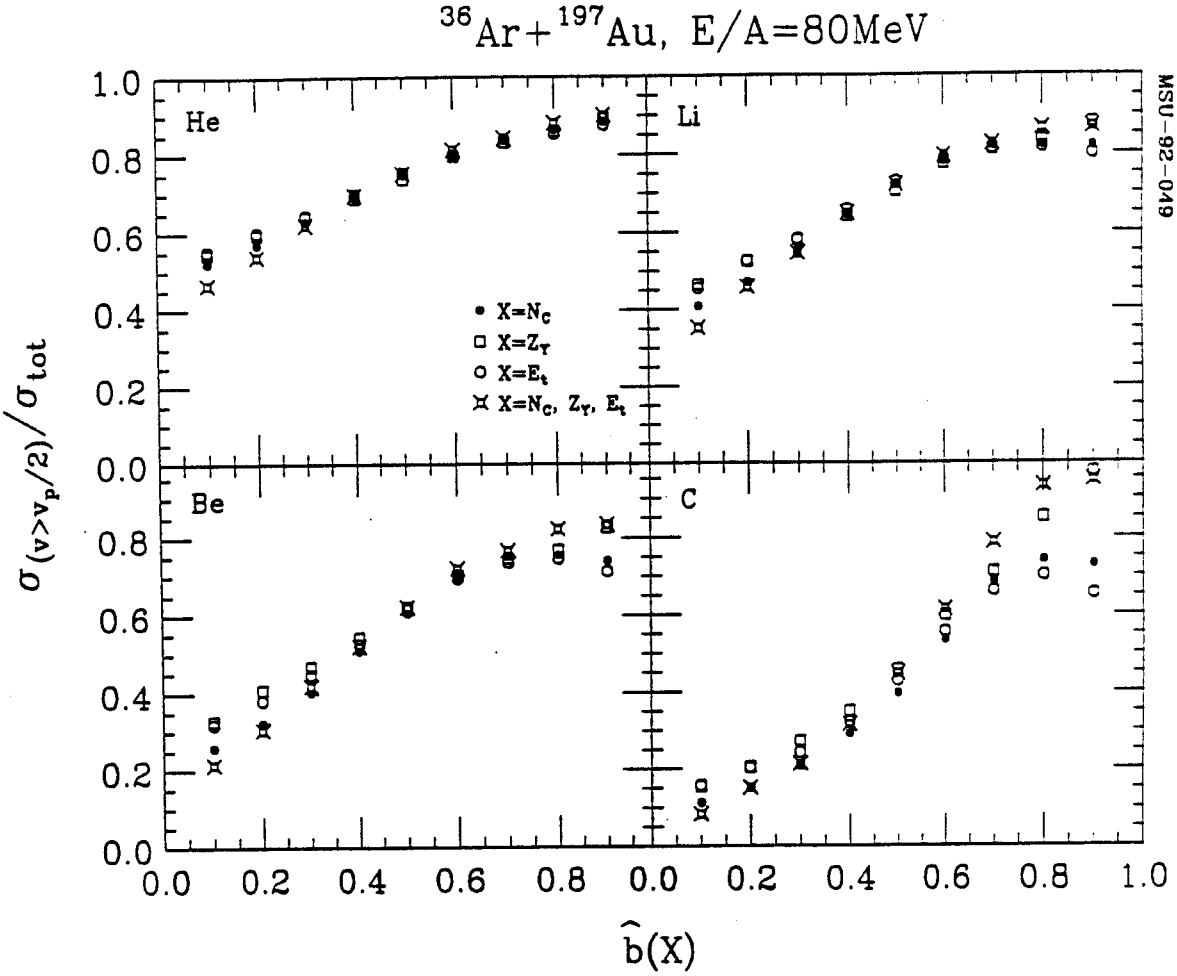


Figure 4.15 As Figure 4.14, for E/A=80 MeV.

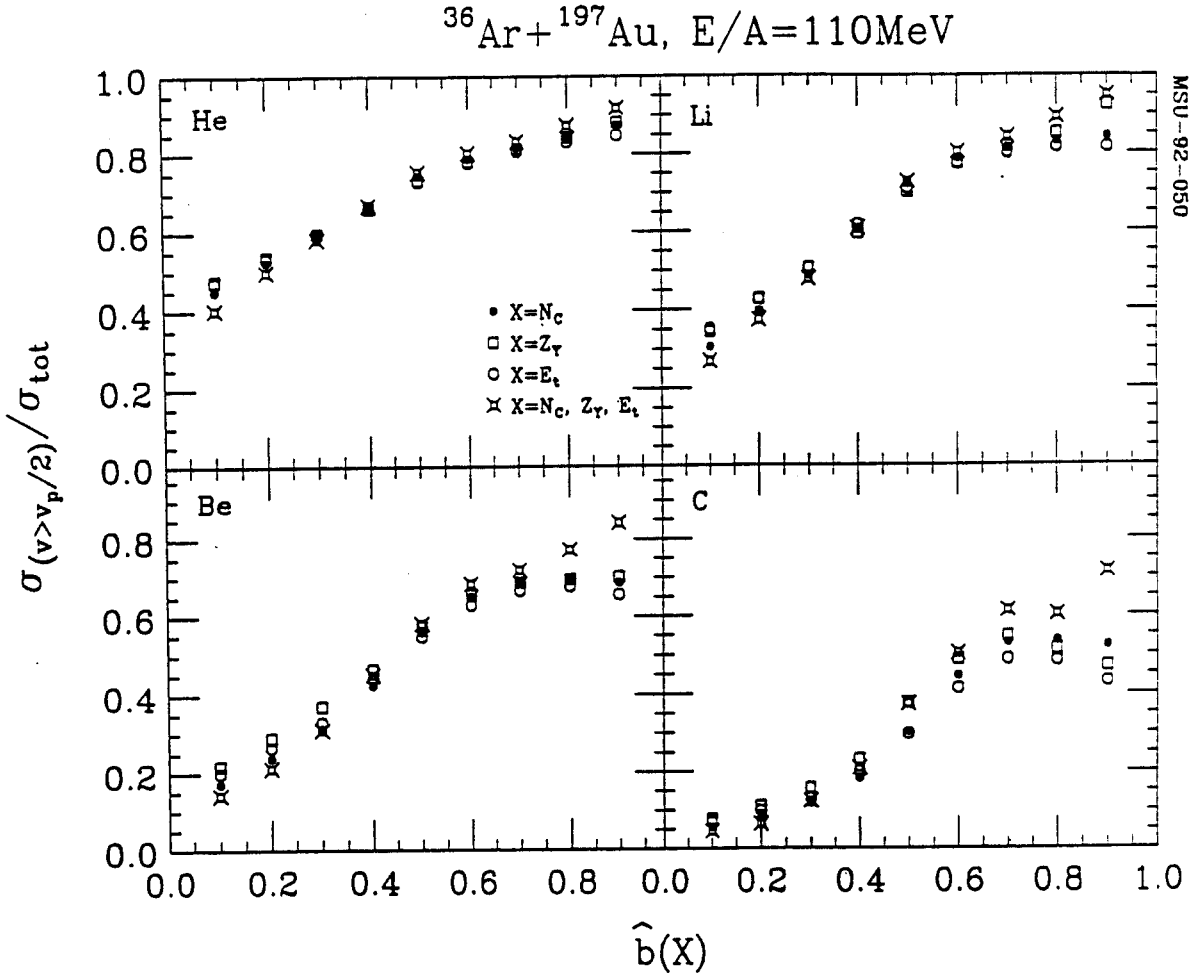


Figure 4.16 As Figure 4.14, for E/A=110 MeV.

## 4.5 Suppression of azimuthal correlations

In the previous section we have shown that impact parameter selection techniques based on $N_C$, $E_t$ and $Z_y$ provide rather similar event selection and that, indeed, cuts on small, reduced impact parameters strongly suppress contributions from projectile-like fragments as expected from qualitative arguments. A recent analysis of data with solid angle coverage restricted to forward angles ($\theta_{lab} \leq 30°$) suggests that improved selectivity for central collisions could be achieved by introducing a new observable, the transverse momentum directivity (defined in equation (4.11), below) and by simultaneous cuts on large charged-particle multiplicities and small transverse-momentum directivities [Alar 92].

In the next two sections, we address two questions: (i) can previously used impact parameters filters ($N_C$, $E_t$ and $Z_y$ ) be used to select central collisions, i.e. collisions with small angular momenta?, and (ii) do cuts on the directivity significantly improve central event selection when used with detectors providing $4\pi$ coverage? In order to quantify the selection of collisions with small impact parameters, we explore the azimuthal correlations between emitted light particles [Tsan 84a, Chit 86, Fiel 86, Tsan 90, Ardo 90, Elma 91, Wang 91]. For truly central collisions, a reaction plane is undefined and the azimuthal distribution of emitted particles must be symmetric about the beam axis. If the azimuthal correlations between two emitted particles reflect their single-particle emission patterns, the azimuthal correlation function must become flat for central collisions. (Deviations from strict azimuthal isotropy may arise from final state interactions such as the sequential decay of primary reaction products produced in particle unbound states [Poch 87] or, for small systems, from momentum conservation effects [Chit 86, Lync 87].) For peripheral collisions on the other hand, transverse

flow effects or other ordered motion in the reaction plane [Tsan 84a, Chit 86, Fiel 86, Tsan 90, Ardo 90, Elma 91, Wang 91, Tsan 84b, Tsan 86, Tsan 88, Wils 90, Tsan 91] can cause large anisotropies in the azimuthal correlations. We apply this analysis to our previously measured [Phai 92a, Tsan 88, Bowm 91, deSo 91, Kim 92, Bowm 92] data of $^{36}Ar+^{197}Au$ collisions at E/A=35, 50, 80 and 110 MeV, and $^{129}Xe+^{197}Au$ collisions at E/A=50 MeV.

In this section we will define the azimuthal correlations and use them to test the effectiveness of the different impact parameter filters. In section 4.6 we explore the usefulness of a directivity cut in selecting central collisions. A summary and conclusions are given in section 4.7.

In the previous section it was demonstrated that impact parameter filters based upon $N_C$, $E_t$ and $Z_y$ were similarly effective in suppressing particles emitted with near-projectile velocities when cuts on small reduced impact parameters were applied. While the suppression of beam velocity particles is qualitatively expected for collisions between a relatively small projectile and a relatively large target nucleus, a suppression of beam velocity fragments may not necessarily be the best indicator for event centrality. Therefore, in the following sections we evaluate an alternative observable which depends less on a participant-spectator picture and which is more closely related to the angular momentum effects as evidenced by an ordered motion of the emitted particles in the entrance channel reaction plane.

## Azimuthal correlation functions

Ordered motion of the emitted particles can be detected by measurements of azimuthal correlation functions [Tsan 84a, Chit 86, Fiel 86, Tsan 90, Wang 91] defined by the ratio

$$\left.\frac{Y(\Delta\phi)}{Y'(\Delta\phi)}\right|_{\theta,\hat{b}} = C\left[1+R(\Delta\phi)\right]\Big|_{\theta,\hat{b}}. \qquad (4.9)$$

Here, $Y(\Delta\phi)$ is the coincidence yield of two (identical) particles emitted with relative azimuthal angle $\Delta\phi$ at a polar laboratory angle $\theta$ and in collisions selected by a specified cut on reduced impact parameter $\hat{b}$; $Y'(\Delta\phi)$ is the background yield constructed by mixing particle yields from different coincidence events, but selected by identical cuts on the reduced impact parameter; C is a normalization constant such that the average value of the correlation $1+R(\Delta\phi)$ is one. All azimuthal correlation functions presented in this paper were constructed from particles detected at $\theta = 31° - 50°$.

Azimuthal correlation functions may provide an additional diagnostic tool with regard to the selection of central collisions which is complementary to the suppression of beam velocity particles investigated in the previous section. For example, if projectile and target nuclei fuse at finite impact parameters, the emission of beam velocity particles will be suppressed for all impact parameters below a certain value. However, off-center fusion reactions will induce a collective rotation of the residue. The angular velocity of this collective rotation depends on impact parameter. Particle emission from a rotating compound nucleus is focused in a plane perpendicular to the angular momentum vector, i.e. the emission will be enhanced in the reaction plane [Chit 86]. The degree of this enhancement increases with the angular velocity of rotation, and it decreases as a function of temperature. The effect becomes more pronounced for heavier emitted particles [Chit 86]. For the case of equilibrium emission from a long-lived rotating system, the emission becomes left-right symmetric and the azimuthal correlation functions exhibit a characteristic V-shape [Chit 86]. In the limit of $\hat{b} \rightarrow 0$, the collective rotation ceases and the azimuthal correlation function becomes flat, i.e. $R(\Delta\phi) \rightarrow 0$.

Nonvanishing azimuthal correlation functions have been observed in a large number of intermediate-energy heavy ion collision experiments. In many instances, slightly distorted "V"-shapes were observed [Tsan 84a, Chit 86, Fiel 86, Tsan 90, Elma 91] which could be understood in terms of a collective rotational motion in the reaction plane caused by the attractive mean nuclear field [Tsan 84a, Tsan 86, Tsan 88, Wils 90]. A number of other physical effects can influence the shape of the azimuthal correlation functions and lead to deviations from symmetric V-shapes. An important example is the directed transverse flow caused by the interplay of mean field deflection and pressure due to nuclear compression [Tsan 89a, Moli 85, Ogil 90, Wils 90, Sull 90]. Additional distortions may arise from phase space constraints imposed on finite systems by momentum conservation [Lync 82, Ogil 89b] or final state interactions [Elma 91].

Figure 4.17 shows azimuthal correlation functions of protons, deuterons, tritons and He nuclei ($^3$He and $^4$He combined) detected in peripheral ($\hat{b} > 0.75$) $^{36}$Ar + $^{197}$Au collisions at E/A=50 MeV. (For brevity of notation, all emitted He nuclei are denoted by the symbol $\alpha$ in the figures; contributions from $^3$He are smaller than those from $^4$He by a factor of about 5). A uniform software energy threshold of E/A=12 MeV was applied. In addition, the energies of protons, deuterons and tritons were required to be smaller than 75, 100 and 119 MeV respectively (the punch-through energies for the 2 cm thick CsI crystals). For He nuclei, no upper energy threshold was imposed since punch-through He nuclei could still be cleanly identified since no distinction is being made between $^3$He and $^4$He. Consistent with previous observations for slightly different systems [Tsan 84a, Chit 86, Jiel 86, Tsan 90, Ardo 90, Elma 91], the azimuthal correlation functions exhibit (slightly distorted) V-shaped patterns with a clear minimum at $\Delta\phi \approx 90°$, reflecting the

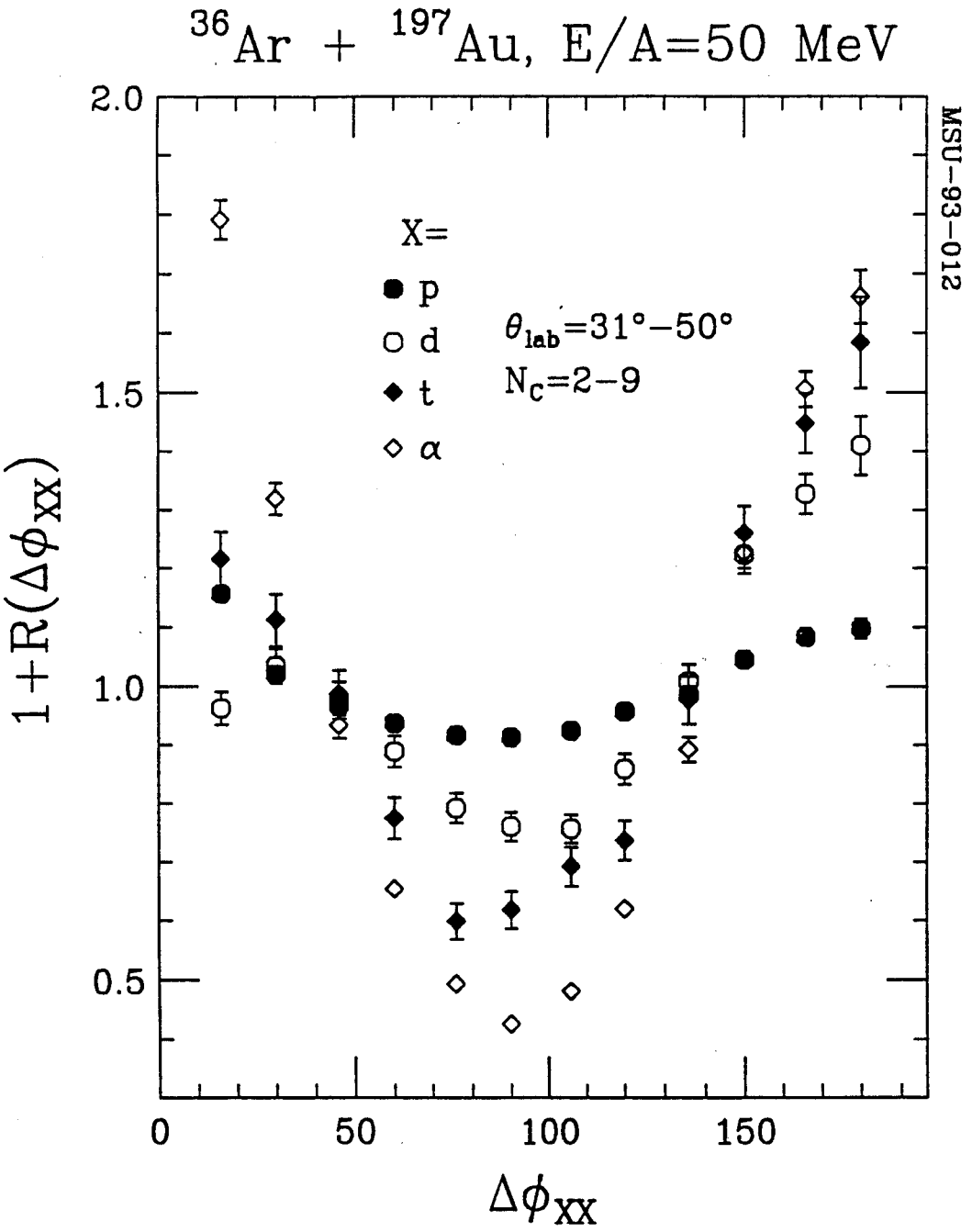


Figure 4.17 Azimuthal correlation functions constructed from particle pairs of protons, deuterons, tritons and He nuclei emitted in peripheral $^{36}Ar+^{197}Au$ collisions ($\hat{b}$>0.75, $N_c$=2-9) at E/A=50 MeV. The correlation functions were constructed for particles emitted at polar angles of $\theta_{lab}$=31°-50° using an energy threshold $E_{th}$/A=12 MeV.

known preferential emission of nonequilibrium particles in the entrance channel reaction plane [Tsan 84a, Chit 86, Fiel 86, Tsan 90, Ardo 90, Elma 91, Tsan 84b, Tsan 86, Tsan 88, Wils 90, Tsan 91]. Again consistent with previous observations [Tsan 84a, Chit 86, Fiel 86, Tsan 90, Ardo 90, Elma 91, Tsan 84b, Tsan 86, Tsan 88, Wils 90, Tsan 91], the azimuthal anisotropies become stronger with increasing mass of the particle pair. Since the effect is particularly pronounced for He nuclei and since He nuclei are emitted in great abundance, we utilize the He azimuthal correlation function as a diagnostic tool for assessing whether cuts on small reduced impact parameters do, indeed, select central collisions.

## Comparison of relative scales

Figures 4.18-22 show azimuthal correlation functions for He nuclei emitted in $^{36}Ar$ + $^{197}Au$ collisions at E/A = 35, 50, 80 and 110 MeV and for $^{129}Xe$ +$^{197}Au$ collisions at E/A = 50 MeV. A software threshold of E/A=8 MeV was used in selecting the He nuclei. Different panels of the figures show results for different cuts on the charged-particle multiplicity $N_C$. For each panel, the overlapping circles present a simple geometric picture of the collision geometry deduced by means of equation (4.4). At large impact parameters, i.e. low values of $N_C$, the correlation functions show a strong preference of emission at relative azimuthal angles of $\Delta\phi \approx 0°$ and 180°, characteristic of preferential emission in the reaction plane. At larger values of $N_C$, the azimuthal correlation functions become more isotropic. For a given cut on reduced impact parameter, the azimuthal correlation functions become increasingly damped as the beam energy is increased. The effect may be related to the disappearance of flow predicted and observed [Moli 86, Ogil 90, Wils 90, Sull 90] in symmetric projectile-target collisions at comparable

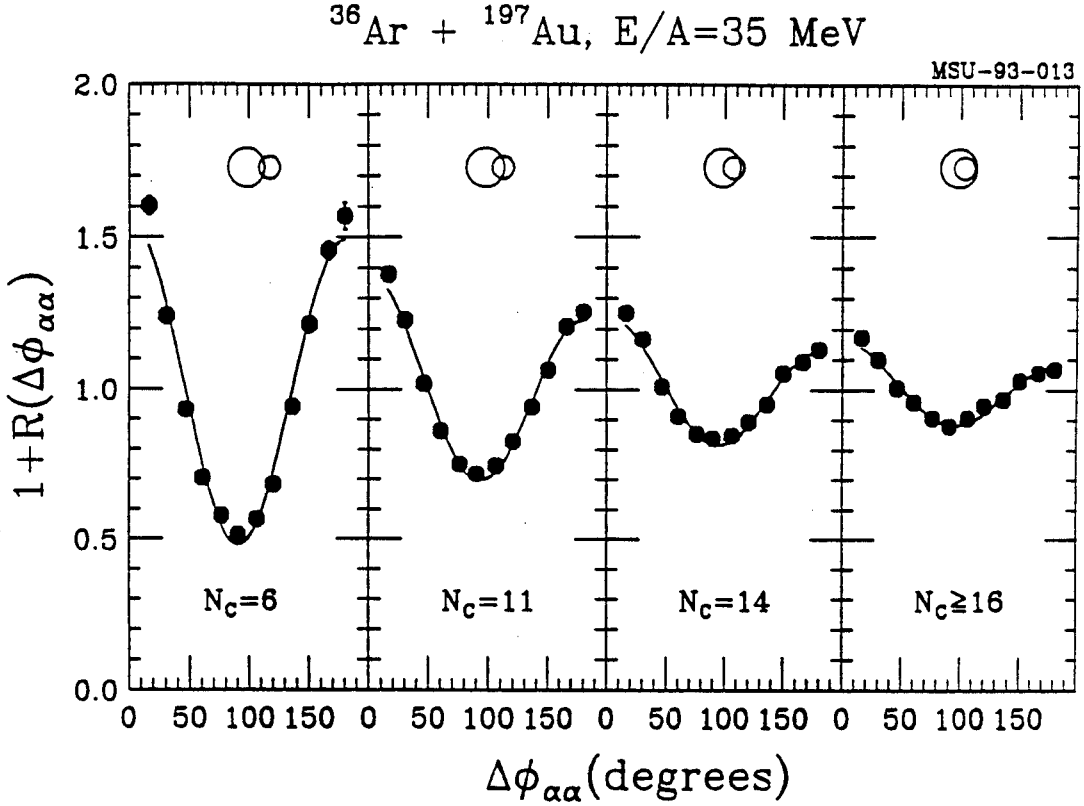


Figure 4.18 Azimuthal correlation functions for He nuclei emitted in $^{36}$Ar+$^{197}$Au collisions at E/A = 35 MeV. Panels from left to right show data selected by cuts on reduced impact parameters $\hat{b}$ = 0.8, 0.6, 0.4, and <0.2, respectively; the actual cuts on charged-particle multiplicity $N_c$ are indicated in the figure. The circles show the approximate geometric overlap between target and projectile for the different cuts in $N_c$.

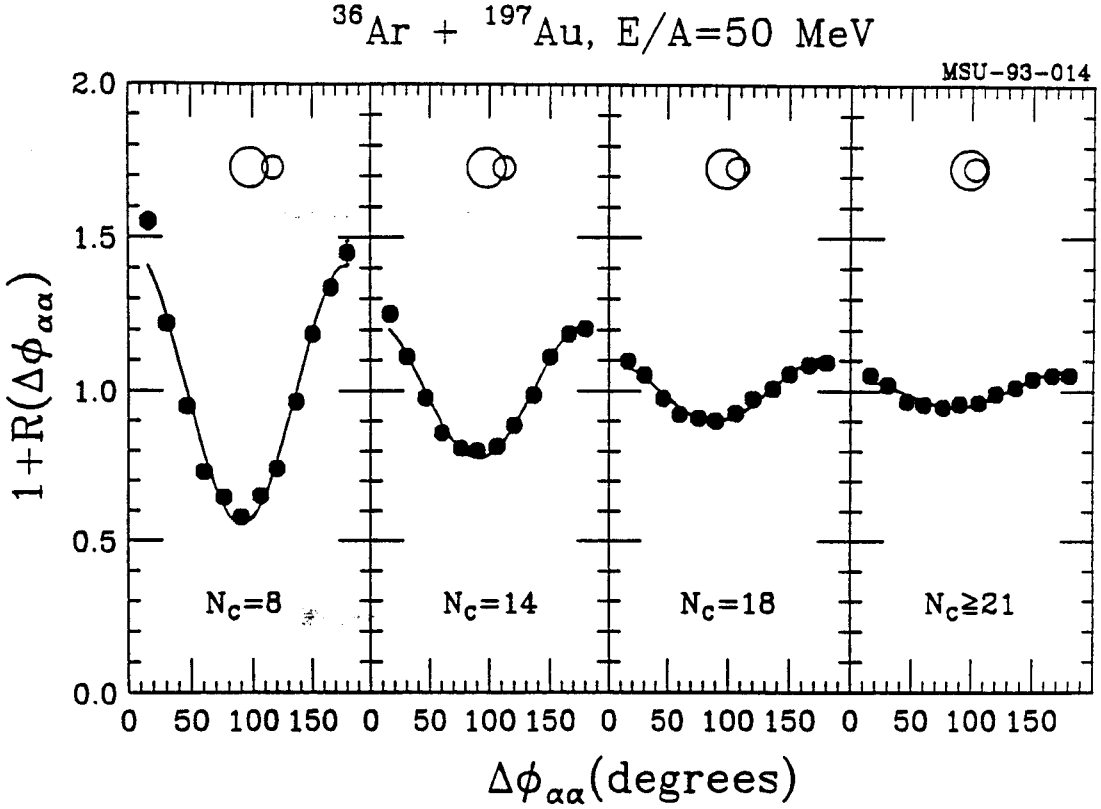


Figure 4.19 As Figure 4.18, for E/A = 50 MeV.

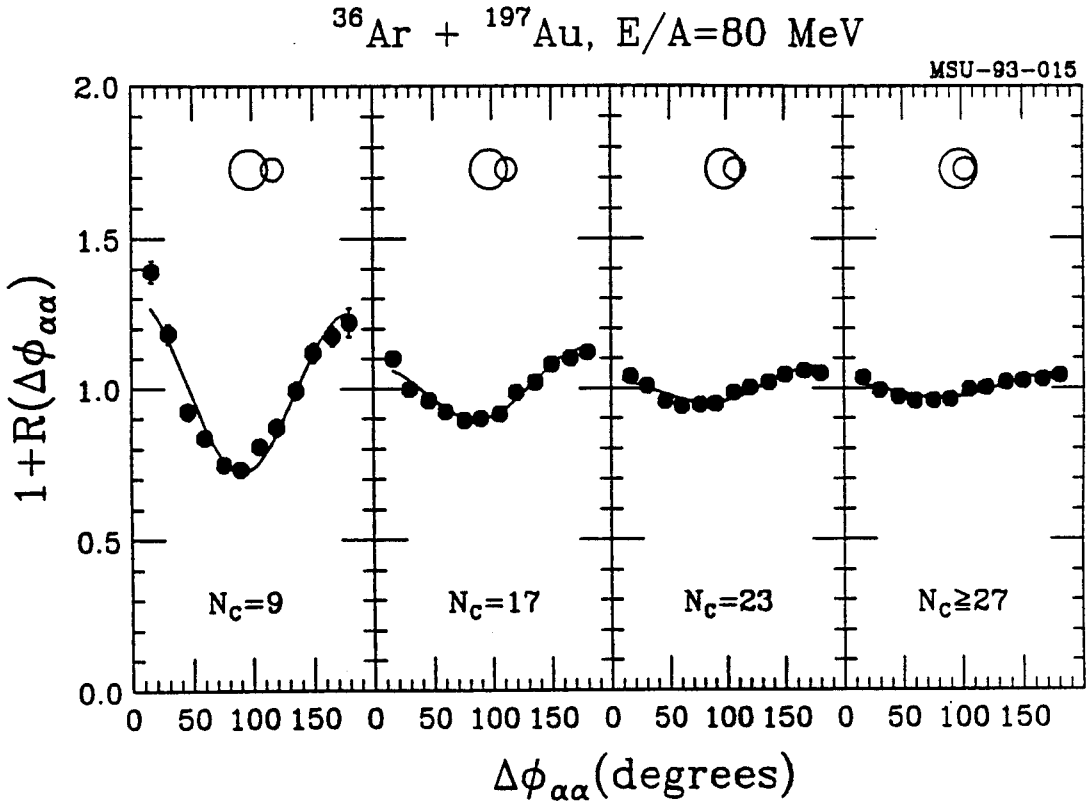


Figure 4.20 As Figure 4.18, for E/A = 80 MeV.

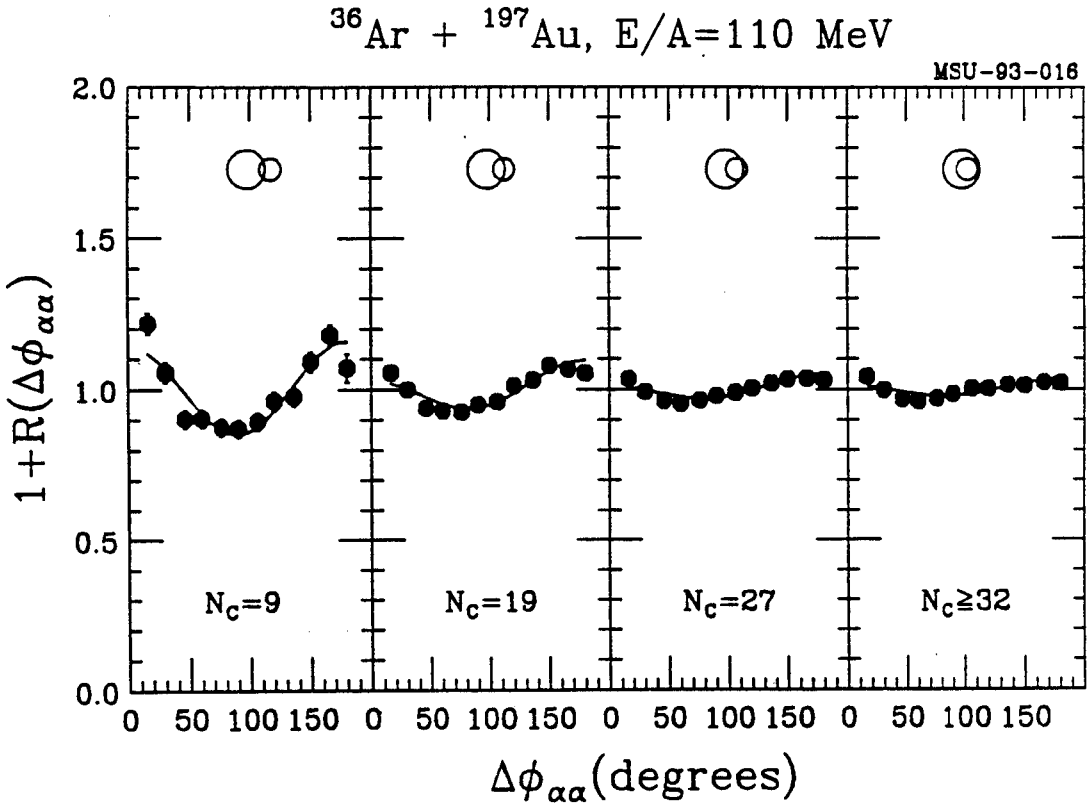


Figure 4.21 As Figure 4.18, for E/A = 110 MeV.

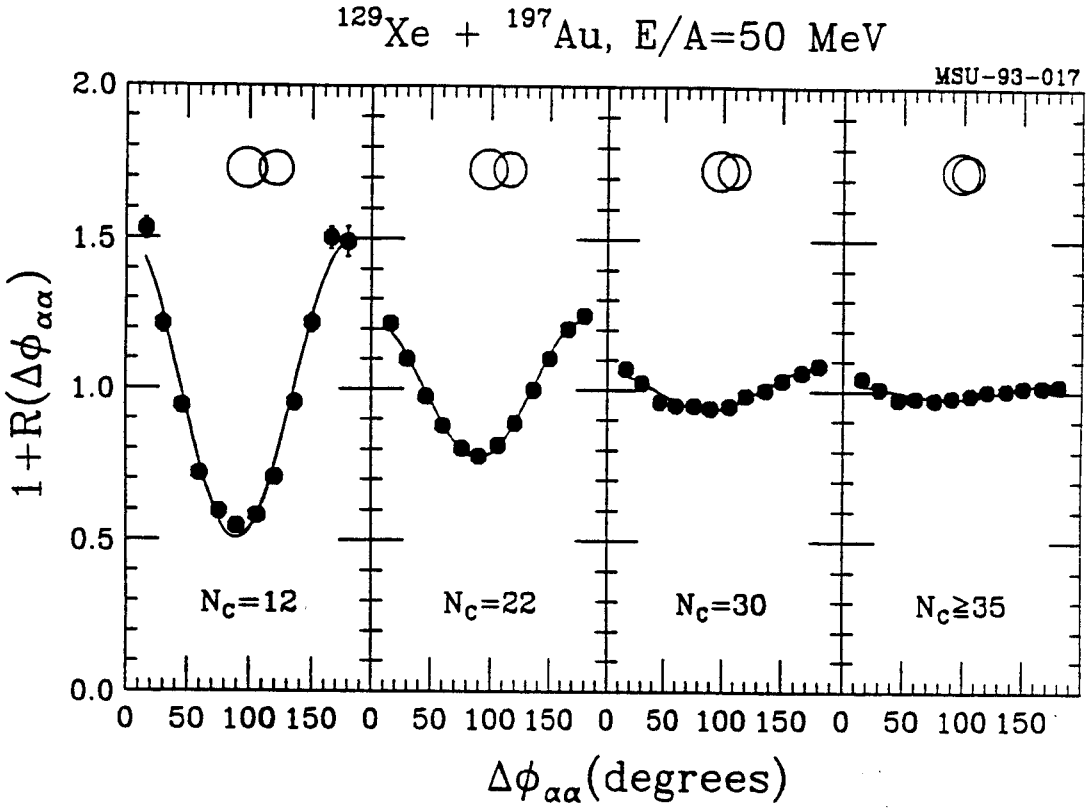


Figure 4.22 Azimuthal correlation functions for He nuclei emitted in $^{129}$Xe+$^{197}$Au collisions at E/A = 50 MeV. Panels from left to right show data selected by cuts on reduced impact parameters $\hat{b}$ = 0.8, 0.6, 0.4, and <0.2, respectively; the actual cuts on charged-particle multiplicity $N_c$ are indicated in the figure. The circles show the approximate geometric overlap between target and projectile for the different cuts in $N_c$.

energies, possibly reflecting an increased balancing of attractive and repulsive forces from the mean nuclear field and from pressure, respectively.

In order to allow a more compact presentation of the main features of the observed azimuthal correlation functions, we have fitted them by functions of the form

$$1+\lambda_1\cos(\Delta\phi)+\lambda_2\cos(2\Delta\phi)\ , \qquad (4.10)$$

where $\lambda_1$ and $\lambda_2$ are treated as free parameters. Large values of $\lambda_2$ may be associated with collective motion resembling a rotation [Lace 93]. Positive (negative) values of $\lambda_1$ indicate preferential emission of the particle pair to the same side (opposite sides) of the beam. Positive values of $\lambda_1$ can come from large final state interactions (e.g. the decay $^8Be \rightarrow 2\alpha$) or, alternatively, from directed sideward flow. Negative values of $\lambda_1$ (preferred emission on opposite sides of the beam) may reflect phase space constraints for small systems due to momentum conservation [Lync 82, Ogil 89b]. For isotropic distributions $\lambda_1=\lambda_2=0$.

Figure 4.23 presents the values of the parameters $\lambda_1$ and $\lambda_2$, extracted as a function of reduced impact parameter $\hat{b}(N_C)$ for $^{36}Ar + ^{197}Au$ collisions at the different bombarding energies. At all bombarding energies, $\lambda_2$ decreases as a function of decreasing reduced impact parameter. Indeed, for E/A ≥ 50 MeV, $\lambda_2 \rightarrow 0$ as $\hat{b}(N_C) \rightarrow 0$ with rather good accuracy, indicating that small reduced impact parameters do, indeed, select near-central collisions for which $R(\Delta\phi) \approx 0$ by necessity. At E/A=35 MeV, the selection of central collisions appears to be of slightly reduced quality since $\lambda_2 \geq 0.1$ even for very small values of $\hat{b}(N_C)$. To some extent, reduced selectivity for very central collisions at the lower energy may result from a loss of statistical resolution as $\Delta N_C / N_C$ becomes larger at lower incident energy. It is more likely, however, that this loss of resolution is related to the breakdown of the participant-spectator picture

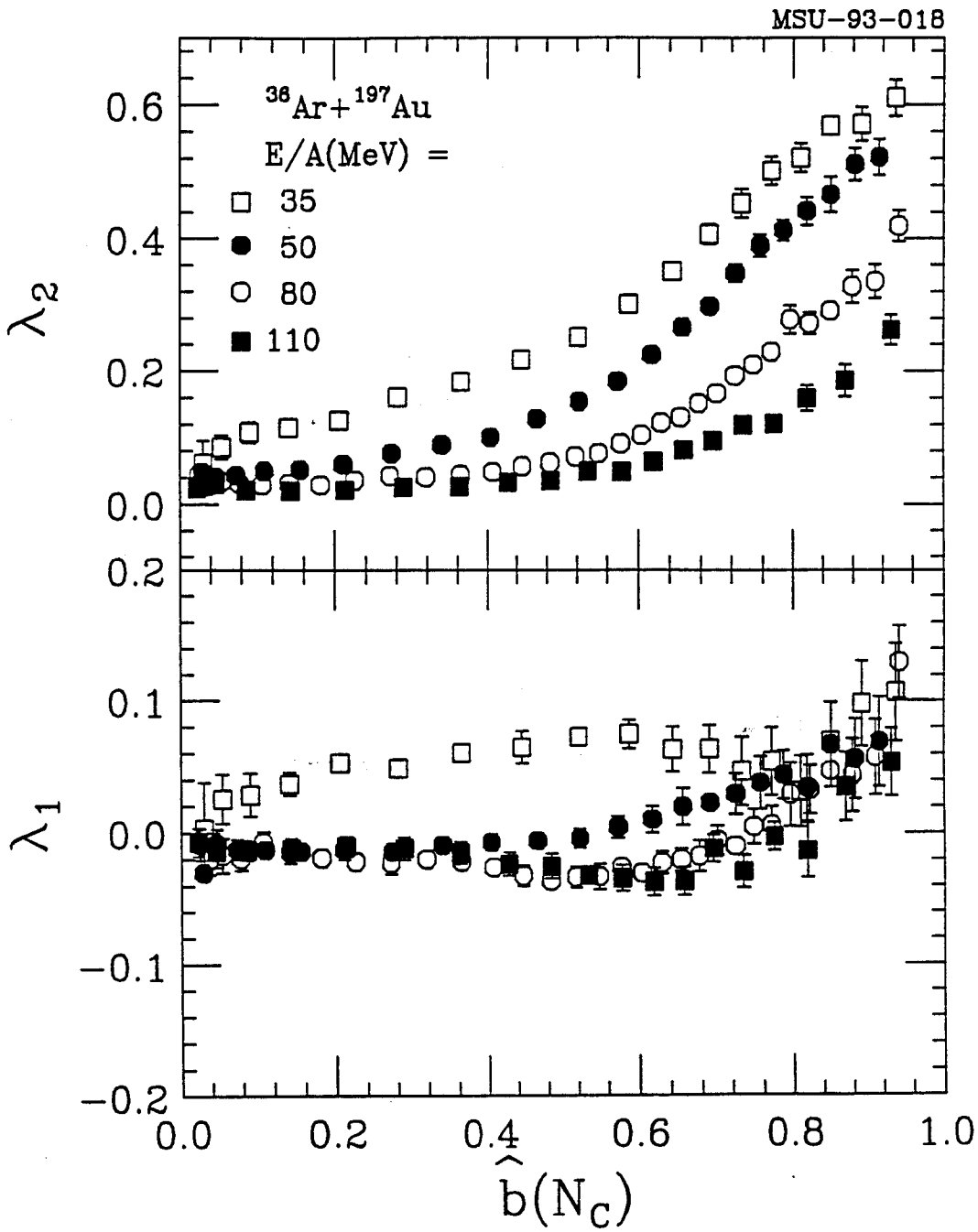


Figure 4.23 Reduced-impact-parameter dependence of the coefficients $\lambda_1$ and $\lambda_2$ used to fit the measured azimuthal correlation functions for emitted He nuclei emitted in $^{36}$Ar+$^{197}$Au collisions at E/A = 35, 50, 80 and 110 MeV.

which underlies impact parameter filters measuring the "violence" of the collision.

As expected from the qualitative trends apparent in Figures 4.18-22, the values of $\lambda_2$ at fixed $\hat{b}(N_c)$ are largest for the lowest bombarding energy where rotational deflection of the emitted particles by the mean nuclear fields is most pronounced. At E/A=50, 80 and 110 MeV, $\lambda_1$ is nearly zero for reduced impact parameters $\hat{b}(N_c) < 0.4$. For larger reduced impact parameters, as well as for E/A=35 MeV, $\lambda_1$ assumes small but positive values. Positive values of $\lambda_1$ may indicate a weak sideward directed flow, but they can also arise from the sequential decay of particle unstable nuclei, in this case $^8$Be.

In order to discern between these two possibilities, we show in Figures 4.24 and 4.25 the parameters $\lambda_1$ and $\lambda_2$ which characterize the azimuthal correlations of protons, deuterons, tritons and He nuclei emitted in $^{36}$Ar + $^{197}$Au and $^{129}$Xe + $^{197}$Au collisions, respectively, at E/A = 50 MeV. The clear monotonic dependence of the extracted values of $\lambda_2$ on the mass of the detected particle pair (top panels) illustrates the well-known fact [Chit 86] that collective effects are most readily discerned in the emission patterns of heavy particles. In contrast, the parameters $\lambda_1$ do not exhibit a monotonic mass dependence. At large impact parameters, the extracted values of $\lambda_1$ are consistent with zero for protons, they assume small negative values for deuterons and tritons and small positive values for He nuclei.

Most likely, the small negative and positive values of $\lambda_1$ reflect distortions due to final state interactions (possibly modified by additional momentum conservation effects [Lync 82]). Indeed, the changes in sign of $\lambda_1$ follow the qualitative differences of the final state interactions which determine the shapes of small angle correlation functions of these particles, (see e.g. ref. [Poch 87]). For pairs of deuterons and tritons, correlations at small

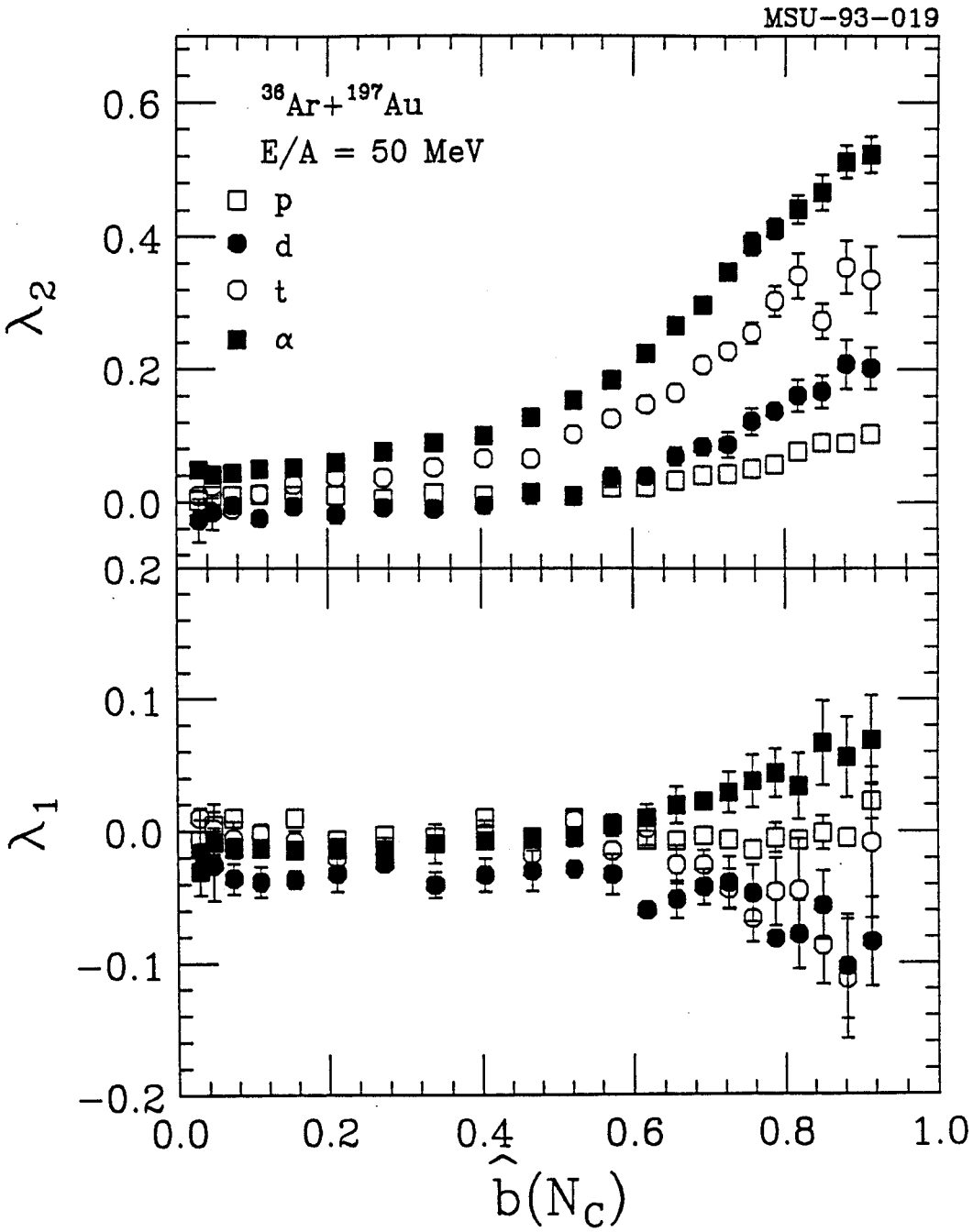


Figure 4.24 Reduced-impact-parameter dependence of the coefficients $\lambda_1$ and $\lambda_2$ used to fit the measured azimuthal correlation functions of protons, deuterons, tritons or He-nuclei emitted in $^{36}$Ar+$^{197}$Au collisions at E/A = 50 MeV.

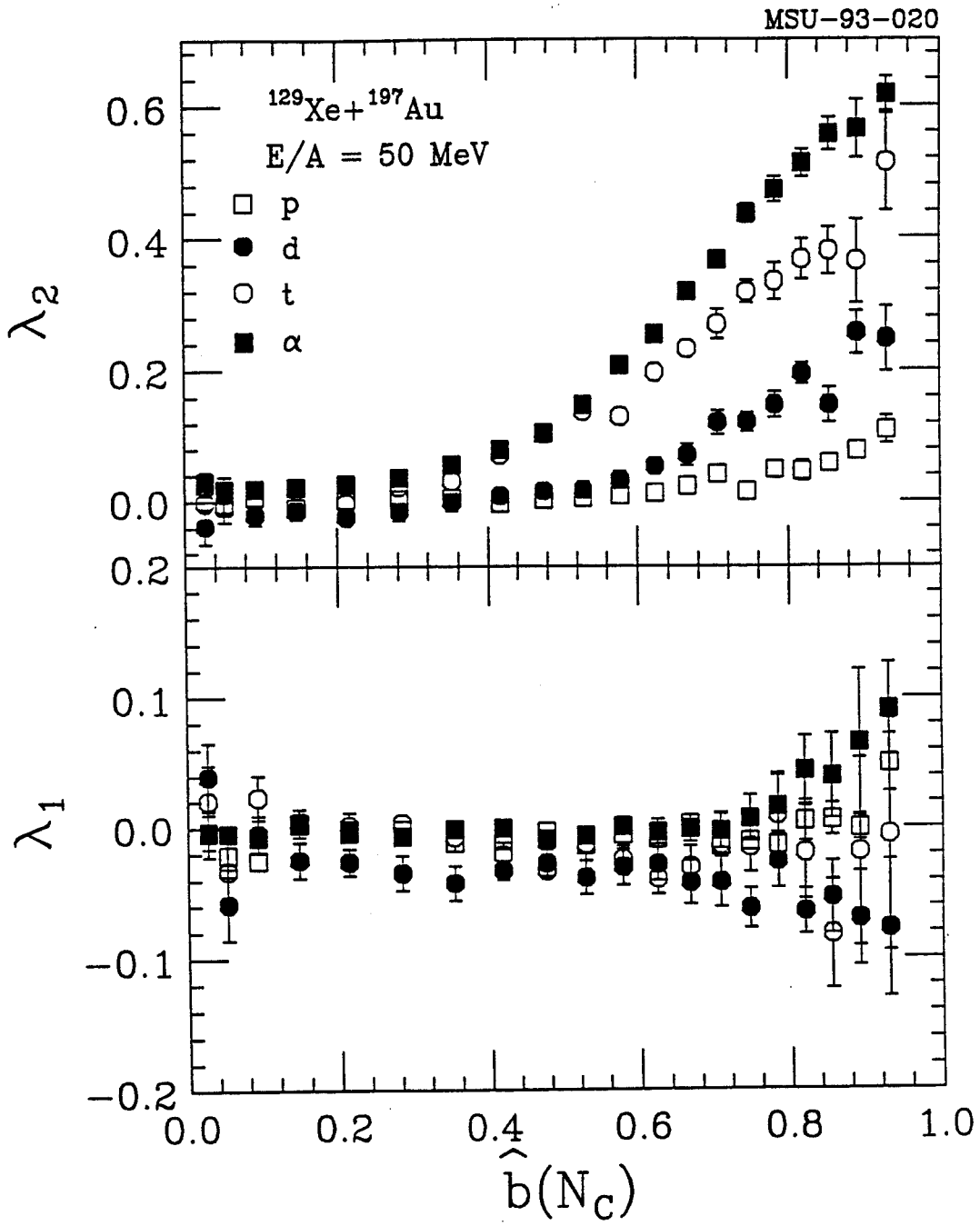


Figure 4.25 Reduced-impact-parameter dependence of the coefficients $\lambda_1$ and $\lambda_2$ used to fit the measured azimuthal correlation functions of protons, deuterons, tritons or He-nuclei emitted in $^{129}$Xe+$^{197}$Au collisions at E/A = 50 MeV.

relative momenta are suppressed [Poch 87]. For these particles, the final state interaction is dominated by the repulsive Coulomb interaction, since there are no contributions from low-lying resonances. For α-particles, on the other hand, correlations at small relative momenta are strongly enhanced due to large contributions from the decay of $^{8}$Be [Poch 87]. The case of two-proton correlations lies in between: here the correlation function exhibits a minimum at very small relative momenta followed by a broad maximum at relative momentum 20 MeV/c [Poch 87]. For the present data, a quantitative interpretation of the parameter $\lambda_1$ solely in terms of collective flow effects appears inappropriate, and final state interactions or other many-body correlations may have to be considered. Since these effects are of little interest in the context of the present work, we do not pursue this issue further.

Figures 4.26 and 4.27 show that impact parameter filters based upon $N_C$, $E_t$ and $Z_y$ select, as expected (Section 4.3), classes of events characterized by very similar azimuthal distributions. The figures show the reduced-impact-parameter dependence of the parameters $\lambda_1$ and $\lambda_2$ which characterize the azimuthal correlations functions of He nuclei emitted in $^{36}$Ar +$^{197}$Au and $^{129}$Xe +$^{197}$Au reactions at E/A = 50 MeV. The different symbols in the figures indicate the use of different impact parameter filters, $\hat{b}(N_C)$ (solid circles), $\hat{b}(E_t)$ (open circles), and $\hat{b}(Z_Y)$ (solid diamonds). As determined from the shape of azimuthal correlation functions, the three impact parameter scales provide equivalent event selection. Only for the most peripheral reactions, some slight differences exist. Small discrepancies between different impact parameter filters for peripheral collisions are not surprising since the determination of large impact parameters must be associated with relatively large statistical and systematic uncertainties.

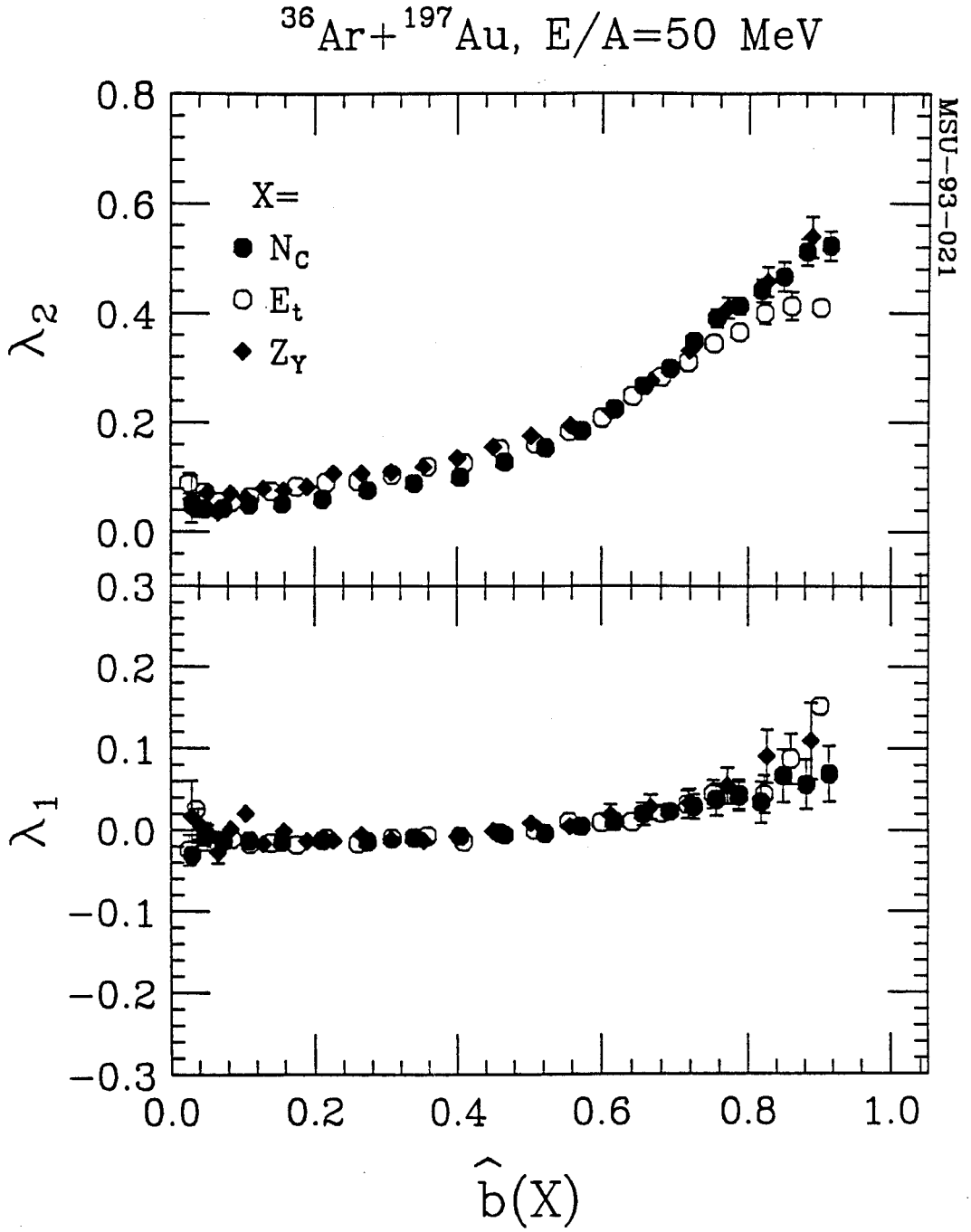


Figure 4.26 Reduced-impact-parameter dependence of the coefficients $\lambda_1$ and $\lambda_2$ used to fit the measured azimuthal correlation functions of He nuclei emitted in $^{36}$Ar+$^{197}$Au collisions at E/A = 50 MeV. Results from different impact parameters filters are shown by the different symbols indicated in the figure.

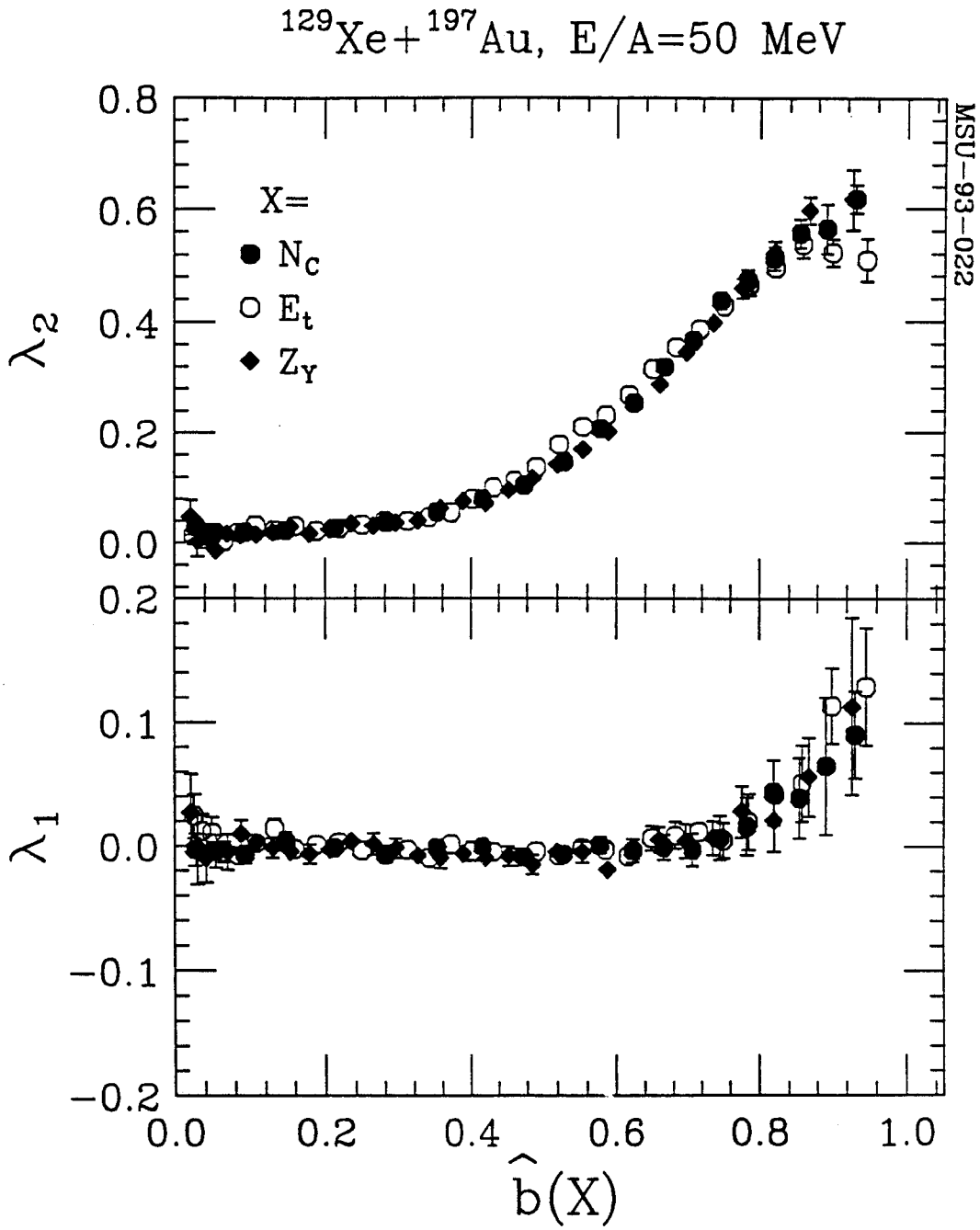


Figure 4.27 Reduced-impact-parameter dependence of the coefficients $\lambda_1$ and $\lambda_2$ used to fit the measured azimuthal correlation functions of He nuclei emitted in $^{129}$Xe+$^{197}$Au collisions at E/A = 50 MeV. Results from different impact parameters filters are shown by the different symbols indicated in the figure.

## 4.6 Directivity

For intermediate energy nucleus-nucleus collisions, the highest degree of equilibration is expected to occur in central collisions. Investigations of the thermodynamic properties of nuclear matter should therefore be performed with reaction filters optimized to provide high selectivity of very small impact parameters. Recently an improved method for the selection of central collisions was suggested [Alar 92] which employed simultaneous cuts on large charged-particle multiplicities and small transverse-momentum directivities. The experimental evidence for improved selectivity of small impact parameters was based upon data at significantly higher incident energy and with experimental apparatus of restricted solid angle coverage ($\theta_{lab} < 30°$). In this section we explore whether similar improvements in small-impact-parameter selectivity can be obtained for the present data taken at lower beam energies and with more complete solid angle coverage.

The transverse-momentum directivity D is defined as

$$D = \left\{ \frac{\left| \sum_i \mathbf{p}_i^{\perp} \right|}{\sum_i \left| \mathbf{p}_i^{\perp} \right|} \right\}_{y_i \geq y_{cm}} . \qquad (4.11)$$

In equation (4.11), the sum includes all identified particles with rapidities larger than the center-of-mass rapidity, and $\mathbf{p}_i^{\perp}$ denotes the transverse momentum of detected particle *i*. The momenta are calculated assuming A=2Z for 3≤Z≤18.

Following the procedure outlined in Section 4.3, we explored the conditional distribution of impact parameters $\hat{b}(E_t)$ selected by the cuts $\hat{b}(N_C) = 0.05 - 0.1$ and D ≤ 0.2. The results are shown in Figure 4.28. The

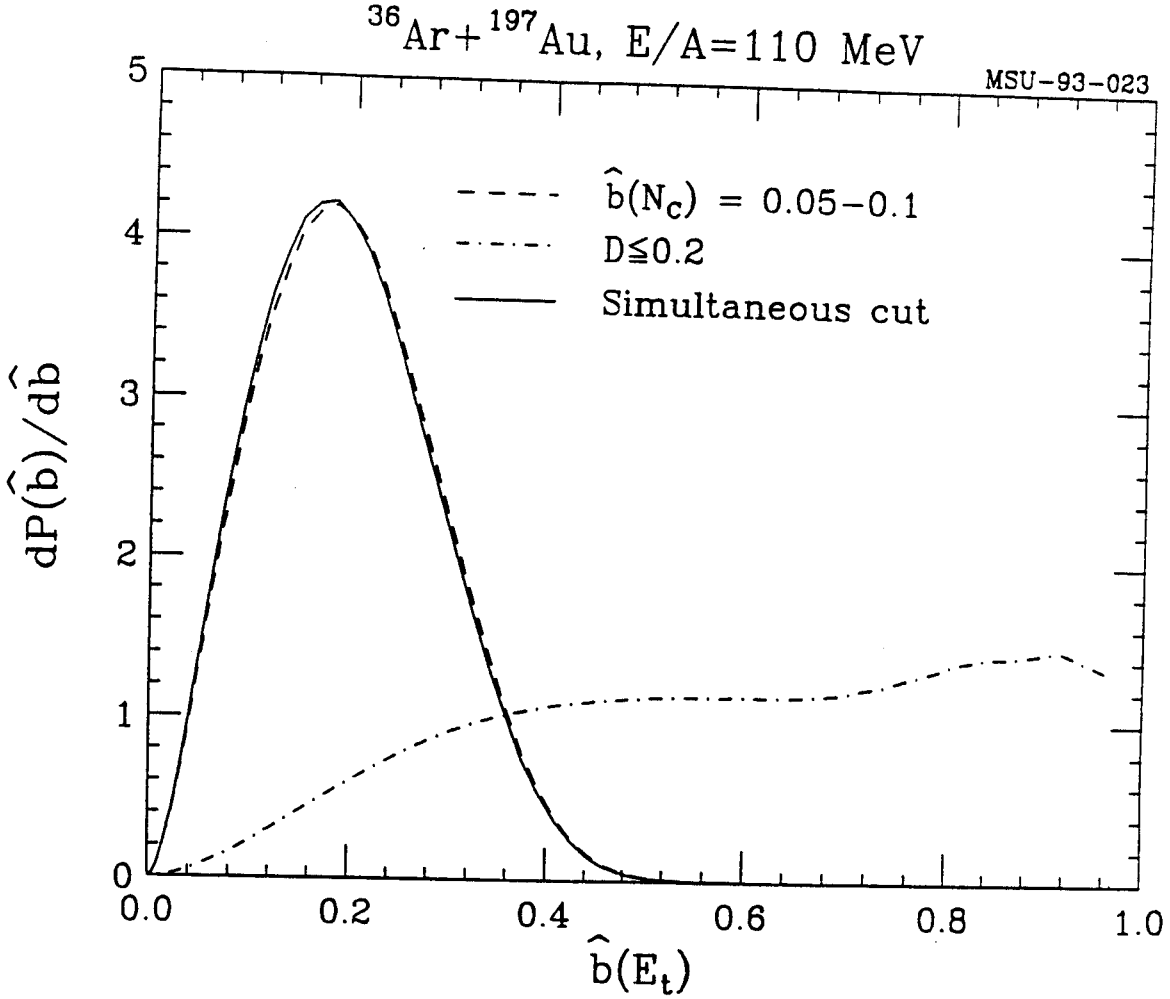


Figure 4.28 Conditional impact parameter distributions, $dP\left[\hat{b}(E_t)\right] / d\hat{b}(E_t)$, for $^{36}$Ar+$^{197}$Au collisions at E/A = 110 MeV selected by cuts on $\hat{b}(N_C)$ = 0.05 - 0.1 (dashed curve), directivity D ≤ 0.2 (dotted-dashed curve), and for the simultaneous cuts $\hat{b}(N_C)$ = 0.05 - 0.1 and D ≤ 0.2 (solid curve).

dashed and dotted-dashed lines show the results for cuts on $\hat{b}(N_C)$ and D only, and the solid line shows the results for a simultaneous cut on $\hat{b}(N_C)$ and D. A single cut on D alone provides little selectivity of central collisions, and no improvement in the $\hat{b}(E_t)$-distribution is observed if an additional cut on D<0.2 is imposed beyond the cut $\hat{b}(N_C) = 0.05 - 0.1$. This insensitivity to additional cuts on D should be compared to that observed for other impact parameter filters, based for example on the mid-rapidity charge $Z_y$: narrower $\hat{b}(E_t)$ distributions were obtained when double cuts on $N_c$ and $Z_y$ were employed (Figures 4.6-8). We conclude that cuts on directivity provide little additional selectively, at least for the present set of data taken at lower energy and with full $4\pi$-coverage.

Cuts on small values of the transverse-momentum directivity suppress collisions which exhibit significant transverse flow. Hence, such cuts are ineffective in systems for which transverse flow is small or negligible. Indeed, for the reactions investigated here, small values of $\lambda_1$ were extracted from the azimuthal distributions, and these small values could not be associated with transverse flow effects. The dashed curve in Figure 4.29 shows the distribution in transverse momentum directivity for $^{36}Ar+^{197}Au$ collisions at E/A=110 MeV selected by a cut on small reduced impact parameters, $\hat{b}(N_C) \leq 0.2$. For comparison, the solid curve shows the distribution for the same set of events after randomization of the azimuthal emission angles, i.e. after an artificial elimination of any existing flow effects. The true experimental distribution and the randomized distribution are very similar. In particular, the experimental distribution does not exhibit an excessive tail toward larger values of D which could be eliminated by cuts on small values of D. For the present reactions, additional cuts on transverse directivity do not enhance the selectivity of central collisions beyond that

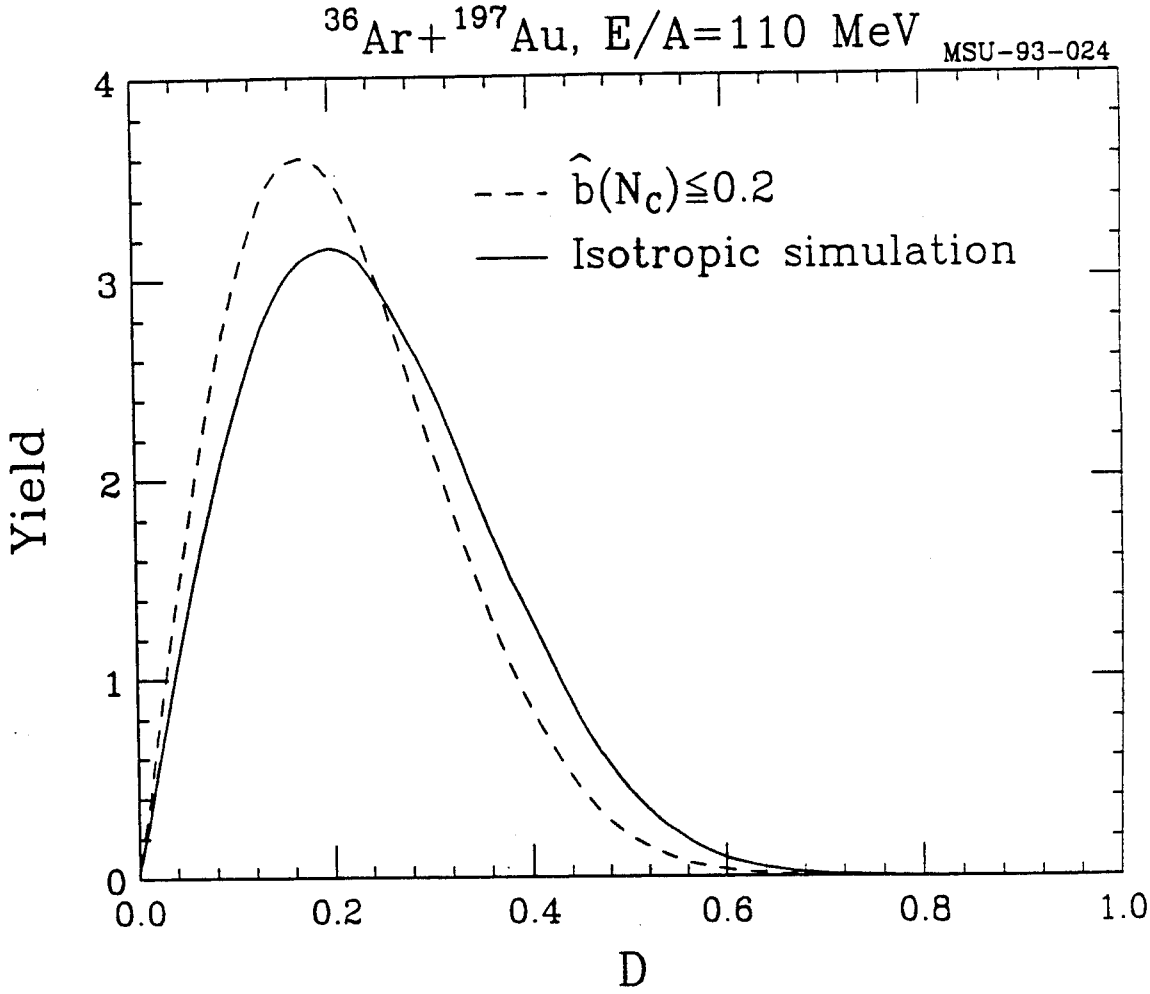


Figure 4.29 Distribution of transverse momentum directivity D for $^{36}$Ar + $^{197}$Au collisions at E/A = 110 MeV selected by cuts on $\hat{b}(N_C)$ <0.2 (dashed curve). The solid curve shows the distribution of the transverse momentum directivity obtained after randomizing the azimuthal distribution of the emitted particles according to an isotropic distribution (solid curve).

achieved by tight cuts on small reduced impact parameters. The success of applying cuts on the transverse directivity at higher energies [Alar 92] may be due to the presence of larger transverse flow effects at these energies, and partly due to a relatively poor impact parameter selection by multiplicity filters which only cover part of the full solid angle [Tsan 89a, Tsan 89b].

## 4.7. Summary

In this chapter, we explored the selection of impact parameters via impact parameter filters based upon the detected charged-particle multiplicity $N_C$, the transverse energy $E_t$, the intermediate rapidity charge $Z_y$, and the identified hydrogen multiplicity $N_1$ (which is the complement of $Z_{bound}$, the summed charge of clusters with Z≥2 [Hube 91]). For the reactions studied in this work, all of these quantities were shown to be correlated with each other and all display some sensitivity to the impact parameter. By applying a simple geometric prescription for the construction of a reduced impact parameter scale, quantitative comparisons of the various impact parameter scales were performed.

Average impact parameters deduced from these quantities were found to be mutually consistent, with small deviations occurring at the boundaries of the reduced impact parameter scale, $\hat{b}$=0 and $\hat{b}$=1. In order to assess the relative resolutions of the various impact parameter filters, we explored distributions of impact parameters $\hat{b}(Y)$ for events selected by narrow cuts on alternative impact parameter scales $\hat{b}(X)$, where $X$, $Y$ = $N_C$, $E_t$, $Z_y$, and $N_1$. As an alternative measure, we compared the suppression of fast fragments emitted at forward angles by corresponding cuts on $\hat{b}(N_C)$, $\hat{b}(E_t)$ and $\hat{b}(Z_y)$.

Based upon these criteria, impact parameter selections derived from the total charged-particle multiplicity $N_C$, the transverse energy $E_t$ and the

intermediate rapidity charge $Z_y$ were found to be very similar, with some differences occurring at large impact parameters where fluctuations appear to become a limiting factor. Somewhat worse resolution was obtained by employing the hydrogen multiplicity $N_1$ (the complement of $Z_{bound}$). This effect is related to the fact that $N_1 \leq N_C$ and, hence, $\Delta N_1 / N_1 \geq \Delta N_C / N_C$. For a given impact parameter, the larger fractional fluctuations of $\Delta N_1 / N_1$ therefore lead to larger fluctuations $\Delta\hat{b}(N_1) / \hat{b}(N_1)$ in the deduced impact parameter.

Slightly improved selection of central collisions can be obtained by the use of multi-dimensional gates placed on different observables. In this regard, the future use of instruments capable of detecting neutral and charged-particle observables in $4\pi$ geometry appears particularly promising.

We also explored the effect of impact parameter filters (based on $N_C$, $E_t$, and $Z_y$) on the azimuthal correlation function between emitted light particles. Azimuthal correlation functions are sensitive to the presence of collective velocity components in the reaction plane. In many reaction scenarios, the ordered motion in the reaction plane depends on the angular momentum of the emitting system and, hence, upon impact parameter. This impact parameter dependence is complementary to quantities which provide a measure of the geometric overlap of projectile and target nuclei, for example, the relative intensity of emission from a projectile-like source explored in Section 4.4.

As was done in Section 4.2, we employed a simple geometric prescription for the construction of reduced impact parameter scales based on the observables $N_C$, $E_t$ and $Z_y$ to provide a quantitative basis for the comparison of these different impact parameter filters. For the reactions studied in this chapter, these reduced impact parameter scales were found to select classes of events with very similar azimuthal correlation functions. At

large reduced impact parameters, the azimuthal correlation functions exhibit strong anisotropies indicating preferred emission in the reaction plane. At small reduced impact parameters, the correlations are nearly flat indicating isotropic emission. This evolution of the azimuthal correlation functions as a function of reduced impact parameter is consistent with the expected dependence on the true impact parameter of the reaction. For the reactions investigated in this chapter, cuts on small reduced impact parameters were found to be effective in selecting central or near-central collisions. No additional selectivity for central collisions was found by imposing additional cuts on transverse momentum directivity.

# Chapter 5 General Reaction Characteristics Selected by Impact Parameter

## 5.1 Multiplicity distributions

Intermediate-energy heavy-ion reactions exhibit broad multiplicity distributions shown in Figure 5.1. The upper panel shows that with increasing bombarding energy, the charged particle multiplicity ($N_C$) distribution extends to larger $N_C$ values, reaching as many as 40 charged particles at the highest bombarding energy. A simple model (see Chapter 4) can be used to relate the charged particle multiplicity to a "reduced" impact parameter $\hat{b}$ that ranges from zero (most central collisions) to one (most peripheral collisions).

The lower panel shows the inclusive measurement of the number of intermediate mass fragments ($N_{IMF}$) for the four different bombarding energies. At all bombarding energies the inclusive measurement is peaked at zero IMFs with the tail of the distribution pushing out to larger $N_{IMF}$ for increasing bombarding energy. At the highest bombarding energy the tail extends to nearly 10 IMFs.

A qualitative perspective of the evolution of the reaction with increasing bombarding energy is provided by Figure 5.2. In this figure, the correlation between the total detected charge, $Z_{sum}$, of all particles ($Z \leq 25$) and

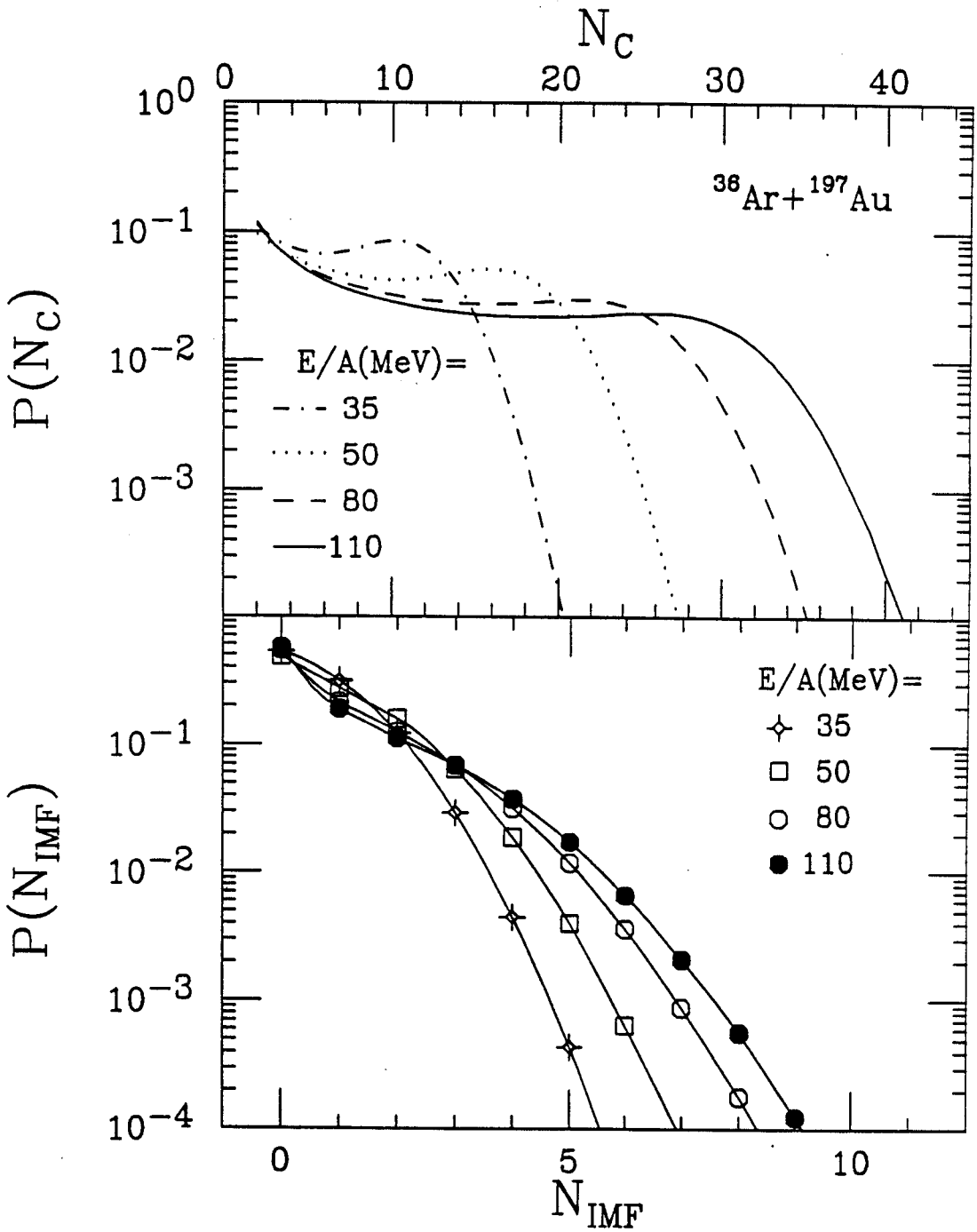


Figure 5.1 Upper panel – $N_C$ distributions. Lower panel – $N_{IMF}$ distributions. Both from the reaction $^{36}Ar+^{197}Au$ at E/A=35, 50, 80 and 110 MeV.

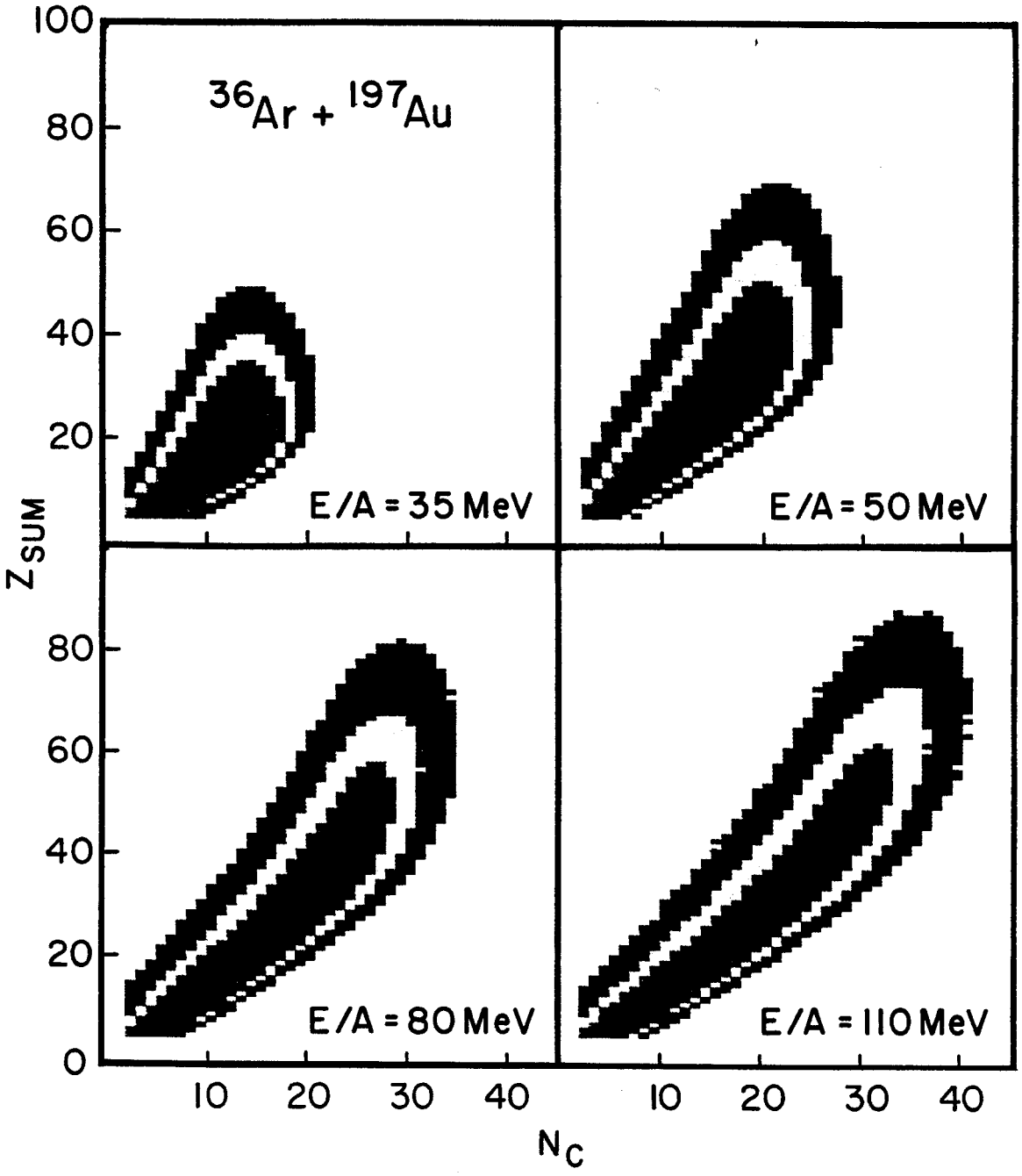


Figure 5.2 Measured relation between charged particle multiplicity, $N_c$, and total charge of identified particles ($Z \leq 25$) for the reaction $^{36}Ar + ^{197}Au$ at the indicated energies. Different colors represent contours that change by factors of 3.

the total charged particle multiplicity, $N_C$, is presented. At each bombarding energy, the total detected charge increases with increasing multiplicity as the collisions evolve from peripheral to central. At the lowest energy, E/A=35 MeV, the charged particle multiplicities are relatively small and only a small fraction of the nuclear system is observed as light particles and intermediate mass fragments. This observation is consistent with the survival of heavy reaction residues which are not identified in the present experiment and therefore not included in $Z_{sum}$. As the bombarding energy per nucleon is increased to 50, 80 and finally 110 MeV, one observes a correlated increase in both the total charged particle multiplicity and the total detected charge. The multiplicity associated with central collisions increases from $N_C$=11 at E/A=35 MeV to $N_C$=32 at E/A=110 MeV. The average total detected charge for central collisions increases from 22% of the total charge of the system at E/A=35 MeV to 57% at E/A=110 MeV, where a number of events were observed for which more than 80% of the total charge of the system was detected. These latter events correspond to a nearly complete disintegration of the system into light particles and intermediate mass fragments.

Figure 5.3 shows the contributions of charged particles bound in clusters (A>1) and bound in intermediate mass fragments to the detected total charge, $Z_{sum}$. For this measurement all hydrogen nuclei punching through the CsI crystals were treated as mass number A=1. The percentage of the detected charge $Z_{sum}$ observed in clusters (open symbols) and in intermediate mass fragments (solid symbols) is plotted as a function of $\hat{b}(N_C)$ for the three bombarding energies E/A=50, 80 and 110 MeV. At all bombarding energies nearly 30% of the detected charge appears in the form of intermediate mass fragments for central collisions. The charge bound in clusters accounts for about 80% of the detected charge, independent of beam energy.

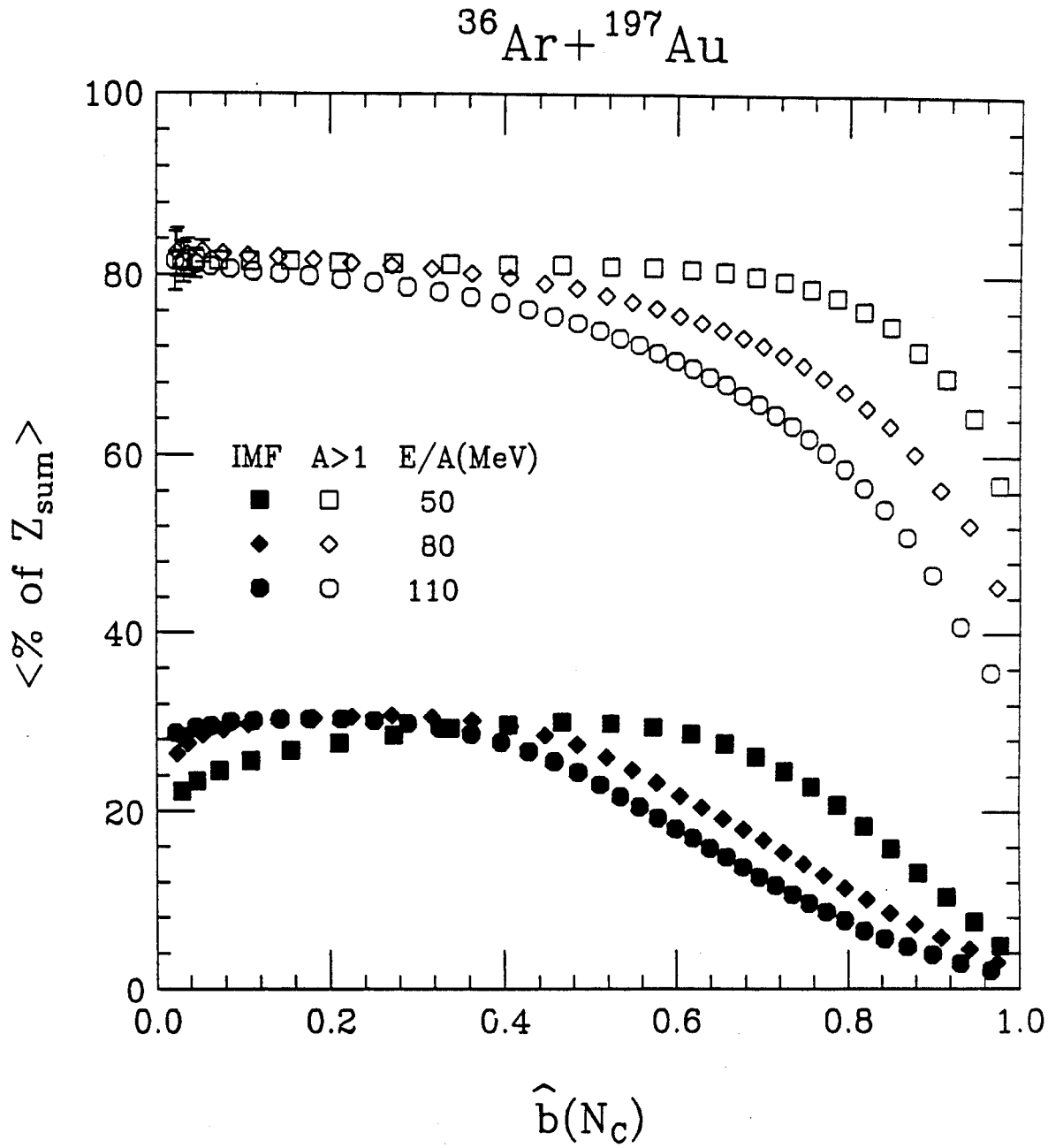


Figure 5.3 Percentage of detected charge $Z_{sum}$ appearing in clusters (A>1) and intermediate mass fragments (IMF) as a function of reduced impact parameter for the reaction $^{36}Ar+^{197}Au$ at E/A=50, 80 and 110 MeV.

To better characterize the various classes of multifragment events, we have extracted the probability distributions $P(N_{IMF})$ of detecting $N_{IMF}$ intermediate mass fragments in a single collision for different gates on the charged particle multiplicity $N_C$. The four panels in Figure 5.4 depict these distributions. At each energy, the IMF multiplicity distributions become wider and shift toward higher average multiplicities as the charged-particle multiplicity increases. Peripheral reactions, selected by $N_C<7$, exhibit narrow IMF multiplicity distributions peaked at $N_{IMF}=0$. For these collisions, IMF emission is an unlikely process. On the other hand, for central collisions selected by large values of $N_C$, IMF emission is a common process for which the average IMF multiplicity increases from $\langle N_{IMF}\rangle \approx 1$ at E/A=35 MeV to $\langle N_{IMF}\rangle \approx 4$ at E/A=110 MeV. At the highest incident energy, events are observed in which as many as 10 intermediate mass fragments are detected in the exit channel.

To allow quantitative comparisons of IMF multiplicity distributions, we have determined their first and second moments, $\langle N_{IMF}\rangle$ and $\sigma^2_{IMF}$. The dependence of these moments on the total charged particle multiplicity $N_C$ is shown in Figure 5.5. Values extracted at different incident energies are shown by different symbols as indicated by the key in the figure. At all energies, $\langle N_{IMF}\rangle$ and $\sigma^2_{IMF}$ exhibit an initial, approximately linear increase as a function of $N_C$. The slope of this increase is rather similar for the four energies investigated. For large values of $N_C$, corresponding to the extreme tails of the respective $N_C$ distributions, both $\langle N_{IMF}\rangle$ and $\sigma^2_{IMF}$ increase only marginally as a function of $N_C$. This saturation arises from working in the high multiplicity tail of the $N_C$ distribution where the excitation energy is roughly constant. For lower $N_C$ , the average violence of the collision is smaller when changing the gate on $N_C$. But making a higher $N_C$ gate does not increase the average

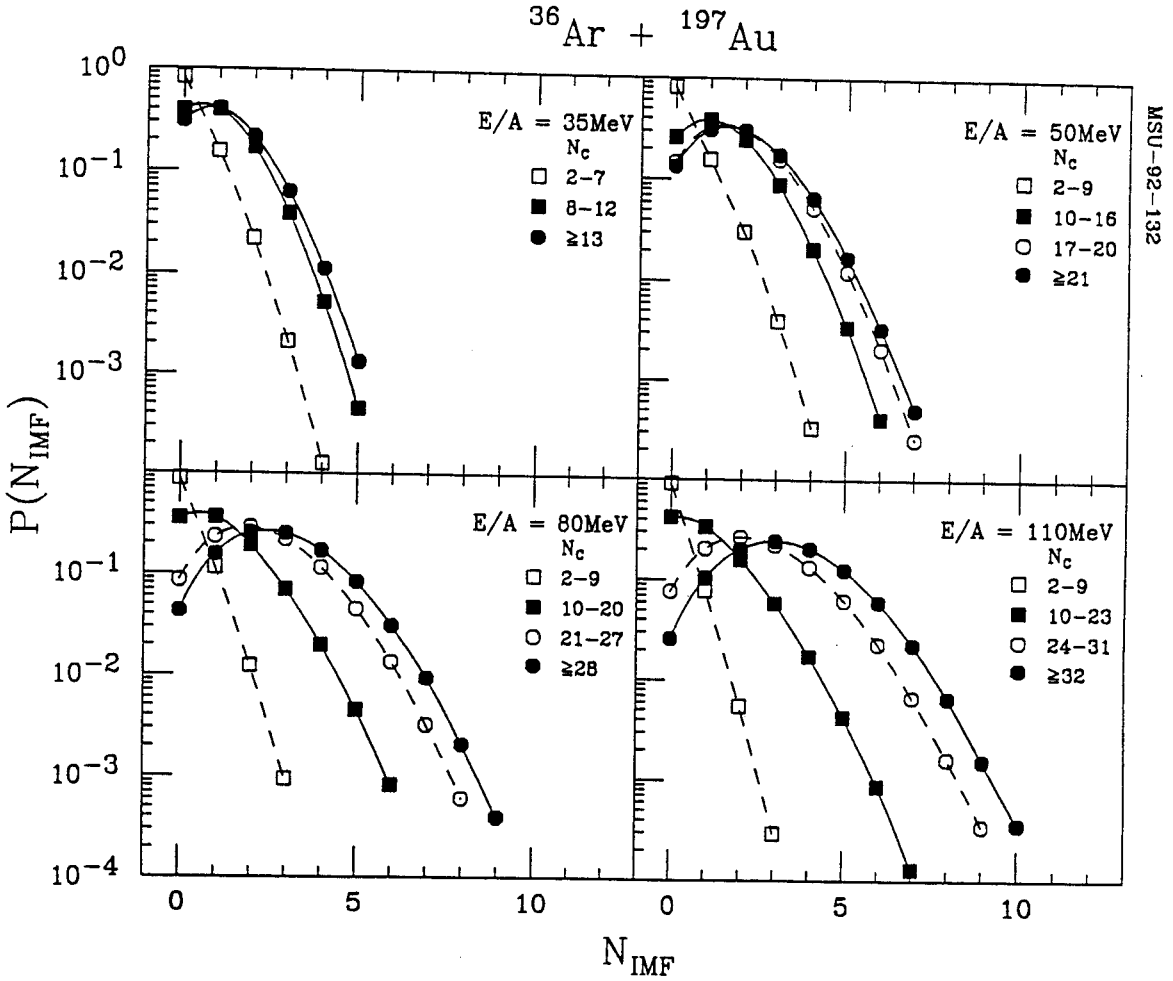


Figure 5.4 Measured IMF multiplicity distributions for the indicated gates on charged particle multiplicity $N_c$. Panels are labeled by incident energy.

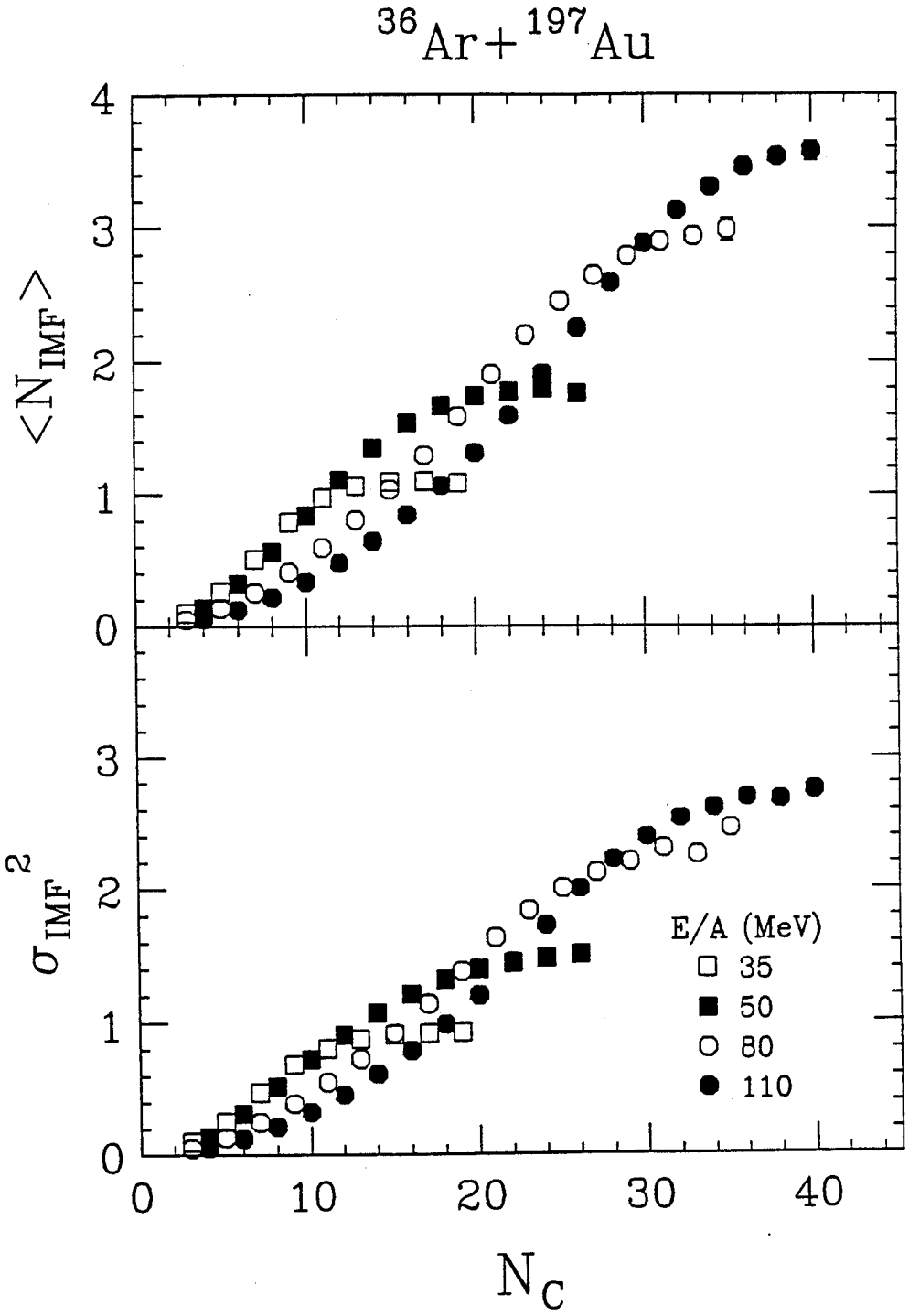


Figure 5.5 First and second moments of IMF multiplicity distributions as a function of charged particle multiplicity, $N_c$. Different symbols represent results for the indicated beam energies.

excitation energy of your event selection, thus giving a saturated value of $\langle N_{IMF} \rangle$.

This same information can be plotted as a function of $\hat{b}$ instead of $N_C$ and this is done in Figure 5.6. This allows an easier comparison of the different reactions as a function of impact parameter. Most striking is the saturation of $\langle N_{IMF} \rangle$ at E/A=50 MeV. This could come from a breakdown in the assumption of the participant spectator picture upon which $\hat{b}$ is based. Another possibility is that $N_C$ is not the best measure of centrality at this bombarding energy. As an alternative scale we plot the $\langle N_{IMF} \rangle$ and $\sigma^2_{IMF}$ as a function of $\hat{b}(E_t)$ (Figure 5.7). For this impact parameter scale the saturation in $\langle N_{IMF} \rangle$ and $\sigma^2_{IMF}$ is much less pronounced. In addition, a central cut ($\hat{b}$<0.3) using the impact parameter scale $\hat{b}(E_t)$ selects events with larger numbers of intermediate mass fragments than that from the corresponding cut using $\hat{b}(N_C)$. The $\langle N_{IMF} \rangle$ measured for the two impact parameter scales (from $N_C$ and $E_t$) are similar down to $\hat{b} \approx 0.3$ for the highest bombarding energies (80 and 110 MeV/nucleon). For the 50 MeV/nucleon reaction the measurements diverge for $\hat{b} \approx 0.4$.

A saturation in $\langle N_{IMF} \rangle$ as a function of $\hat{b}(E_t)$ is not observed because $E_t$ is perhaps a better measure of the violence of the collision than $N_C$. $E_t$ is also not a bounded quantity. At very high bombarding energies, $N_C$ is limited by the fact that $N_C \leq Z_{system}$. For very large $N_C$ an auto-correlation between $N_C$ and $\langle N_{IMF} \rangle$ is introduced. The obvious extreme example is $N_C = Z_{system}$, where by constraint $N_{IMF}$=0.

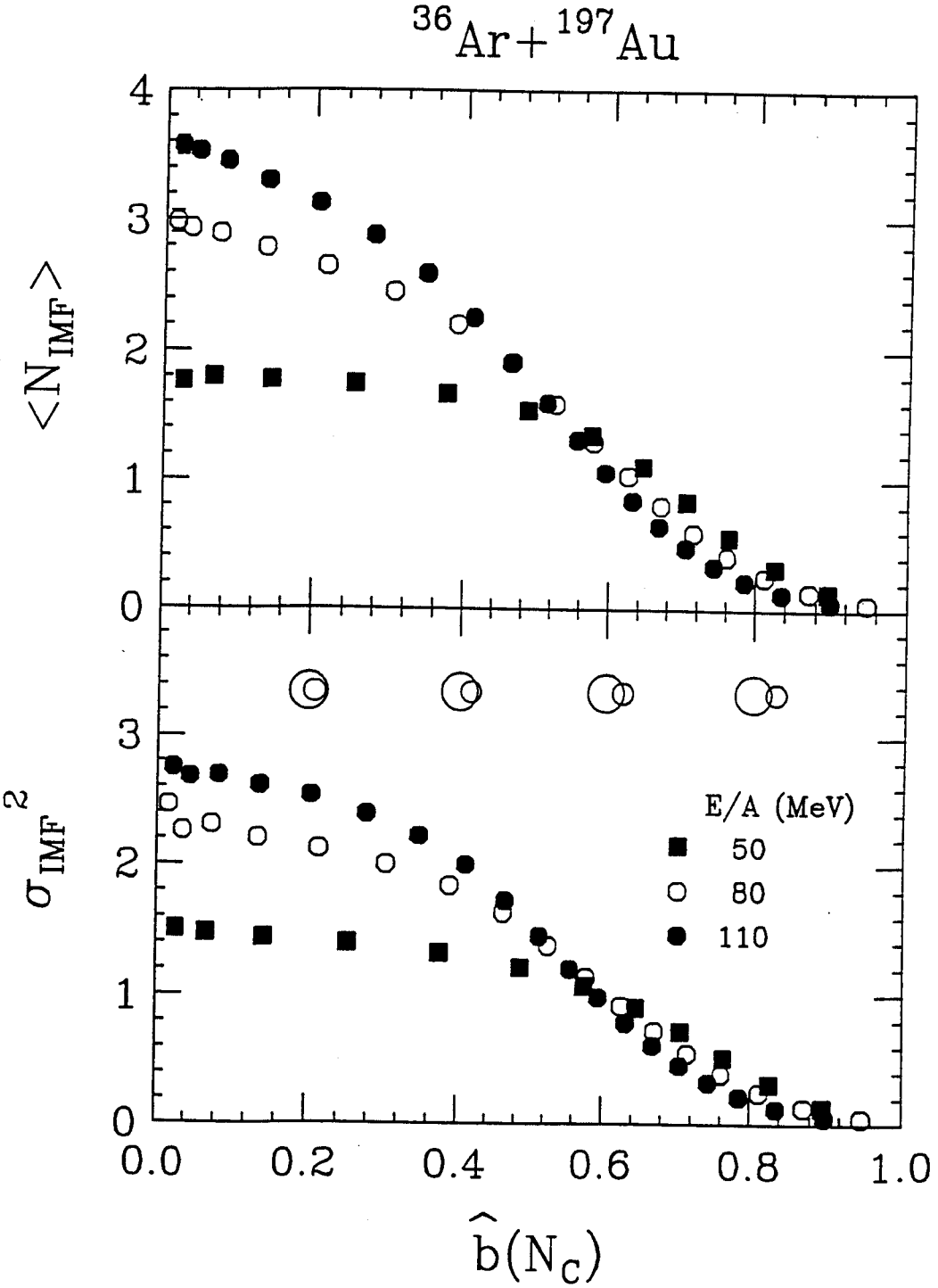


Figure 5.6 First and second moments of IMF multiplicity distributions as a function of $\hat{b}(N_c)$. The two circles show the approximate overlap between target and projectile for $\hat{b}$=0.2, 0.4, 0.6 and 0.8.

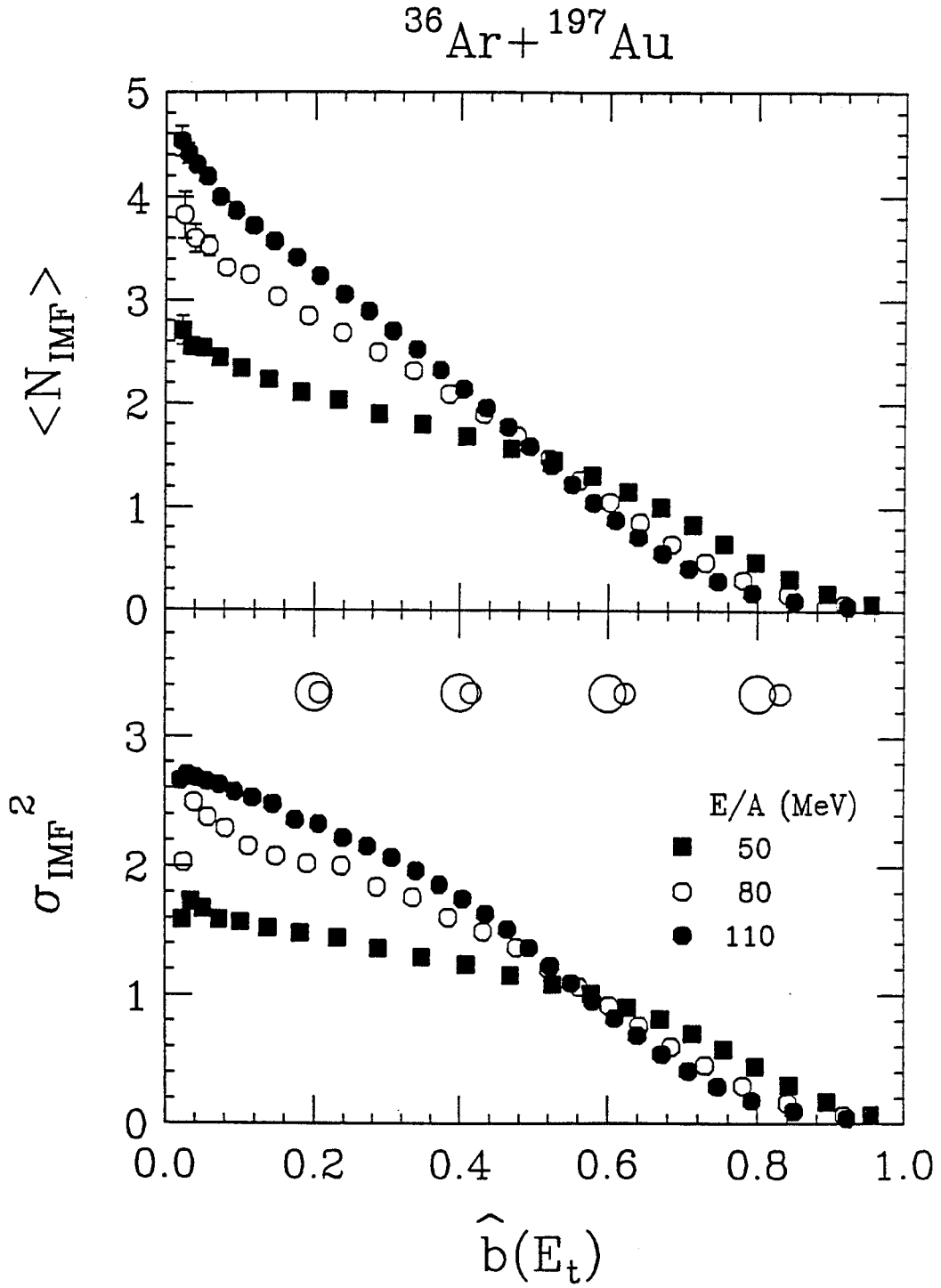


Figure 5.7 First and second moments of IMF multiplicity distributions as a function of $\hat{b}(E_t)$. The two circles show the approximate overlap between target and projectile for $\hat{b}$=0.2, 0.4, 0.6 and 0.8.

## 5.2 Element distributions

Element distributions for three different impact parameter cuts are shown in Figure 5.8 for the three bombarding energies. The solid lines are fits for Z=3-20 assuming a functional form for the average yield of

$$N(Z) \propto e^{-\alpha Z} \tag{5.1}$$

The different distributions are normalized such that $N(Z)$ is the average multiplicity of $Z$ for a given cut on $\hat{b}$. The steeper distributions come from the highest bombarding energy. This can be seen more clearly in Figure 5.9. The fit parameter $\alpha$ is plotted as a function of $\hat{b}$ (constructed from $N_c$) for the three bombarding energies. With this impact parameter scale the flatness of the element distributions (as measured by $\alpha$) seems to saturate at about $\hat{b}(N_c)\approx 0.5$. For $\hat{b}(N_c)<0.3$, $\alpha$ begins to rise again. If we instead extract $\alpha$ from element distributions constructed with cuts on $\hat{b}(E_t)$ (see Figure 5.10), the saturation in $\alpha$ is less pronounced. There is a change in slope near $\hat{b}(E_t)\approx 0.5$, but $\alpha$ always decreases for smaller $\hat{b}(E_t)$.

The observed saturation and subsequent rise of $\alpha$ at small $\hat{b}(N_c)$ in Figure 5.9 can be caused by autocorrelations. For a fixed excitation energy, the $N_c$ distribution has a finite width. Gating in the extreme tails of the distribution may not select more central collisions or higher excitation energies. If we make cuts on large $N_c$ in the tail of the distribution (where the excitation energy does not increase) we may force the IMF spectrum to become more steep due to the selection of events with more light particles emitted. We simulated such a scenario with a standard bond percolation model (see Chapter 6) and the results are shown in Figures 5.11 and 5.12. In this percolation simulation, each nucleon in the compound system is represented by a lattice site. The nucleons are bonded to their six nearest neighbors in a simple cubic lattice structure. The simulation consists of

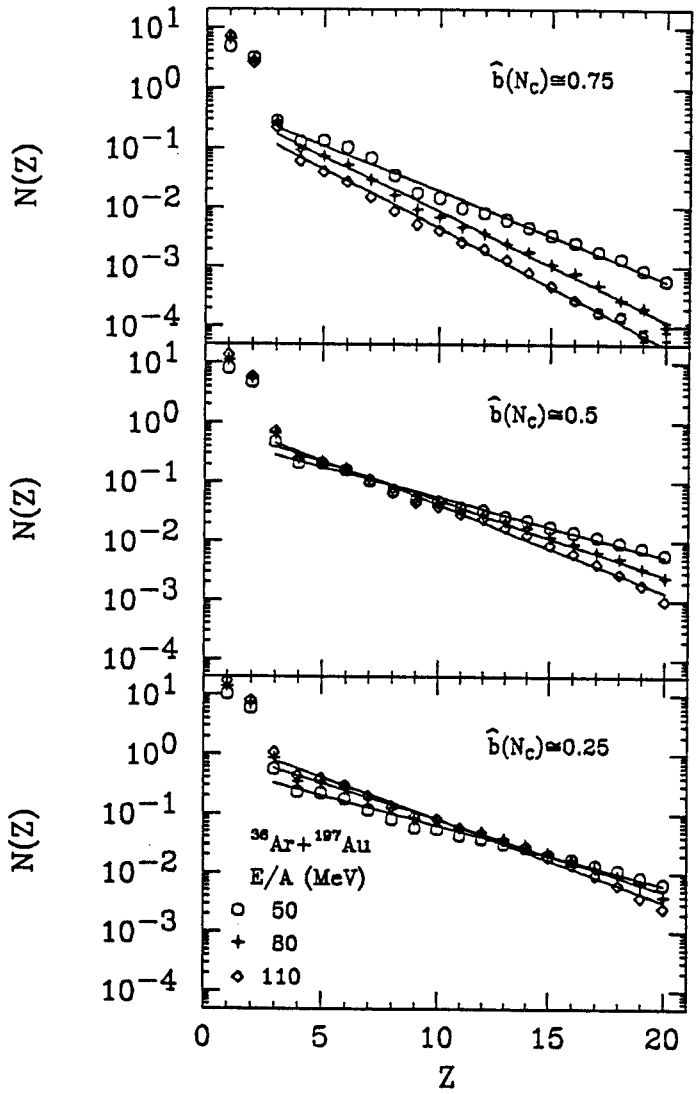


Figure 5.8 Elemental distributions at E/A=50 (circles), 80 (stars) and 110 MeV (diamonds) for $\hat{b}\approx 0.75$ (top), 0.5 (middle) and 0.25 (bottom). Solid lines are exponential fits using Equation (5.1).

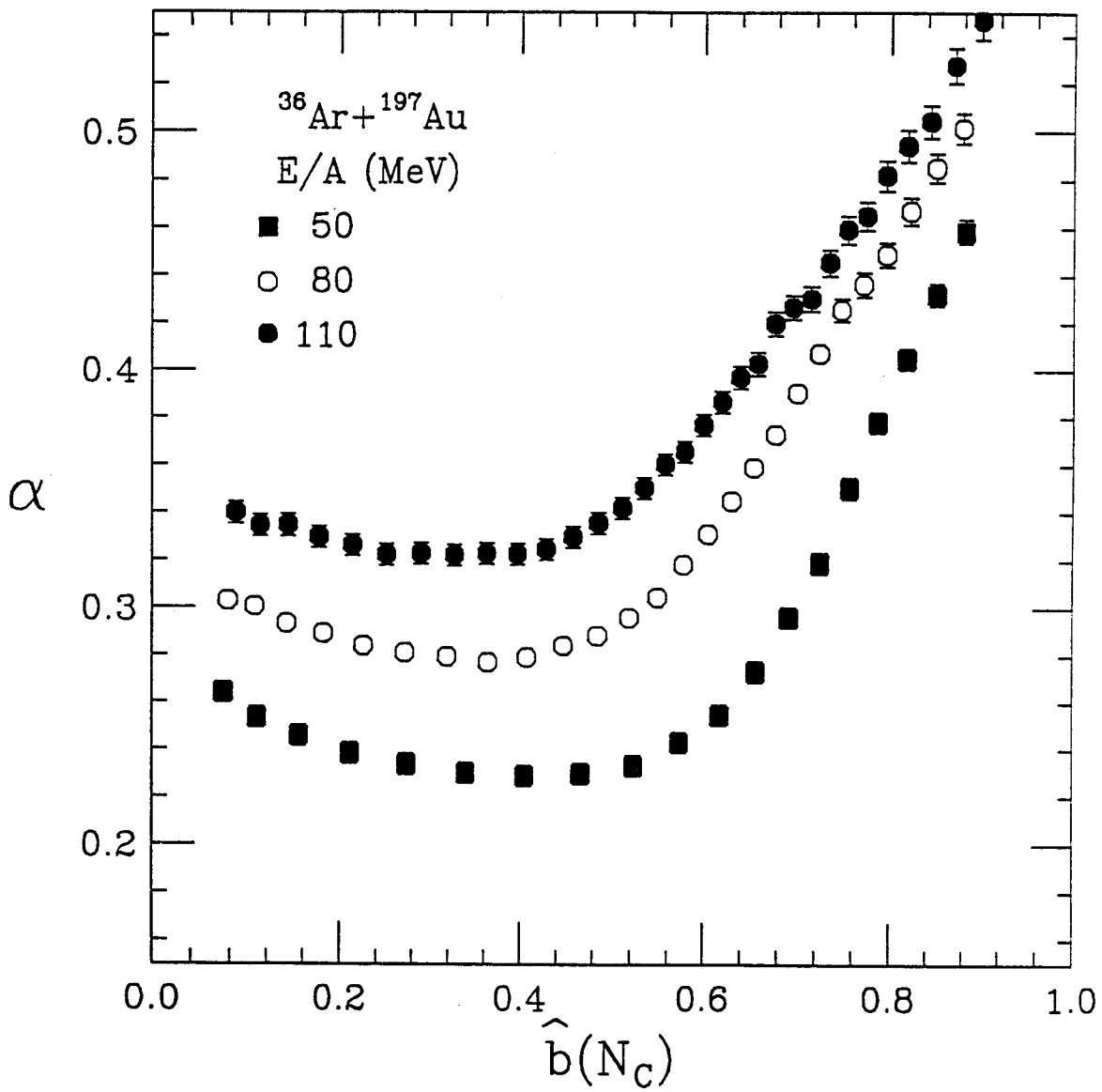


Figure 5.9 $\alpha$ as a function of $\hat{b}(N_c)$ for E/A=50, 80 and 100 MeV.

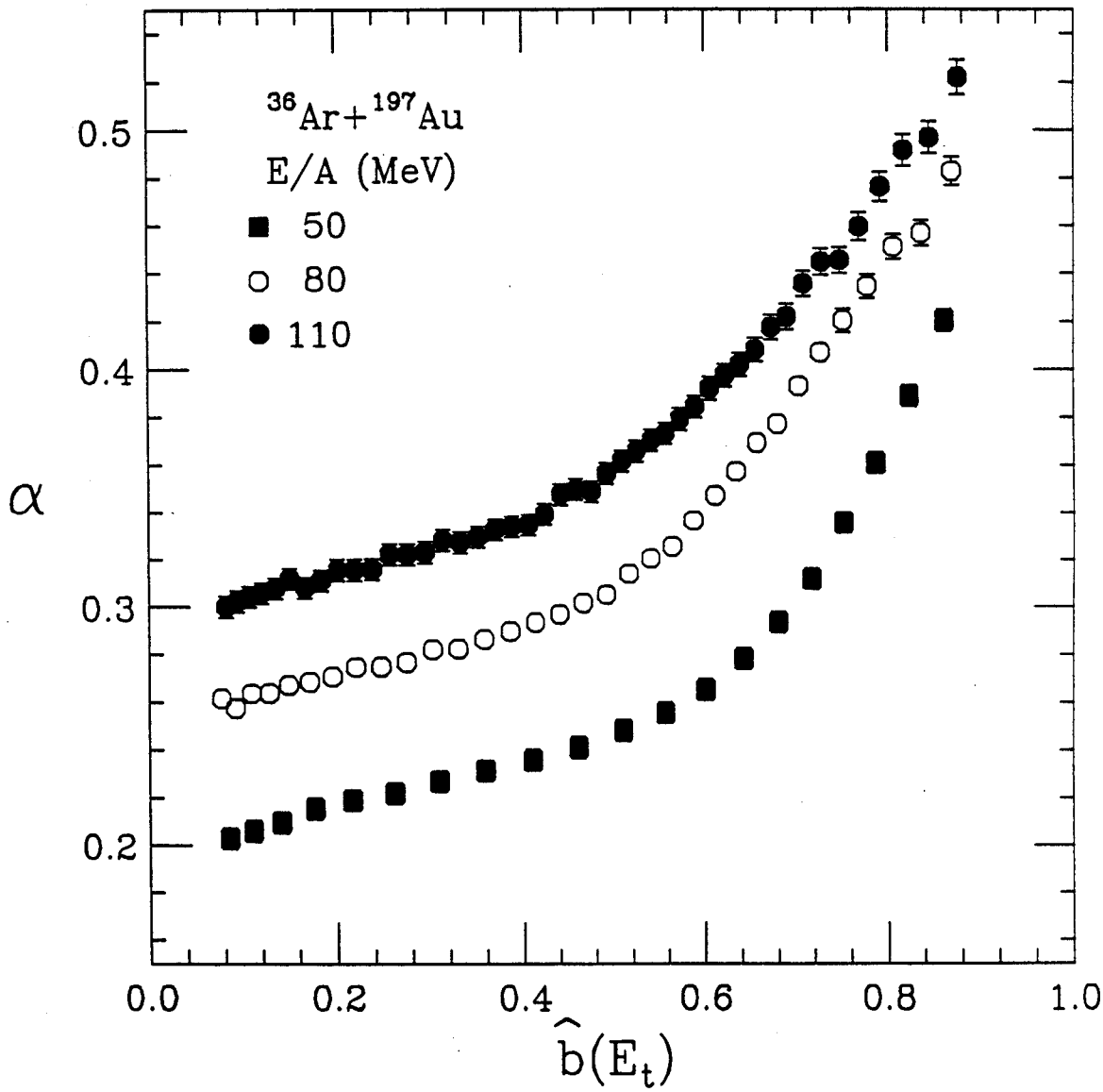


Figure 5.10 $\alpha$ as a function of $\hat{b}(E_t)$ for E/A=50, 80 and 100 MeV.

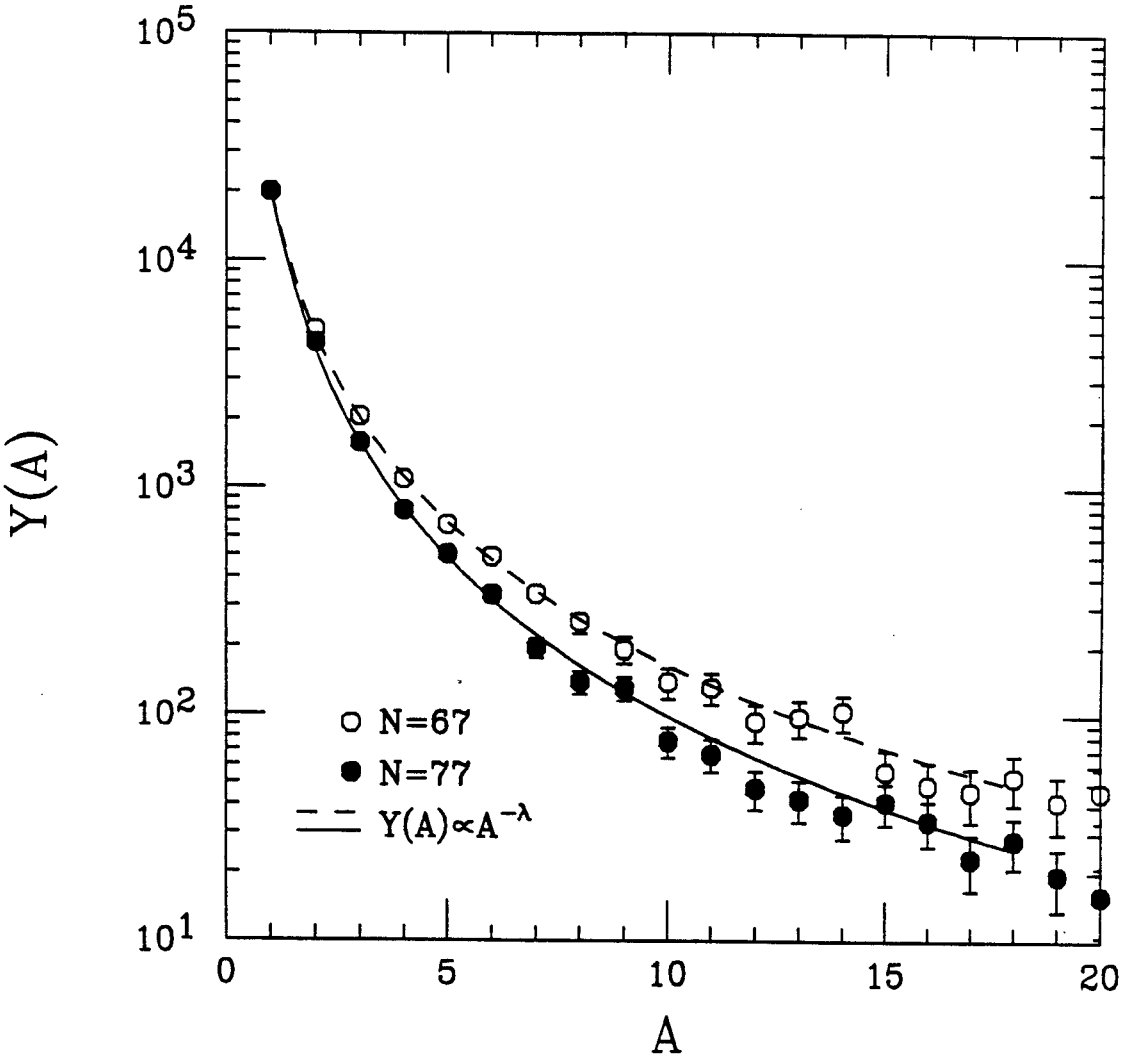


Figure 5.11 Mass yields for a percolation simulation at fixed excitation energy. The open (solid) symbols correspond distributions constructed for multiplicity $N$=67(77). The curves are power law fits.

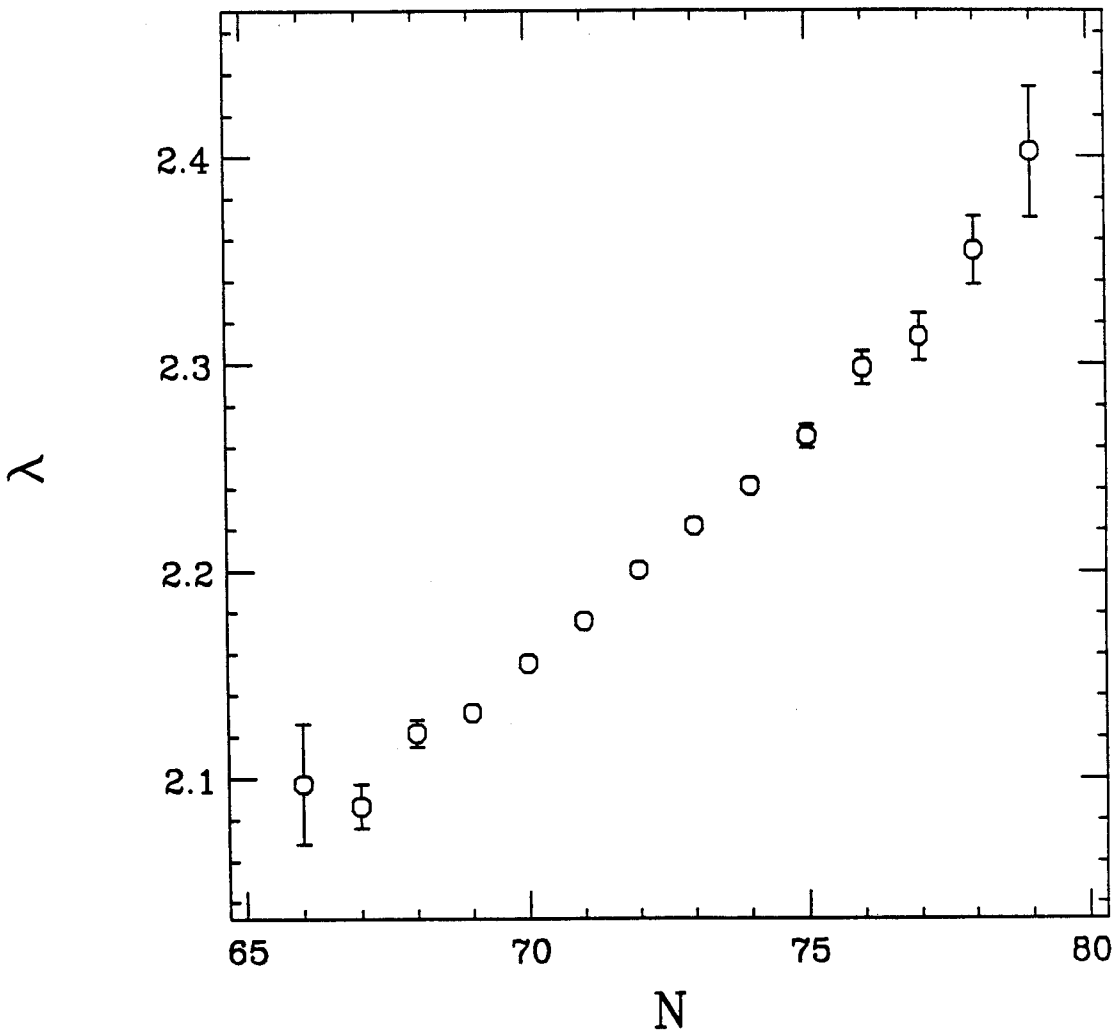


Figure 5.12 Evolution of the fit parameter $\lambda$ as a function of multiplicity $N$ for a percolation simulation at fixed excitation energy.

assigning a fixed number of bonds to be broken (representing a fixed excitation energy) and then randomly breaking the bonds between nucleons in the compound system. Clusters with their bonds intact are identified by mass in each event. Each event is also identified by the multiplicity $N$ , the total number of clusters emitted. In Figure 5.11 is plotted the mass distributions for breakup of an A=233 system at a fixed excitation energy (i.e., fixed number of bonds broken). The two distributions plotted are selected for multiplicities $N$ of 67 (open circles) and 76 (solid circles). The solid lines are a fit with a power law function $Y(A) \propto A^{-\lambda}$. The higher multiplicity cut gives a steeper mass distribution even though the two distributions correspond to events with the same excitation energy. Figure 5.12 shows the auto correlation more clearly. The fit parameter $\lambda$ is plotted as a function of multiplicity. Again we observe larger values of $\lambda$ (steeper mass distributions) for increasing $N$. We therefore conclude that the rise of $\alpha$ for very small $\hat{b}(N_C)$ likely an artifact produced by an autocorrelation of the particular impact parameter filter. This autocorrelation is not apparent for the impact parameter filter based upon the observable $E_t$.

## 5.3 Angular distributions

Angular distributions as a function of bombarding energy and event centrality for elements with Z=1-6 are shown in Figures 5.13-15. The distributions are normalized such that the integrated yield (over solid angle acceptance) is equal to the average multiplicity of a given element for the given impact parameter cut. The open circles are the angular distributions for a peripheral cut, $\hat{b}$>0.75, and the solid circles are for a central cut, $\hat{b}$<0.25. The yield for lithium is not plotted for the last two rings. Poor separation of lithium and helium in these detectors prevented an accurate measurement of the lithium yield at these backward angles (see discussion in Section 3.3). The

fragment yield is suppressed at $\theta$=90° because of target shadowing at this angle. The fragment yield is also suppressed at the most backward angle ($\theta$=150°) because of the Pb-Sn foils used to suppress electron detection (see Section 3.1). The slopes of the angular distributions are steeper for peripheral collisions than for central collisions which indicates more equilibration and smaller contributions from projectile-like sources for events with large multiplicities (see Section 4.4). In addition, for central collisions the distributions become less steep as one goes up in bombarding energy.

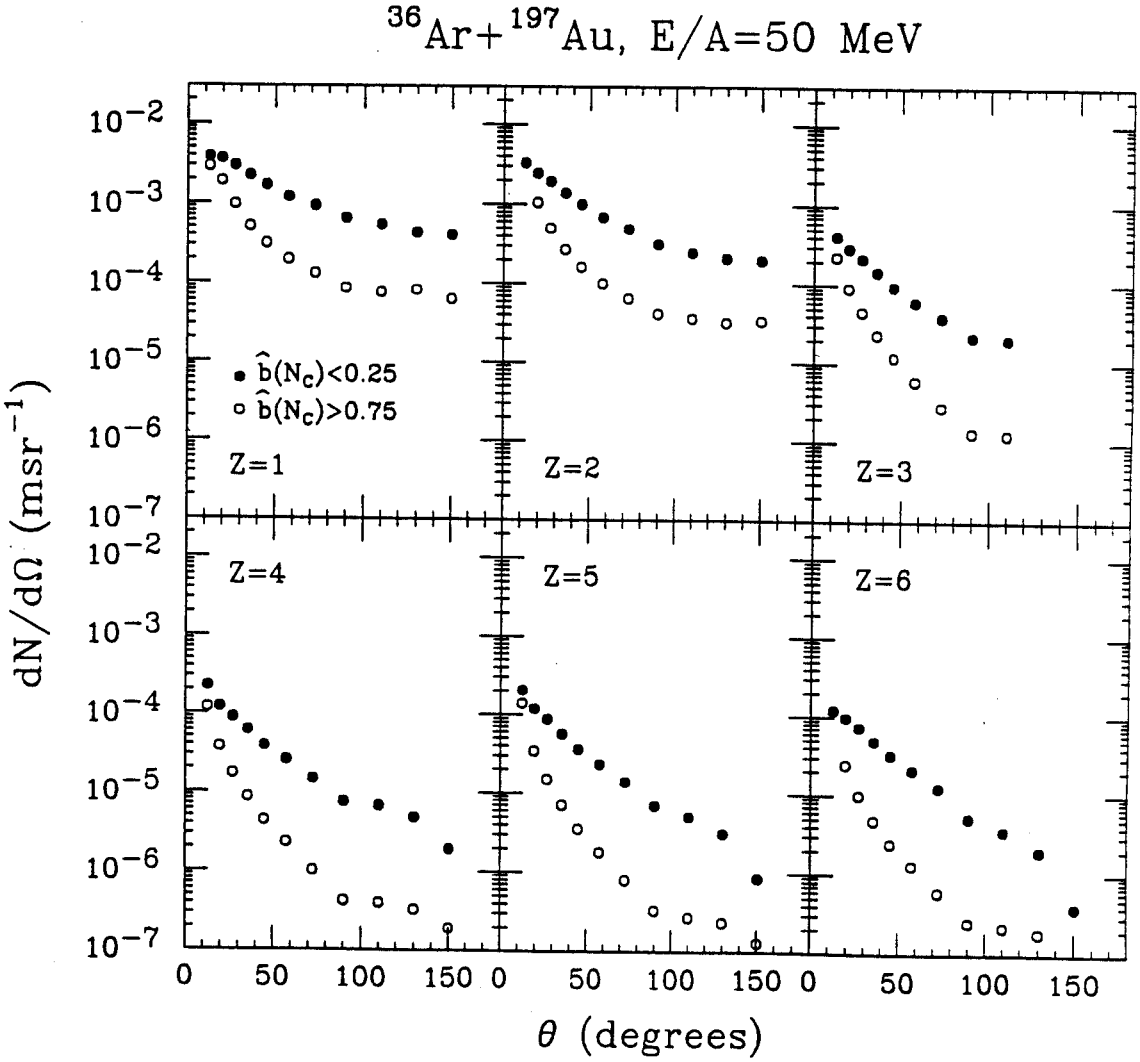


Figure 5.13 Angular distribution of elements Z=1-6 from the reaction $^{36}$Ar+$^{197}$Au at E/A=50 MeV. Solid symbols - central cut $\hat{b}(N_C)$<0.25. Open symbols - peripheral cut $\hat{b}(N_C)$>0.75.

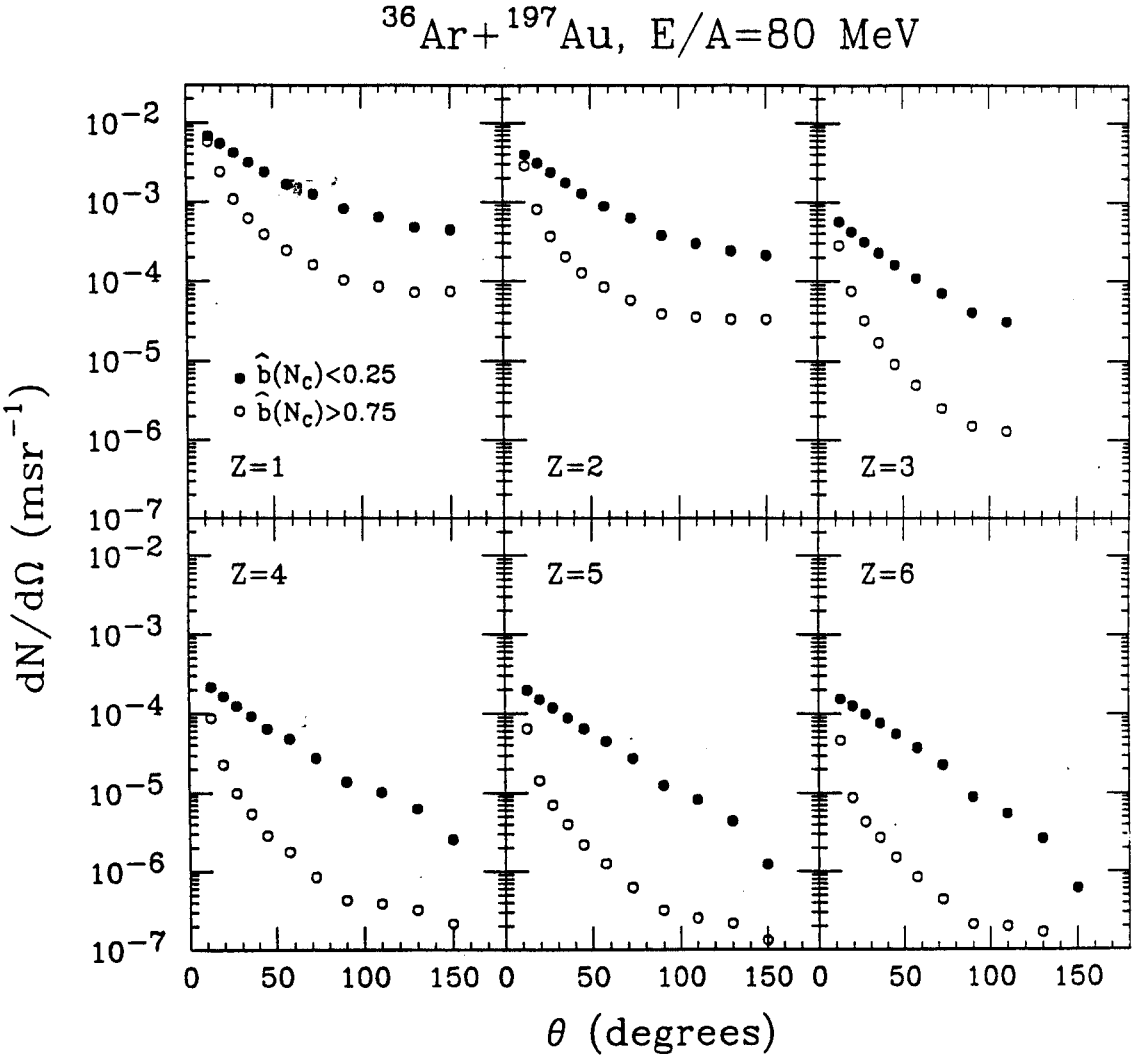


Figure 5.14 Same as Figure 5.13 for E/A=80 MeV.

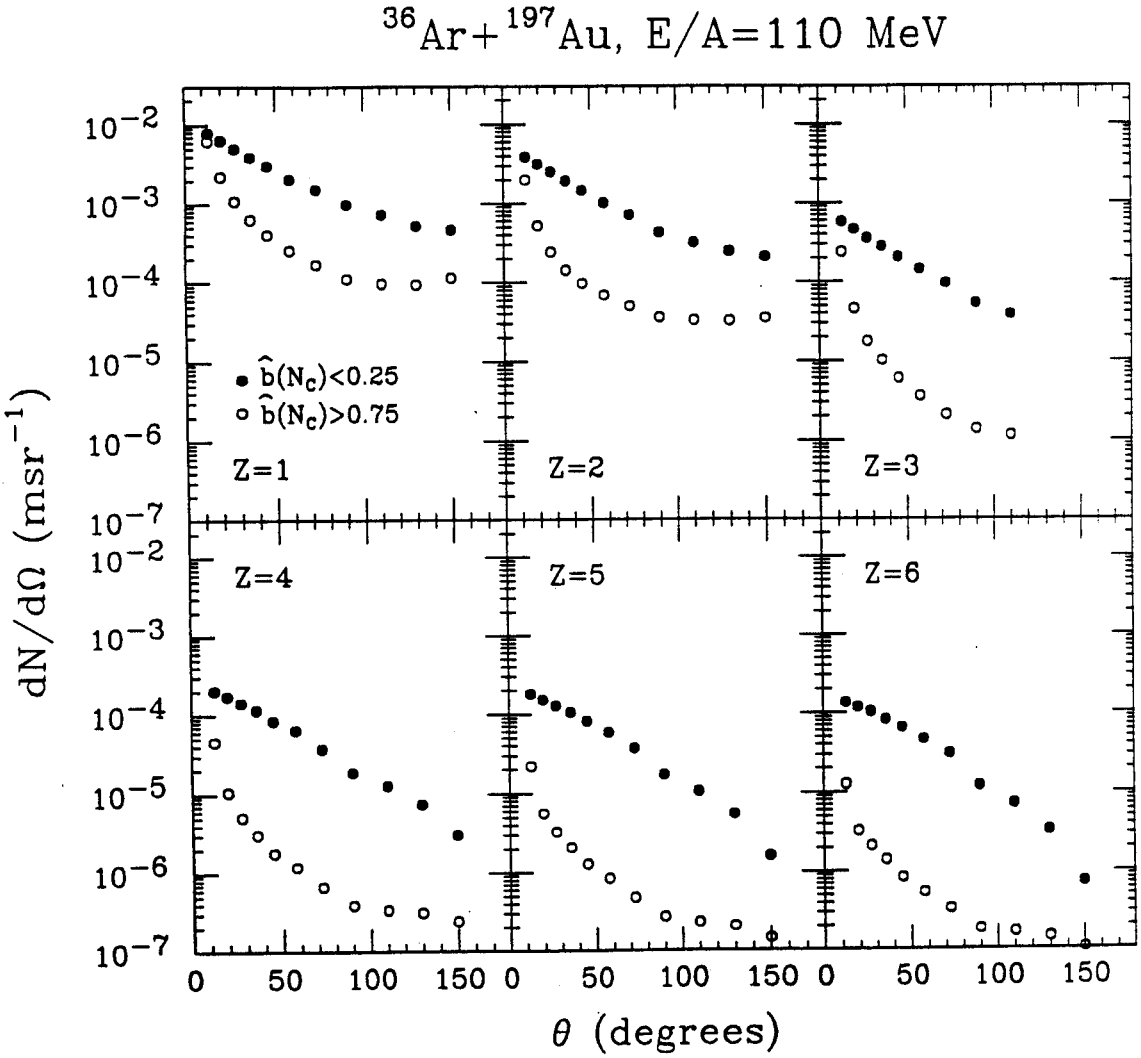


Figure 5.15 Same as Figure 5.13 for E/A=110 MeV.

# Chapter 6 Model comparisons

Over the broad range of incident energies in this study of $^{36}Ar+^{197}Au$, the mean values and variances of the intermediate mass fragment multiplicity distributions exhibit an approximate scaling with the total charged-particle multiplicity (see Figure 5.5). The relationship between the IMF and total charged-particle multiplicities can be qualitatively understood by assuming that the charged-particle multiplicity is strongly correlated with energy deposition and that the production of intermediate mass fragments depends primarily upon this energy deposition. The nearly universal increase of $\langle N_{IMF} \rangle$ as a function of $N_C$ can thus be viewed as due to the selection of interactions involving a progressively increasing amount of internal energy deposition. Deviations from a universal relationship between $\langle N_{IMF} \rangle$ and $N_C$ can arise from different amounts of preequilibrium emission and/or angular momentum transfers to the equilibrated nuclear systems at the different incident energies. In addition, different impact parameters can be expected to involve decaying systems of different mass. The measured multiplicities of light particles and intermediate mass fragments are compared in this chapter with both a model involving statistical decay of an expanding compound nucleus and with a model involving percolation theory.

## 6.1 Expanding emitting source model

We have compared the experimentally measured IMF multiplicity distributions with the predictions of the expanding emitting source model of Friedman [Frie 90]. This schematic model couples the phase-space features of statistical decay with the dynamical features of expansion driven by thermal pressure. It has the capacity for predicting multiplicity distributions for different species of particles (IMFs in particular). The model has been successfully employed [Frie 88] to interpret the low emission temperatures deduced from the relative population of states [Chen 87], as well as trends in IMF multiplicity with excitation energy [Troc 89] where the IMF multiplicity was found and predicted to be less than one [Frie 90] (lower than predicted by the instantaneous breakup model of [Bond 85b]). The model also predicted [Frie 90] a sharp rise in multiplicity for excitation energies on the order of 8 MeV/nucleon.

The expanding emitting source (EES) model characterizes an ensemble of emitting sources by a time-varying average density $\rho(t)$ to which the level densities of the source are calculated via the Fermi-gas approximation. For the purpose of calculating the mean collective expansion energy, the model assumes that the density of the source is uniform. This assumption requires that the collective radial velocity increase linearly with radius.

In the EES model, the dynamical response of the source is governed by the interplay of thermal pressure and the nuclear binding forces, which tend to return the density to its equilibrium value $\rho_0$. The binding effects are parameterized in terms of the finite-nucleus compressibility. For simplicity, the binding energy per nucleon at densities different from $\rho_0$ is assumed to deviate from liquid-drop values by a quadratic function of density,

$$\frac{E(\rho)}{A} = \frac{E_{LD}(\rho_0)}{A} + \frac{K}{18}\left(1 - \frac{\rho}{\rho_0}\right)^2 \qquad (6.1)$$

where the first term on the right represents the liquid drop binding energy values (≈-8 MeV) and K is the finite-nucleus compressibility coefficient. This compressibility includes surface and Coulomb effects.

The calculations require an assumption of initial source mass, charge and thermal excitation energy when the system is at normal density. For simplicity we assumed the decaying source to be the full composite system (A=233, Z=97), and we further assumed that the system expanded with no initial expansion velocity from normal density. For different compressibilities we calculated the correlation between the predicted total charged-particle and IMF multiplicity distributions. The results are shown by the curves in Figure 6.1 (the data were described previously in Chapter 5, Figure 5.5).

For orientation, the upper panel of Figure 6.1 includes an approximate scale of the relation between the excitation energy of the emitting system and the mean charged-particle multiplicity calculated from the EES model. In the extreme tails of the $N_C$ distributions, the correlation between internal energy and $N_C$ becomes dominated by fluctuations of the charged-particle multiplicity. Hence, very large values of $N_C$ become ineffective in selecting nuclei of increasing internal energy thus causing the observed saturation of $\langle N_{IMF} \rangle$ and $\sigma^2_{IMF}$ at large values of $N_C$ (see discussion in Section 5.1).

The calculations are sensitive to the nuclear compressibility at low density. The solid, dashed and dashed-dotted curves in Figure 6.1 show predictions for the relationship between the $\langle N_{IMF} \rangle$and $\langle N_C \rangle$ for finite-nucleus compressibilities of K=144, 200 and 288 MeV, respectively [Blai 80]. IMF

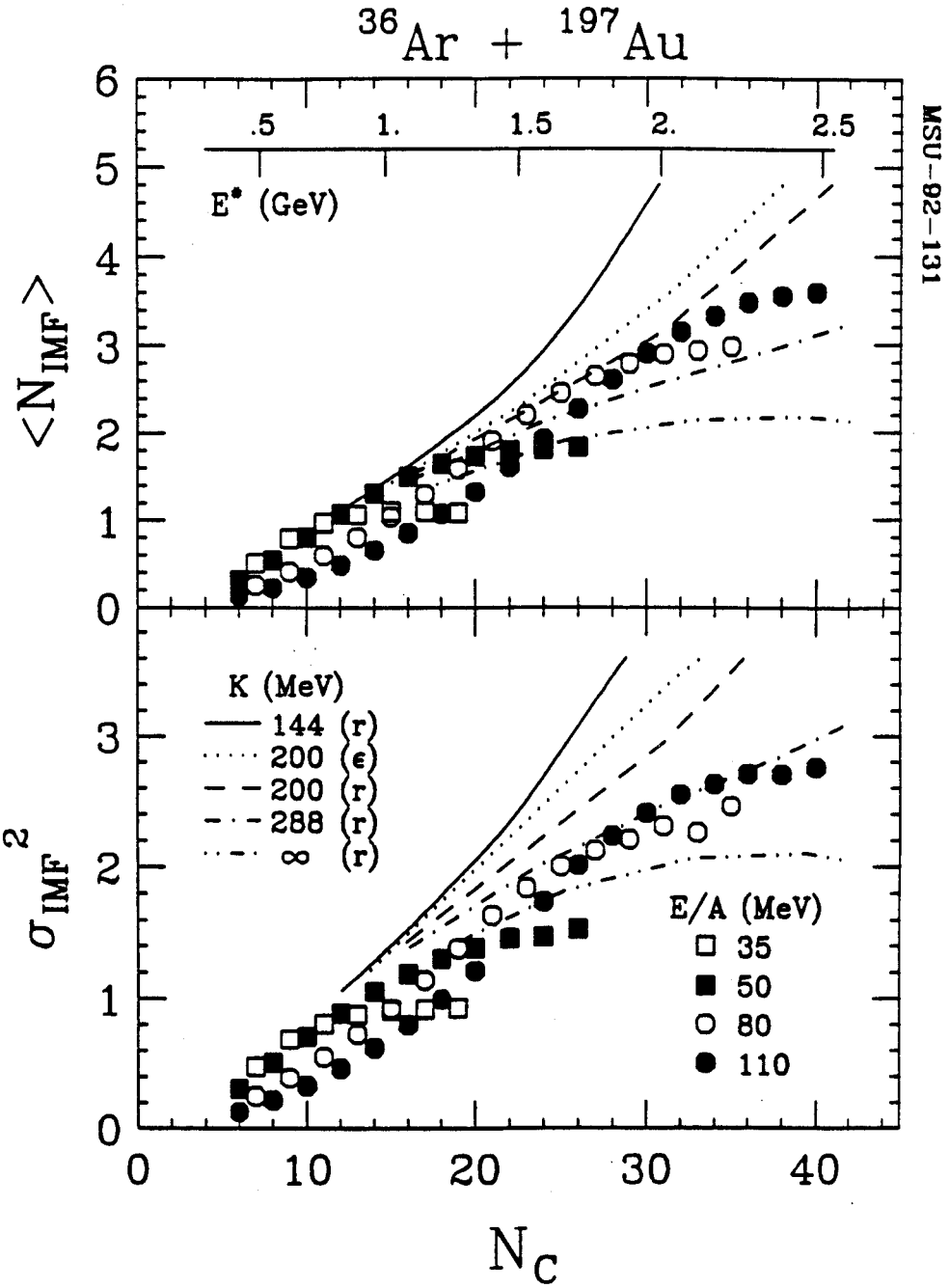


Figure 6.1 First and second moments of IMF multiplicity distributions as a function of charged-particle multiplicity, $N_c$. Different symbols represent results for indicated beam energies. The solid, dashed, dotted-dashed and dashed-dotted-dotted curves show results calculated for the statistical decay of expanding compound nuclei of finite-nucleus compressibility K=144, 200, 288 and ∞, respectively. The dotted curves represent the calculations for K=200, filtered by the detector response.

multiplicities for a non-expanding compound nucleus, corresponding to the limit K→∞, are shown by the dashed-dotted-dotted curves. To illustrate instrumental distortions, the dotted curves show the calculations for K=200 MeV, filtered by the response of the experimental apparatus. At low multiplicities, corresponding to low excitation in this model, the nucleus does not expand and all calculations predict IMF multiplicities consistent with the measured values. For multiplicities larger than $N_C$=20, however, expansion strongly influences the predicted number of clusters in the final state. Large observed IMF multiplicities, comparable to the measured values, are only predicted for an equation of state that is sufficiently soft to allow the nucleus to expand in response to thermal pressure. Very stiff low-density equations of state hinder the expansion of the system leading to a suppression of the production of multifragment final states and a consequent underprediction of the observed mean IMF multiplicities by nearly a factor of two.

The model ignores angular momentum, fluctuations in source size and excitation energy, and the lack of thermal equilibrium. While the inclusion of such effects might affect the final observations, we nonetheless find that the essential features of the observed data are included in the predictions of the schematic model shown by the curves in Figure 6.1. The sensitivity to the source size was explored by changing the initial mass and charge by 20%. The qualitative conclusions remain valid despite this change.

The calculations with the schematic model suggest that multifragment decays of highly-excited nuclear systems may exhibit considerable sensitivity to the low-density nuclear equation of state. They indicate that the expansion dynamics, which is governed by the compressibility, may be intimately connected to the production of IMFs. A more quantitative exploration of

these properties, however, will require a more complete model which also incorporates non-equilibrium effects.

## 6.2 Percolation

In the search for a signature of the liquid-gas phase transition in low density nuclear matter, percolation models are attractive since they exhibit a well-defined phase transition for infinite systems and since they allow straightforward generalizations to finite systems and the incorporation of important geometrical ingredients [Biro 86] for multifragmenting systems. In rather general terms [Siem 83, Hirs 84], the fluctuations at the critical point of the nuclear matter phase diagram are expected to lead to mass distributions which follow a power law, $\sigma(A) \propto A^{-\tau}$, with a critical exponent of the order of $\tau$=2.2-2.3. A number of theoretical investigations of phase transitions in finite nuclear systems have been based on percolation models [Baue 85, Baue 86, Baue 88, Camp 86, Camp 88, Ngô 90, Biro 86, Jaqa 90].

Most percolation models are governed by a single bond-breaking or site-vacancy parameter and cannot be expected to reproduce the two-dimensional phase diagram of nuclear matter in the temperature vs. density plane. Despite this limitation, they have been rather successful [Baue 85, Baue 86, Baue 88] in describing the observed [Hirs 84] power-law behavior of measured fragment mass distributions and in developing techniques to extract critical exponents from exclusive fragmentation data [Camp 88, Ngô 90]. In this section, we provide a test of the bond percolation model of references [Baue 85, Baue 86, Baue 88] and compare its predictions to fragment yields measured for the reactions $^{129}Xe+^{197}Au$ at E/A=50 MeV and $^{36}Ar+^{197}Au$ at E/A=50, 80 and 110 MeV.

Calculations were performed with the bond percolation model of ref. [Baue 85, Baue 86, Baue 88]. In this model, the nucleus is considered to be a cubic lattice, the sites of which are randomly occupied by protons and neutrons within a spherical volume of radius $R \approx \left(\frac{3}{4\pi}A\right)^{1/3} a$, where $a$ is the lattice parameter ($a = \rho_0^{-1/3} \approx 1.8$ fm). Initially, all nucleons are connected in one cluster. The bonds between the sites are randomly broken with a probability $p$. Each nucleon is assigned a random momentum consistent with the momentum distribution of a Fermi-gas of temperature $T$ estimated [Baue 88] from the bond-breaking probability as $T$=11.7$\sqrt{p}$ MeV (see Appendix B). Emitted fragments are defined in terms of connected clusters. Initial fragment energies are calculated from the total momenta of the clusters. Final kinetic energies are calculated by incorporating the final state Coulomb repulsion between the fragments. For this purpose a given fragment partition is translated into a spatial distribution of clusters characterized by an average freeze-out density $\rho$=0.2$\rho_0$, where $\rho_0$ =0.17 fm$^{-3}$ is the density of normal nuclear matter. (Different choices of the freeze-out density lead to slightly different shapes of the low-energy portion of the energy spectrum due to changes in the Coulomb repulsion between the fragments. These Coulomb barrier fluctuations are of minor importance in the present context.) The final momenta of the emitted fragments are boosted by the velocity of the center-of-mass of projectile and target. In order to allow meaningful comparisons with our data, we have filtered the theoretical distributions with the response of the experimental apparatus.

Elemental multiplicity distributions measured for the reactions $^{36}$Ar+$^{197}$Au and $^{129}$Xe+$^{197}$Au are shown (as points) in the top and bottom panels of Figure 6.2. These distributions were obtained by integrating all identified fragments over all detectors. In order to select central collisions,

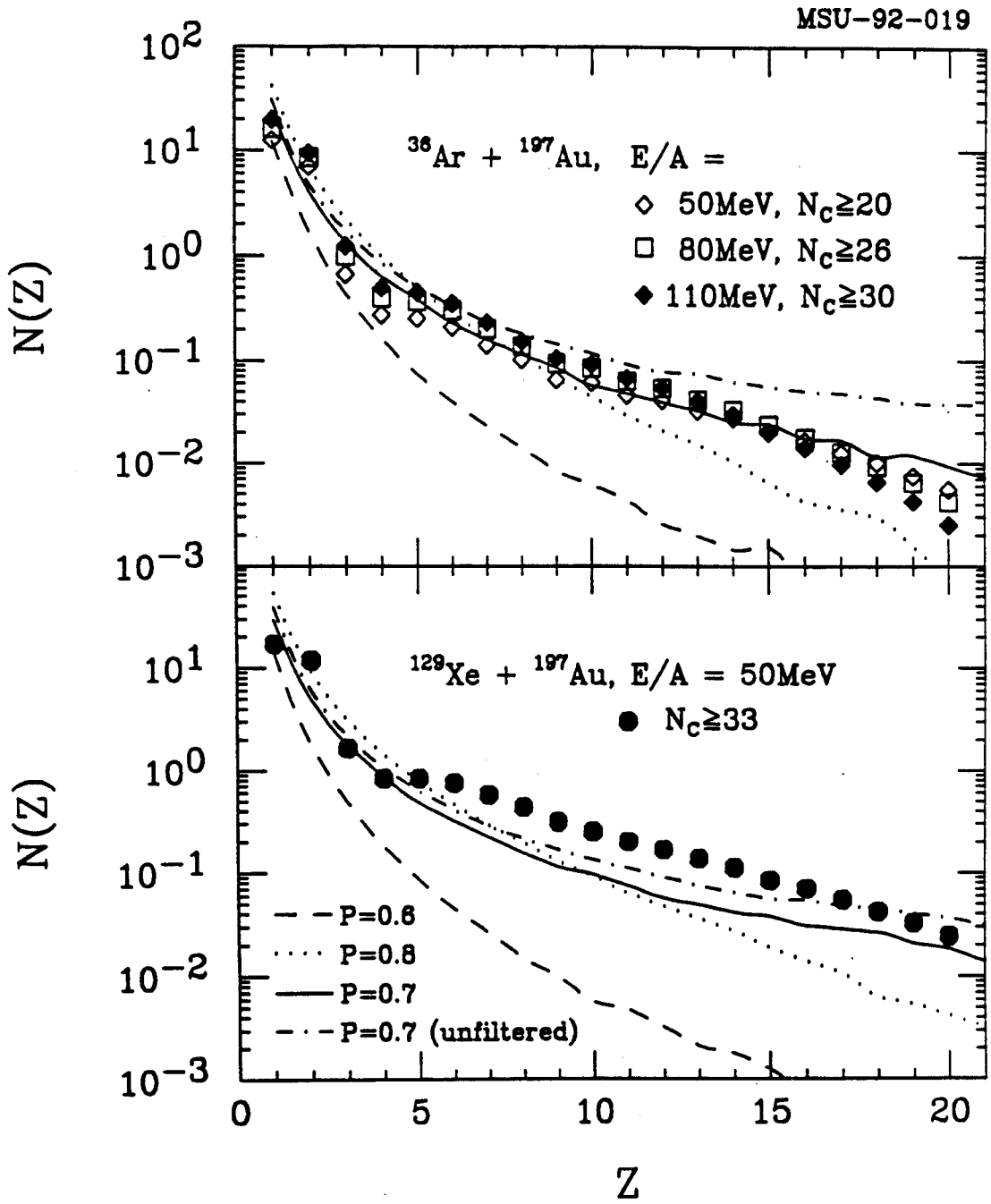


Figure 6.2 Elemental multiplicity distributions detected in $^{36}$Ar+$^{197}$Au collisions at E/A=50, 80, 110 MeV (top panel) and in $^{129}$Xe+$^{197}$Au collisions at E/A=50 MeV (bottom panel). The curves represent calculations with the bond percolation model (described in the text) for the indicated bond-breaking probabilities *p*. All calculations are filtered by the response of the experimental apparatus except for the dot-dashed curve.

these Z-distributions were selected by the total charged-particle multiplicity cuts indicated in the figure. When one adopts a strictly geometric interpretation of the measured charged-particle multiplicity [Cava 90, chapter 4], these cuts were chosen to represent the range of impact parameters of $\hat{b} \leq 0.3$ . The elemental distributions observed for the various reactions exhibit rather similar shapes. For the $^{36}Ar+^{197}Au$ system (top panel), the elemental multiplicity distributions become slightly steeper with increasing bombarding energy. The multiplicities for heavier IMFs are significantly larger for the $^{129}Xe+^{197}Au$ system (bottom panel) than for the $^{36}Ar+^{197}Au$ system (top panel). Part of this difference in the observed yields of heavier fragments may be due to an increased detection efficiency in $^{129}Xe+^{197}Au$ reactions resulting from the larger center-of-mass velocity.

The curves in Figure 6.2 depict elemental multiplicities predicted by the standard bond percolation model and filtered by the detection efficiency of the experimental apparatus. Calculations are shown for representative bond-breaking probabilities above and below the near-critical bond-breaking parameter of $p$=0.7. (In the percolation model, the critical point marks a second order phase transition: for $p$>0.7, the percolation cluster disappears and the system breaks up completely.) Calculations performed for bond-breaking probabilities much larger or smaller than the critical value predict Z-distributions which are too steep. For the $^{36}Ar+^{197}Au$ reactions, the overall magnitudes and shapes of the experimental Z-distributions are in reasonable agreement with predictions of the percolation model when the bond-breaking parameter is taken close to the critical value. However, for the $^{129}Xe+^{197}Au$ reaction, the percolation model underpredicts the yield of heavier fragments (Z=6-20) for any choice of bond-breaking parameter.

Representative angular distributions of emitted particles are shown in Figure 6.3. The top and bottom panels show results for the $^{36}Ar+^{197}Au$ reaction at E/A=110 MeV and for the $^{129}Xe+^{197}Au$ reaction at E/A=50 MeV, respectively. The angular distributions are shown for three different ranges of element numbers, Z=1-2 (circles), Z=3-5 (squares), and Z=6-12 (diamonds). For both systems, the angular distributions become more forward peaked with increasing fragment charge. Angular distributions for the $^{129}Xe+^{197}Au$ system are more forward peaked than those for the $^{36}Ar+^{197}Au$ system. These effects are largely due to kinematics. Differences between the angular distributions of the two reactions arise primarily from the larger velocity of the emitting source of the $^{129}Xe+^{197}Au$ system.

The curves in Figure 6.3 show results of percolation calculations. To facilitate a better comparison of shapes between observed and predicted angular distributions, the calculated angular distributions were normalized to the experimental yields at $\theta$=45°. To display the effects of the detector response, filtered and unfiltered calculations are shown by solid and dashed curves, respectively. In view of the fact that the percolation model does not include dynamical preequilibrium effects, the shapes of the experimental angular distributions are reasonably well reproduced by the calculations. Discrepancies between theoretical and experimental angular distributions due to preequilibrium emission are most pronounced for lighter fragments emitted at forward angles. For such fragments the measured angular distributions are slightly more forward peaked in the laboratory than the calculated angular distributions. Similar discrepancies exist for other treatments in which statistical equilibrium is assumed. For this purpose, the calculated angular distributions may be sufficiently realistic to assess effects of

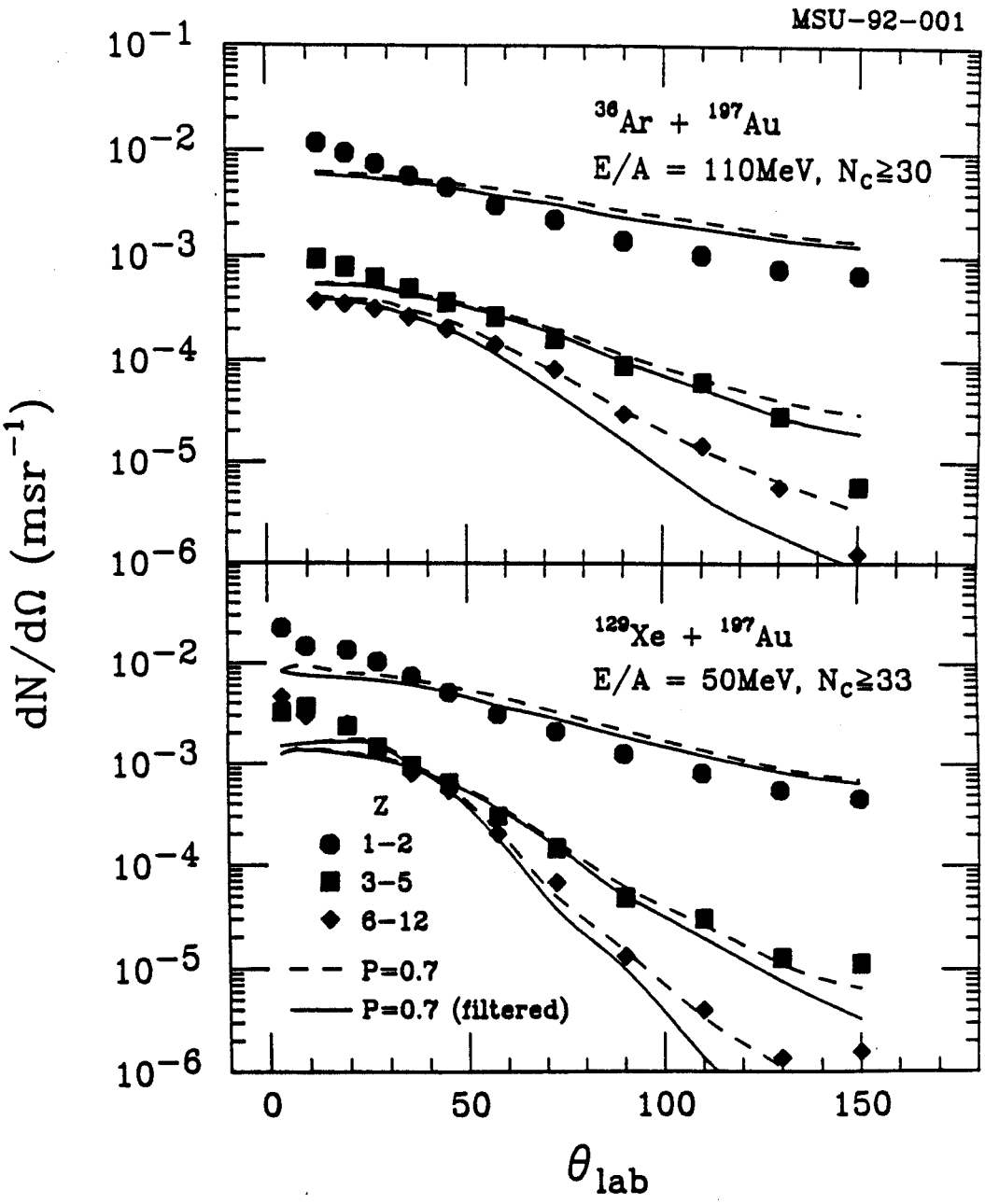


Figure 6.3 Angular multiplicity distributions of light particles, Z=1,2 (circles), and intermediate mass fragments of Z=3-5 (squares) and Z=6-12 (diamonds) detected in $^{36}$Ar+$^{197}$Au collisions at E/A=50, 80, 110 MeV (top panel) and in $^{129}$Xe+$^{197}$Au collisions at E/A=50 MeV (bottom panel). The curves represent calculations with the bond percolation model for a bond-breaking probability of $p$=0.7. The calculations have been normalized to the data at θ=45°. Dashed and solid curves show raw calculations and calculations filtered by the response of the experimental apparatus.

instrumental distortions on the energy- and angle-integrated particle distributions presented in Figures 6.2 and 6.3.

In order to display more clearly the fraction of IMFs among the emitted charged particles, Figure 6.4 presents the average IMF multiplicity, $\langle N_{IMF} \rangle$, as a function of charged-particle multiplicity, $N_C$ [Bowm 91] (see Figure 5.5). Points in the figure show the average IMF multiplicity $\langle N_{IMF} \rangle$ as a function of charged-particle multiplicity $N_C$. For a given charged-particle multiplicity, more intermediate mass fragments are observed for the $^{129}$Xe+$^{197}$Au reaction than for the $^{36}$Ar+$^{197}$Au reactions. At large charged-particle multiplicities ($N_C$ ≥30), IMF admixtures of $\langle N_{IMF} \rangle / N_C$ =0.18 and 0.1 are observed for the systems $^{129}$Xe+$^{197}$Au and $^{36}$Ar+$^{197}$Au, respectively.

If the elemental distributions strictly followed a power law distribution, $\sigma(Z) = \sigma_0 Z^{-\tau}$, the IMF-admixture would be determined by the exponent $\tau$:

$$\frac{N_{IMF}}{N_C} = \frac{\sum_{Z=3}^{20} \sigma_0 Z^{-\tau}}{\sum_{Z=1}^{Z_{max}} \sigma_0 Z^{-\tau}} \qquad (6.2)$$

For power law distributions, the (raw detected) ratios of $\langle N_{IMF} \rangle / N_C$ ≈0.18 and 0.10 correspond to exponents of $\tau$≈2.15 and 2.6 (see Figure 6.5). If we use the shapes of the energy and angular distributions predicted by the percolation model to correct for the detector efficiency, we obtain efficiency corrected values of $\langle N_{IMF} \rangle / N_C$ ≈0.19 and 0.116, corresponding to $\tau$≈2.12 and 2.5. These values are slightly below and above the value, $\tau_{crit}$≈2.2, at the critical point.

According to Figure 6.2, the percolation model underpredicts the yield of IMFs with Z>5 for the $^{129}$Xe+$^{197}$Au reaction. This failure is displayed more clearly by the curves in Figure 6.4 which show maximum IMF admixtures predicted by the percolation model. Thick and thin curves represent results of filtered and unfiltered percolation calculations, respectively, using the near-

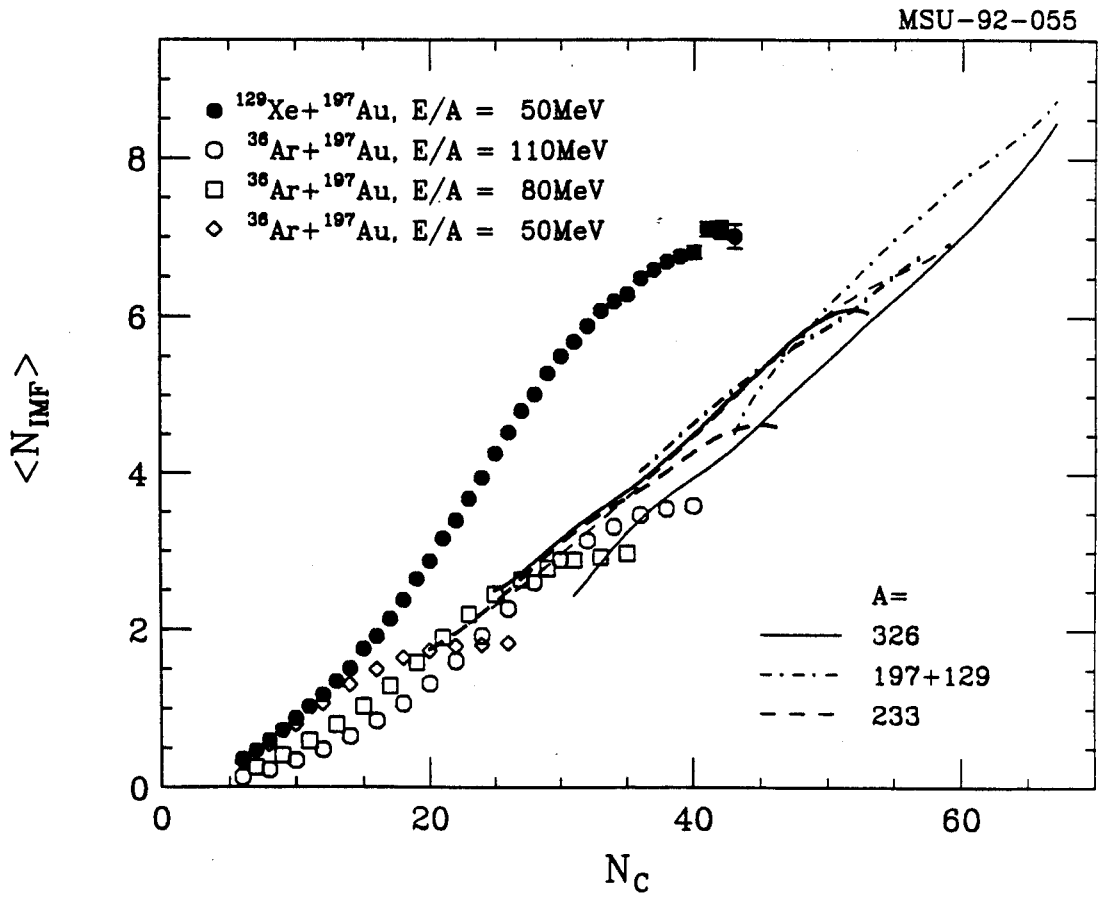


Figure 6.4 Relation between average IMF and charged-particle multiplicities detected in $^{36}$Ar+$^{197}$Au collisions at E/A=50, 80, 110 MeV (open diamonds, open squares, and open circles, respectively) and in $^{129}$Xe+$^{197}$Au collisions at E/A=50 MeV (solid circles). Thick and thin curves show the results of filtered and unfiltered percolation calculations, respectively. Details are given in text.

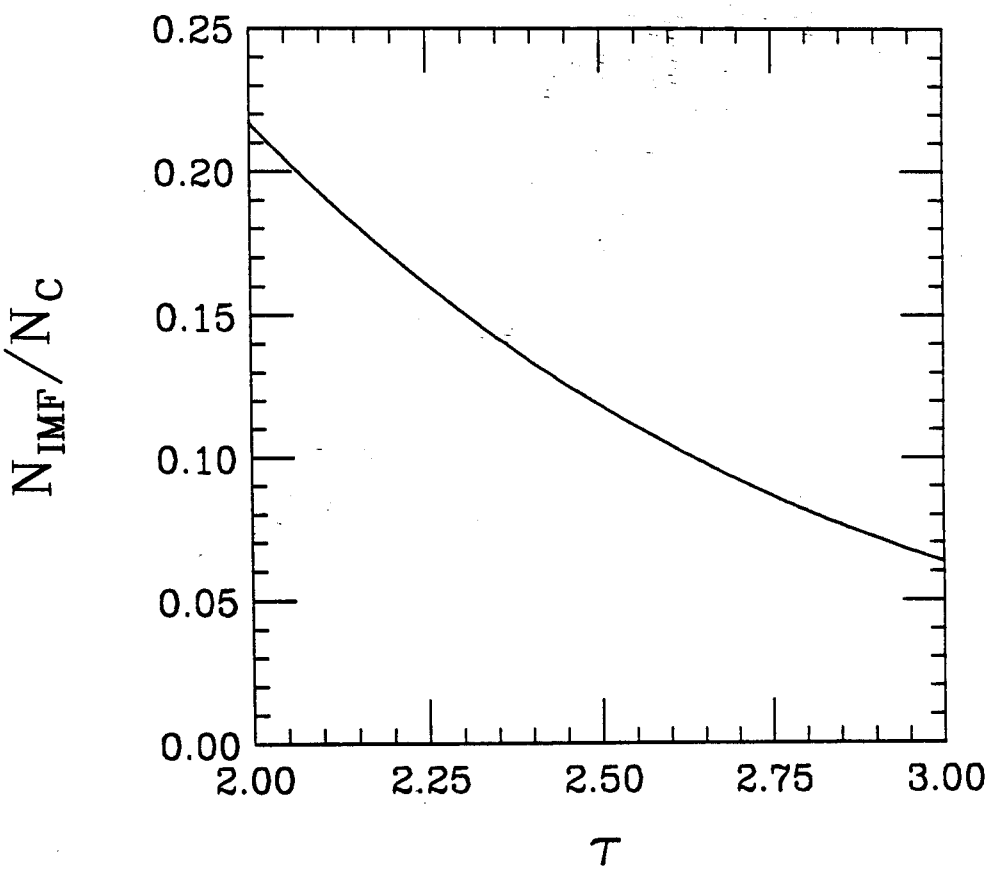


Figure 6.5 IMF admixture as a function of $\tau$, according to Equation (6.2).

critical bond-breaking parameter, $p$=0.7. (For the percolation model, these calculations give upper bounds for the admixture of IMFs among the emitted charged particles. Smaller IMF admixtures can be obtained by using larger or smaller bond-breaking parameters.) The dashed curves in Figure 6.4 show percolation calculations for the combined $^{36}Ar+^{197}Au$ system. For this system, filtered and unfiltered IMF admixtures are very similar, and the relative abundance of IMFs observed in central collisions can be reproduced by the model calculations. The solid curves represent percolation calculations for the combined $^{129}Xe+^{197}Au$system. Here, the filtered calculations represent slightly higher IMF admixtures than the unfiltered calculations. This effect is largely due to an increased IMF detection efficiency resulting from the larger center-of-mass velocity of the $^{129}Xe+^{197}Au$ center-of-mass system. However, both filtered and unfiltered calculations predict IMF admixtures that are too small. This failure is most dramatic for central $^{129}Xe+^{197}Au$ collisions for which the comparison with an equilibrium model is most meaningful.

As an alternative scenario, we have also performed percolation model calculations for the separate multifragment decay of excited projectile and target nuclei. The unfiltered calculations, shown by the thin dot-dashed curve, predict slightly higher IMF admixtures. The thick dot-dashed curve illustrates the effect of filtering for an extreme two-source scenario in which the relative velocity of projectile and target was reduced by only 50% from the initial value, taking total momentum conservation into account. Even in such an extreme scenario, the major discrepancy remains.

High-resolution coincidence experiments indicate that a significant portion of primary fragments can be expected to be produced in highly excited, particle unbound states which decay by light particle emission [Naya 92]. Such sequential decay processes will result in secondary fragment yields which are

smaller and secondary light particle yields which are larger than the corresponding primary yields. The portion of primary fragments may therefore be even larger than the portion of particle-stable secondary fragments. This aggravates the failure of the percolation model to predict the large proportion of intermediate mass fragments among the particles emitted in the $^{129}Xe+^{197}Au$ reaction.

The inability of the bond-percolation model to reproduce the large intermediate mass fragment multiplicities observed for the $^{129}Xe+^{197}Au$ system is unexpected and represents, to our knowledge, the first significant failure of the percolation model. This model is only one representation of a large number of phase transition models which all belong to the same universality class and should therefore show similar deficiencies. At present it is not clear whether one can rule out all such models or whether one may be forced to consider dynamical enhancements of fragment yields due to collective expansion or rotation.

## Toroids and bubbles

In the bond-percolation calculations of the previous section, the disintegrating systems were assumed to have compact spherical configurations. Recent microscopic transport calculations [Baue 92, More 92] indicate, however, that multifragment decays may proceed via more complex toroidal or bubble-shaped decay configurations. In this section, we employ the bond-percolation model used previously to investigate how multifragment disintegrations might be affected by the occurrence of ring- and bubble-shaped decay configurations.

All calculations presented in this section were performed for a system consisting of A=N+Z=250 nucleons, with Z=102. The decaying system is

represented by those points on a simple three-dimensional cubic lattice which fall within the specified decay volume. Each site represents a nucleon that is "bonded" to its nearest neighbors as described in the previous section. In the following discussion of non-compact breakup geometries, instrumental distortions will be ignored since we wish to outline some general trends without trying to fit a specific set of data. Nevertheless, it is useful to provide a reference which allows the reader to gauge the magnitude of various effects. For this purpose, the solid points in Figures 6.6 and 6.7 show the fragment admixtures (i.e. the mean number of detected intermediate mass fragments, $\langle N_{IMF} \rangle$, as a function of the detected charged-particle multiplicity, $N_C$) measured [Bowm 91] for the $^{129}Xe + ^{197}Au$ reaction at E/A = 50 MeV. The solid lines in the figures show previous calculations with the bond percolation model for a compact spherical breakup configuration using a near-critical bond-breaking parameter $p = 0.7$. These calculations represent the maximum fragment admixtures predicted by the bond-percolation model for a compact spherical geometry; they underpredicted the measured fragment multiplicities (see previous section). The difference between the thin and thick lines illustrates the magnitude of instrumental distortions. The thin line represents the "raw" calculation (not corrected for the acceptance of the experimental apparatus), and the thick line represents the calculation filtered by the acceptance of the experimental apparatus.

The hatched area in Figure 6.6 shows fragment admixtures predicted for toroidal breakup configurations. In these calculations, the bond-breaking probabilities were varied between $p = 0.5 - 0.8$, and the central radii of the toroids were varied between $R_t = (2.0 - 4.5) \times a$, where $a = \rho_0^{1/3} \approx 1.8$ fm denotes the spacing between adjacent lattice sites (see insert in the figure for a definition of the geometry). Because of volume conservation, the thickness d

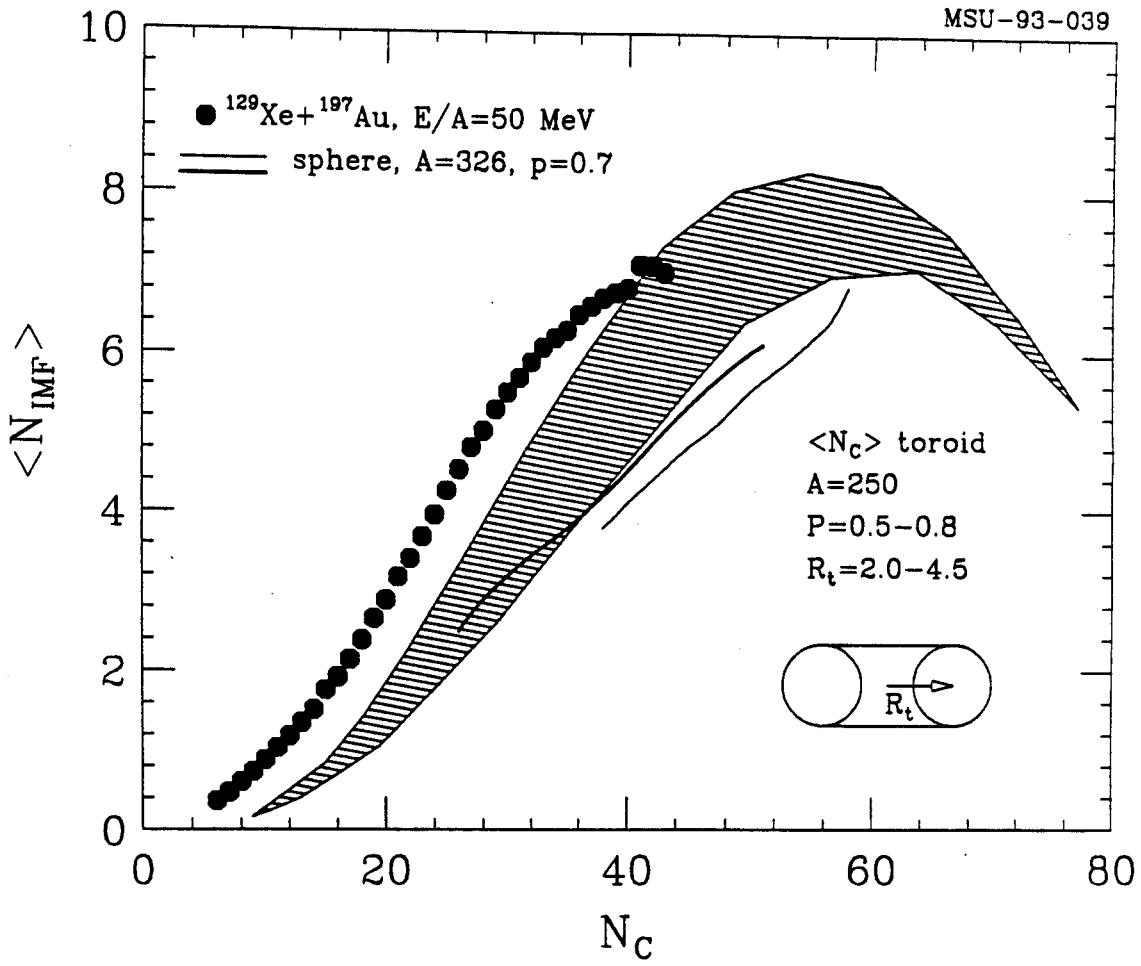


Figure 6.6 Relation between average IMF and charged-particle multiplicities. Solid points represent values measured for $^{129}$Xe + $^{197}$Au at E/A=50 MeV. Thin (thick) solid line shows the raw (efficiency corrected) percolation calculation for a solid sphere. The hatched area shows the range of average IMF and *average* charged-particle multiplicities predicted by percolation calculations for toroidal breakup configurations.

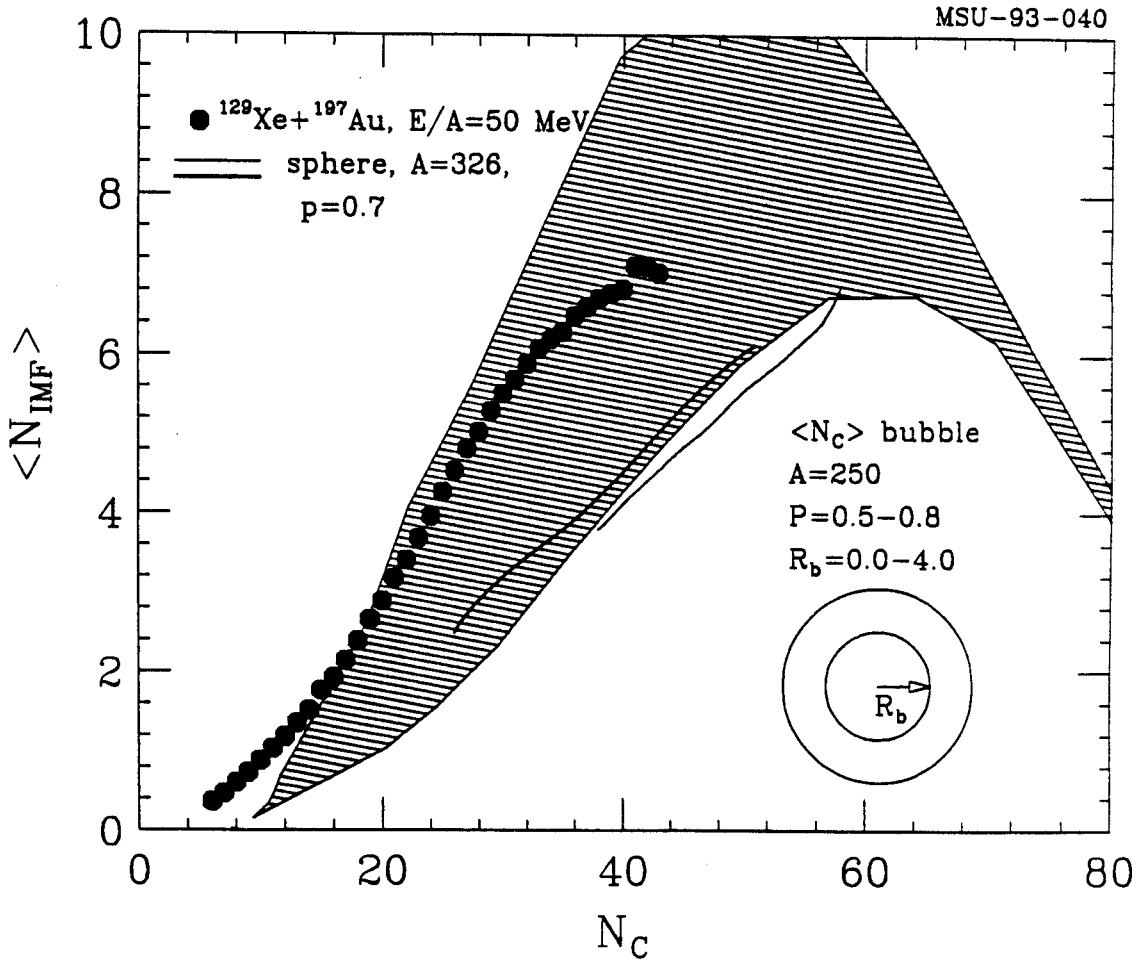


Figure 6.7 Relation between average IMF and charged-particle multiplicities. Solid points represent values measured for $^{129}$Xe + $^{197}$Au at E/A=50 MeV. Thin (thick) solid line shows the raw (efficiency corrected) percolation calculation for a solid sphere. The hatched area shows the range of average IMF and *average* charged particle multiplicities predicted by percolation calculations for bubble-shaped breakup configurations.

of the toroid is defined by $R_t$ and the nucleon number: $A \approx \pi^2 R_t d^2/2$. For A=250, the toroid has a hole in the center only for $R_t > 2.5 \times a$. The upper boundary of the hatched area is determined by the breakup of a toroid of radius $R_t = 4.5 \times a$, and the lower boundary represents the breakup of an oblate object of $R_t = 2.0 \times a$. Over the range of $N_c \approx 30 - 50$, the percolation model can produce significantly larger fragment multiplicities for toroidal than for spherical breakup configurations. Qualitatively such an effect may be expected since the surface of a toroid is larger than that of a sphere.

Enhanced fragment admixtures can also be obtained for bubble-shaped breakup configurations. In Figure 6.7 the hatched area shows the range of average IMF multiplicities predicted for bubble shaped density distributions using bond-breaking probabilities of $p = 0.5 - 0.8$ and inner bubble radii of $R_b = (0.0 - 4.0) \times a$ (see insert in the figure for a definition of the geometry). For A = 250 and $R_t > 4.0 \times a$, the bubble has a thickness less than $1.0 \times a$, and the simulation models the breakup of a thin sheet. The upper rising boundary of the hatched area corresponds to calculations with a fixed bond-breaking probability of $p = 0.5$ and varying inner radii, $R_b = (0.0 - 4.0) \times a$. The falling part of the upper boundary represents calculations for an inner radius of $R_b = 4.0 \times a$ and varying bond-breaking probabilities $p = 0.5 - 0.8$. For $\langle N_c \rangle \leq 70$, the lower boundary is given by the breakup of a sphere with varying bond-breaking probabilities, $p = 0.5 - 0.8$.

The results in Figures 6.6 and 6.7 demonstrate that objects with larger surfaces can produce more fragments than objects with smaller surfaces. Hence, geometrical considerations may play an important role for multifragment disintegrations. A relatively cool object (small bond-breaking probability) with a large surface may decay into more fragments than a hotter object (larger bond-breaking probability) with a smaller surface. For

noncompact breakup geometries, the large fragment multiplicities observed for the $^{129}Xe$ + $^{197}Au$ reaction can be reconciled with predictions of the bond percolation model.

A number of investigations have aimed at obtaining information of near-critical behavior from the shape of fragment mass or charge distributions [Gros 90, Pana 84, Mahi 88, Ogil 91, Li 93]. Near the critical region, scaling theory of large systems predicts mass distributions of the form:

$$N_A(p) \propto A^{-\tau} f\left(A^{\sigma}(p - p_c)\right). \tag{6.3}$$

Here, $\tau$ and $\sigma$ are critical exponents and $f(A^{\sigma}(p-p_c))$ is a scaling function that modulates the power law behavior near the critical bond-breaking probability, $p=p_c$, above which the "infinite" percolation cluster ceases to exist. In the Fisher droplet model $f$ is an exponential so that

$$N_A(p) \propto A^{-\tau} \exp\left(const \cdot A^{\sigma}(p - p_c)\right). \tag{6.4}$$

$f$ has the appropriate limiting behavior of $f=1$ at $p = p_c$ so that $N_A \propto A^{-\tau}$

In practice, the mass or charge distributions are often fit [Pana 84, Mahi 88, Ogil 91, Li 93] by a simple power law,

$$Y(A) \propto A^{-\lambda}, \tag{6.5}$$

where $\lambda$ is treated as a fit parameter, and the critical exponent $\tau$ is identified with the extracted minimum value of $\lambda$ [Baue 85].

We will now show that this empirical approach can lead to misleading results if the geometry at breakup is not compact. For this purpose, we performed power law fits to the mass distributions predicted by the bond percolation model over a broad range of parameters and geometrical configurations. The results of these calculations are summarized in Figures 6.8 and 6.9 for toroidal and bubble-shaped geometries, respectively. In both cases, the best fit-parameter $\lambda$ exhibits a clear valley as a function the bond-

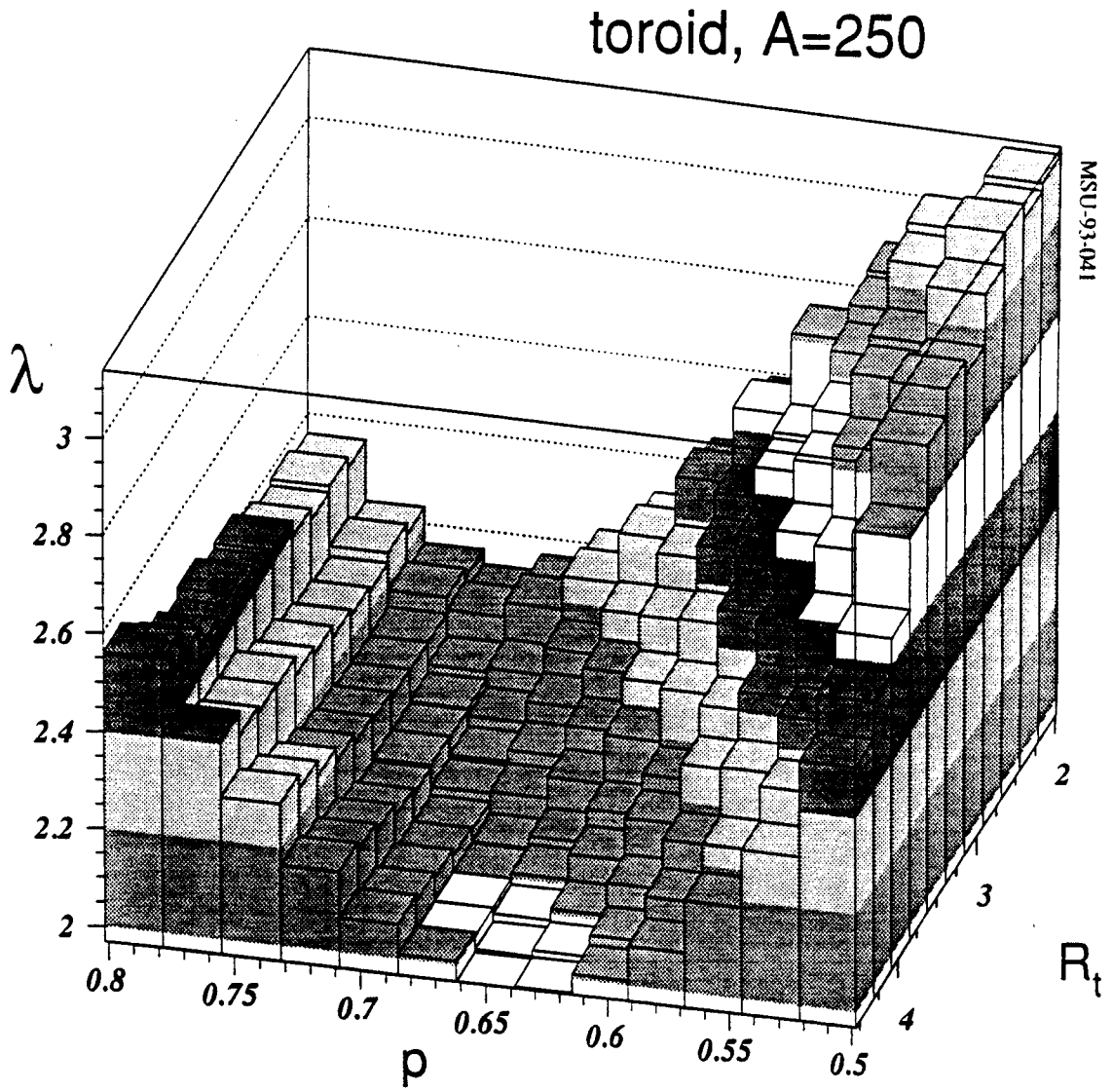


Figure 6.8 Extracted power-law exponents λ fit to mass distributions predicted by the bond percolation model for the break up of toroidal systems as a function of $R_t$ and $p$.

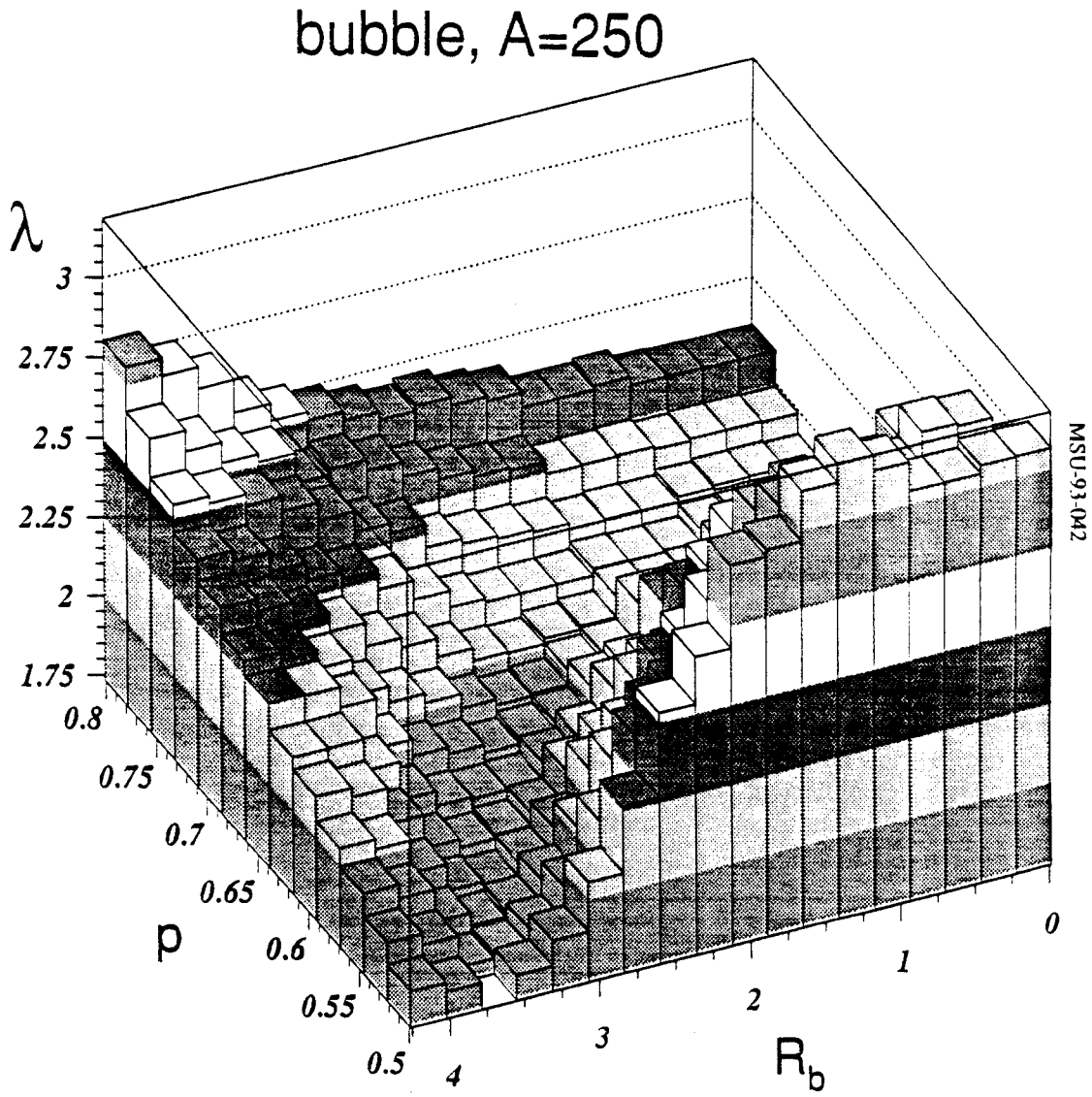


Figure 6.9 Extracted power-law exponents λ fit to mass distributions predicted by the bond percolation model for the break up of bubble shaped systems as a function of $R_b$ and $p$.

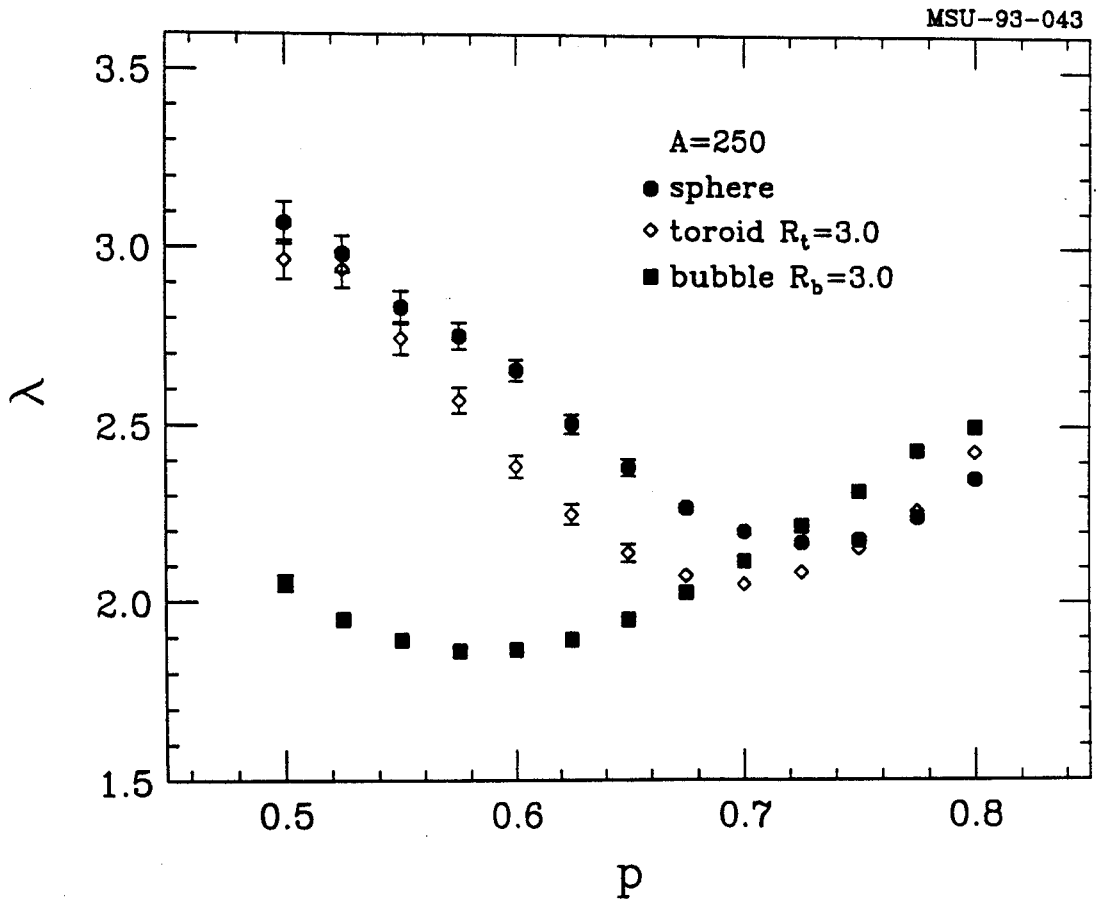


Figure 6.10 λ as function of p for a solid sphere (circles), a toroid of radius $R_t$ = 3.0×a (diamonds), and bubble with inner radius $R_b$ = 3.0×a (squares).

breaking ($p$) and geometry ($R_t$ and $R_b$) parameters. In this valley, smaller values of $\lambda$ occur for less compact breakup geometries.

The strong geometry-dependence of the relation between the power-law exponent $\lambda$ and the bond-breaking parameter $p$ is depicted more clearly in Figure 6.10 for three representative breakup configurations, a solid sphere (solid circles), a toroid of central radius $R_t = 3.0 \times a$ (open diamonds) and a bubble with inner radius $R_b = 3.0 \times a$ (solid squares).

Microscopic transport calculations [Baue 92, More 92] predict a strong dependence of the breakup geometry upon beam energy, impact parameter and projectile-target combination. Indeed, under favorable conditions, the formation of unstable bubbles and rings has been predicted [Baue 92, More 92]. The present model calculations for finite systems indicate a strong dependence of extracted "critical" parameters ($\tau$ and $p_c$) on the geometrical configuration of the system at breakup. Compilations of power law exponents $\lambda$ determined from data for different entrance channels [Pana 84], for different impact parameters [Ogil 91] or for excitation functions covering broad ranges of energies [Pana 84, Mahi 88, Li 93] may contain samples representing sufficiently different geometrical configurations to render a minimum in $\lambda$ difficult to interpret. For infinite systems, critical exponents govern the scaling laws near critical points. We suspect that the application of scaling laws to finite systems of potentially complex breakup geometries is much less straight forward than originally surmised [Camp 92].

# Chapter 7 Fluctuations in multifragment emission

A recent analysis [Plos 90] of fragment-size distributions observed in reactions induced by gold on emulsion at E/A=1 GeV [Wadd 85] saw evidence for intermittency, which might indicate that fragmentation processes are scale invariant. We take up the problem of intermittency by analyzing the factorial moments of charge distributions observed in $^{36}Ar+^{197}Au$ reactions at beam energies between 35 and 110 MeV per nucleon [deSo 91].

The occurrence of intermittency is deduced from the factorial moments [Bial 86, Bial 88]

$$F_k(\Delta) = \frac{\sum_{i=1}^{Z_0/\Delta} \langle N_i(N_i-1)\ldots(N_i-k+1)\rangle}{\sum_{i=1}^{Z_0/\Delta} \langle N_i\rangle^k} \tag{7.1}$$

where $Z_0$ is the total charge of the disintegrating nuclear system, $\Delta$ is a binning parameter, and $N_i$ is the number of fragments with charges in the interval $(i-1)\Delta < Z \le i\Delta$ where $i=1,\ldots,Z_0/\Delta$. The ensemble average $\langle\ \rangle$ is performed over all fragmentation events considered. Intermittency is defined by a relation [Bial 86, Bial 88]

$$F_k(\Delta') = F_k(a\Delta) = a^{-f(k)}F_k(\Delta) \tag{7.2}$$

between factorial moments $F_k(\Delta')$ and $F_k(\Delta)$ obtained for two different binning parameters $\Delta$ and $\Delta' = a\Delta$. Generally, evidence for intermittency has been obtained by examining the double logarithmic plot of $\ln F_k$ versus $-\ln\Delta$. Plots which show lines of positive slope are consistent with nonzero fractal dimension and considered to display intermittency. By construction, the factorial moments $F_k(\Delta)$ are unity for Poisson distributions. Hence, Poisson distributions do not exhibit intermittency. The expression for the second factorial moment can be written as

$$F_2(\Delta) = 1 + \frac{\sum_i \left(\sigma_i^2 - \langle N_i \rangle\right)}{\sum_i \langle N_i \rangle^2} \tag{7.3}$$

where $\langle N_i \rangle$and $\sigma_i^2$ denote the mean value and the variance of the multiplicity distribution in the $i$th bin. Distributions which are narrower (broader) than Poisson distributions possess moments which are less (greater) than unity. For $\Delta = Z_0$, the right hand side of Equation (7.3) reduces to $1 + \left(\sigma_C^2 - \langle N_C \rangle\right) / \langle N_C \rangle^2$, where $\langle N_C \rangle$ and $\sigma_C^2$ are the mean value and the variance of the charged particle multiplicity distribution.

Intermittency as an indicator of nontrivial physics is generally sought for in systems exhibiting larger than Poisson fluctuations. Evidence for such large fluctuations must be sought in events representing similar initial conditions. However, constraints from conservation laws may lead to reduced fluctuations because statistical independence of individual bin occupations is lost. As the number of bins becomes larger, the individual bin occupations may become more independent, and the moments may increase. The corresponding rise in the factorial moments as a function of decreasing bin size would be of little interest.

In order to explore whether there is a basis for non-trivial intermittent behavior in a reaction in which multifragment emission has been observed,

we analyzed the first and second moments of the charged particle multiplicity distributions measured (see Section 5.2), with the Miniball [deSo 90] for $^{36}Ar+^{197}Au$ collisions over a broad range of energies, 35≤ E/A≤110 MeV. Event selection was performed by cuts on the total transverse energy, $E_t = E\sin^2\theta$, of the emitted charged particles. For orientation, we also provide an empirical impact parameter scale by using the geometrical prescription of Section 4.2 to construct a "reduced" impact parameter $\hat{b}$. The reduced impact parameter assumes values of $\hat{b} \approx 1$ for peripheral collisions and $\hat{b} \approx 0$ for the most violent collisions characterized by large values of $E_t$.

The top panel in Figure 7.1 shows the measured two-dimensional correlation between transverse energy $E_t$ and charged particle multiplicity $N_C$ for $^{36}Ar+^{197}Au$ collisions at E/A=110 MeV. The dashed and dot-dashed curves in the bottom panel of Figure 7.1 depict charged particle distributions selected by narrow cuts on $E_t$, corresponding to reduced impact parameters $\hat{b} \approx 0.1$ and 0.6. The dotted curves illustrate the effects of increasing the widths, $\Delta E_t$, of the cuts as indicated by dotted horizontal lines in the top panel. For central collisions, the $N_C$ distribution is rather insensitive to $\Delta E_t$, but for more peripheral collisions it suffers considerable broadening as $\Delta E_t$ is increased.

The broadening due to impact parameter averaging is illustrated more quantitatively in Figure 7.2. Top, center and bottom panels of the figure depict the quantities $\sigma_C^2 / \langle N_C \rangle$, $\sigma_C^2$ and $\langle N_C \rangle$, respectively, as a function of transverse energy. Solid circular, open square-shaped and star-shaped points show values obtained for cuts of widths $\Delta E_t$=20, 180 and 340 MeV, respectively. For narrow cuts on $\Delta E_t$, the charged particle multiplicity distributions are inconsistent with $F_2(\Delta = Z_0) > 1$, since $\sigma_C^2 / \langle N_C \rangle < 1$. For near-central collisions, $\hat{b}$<0.3, the extracted values of $\sigma_C^2 / \langle N_C \rangle$ exhibit little dependence on the

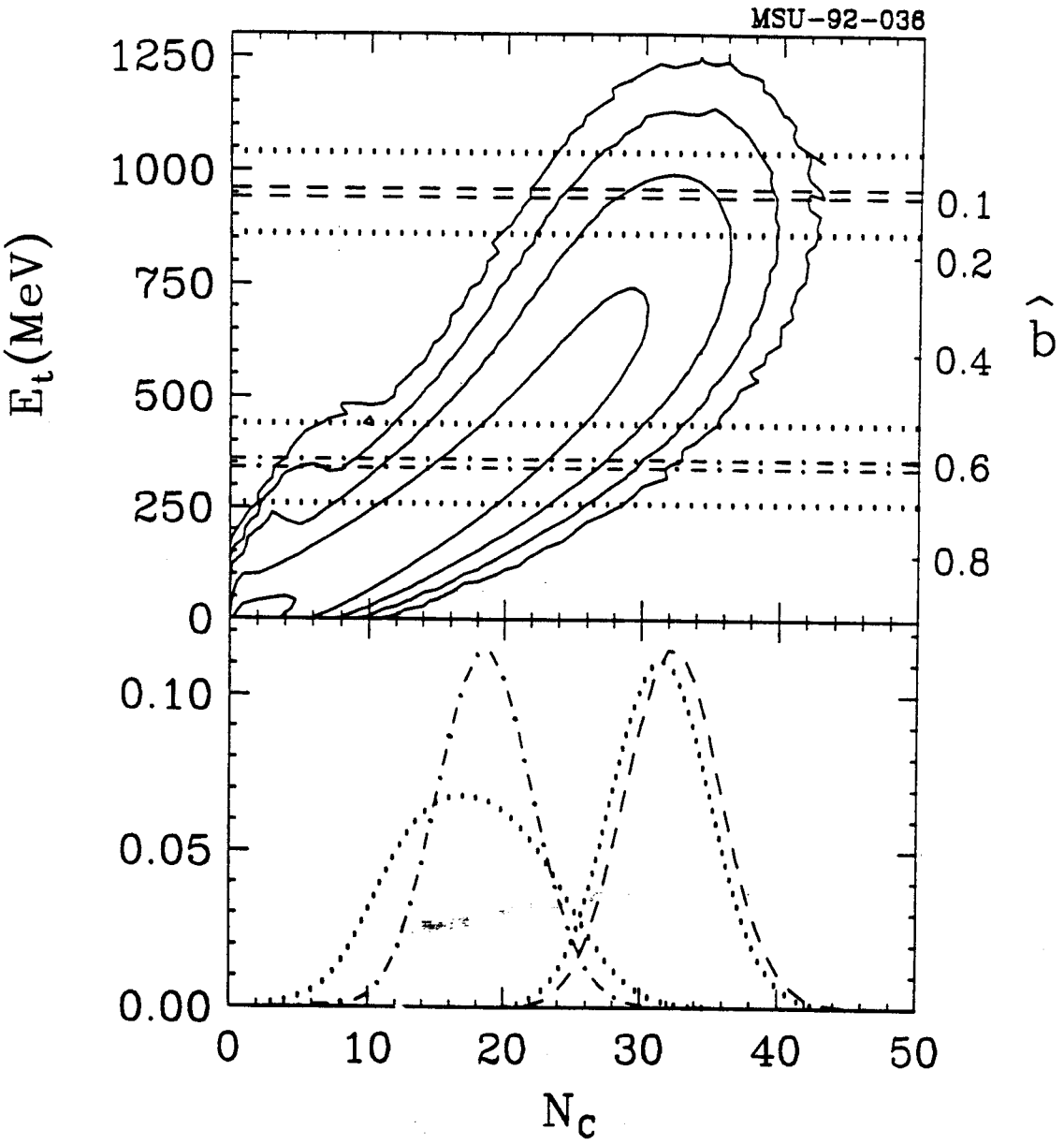


Figure 7.1 Upper part – Measured relation between transverse energy $E_t$ and total charged particle multiplicity for $^{36}Ar+^{197}Au$ reactions at E/A=110 MeV. Lower part – Charged particle multiplicity distributions for the cuts on $E_t$ indicated in the top panel.

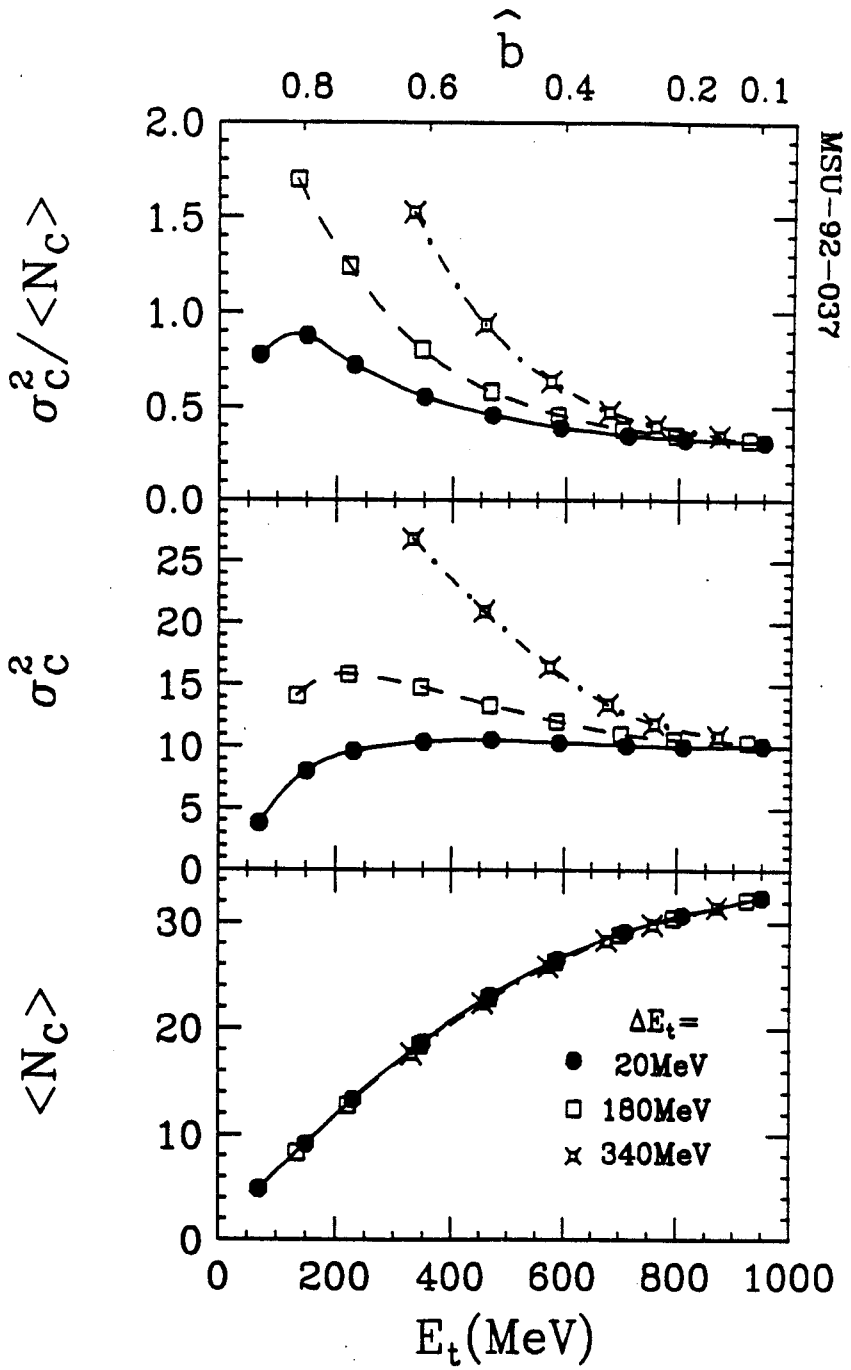


Figure 7.2 Bottom, center and top panels show the mean values $\langle N_c \rangle$, variances $\sigma_c^2$, and ratios $\sigma_c^2 / \langle N_c \rangle$ of the charged particle multiplicity distributions for $^{36}Ar+^{197}Au$ reactions at E/A=110 MeV. These quantities were selected by various cuts on the transverse energy; the mean values of these cuts are given by the abscissa and the widths are given in the figure. The upper scale gives the reduced impact parameter $\hat{b}(E_t)$.

widths of the applied cuts. However, for larger impact parameters, $\hat{b}$>0.4, wide cuts on $E_t$ cause an artificial broadening of the multiplicity distributions resulting from the superposition of distributions with different centroids. Poorly defined ensembles of events may therefore exhibit larger than Poisson variances, $\sigma_C^2 / \langle N_C \rangle > 1$. However, these large variances are an artifact from impact parameter averaging, and they do not represent intrinsic fluctuations of the decaying system.

Figure 7.3 depicts the relation between $\langle N_C \rangle$ and $\sigma_C^2 / \langle N_C \rangle$ extracted for central ($\hat{b}$<0.3) $^{36}$Ar+$^{197}$Au collisions at the incident energies of E/A=35, 50, 80 and 110 MeV. At all energies, the fluctuations of the charged particle multiplicity are considerably smaller than expected for Poisson distributions.

In order to explore effects resulting from phase space constraints such as energy conservation, we performed calculations with the bond-percolation model of refs. [Baue 85, Baue 86, Baue 88]. For simplicity, we assumed the decay of the composite system (A=233, Z=97). Calculations with bond-breaking parameters close to the critical value of $p$=0.7 have already been shown (Section 6.2) to reproduce the element distributions measured for the present reaction. Standard percolation calculations (in which the number of broken bonds is allowed to fluctuate from event to event) predict fluctuations in $N_C$ which are much larger than observed experimentaliy. Open circular points in Figure 7.3 show representative results for $p$=0.6 and 0.7. The indicated shift from the open circle to the open triangular point illustrates the magnitude of instrumental distortions for the case $p$=0.7. These distortions are too small to affect our conclusions. If one introduces a constraint analogous to energy conservation by requiring a fixed number of broken bonds, much narrower charged-particle distributions are produced (see open diamonds). These illustrative calculations suggest that the widths of impact-parameter-selected

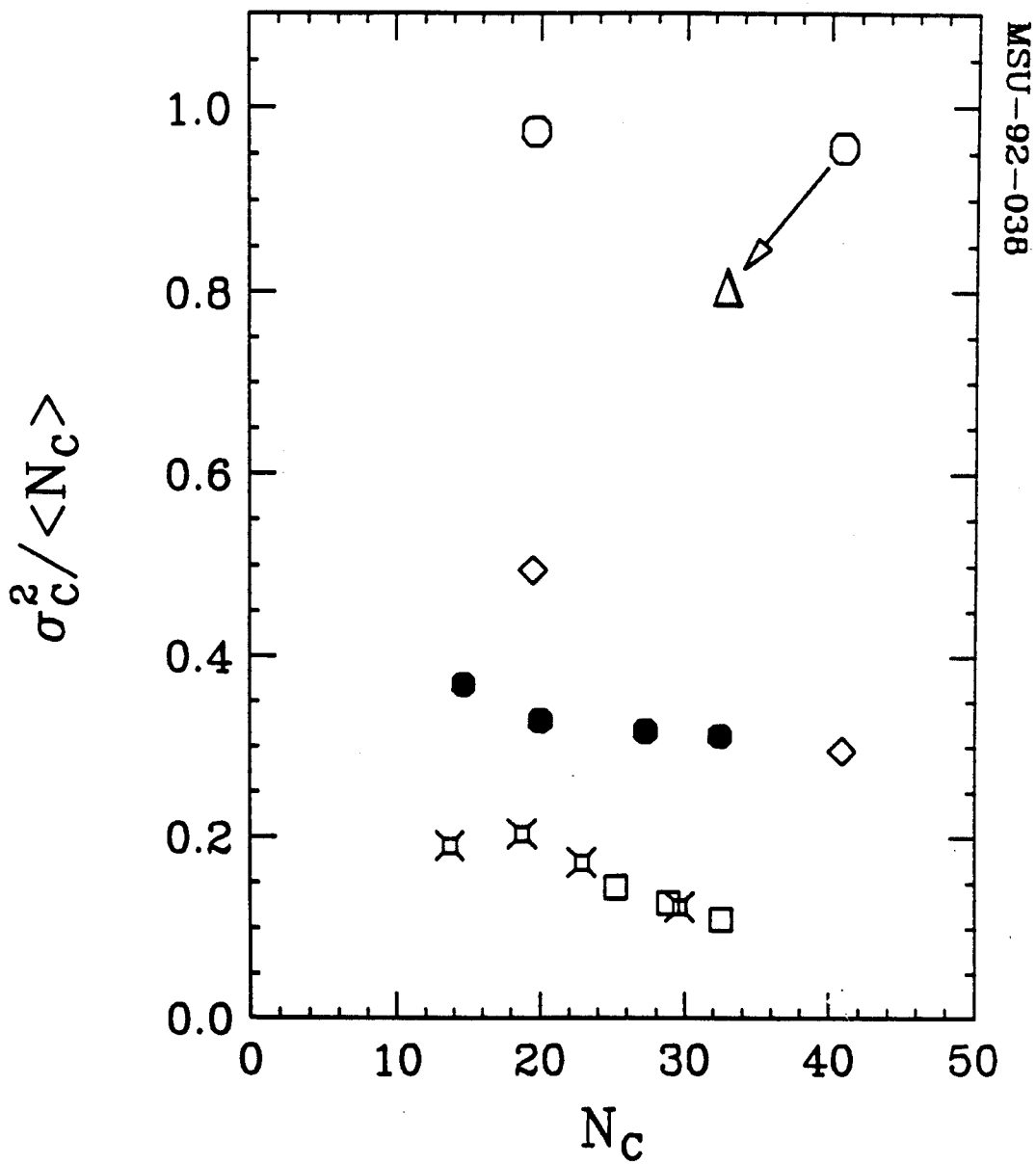


Figure 7.3 Relation between mean charged particle multiplicity $\langle N_c \rangle$ and the ratios $\sigma_c^2 / \langle N_c \rangle$. Solid circular points – experimental values extracted from near-central $^{36}$Ar+$^{197}$Au reactions at E/A=35, 50, 80 and 110 MeV. Open symbols are explained in the text.

charged-particle-multiplicity distributions are strongly affected by phase space constraints due to energy conservation.

This conclusion is corroborated by more realistic statistical model calculations which incorporate energy conservation on an event-by-event basis. The open square and star-shaped points show predictions of the sequential decay model GEMINI [Char 88] and of the Copenhagen fragmentation model [Bond 85a, Bond 85b, Barz 86], respectively. (The individual points represent results obtained for the decay of heavy compound nuclei at various excitation energies.) Both microcanonical and sequential decay models predict ratios $\sigma_c^2 / \langle N_c \rangle$ somewhat smaller than observed experimentally, and they do not show intermittency [Ella 92, Barz 92]. These smaller ratios from theoretical predictions may not indicate an inconsistency with experiment since we do not select a sharp value of impact parameter and/or excitation energy for the data in our event selection. In other words, the data contain some residual impact parameter averaging and represent an upper limit on the ratio $\sigma_c^2 / \langle N_c \rangle$.

In Figure 7.4, second factorial moments calculated from Equation (7.1) are presented as a function of binning resolution. The solid points represent experimental data selected by a narrow cut on central collisions at E/A=110 MeV. A slightly positive slope is observed, but the moments are smaller than unity. As argued above, this positive slope may be of trivial origin. In order to corroborate this point, we include the results of percolation calculations performed for $p$=0.7. Standard calculations for which the total number of broken bonds is allowed to fluctuate (open squares) predict large factorial moments, but no intermittency. When the number of broken bonds is constrained to be constant (open diamonds), the factorial moments are strongly reduced in magnitude, and they exhibit a small increase as a function

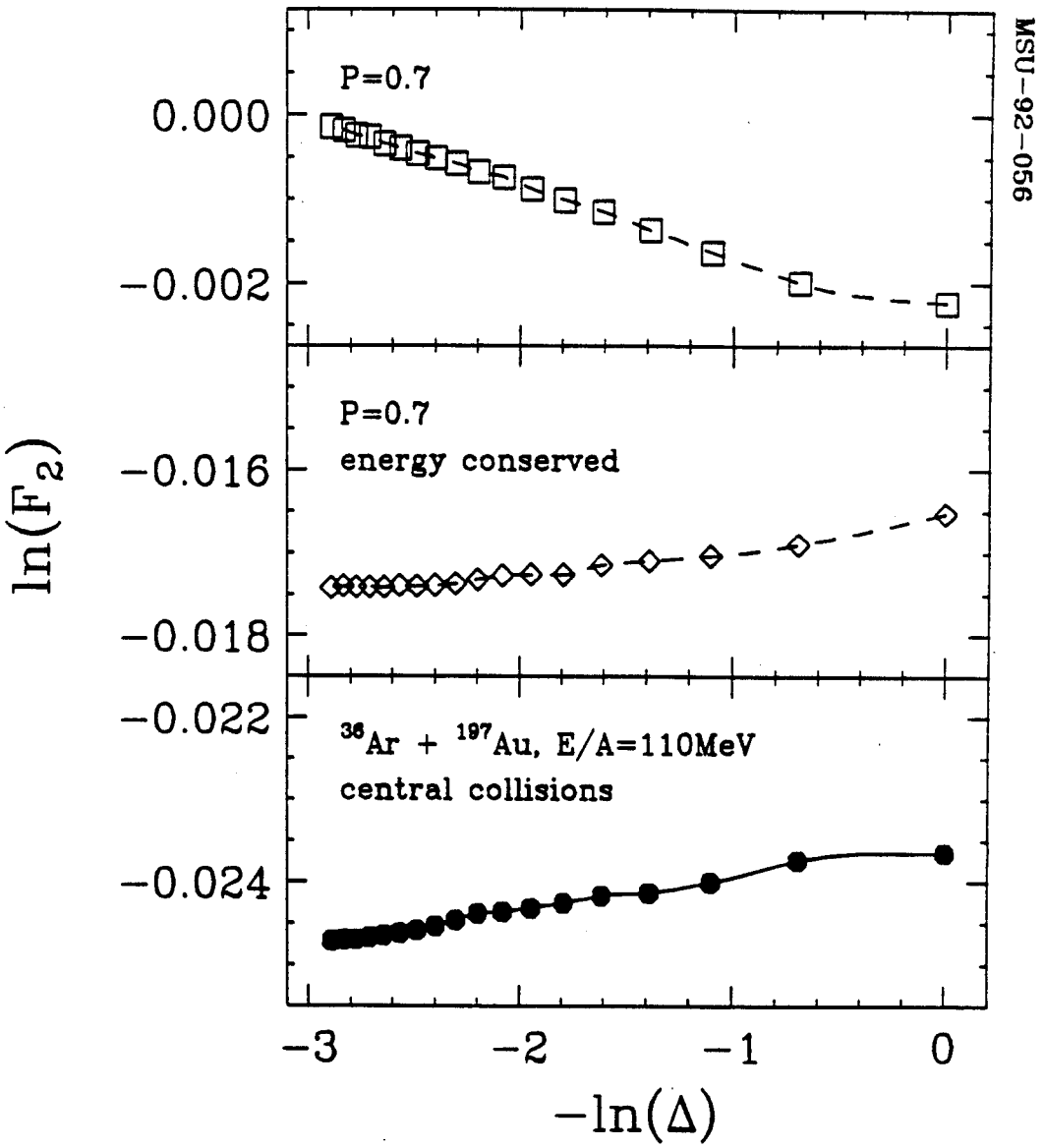


Figure 7.4 Scaled factorial moments as a function of binning resolution. Solid points show experimental results for central $^{36}$Ar+ $^{197}$Au collisions at E/A=110 MeV. Open points show results from percolation calculations using $p$=0.7. Open squares depict calculations in which the total number of broken bonds is allowed to fluctuate; open diamonds represent calculations in which the total number of bonds is kept fixed.

of binning resolution, similar to that observed experimentally. This increase appears to be of little significance.

It has recently been shown [Elat 92] that rate-equation models used to describe sequential decay processes are incapable of producing intermittency in fragment mass distributions. The few statistical models that could produce intermittency signals [DeAn 92, Barz 92] had to resort to mixing fragmentation events of very different initial excitation energies (effectively averaging over impact parameter). Our results are consistent with the small fluctuations predicted from the statistical multifragmentation approach for initial conditions with a narrow range of excitation energies.

# Chapter 8 Summary

In this work we have studied multifragment emission in $^{36}Ar+^{197}Au$ reactions at incident energies of E/A=50, 80 and 110 MeV. Of particular interest are central collisions, where the chance for equilibration of the system is the highest. To select such collisions we have made a detailed comparison of impact parameter scales constructed from the following global observables: the charged particle multiplicity $N_C$, the total transverse energy of an event $E_t$, the sum of the charge emitted at midrapidity $Z_y$ and the hydrogen multiplicity $N_1$ (the complement of $Z_{bound}$, the total charge bound in clusters of Z≥2). Each of these observables was evaluated in its ability to select events with suppressed projectile-like fragment emission and azimuthally anisotropic emission patterns. We found that scales constructed from $N_C$, $E_t$ and $Z_y$ provide comparable measures of impact parameter. Impact parameter scales based on $E_t$ provide slightly better resolution those based on $N_C$ or $Z_y$, while the scale constructed from $N_1$ is the worst. No additional selectivity for central collisions was found by imposing additional cuts on the transverse momentum directivity $D$, a variable which has been applied successfully in symmetric systems at higher bombarding energies where flow effects are important.

The mean values and variances of the multiplicity distributions of intermediate mass fragments were found to increase as a function of the total

charged-particle multiplicity; this may be interpreted as a rough measure of the internal energy of the fragment emitting system. An average multiplicity of 4 intermediate mass fragments is observed for the most central collisions at E/A=110 MeV. These large IMF multiplicities are consistent with predictions of a statistical model for evaporation from an expanding compound nucleus. The statistical decay model predictions are sensitive to the low-density nuclear equation of state.

In our investigation of fragment admixtures predicted by a standard bond-percolation model, we found rather good agreement with the values measured for $^{36}Ar + ^{197}Au$ collisions. On the other hand, larger fragment admixtures measured for $^{129}Xe + ^{197}Au$ collisions were found to be inconsistent with the model (for compact geometries).

We have also explored the multifragment breakup of different geometrical configurations (toroids and bubbles) with a bond-percolation model. Calculations for these finite systems predict enhanced fragment production for less compact decay configurations. For noncompact breakup geometries, the large fragment multiplicities observed for the $^{129}Xe + ^{197}Au$ reaction can be reconciled with predictions of the bond percolation model. Power law fits to the predicted mass distributions reveal a strong sensitivity of the extracted critical exponents to the geometry of the decaying system. Of course, the existence of such non-compact breakup configurations is not yet established. This question still remains to be answered.

In this fragmentation study we also include an intermittency analysis based on factorial moments that should permit the establishment of deviations from Poissonian fluctuations in the fragmentation process. We argue that an intermittency signal is meaningful only when it is observed in data selected by a narrow cut in impact parameter, and only when $F_2(\Delta)>1$.

These two conditions are never simultaneously met in our data. A surprisingly small value of about $\sigma_c^2 / \langle N_c \rangle \approx 0.3$ was measured in central collisions, independent of beam energy. The small widths of the charged particle distributions may be caused by the constraints imposed by energy conservation.

# Appendix A

## Physics tape format

The information is stored in buffers 4096 words long (integer*2). The first 16 words are the header. The first word past the header is the multiplicity of the event. This number is negative. The second word is the ringmask (one bit is set in this word for every ring that is hit). The third word is the RF word. The fourth is the number of intermediate mass fragments in the event.

Knowing the event multiplicity (number of detectors that fired), we can calculate the length of the event.

$$\text{length} = (\text{multiplicity}*5) + 4 \qquad \text{(A.1)}$$

To get to the next event you need to increment the pointer in the buffer by this length, i.e.

$$\text{next event} = \text{last event} + \text{length}. \qquad \text{(A.2)}$$

The information of the current event is stored and accessed as follows:

```
pointer = pointer + 4        ! move past the multiplicity, ringmask, RF,
                             ! and N_IMF words
do ii = pointer, next event, 5
      detector number = buffer(ii)     ! from 1-188
      slow = buffer(ii+1)              ! slow channel number 1-2048
      "real Z"= buffer(ii+2)           ! Z*25 from the PID maps
      PID number = buffer(ii+3)        ! two byte word: first byte=ISO, for
                                       ! isotope resolution
                                       ! second byte=IZ of the particle
      energy = buffer(ii+4)            ! in 100 keV units
end do
```

Particle identification is accomplished through the two words ISO and IZ as shown in the following table:

Table A.1 Physics tape format for particle identification.

| Particle type | IZ | ISO |
|---|---|---|
| Hydrogen punch through | 1 | 1 |
| Proton | 1 | 2 |
| Deuteron | 1 | 3 |
| Triton | 1 | 4 |
| $^{3}$He | 2 | 6 |
| $^{4}$He | 2 | 7 |
| $^{6}$He or Be decay to 2$\alpha$ | 2 | 9 |
| He punch through | 2 | 12 |
| Li punch through | 3 | 13 |
| 2$\alpha$ punch through | 2 | 14 |
| Unidentified particles | 0 | 8 |
| Fragments that punch through fast plastic | Z | 10 |
| Fission fragment | 64 | 11 |
| Fragments that stopped in the plastic, above the LCP reject line, in the prompt branch of fast-time spectrum | Z | 11 |
| Particles that stopped in the plastic, below the LCP reject line, in the prompt branch of fast-time spectrum | 0 | 11 |
| No isotope resolution | 1,2 | 5 |
| Hit detector (ring 1, position 5) | 0 | 0 |

The following detectors did not work properly during the experiment:

| Detector | Problem | Result |
|---|---|---|
| 5 | PMT pulsed | Hit detector |
| 16 | double image | no isotope resolution |
| 48 | discriminator double fired | no Z greater than 2 |
| 70 | double image | no Z greater than 2 |
| 169 | very small signal | no Z greater than 2 |

None of the above detectors have energies.

# Appendix B

## Temperature estimate from percolation theory

In the standard percolation model the bond breaking probability $p$ is linearly related to the excitation energy per nucleon $E^*$ of the compound system such that

$$p = \frac{E^*}{E_B} = \frac{E^*}{E_{bond}\frac{z}{2}} \tag{B.1}$$

where $E_B$ is nuclear matter binding energy per nucleon (16 MeV), $E_{bond}$ is the energy required to break one bond and $z$ is the number of nearest neighbors on the lattice ($z$=6). (By placing the nucleons on a lattice, the volume and surface effects in the binding energy are well approximated [Baue 88].) The total excitation energy of the system is simply

$$E^*_{tot} = pE_B A_{sys}. \tag{B.2}$$

$E^*_{tot}$ in the Fermi gas model is

$$E^*_{tot} = aT^2 \tag{B.3}$$

where $a$ is the level density parameter ($a = A_{sys}/8.5$ MeV) and $T$ is the temperature. The expression for the temperature is then

$$T = \sqrt{\frac{E_B A_{sys} p}{a}} = 11.7 MeV\sqrt{p}. \tag{B.4}$$

For the near-critical bond-breaking probability $p$=0.7, $T$=9.8 MeV.

# List of References


[Alar 92] J.P. Alard, Z. Basrak, N. Bastid, I.M. Belayev, M. Bini, Th. Blaich, R. Bock, A. Buta, R. Caplar, C. Cerruti, N. Cindro, J.P. Coffin, M. Crouau, P. Dupieux, J. Erö, Z.G. Fan, P. Fintz, Z. Fodor, R. Freifelder, L. Fraysse, S. Frolov, A. Gobbi, Y. Grigorian, G. Guillaume, N. Gerrmann, K.D. Hildenbrand, S. Hölbling, O. Houari, S.C. Jeong, M. Jorio, F. Jundt, J. Kecskemeti, P. Koncz, Y. Korchagin, R. Kotte, M. Krämer, C. Kuhn, I. Legrand, A. Lebedev, C. Maguire, V. Manko, T. Matulewicz, G. Mgebrishvili, J. Mösner, D. Moisa, G. Montarou, P. Morel, W. Neubert, A. Olmi, G. Pasquali, D. Pelte, M. Petrovici, G. Poggi, F. Rami, W. Reisdorf, A. Sadchikov, D. Schüll, Z. Seres, B. Sikora, V. Simion, S. Smolyankin, U. Sodan, N. Taccetti, K. Teh, R. Tezkratt, M. Trzaska, M.A. Vasiliev, P. Wagner, J.P. Wessels, T. Wienold, Z. Wilhelmi, D. Wohlfarth, and A.V. Zhilin, Phys. Rev. Lett. **69**, 889 (1992).

[Ardo 90] D. Ardouin, Z. Basrak, P. Schuck, A. Péghaire, F. Saint-Laurent, H. Delagrange, H. Doubre, C. Grégoire, A. Kyanowski, W. Mittig, J. Péter, Y.P. Viyogi, J. Québert, C.K. Gelbke, W.G. Lynch, M. Maier, J. Pochodzalla, G. Bizard, F. Lefèbvres, B. Tamain, B. Remaud, and F. Sébille, Nucl. Phys. **A514**, 564 (1990).

[Awes 81] T.C. Awes, G. Poggi, C.K. Gelbke, B.B. Back, B.G. Glagola, and V.E. Viola, Jr., Phys. Rev. **C24**, 89 (1981).

[Barz 86] H.W. Barz et al., Nucl. Phys. **A448**, 753 (1986).

[Barz 92] H.W. Barz, J.P. Bondorf, A.S. Botwina, R. Donangelo, I.N. Mishustin, H. Schulz and K. Sneppen, Nucl. Phys. **A545**, 213c (1992).

[Baue 85] W. Bauer, D.R. Dean, U. Mosel, and U. Post, Phys. Lett. B **150**, 53 (1985).

[Baue 86] W. Bauer, U. Post, D.R. Dean and U. Mosel, Nucl. Phys. **A452**, 699 (1986).

[Baue 87] W. Bauer et al., Phys. Rev. Lett. **58**, 863 (1987).

[Baue 88] W. Bauer, Phys. Rev. C **38**, 1927 (1988).

[Baue 92] W. Bauer, G.F. Bertsch and H. Schulz, Phys. Rev. Lett. **69**, 1888 (1992).

[Bert 83] G. Bertsch and P.J. Siemens, Phys. Lett. **126B**, 9 (1983).

[Bial 86] A. Bialas and R. Peschanski, Nucl. Phys. **B273**, 703 (1986).

[Bial 88] A. Bialas and R. Peschanski, Nucl. Phys. **B308** (1988) 857.

[Birk 64] J.B. Birks, *The Theory and Practice of Scintillation Counting* (Pergamon Press, New York, 1964) p.2

[Biro 86] T.S. Biro, J. Knoll and R. Richert, Nucl. Phys. **A459**, 692 (1986).

[Blai 80] J.P. Blaizot, Phys. Reports **64**, 171 (1980).

[Blum 91] Y. Blumenfeld et al., Phys. Rev. Lett. **66**, 576 (1991).

[Boal 88] D.H. Boal and J.N. Glosli, Phys. Rev. **C37**, 91 (1988).

[Boal 90] D.H. Boal and J.N. Glosli, Phys. Rev. **C42**, R502 (1990).

[Bond 85a] J.P. Bondorf et al., Nucl. Phys. **A443**, 321 (1985).

[Bond 85b] J.P. Bondorf et al., Nucl. Phys. **A444**, 460 (1985).

[Boug 88] R. Bougault, et al., Nucl. Phys. **A488**, 255c (1988).

[Boug 89] R. Bougault et al., Phys. Lett. **B232**, 291 (1989).

[Bowm 91] D.R. Bowman, G.F. Peaslee, R.T. de Souza, N. Carlin, C.K. Gelbke, W.G. Gong, Y.D. Kim, M.A. Lisa, W.G. Lynch, L. Phair, M.B. Tsang, C. Williams, N. Colonna, K. Hanold, M.A. McMahan, G.J. Wozniak, L.G. Moretto, and W.A. Friedman, Phys. Rev. Lett. **67**, 1527 (1991).

[Bowm 92] D.R. Bowman, C.M. Mader, G.F. Peaslee, W. Bauer, N. Carlin, R.T. de Souza, C.K. Gelbke, W.G. Gong, Y.D. Kim, M.A. Lisa, W.G. Lynch, L. Phair, M.B. Tsang, C. Williams, N. Colonna, K. Hanold, M.A. McMahan, G.J. Wozniak, L.G. Moretto, and W.A. Friedman, Phys. Rev. **C46**, 1834 (1992).

[Camp 86] X. Campi, J. Phys. **A19**, L917 (1986).

[Camp 88] X. Campi, Phys. Lett. **208B**, 351 (1988).

[Camp 92] X. Campi and H. Krivine, Z. Phys. **A344**, 81 (1992).

[Cava 90] C. Cavata, M. Demoulins, J. Gosset, M.C. Lemaire, D. L'Hôte, J. Poitou, and O. Valette, Phys. Rev. **C42**, 1760 (1990).

[Cerr 88] C. Cerruti et al., Nucl. Phys. **A476**, 74 (1988).

[Char 88] R.J. Charity et al., Nucl. Phys. **A483**, 371 (1988).

[Chen 87] Z. Chen, C.K. Gelbke, J. Pochodzalla, C.B. Chitwood, D.J. Fields, W.G. Gong, W.G. Lynch, and M.B. Tsang, Nucl. Phys. **A473**, 564 (1987).

[Chit 86] C.B. Chitwood, D.J. Fields, C.K. Gelbke, D.R. Klesch, W.G. Lynch, M.B. Tsang, T.C. Awes, R.L. Ferguson, F.E. Obenshain, F. Plasil, R.L. Robinson and G.R. Young, Phys. Rev. **C34**, 858 (1986).

[Coll 75] J.C. Collins and M.J. Perry, Phys. Rev. Lett. **34**, 1353 (1975).

[Cser 86] L.P. Csernai, and J.I. Kapusta, Phys. Rep. **131**, 233 (1986), and references therein.

[Curt 83] M.W. Curtin, H. Toki, and D.K. Scott, Phys. Lett. **B123**, 289 (1983).

[DeAn 92] A.R. DeAngelis, D.H.E. Gross and R. Heck, Nucl. Phys. A537, 606 (1992).

[deSo 90] R.T. de Souza et al., Nucl. Instr. and Meth. **A295**, 109 (1990).

[deSo 91] R.T. de Souza, L. Phair, D.R. Bowman, N. Carlin, C.K. Gelbke, W.G. Gong, Y.D. Kim, M.A. Lisa, W.G. Lynch, G.F. Peaslee, M.B. Tsang, H.M. Xu, F. Zhu, and W.A. Friedman, Phys. Lett. **B268**, 6 (1991).

[Dins 62] A. Dinsdale and F. Moore, "Viscosity and its Measurement", Chapman–Hill, London, 1962.

[Doss 87] K.G.R. Doss et al., Phys. Rev. Lett. **59**, 2720 (1987).

[Elat 92] B. Elatari, J. Richert and P. Wagner, Phys. Rev. Lett. **69**, 45 (1992).

[Elma 91] A. Elmaani, N.N. Ajitanand, J.M. Alexander, R. Lacey, S. Kox, E. Liatard, F. Merchez, T. Motobayashi, B. Noren, C. Perrin, D. Rebreyend, T.U. Chan, G. Anges, and S. Groult, Phys. Rev. **C43**, R2474 (1991).

[Fiel 86] D.J. Fields, W.G. Lynch, T.K. Nayak, M.B. Tsang, C.B. Chitwood, C.K. Gelbke, R. Morse, J. Wilczynski, T.C. Awes, R.L. Ferguson, F. Plasil, F.E. Obenshain, and G.R. Young, Phys. Rev. **C34**, 536 (1986).

[Fox 93] D. Fox, R.T. de Souza, L. Phair, D.R. Bowman, N. Carlin, C.K. Gelbke, W.G. Gong, Y.D. Kim, M.A. Lisa, W.G. Lynch, G.F. Peaslee, M.B. Tsang and F. Zhu, Phys. Rev. **C47**, R421 (1993).

[Frie 83a] W.A. Friedman and W.G. Lynch, Phys. Rev. **C28**, 16 (1983).

[Frie 83b] W.A. Friedman and W.G. Lynch, Phys. Rev. **C28**, 950 (1983).

[Frie 88] W.A. Friedman, Phys. Rev. Lett. **60**, 2125 (1988).

[Frie 89] W.A. Friedman, Phys. Rev. **C40**, 2055 (1989).

[Frie 90] W.A. Friedman, Phys. Rev. **C42**, 667 (1990).

[Gali 85] J. Galin, Nucl. Phys. **A447**, 519c (1985).

[Gold 78] A.S. Goldhaber and H.H. Heckman, Ann. Rev. Nucl. Part. Sci. **28**, 161 (1978).

[Gong 88] W.G. Gong, Y.D. Kim, G. Poggi, Z. Chen, C.K. Gelbke, W.G. Lynch, M.R. Maier, T. Murakami, M.B. Tsang, H.M. Xu and K. Kwiatkowski, Nucl. Instr. and Meth. **A268**, 190 (988).

[Gong 90] W.G. Gong, N. Carlin, C.K. Gelbke and R. Dayton, Nucl. Instr. and Meth. **A287**, 639 (1990).

[Gros 90] D.H.E. Gross, Rep. Prog. Phys. **53**, 605 (1990), and refs. therein.

[Hirs 84] A.S. Hirsch, A. Bujak, J.E. Finn, L.J. Gutay, R.W. Minich, N.T. Porile, R.P. Scharenberg, B.C. Stringfellow, and F. Turkot, Phys. Rev. **C29**, 508 (1984).

[Hube 91] J. Hubele, P. Kreutz, J.C. Adloff, M. Begemann-Blaich, P. Bouissou, G. Imme, I. Iori, G.J. Kunde, S. Leray, V. Lindenstruth, Z. Liu, U. Lynen, R.J. Meijer, U. Milkau, A. Moroni, W.F.J. Müller, C. Ngô, C.A. Ogilvie, J. Pochodzalla, G. Raciti, G. Rudolf, H. Sann, A. Schüttauf, W. Seidel, L. Stuttge, W. Trautmann, and A. Tucholski, Z. Phys. **A340**, 263 (1991).

[Jaqa 83] H.R. Jaqaman, A.Z. Mekjian, and L. Zamick, Phys. Rev. **C27**, 2782 (1983).

[Jaqa 84] H.R. Jaqaman, A.Z. Mekjian, and L. Zamick, Phys. Rev. **C29**, 2067 (1984).

[Jaqa 90] H.R. Jaqaman, G. Papp, and D.H.E. Gross, Nucl. Phys. **A514**, 327 (1990).

[Keho 92] W.L. Kehoe, A.C. Mignerey, A. Moroni, I. Iori, G.F. Peaslee, N. Colonna, K. Hanold, D.R. Bowman, L.G. Moretto, M.A. McMahan, J.T. Walton, and G.J. Wozniak, Nucl. Instr. Meth. A **311**, 258 (1992).

[Kim 89] Y.D. Kim et al., Phys. Rev. Lett. **63**, 494 (1989).

[Kim 92] Y.D. Kim, R.T. de Souza, D.R. Bowman, N. Carlin, C.K. Gelbke, W.G. Gong, W.G. Lynch, L. Phair, M.B. Tsang, and F. Zhu, Phys. Rev. **C45**, 338 (1992).

[Kuti 81] J. Kuti, J. Polònyi and K. Szlachányi, Phys. Lett. **B98**, 199 (1981).

[Lace 93] R. Lacey, A. Elmaani, J. Lauret, T. Li, W. Bauer, D. Craig, M. Cronqvist, E. Gualtieri, S. Hannuschke, T. Reposeur, A. Vander Molen, G.D. Westfall, W.K. Wilson, J.S. Winfield, J. Yee, S. Yennello, A. Nadasen, R.S. Tickle, and E. Norbeck, Phys. Rev. Lett. **70**, 1224 (1993).

[Li 93] T. Li et al., Phys. Rev. Lett. **70**, 1924 (1993).

[Litt 80] U. Littmark and J.F. Ziegler, *Handbook of Range Distributions for Energetic Ions in All Elements*, vol. 6 of *The Stopping and Ranges of Ions in Matter*, ed. J.F. Ziegler (Pergamon, New York, 1980).

[Lync 82] W.G. Lynch, L.W. Richardson, M.B. Tsang, R.E. Ellis, C.K. Gelbke and R.E. Warner, Phys. Lett. **108B**, 274 (1982).

[Lync 87] W.G. Lynch, Ann. Rev. Nucl. Part. Sci. **37**, 493 (1987), and references therein.

[Mahi 88] M. Mahi et al., Phys. Rev. Lett. **60**, 1936 (1988).

[Mana 62] W.W. Managan, IRE Trans. Nucl. Sci. NS-9 (3) (1962) 8.

[McLe 81] L.D. McLerran and B. Svetitsky, Phys. Lett. **B98**, 195 (1981).

[McMa 86] M.A. McMahan, G.J. Wozniak, C.M. Lyneis, D.R. Bowman, R.J. Charity, Z.H. Liu, L.G. Moretto, A.C. Mignerey and M.N. Namboodiri, Nucl. Instr. Meth. A **253**, 1 (1986).

[Meye 78] D. Meyerhofer, J. Appl. Phys. **49**, 3993 (1978).

[Moli 85] J.J. Molitoris and H. Stöcker, Phys. Lett. **162B** (1985) 47.

[More 75] L.G. Moretto, Nucl. Phys. **A247**, 211 (1975).

[More 92] L.G. Moretto et al., Phys. Rev. Lett. **69**, 1884 (1992).

[Morj 88] M. Morjean, et al., Phys. Lett. **B203**, 215 (1988).

[Morl 79] P.D. Morley and M.B. Kislinger, Phys. Rep. **51**, 63 (1979) and references therein.

[Naya 92] T.K. Nayak, T. Murakami, W.G. Lynch, K. Swartz, D.J. Fields, C.K. Gelbke, Y.D. Kim, J. Pochodzalla, M.B. Tsang, F. Zhu, and K. Kwiatkowski, Phys. Rev. **C65**, 132 (1992), and refs. therein.

[Ngô 90] H. Ngô, C. Ngô, F.Z. Ighezou, J. Debois, S. Leray, and Y.-M. Zheng, Z. Phys. **A337**, 81 (1990).

[Norb 87] E. Norbeck, T.P. Dubbs and L.G. Sobotka, Nucl. Instr. and Meth. **A262**, 564 (1987).

[Ogil 89a] C.A. Ogilvie, D. Cebra, J. Clayton, S. Howden, J. Karn, A. Vander Molen, G.D. Westfall, W.K. Wilson, and J.S. Winfield, Phys. Rev. **C40**, 654 (1989).

[Ogil 89b] C.A. Ogilvie, D.A. Cebra, J. Clayton, P. Danielewicz, S. Howden, J. Karn, A. Nadasen, A. Vander Molen, G.D. Westfall, W.K. Wilson, and J.S. Winfield, Phys. Rev. **C40**, 2592 (1989).

[Ogil 90] C.A. Ogilvie, W. Bauer, D.A. Cebra, J. Clayton, S. Howden, J. Karn, A. Nadasen, A. Vander Molen, G.D. Westfall, W.K. Wilson, and J.S. Winfield, Phys. Rev. **C42** (1990) R10.

[Ogil 91] C.A. Ogilvie et al., Phys. Rev. Lett. **67**, 1214 (1991).

[Pana 84] A.D. Panagiotou et al., Phys. Rev. Lett. **52**, 496 (1984).

[Peil 89] G. Peilert et al., Phys. Rev. **C39**, 1402 (1989).

[Phai 92a] L. Phair, D.R. Bowman, C.K. Gelbke, W.G. Gong, Y.D. Kim, M.A. Lisa, W.G. Lynch G.F. Peaslee, R.T. de Souza, M.B. Tsang and F. Zhu, Nucl. Phys. **A458**, 489 (1992).

[Phai 92b] L. Phair et al., Phys. Lett. B **285**, 10 (1992).

[Plos 90] M. Ploszajczak and A. Tucholski, Phys. Rev. Lett. **65**, 1539 (1990).

[Poch 87] J. Pochodzalla, C.K. Gelbke, W.G. Lynch, M. Maier, D. Ardouin, H. Delagrange, H. Doubre, C. Grégoire, A. Kyanowski, W. Mittig, A. Péghaire, J. Péter, F. Saint-Laurent, B. Zwieglinski, G. Bizard, F. Lefèbvres, B. Tamain, and J. Québert, Y.P. Viyogi, W.A. Friedman, and D.H. Boal, Phys. Rev. C35 (1987) 1695.

[Ritt 88] H.G. Ritter, Nucl. Phys. **A488**, 651c (1988).

[Rose 84] J.H. Rose, J.P. Vary, and J.R. Smith, Phys. Rev. Lett. **53**, 344 (1984).

[Saye 76] G. Sayer, H., Chandra, and U. Mosel, U. Nucl. Phys. **A24**, 221 (1976).

[Schl 87] T.J. Schlagel, and V.R. Pandharipande, Phys. Rev. **C36**, 162 (1987).

[Shur 80] E.Shuryak, Phys. Rep. **61**, 71 (1980) and references therein.

[Siem 83] P.J. Siemens, Nature **305**, 410 (1983).

[Snep 88] K. Sneppen and L. Vinet, Nucl. Phys. **A480**, 342 (1988).

[Stoc 86] R. Stock, Phys. Reports. **135**, (1986) 259.

[Stöc 86] H. Stöcker and W. Greiner, Phys. Reports **137**, 277 (1986).

[Sull 90] J.P. Sullivan, J. Péter, D. Cussol, G. Bizard, P. Brou, M. Louvel, J.P. Patry, R. Regimbart, J.C. Steckmeyer, B. Tamain, E. Crema, H. Doubre, K. Hagel, G.M. Jin, A. Péghaire, F. Saint-Laurent, Y. Cassagnou, R. Legrain, C. Lebrun, E. Rosato, R. McGrath, S.C. Jeong, S.M. Lee, Y. Nagashima, T. Nakagawa, M. Ogihara, J, Kasagi, and T. Motobayashi, Phys. Lett. **B249** (1990) 8.

[Troc 89] R. Trockel et al., Phys. Rev. **C39**, 729 (1989).

[Tsan 84a] M.B. Tsang, W.G. Lynch, C.B. Chitwood, D.J. Fields, D.R. Klesch, C.K. Gelbke, G.R. Young, T.C. Awes, R.L. Ferguson, F.E. Obenshain, F. Plasil and R.L. Robinson, Phys. Lett. B **148**, 265 (1984).

[Tsan 84b] M.B. Tsang, C.B. Chitwood, D.J. Fields, C.K. Gelbke, D.R. Klesch, W.G. Lynch, K. Kwiatkowski and V.E. Viola, Jr., Phys. Rev. Lett. **52**, 1967 (1984).

[Tsan 86] M.B. Tsang, R.M. Ronningen, G. Bertsch, Z. Chen, C.B. Chitwood, D.J. Fields, C.K. Gelbke, W.G. Lynch, T. Nayak, J. Pochodzalla, T. Shea, and W. Trautmann, Phys. Rev. Lett. **57**, 559 (1986).

[Tsan 88] M.B. Tsang, W.G. Lynch, R.M. Ronningen, Z. Chen, C.K. Gelbke, T. Nayak, J. Pochodzalla, F. Zhu, M. Tohyama, W. Trautmann, and W. Dünnweber, Phys. Rev. Lett. **60**, 1479 (1988).

[Tsan 89a] M.B. Tsang, G.F. Bertsch, W.G. Lynch, and M. Tohyama, Phys. Rev. **C40**, 1685 (1989).

[Tsan 89b] M.B. Tsang, Y.D. Kim, N. Carlin, Z. Chen, R. Fox, C.K. Gelbke, W.G. Gong, W.G. Lynch, T. Murakami, T.K. Nayak, R.M. Ronningen, H.M. Xu, F. Zhu, L. Sobotka, D. Stracener, D.G. Sarantites, Z. Majka, V. Abenante, and H. Griffin, Phys. Lett. **B220**, 492 (1989).

[Tsan 90] M.B. Tsang, Y.D. Kim, N. Carlin, Z. Chen, C.K. Gelbke, W.G. Gong, W.G. Lynch, T. Murakami, T. Nayak, R.M. Ronningen, H.M. Xu, F. Zhu, L.G. Sobotka, D.W. Stracener, D.G. Sarantites, Z. Majka, and V. Abenante, Phys. Rev. **C42**, R15 (1990).

[Tsan 91] M.B. Tsang, R.T. de Souza, Y.D. Kim, D.R. Bowman, N. Carlin, C.K. Gelbke, W.G. Gong, W.G. Lynch, L. Phair, and F. Zhu, Phys. Rev. **C44**, 2065 (1991).

[Wadd 85] C.J. Waddington and P.S. Freier, Phys. Rev. C **31**, 888 (1985).

[Wang 91] S. Wang, Y.Z. Jiang, Y.M. Liu, D. Keane, D. Beavis, S.Y. Chu, S.Y. Fung, M. Vient, C. Hartnack and H. Stöcker Phys. Rev. **C44**, 1091 (1991).

[Wils 90] W.K. Wilson, W. Benenson, D.A. Cebra, J. Clayton, S. Howden, J. Karn, T. Li, C.A. Ogilvie, A. Vander Molen, G.D. Westfall, J.S. Winfield, and A. Nadasen, Phys. Rev. **C41**, R1881 (1990).